

Photolysis of Azido(5,10,15,20-tetraphenyl-
porphyrin-21,23-diido)iron(III) –
Ultrafast Time-Resolved Infrared and
Visible Spectroscopy

Dissertation
zur
Erlangung des Doktorgrades (Dr. rer. nat.)
der
Mathematisch-Naturwissenschaftlichen Fakultät
der
Rheinischen Friedrich-Wilhelms-Universität Bonn

vorgelegt von
Stefan Flesch
aus Neuwied

Bonn, 2024

Angefertigt mit Genehmigung
der Mathematisch-Naturwissenschaftlichen Fakultät
der Rheinischen Friedrich-Wilhelms-Universität Bonn

1. Gutachter: Prof. Dr. Peter Vöhringer
2. Gutachter: Prof. Dr. Ulrich Kubitscheck

Tag der Promotion: 03.07.2024

Erscheinungsjahr: 2024

Danksagung

An dieser Stelle möchte ich mich bei all denjenigen bedanken, die mir auf vielfältige Art und Weise geholfen haben, diese Forschungsarbeit anzufertigen. Allen voran ist hier natürlich Prof. Dr. Peter Vöhringer zu nennen, der mir dieses faszinierende Thema vorgeschlagen, mir die experimentellen Mittel zur Verfügung gestellt und durch konstruktive Diskussionen den Fortschritt meiner Forschung unterstützt hat. Dabei möchte ich vor allem seine motivierende Einstellung und sein ernstgemeintes Interesse an meiner Arbeit loben. Außerdem möchte ich Dr. Jörg Lindner danken, für seine wertvolle Hilfe und seine verständlichen Erklärungen zum Umgang mit den experimentellen Aufbauten und für das Korrekturlesen dieser Arbeit. Aus denselben Gründen und darüber hinaus für unsere gemeinsamen Messungen am Transient Absorption Spectrometer, deren Ergebnisse in diese Dissertation eingeflossen sind, gebührt mein Dank Dr. Luis Domenianni. Selbstverständlich möchte ich mich neben den Genannten auch den übrigen Mitarbeiterinnen und Mitarbeitern der Arbeitsgruppe Vöhringer, insbesondere meinem Bürokollegen Jonas Schmidt, erkenntlich zeigen. Sie haben meine Promotionszeit durch eine angenehme Arbeitsatmosphäre, gemeinsame Pausen und unterhaltsame Gespräche verschönert. Ebenso sind hier die Mitarbeiter der Werkstätten des Clausius-Instituts für Physikalische und Theoretische Chemie zu nennen, deren Tatkräftigkeit zum Erfolg meiner Forschung beigetragen hat. Darüber hinaus danke ich Prof. Dr. Ulrich Kubitscheck dafür, dass er die Rolle als zweiter Gutachter dieser Dissertation übernommen hat, und Prof. Dr. Connie Lu und Prof. Dr. Sebastian Hofferberth dafür, dass sie sich als Mitglieder der Promotionskommission zur Verfügung gestellt haben. Des Weiteren bedanke ich mich beim Fonds der Chemischen Industrie (Verband der Chemischen Industrie e.V.), für die finanzielle Unterstützung in Form eines Kekulé-Stipendiums. Schließlich drücke ich meinen Dank meinen Freunden, besonders meiner Mitbewohnerin Ramona Roß, und meiner Familie aus, zum einen für ihren moralischen Beistand in dieser Zeit, aber vor allem dafür, dass sie mich davor bewahrt haben, zu sehr in meiner Arbeit zu versinken.

Contents

1	Introduction	1
2	Background	6
2.1	Methodical Background	6
2.1.1	Basics of Spectroscopy	6
2.1.2	Electronic and Vibrational Spectroscopy	8
2.1.3	Time-Resolved Spectroscopy	10
2.1.4	Spectral Line Shapes	14
2.1.5	Kinetic Equations	15
2.2	Chemical Background	17
2.2.1	Photochemistry of Azido Complexes	17
2.2.2	Quenching Reactions	20
2.2.3	Electronic Structure Considerations	23
2.2.4	Structure-Sensitive, Spectroscopic Characteristics of Metalloporphyrins	29
2.2.5	Photochemistry of Metalloporphyrins	32
3	Methods	35
3.1	Synthesis	35
3.2	Spectroscopic Methods	36
3.2.1	Stationary Spectroscopy	36
3.2.2	Rapid-Scan Spectroscopy	36
3.2.3	UV/Vis-Pump/mIR-Probe Spectroscopy	37
3.2.4	UV/Vis-Pump/Vis-Probe Spectroscopy	40
3.3	Computational Methods	41
4	Stationary Spectroscopy	43
4.1	FTIR Spectroscopy	43
4.2	UV-Vis Spectroscopy	46
5	Time-Resolved Spectroscopy	50
5.1	Quantum Yield of Photoconversion and Distribution of the Products	50
5.2	Primary Processes after Photoexcitation – Low-Energy Excitation	53
5.2.1	Dependence on the Pump Pulse Energy	53
5.2.2	400 nm-Pump/1900-2100 cm ⁻¹ -Probe Experiment	55
5.2.3	400 nm-Pump/Vis-Probe Experiment	59
5.2.4	De-excitation Scheme	65
5.3	Electronic Structures of the Photoproducts – High-Energy Excitation	66
5.3.1	400 nm-Pump/1410-1500 cm ⁻¹ -Probe and -1550-1620 cm ⁻¹ -Probe Experiments	66
5.3.2	400 nm-Pump/1300-1370 cm ⁻¹ -Probe Experiment	67

5.3.3	400 nm-Pump/1240-1310 cm ⁻¹ -Probe Experiment	69
5.3.4	Notation of Electron Configurations	72
5.3.5	Quantum Chemical Calculations & Interpretation – Part 1: π -Radical Porphyrin States	73
5.3.6	Quantum Chemical Calculations & Interpretation – Part 2: Triplet Porphyrin States	79
6	Summary and Outlook	84
7	Bibliography	87
8	Appendix	94
8.1	Additional Stationary FTIR Spectra	94
8.2	Natural Transition Orbitals and Excitation Energies	96
8.3	Additional UV/Vis-Pump/mIR-Probe Data	104
8.4	Additional UV/Vis-Pump/Vis-Probe Data	109
8.5	Detailed Computational Procedure and Results	111
8.6	List of Figures	115
8.7	List of Tables	117
8.8	List of Acronyms and Formula Symbols	117
8.9	DFT-Optimized Molecular Geometries	121
8.10	Research Article: Photolysis of an Archetypal Model Complex. Photooxidation Versus Photoreduction of Azido(porphinato)iron(III)	128

List of Publications

1. S. Flesch, P. Vöhringer, *Chem. Eur. J.* **2023**, *29*, e202301207.

DOI: <https://doi.org/10.1002/chem.202301207>

The published version is reproduced in section 8.10 of the thesis. No changes were made.

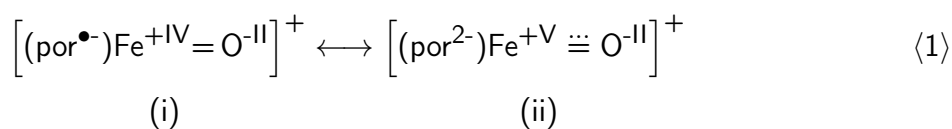
Available under license: CC BY-NC-ND 4.0

<https://creativecommons.org/licenses/by-nc-nd/4.0/>

1 Introduction

For several decades now, exceptional effort has been devoted to the synthetic preparation^[1–3] and examination of the reactivity,^[4–7] molecular,^[8–11] and electronic structures^[12,13] of terminal, high-valent oxidometal and nitridometal complexes. Such compounds are characterized by a transition metal center in a high oxidation state, typically equal or larger than +IV,^[10,14,15] linked to an O²⁻- or N³⁻-ligand via a multiple bond.^[16,17] The tremendous interest in these species arises from the occurrence of oxidoiron(+IV) complexes as reactive intermediates in the catalytic cycles of numerous metalloenzymes.^[18–21] These biocatalysts are capable of performing a variety of remarkable reactions in aqueous solution, under ambient conditions, and (almost) exclusive application of earth-abundant elements,^[22,23] as opposed to many industrial processes, often relying on extreme temperature and pressure, organic solvents, or catalysts based on rare metals.^[24,25] In addition, biosynthetic processes exhibit an outstanding performance with regard to regio- and stereoselectivity. Hence, chemists are tempted to develop a profound understanding of the natural catalysts in order to exploit their unique reactivity in artificial processes.

The presumably most prominent examples are enzymes of the superfamily cytochrome P450, which are widely distributed in nature and responsible for selective hydroxylations of hydrocarbons, epoxidations of alkenes, and other reactions, facilitated by controlled activation of dioxygen molecules.^[26,27] The catalytically active side of these enzymes consists of an iron(+III) protoporphyrin IX complex (see Figure 1(a)), a prosthetic group referred to as 'heme', linked to the protein backbone by an axially coordinated thiolate anion group provided by a deprotonated cysteine (Cys) unit.^[26,28] Due to their universal occurrence in metabolic transformations, the underlying catalytic cycles conducted by these enzymes have been subjected to extensive investigations and several sequential steps can already be considered as largely understood.^[21,29,30] Nevertheless, the details of the crucial oxygen atom insertion into inert C–H bonds are hitherto not fully clarified. This intriguing reaction step is assumed to proceed via a sequence of a hydrogen atom abstraction and an oxygen rebound enabled by an oxidoiron species two oxidizing equivalents above the ferric resting state of the heme group,^[31–33] i.e. formally an iron(+V) complex. In order to elucidate the properties of this reactive compound, several artificial model systems have been prepared, trapped in inert, low-temperature matrices, and analyzed by nuclear magnetic resonance (NMR),^[34–36] ultraviolet-to-visible (UV-Vis),^[37–39] electron paramagnetic resonance (EPR),^[40,41] and Mössbauer^[42–45] spectroscopy. More recently, generation, trapping, and characterization of the elusive intermediates of cytochrome P450 enzymes themselves became feasible.^[46–48] By this means, it was demonstrated that one oxidizing equivalent is in fact not removed from the iron center, but from the π -system of the porphyrindiido ligand. Hence, the reactive intermediate - the so-called *Compound I* - is best described as an oxidoferryl species, carrying a porphyrinidyl radical anion ligand (por^{•-}, a ' π -radical' ligand), [Fe^{+IV}(por^{•-})(O²⁻)]⁺ (i), as depicted in Figure 1(a), rather than an oxidoperferryl species, embedded in a dianionic porphyrin ligand (por²⁻), [Fe^{+V}(por²⁻)(O²⁻)]⁺ (ii).^[37,49]



The possibility of two distinct electronic structures of the same molecule is referred to as *valence tautomerism* (cf. Equation (1)).^[50] In this case, it arises from the fact that the highest occupied π -orbitals of the porphyrindiido ligand are of similar energy as the d-orbitals of the complexed iron atom.^[51–53] With increasing oxidation state of the iron cation, its d-orbitals are lowered in energy and, thus, the alternative oxidation of the macrocyclic ligand becomes more likely.^[54,55] In other words, structure (ii) is not stable because the redox non-innocent porphyrindiido ligand will partially compensate the high electron deficiency at the iron center by an intramolecular one-electron transfer, yielding structure (i).

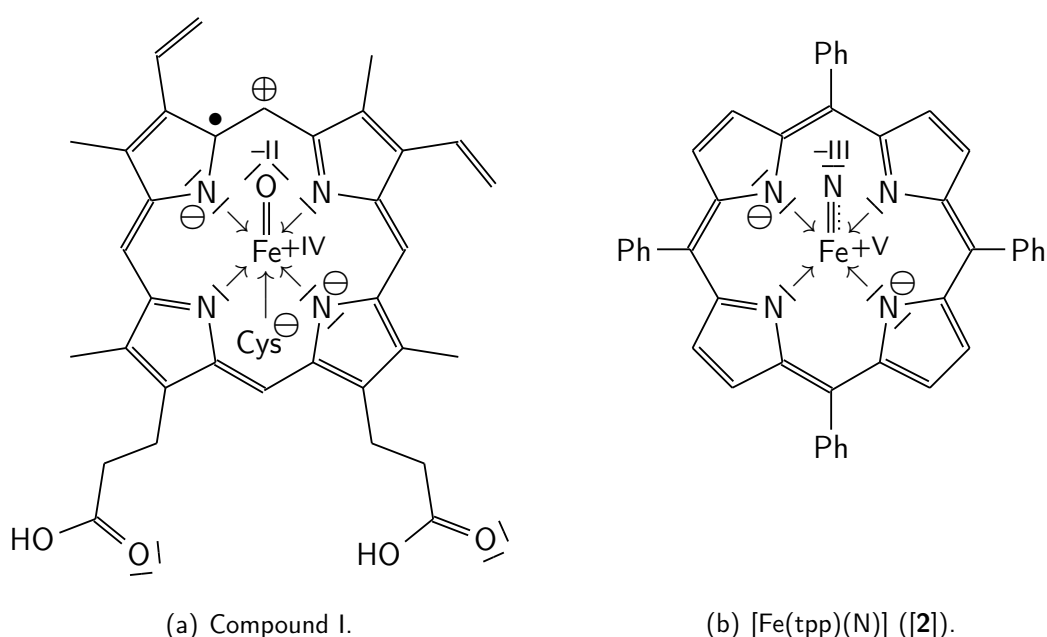


Figure 1: Lewis formulae of (a) Compound I and (b) [Fe(tpP)(N)] ([2]). Roman numerals indicate the oxidation states of iron atoms and the axial oxygen and nitrogen atom. For clarity, only one resonance structure is depicted for each complex. The two negative formal charges at the opposite nitrogen atoms of the porphyrin macrocycle are actually delocalized over the σ -lone pairs of all four nitrogen atoms. Likewise, the unpaired electron and positive formal charge in (a) are in fact delocalized over all atoms contributing to the extended π -system. The cysteine group in (a) connects the oxidoheme group to the protein backbone.

Interestingly, although the ferryl π -radical structure (i) has been proven to be the electronic ground state of Compound I, the perferryl structure (ii), representing an excited state of the complex, was proposed to play a significant role in at least some reactions.^[1,56–60] This hypothesis was suggested as examinations of artificial model complexes of Compound I could not reproduce all aspects of its reactivity successfully.^[61–65] In fact, especially the captivating hydroxylations of alkanes could be hardly mimicked, indicating a more reactive species to be

imperative. These findings pointed out that intrinsic parts of the underlying reaction mechanism are not yet sufficiently understood and more exploration in this field is urgently required.

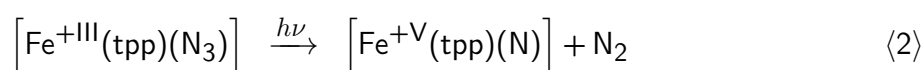
In contrast to the introduction of hydroxyl groups by direct insertion of an oxygen atom into alkanes, nature utilizes preoxidized carbon centers to build amine groups. For instance, the synthesis of glutamate and glutamine from ammonia and α -ketoglutarate represents a key step in the generation of amino acids.^[66] Amino functionalities in other molecules are realized via transamination using glutamate and catalyzed by the metal-free enzyme class of aminotransferases.^[67] Still, the actual starting point of the biogeochemical nitrogen cycle is the conversion of atmospheric dinitrogen to ammonia ('nitrogen fixation'), a process only a few bacterial species are capable of conducting.^[68] This reaction is, however, catalyzed by nitrogenases carrying metal-containing clusters, e.g. $[\text{Fe}_7\text{MoS}_9\text{C}]$,^[69–72] in their active site rather than heme complexes.

In general, the utilization of dinitrogen as a building block for synthesis is more challenging than in the case of dioxygen, in biochemistry as well as in industrial chemistry.^[72] This is a consequence of the lower reactivity of N_2 compared to O_2 , resulting from the higher bond dissociation energy and larger HOMO-LUMO gap.^[73] Despite that, the reduction of dinitrogen to ammonia via the Haber-Bosch process^[73,74] is one of the most important and frequently conducted industrial reactions in the world, with an annual production volume of ca. 150 megatons (in the year 2022),^[75] mostly devoted to the production of fertilizers. The Haber-Bosch process requires a high temperature and the utilization of solid iron as heterogeneous catalyst in order to facilitate the required dissociation of the $\text{N}\equiv\text{N}$ triple bond.^[76,77] In addition, high pressure is needed to shift the thermodynamic equilibrium towards the product. Therefore, it is a highly energy demanding and expensive process and a replacement by a more sustainable and efficient method is desirable.

In spite of nature employing small metal clusters to harness dinitrogen, high-valent, mononuclear nitridometal complexes were suggested as intermediates for potential artificial reactions facilitating both dinitrogen activation and nitrogen transfer reactions.^[4,78–81] In this regard, several studies in recent years have yielded first accomplishments. At least by using rare metals, mononuclear nitrido complexes were generated by cleavage of the $\text{N}\equiv\text{N}$ bond of dinitrogen-bridged, dinuclear complexes,^[82–84] and reactions with dihydrogen to ammonia could be achieved.^[85–88] Moreover, different types of nitridometal complexes were revealed to have 2- e^- -N-transfer reactivity towards phosphines,^[7,11,89,90] carbon monoxide,^[91,92] and isonitriles^[93,94] or to catalyze nitrile-alkyne cross metatheses.^[95–97] Porphyrindiido complexes of manganese and chromium were found to undergo reversible^[98–100] and irreversible^[101,102] 3- e^- -N-transfer reactions. And lastly, derivatives of cytochrome P450 enzymes, artificially provided with a nitrido ligand, were recently observed to facilitate C–H activation via hydrogen atom abstraction from alkanes.^[103]

Despite their starting application as reagents and catalysts and their similarity to the well-examined and biologically relevant Compound I, nitridoiron species complexed by porphyrindiido ligands have been investigated only scarcely so far. This is especially surprising because

seminal work in this research field was focused on exactly these compounds. In fact, the first terminal nitridoiron complex, reported by Wagner and Nakamoto already in the late 1980s, was nitrido(5,10,15,20-tetraphenylporphyrin-21,23-diido)iron(+V), $[\text{Fe}^{+\text{V}}(\text{tpp})(\text{N})]$ ([2]),¹ bearing the symmetrically substituted 5,10,15,20-tetraphenylporphyrin-21,23-diido (tpp^{2-}) auxiliary ligand.^[104,105] In this pioneering work, thin-films of the precursor complex azido(5,10,15,20-tetraphenylporphyrin-21,23-diido)iron(+III), $[\text{Fe}^{+\text{III}}(\text{tpp})(\text{N}_3)]$ ([1]), on copper surfaces at ca. 30 K were irradiated over several minutes with visible light of different wavelengths to undergo a photolytic cleavage of dinitrogen, according to Equation (2). Subsequently, the formation of the product complex [2] was evidenced by detection of the characteristic band of its $\text{Fe}\equiv\text{N}$ stretching vibration at a frequency of 876 cm^{-1} by resonance Raman (RR) spectroscopy. Although vibrational spectroscopy is generally not directly sensitive to the electronic structure of a molecule, the authors suggested [2] to be a high-spin iron(+V) complex having a closed-shell porphyrindiido ligand, based on the collected RR spectra.

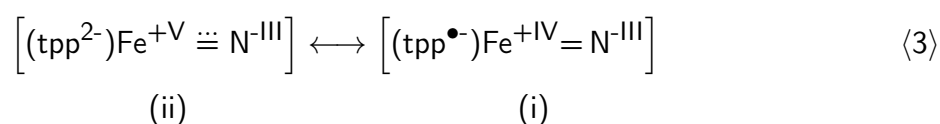


In fact, EPR and Mössbauer spectroscopy are more appropriate methods to clarify the electronic structure of the complex unequivocally, since they give direct information regarding the localization of unpaired electrons^[106] and the oxidation state of the iron center.^[107] Yet, measurements of this compound using these techniques have not been reported until a publication by Ye et al. in 2019.^[108] In this study, [2] was likewise prepared starting from [1] under continuous irradiation with visible light, here in a frozen dichloromethane (DCM) solution. The recorded spectra, in conjunction with results from multi-reference wavefunction theory, revealed [2] to be in fact a closed-shell porphyrindiido complex of iron(+V) (cf. Figure 1(b)), although in a low-spin state as opposed to the earlier assignment. Thus, this nitrido complex exhibits an electronic ground state configuration very different from that of the related Compound I, irrespective of the similar molecular structure.

[2] is known to be a highly reactive and elusive species, undergoing follow-up reactions to a dinuclear complex in solution easily.^[109,110] Moreover, its generation via photolysis of [1] was found to be very inefficient.^[105,108,110] For this reason, both the studies of Nakamoto and Ye relied on trapping the complex in inert, low-temperature environments in order to facilitate the synthesis and the time-consuming measurements by means of conventional spectroscopy. Similarly, investigation on other high-valent nitridoiron complexes carrying various auxiliary ligands, e.g. the redox-innocent, tetradentate 1,4,8,11-tetraazacyclotetradecane (cyclam) ligand and its derivatives, have first applied matrix isolation techniques to increase the lifetime of their transient target compounds.^[111–114] Notwithstanding the valuable results obtained in these works, this method did not allow an examination of the photochemical conversions from azido to nitrido complex, nor of the reactivity of the latter under conditions of practical relevance. In order to address these questions experimentally, the application of (ultra)fast time-resolved spectroscopy is required. In the last decade, femtosecond UV/Vis-pump/mIR-probe

¹ A list of shorthand notations of the complexes is provided in section 8.8 in the appendix.

spectroscopy and step-scan and rapid-scan spectroscopy on timescales of microseconds and seconds, respectively, have already been conducted successfully to discover the reactivities of nitrido(cyclam)iron complexes and the mechanisms of their formation in liquid solution.^[115–121] In contrast, the mechanism and kinetics of the formation of the paradigmatic complex [2] starting from [1] remain undisclosed so far and raise several questions. For instance, it is possible that [2] is not directly formed in its electronic ground state, as suggested for its oxido analogs,^[1,56–60] but intermediately in an excited state, possibly a valence tautomer showing a π -radical configuration (cf. Equation (3)). Furthermore, the outcome of a photolysis^[113,122] and the properties of its products^[123,124] can be strongly dependent on the experimental conditions, i.e. whether conducted in frozen or liquid solution. Here, for example, the release of dinitrogen from [1] competes potentially with two alternative reaction channels, the cleavage of either azide anions or azidyl radicals, which are known to occur in the photolysis of other azido complexes.^[115,121,125,126]



Hence, in this work, the photolysis of [1], yielding the high-valent model complex [2], was conducted and investigated in room-temperature DCM solution to elucidate its unsolved questions. To this end, the primary processes following the photoexcitation and subsequent bimolecular reactions were tracked by means of time-resolved vibrational and electronic spectroscopy on timescales reaching from hundreds of femtoseconds to tens of seconds.

In more detail, the results and discussion of this work can be subdivided into four parts: First, the stationary mid-infrared, visible, and ultraviolet absorption spectra of [1] will be presented and analyzed in section 4. Second, in section 5.1, the total yield of photoconversion and the nature and fractional yields of the photoproducts will be determined. Furthermore, parts of their reactivity towards selected reaction partners will be investigated. In the subsequent section 5.2, transient spectra recorded by means of ultrafast UV/Vis-pump/mIR-probe and -Vis-probe experiments will be presented and interpreted. The data will be evaluated in order to disclose the primary events following the excitation of [1] and their kinetics. Finally, the electronic structures of the photoproducts, in particular with regard to the porphyrin ligand, will be examined in section 5.3. This analysis will be based on transient spectroscopy of structure-sensitive IR absorption bands in conjunction with predictions from density functional theory (DFT).

2 Background

2.1 Methodical Background

2.1.1 Basics of Spectroscopy

The interactions of electromagnetic radiation (light) and matter are the basis of a wide variety of analytic techniques to characterize chemical compounds and examine chemical reactions.^[127,128] A net-energy transfer from light to matter or vice versa can occur if the energy of a photon, E_{ph} , equals the energy difference, $\Delta E_{\underline{1},\underline{2}}$, of two quantum states of the irradiated matter, the lower state $\underline{1}$ and the upper state $\underline{2}$, according to Equation (1).^[129,130]

$$\Delta E_{\underline{1},\underline{2}} = E_{\underline{2}} - E_{\underline{1}} = E_{ph} = h\nu = hc_0\tilde{\nu} = \frac{hc_0}{\lambda} \quad (1)$$

Here, h is the Planck constant, c_0 is the speed of light, and ν , $\tilde{\nu}$, and λ are the frequency, the wavenumber, and the wavelength of the light, respectively. In general, $\underline{1}$ and $\underline{2}$ can be any kind of quantum states, but the following discussion will focus on transitions between vibrational or electronic states of molecules.

There are three processes involving an energy transfer between light and matter:^[129,130]

- ◆ The *absorption* (Equation (2)), promoting a molecule from state $\underline{1}$ to state $\underline{2}$ under consumption of a photon.
- ◆ The *stimulated emission* (Equation (3)), in which a photon triggers the transition of a molecule from state $\underline{2}$ to state $\underline{1}$ under generation of a second photon.
- ◆ The *spontaneous emission* (Equation (4)), in which a molecule relaxes without external influence from state $\underline{2}$ to state $\underline{1}$ under generation of a photon.

According to Equations (2-4), the rates of these processes, $\left(\frac{dn_{\underline{1}}}{dt}\right)$ or $\left(\frac{dn_{\underline{2}}}{dt}\right)$, are proportional to the number of molecules in the starting state, $n_{\underline{1}}$ or $n_{\underline{2}}$. In addition, the rates of the absorption and the stimulated emission are proportional to the spectral radiation density at the resonance frequency, $\rho_l(\tilde{\nu})$. The constants of proportionality, $\mathcal{B}_{\underline{1},\underline{2}}$, $\mathcal{B}_{\underline{2},\underline{1}}$, and $\mathcal{A}_{\underline{2},\underline{1}}$ are called Einstein coefficients, the former two of which are connected to via Equation (5).

$$\left(\frac{dn_{\underline{1}}}{dt}\right) = -\left(\frac{dn_{\underline{2}}}{dt}\right) = -\mathcal{B}_{\underline{1},\underline{2}} n_{\underline{1}} \rho_l(\tilde{\nu}) \quad (2)$$

$$\left(\frac{dn_{\underline{1}}}{dt}\right) = -\left(\frac{dn_{\underline{2}}}{dt}\right) = +\mathcal{B}_{\underline{2},\underline{1}} n_{\underline{2}} \rho_l(\tilde{\nu}) \quad (3)$$

$$\left(\frac{dn_{\underline{1}}}{dt}\right) = -\left(\frac{dn_{\underline{2}}}{dt}\right) = +\mathcal{A}_{\underline{2},\underline{1}} n_{\underline{2}} \quad (4)$$

$$\Omega_{\underline{1}} \cdot \mathcal{B}_{\underline{1},\underline{2}} = \Omega_{\underline{2}} \cdot \mathcal{B}_{\underline{2},\underline{1}} \quad (5)$$

Here, $\Omega_{\underline{1}}$ and $\Omega_{\underline{2}}$ are the degeneracies of states $\underline{1}$ and $\underline{2}$. For a macroscopic system in a thermal equilibrium of temperature T , the relation of the numbers $n_{\underline{1}}$ and $n_{\underline{2}}$ is given by the Boltzmann distribution (6) (where k_B is the Boltzmann constant):^[131]

$$\frac{n_{\underline{2}}}{n_{\underline{1}}} = \frac{\Omega_{\underline{2}}}{\Omega_{\underline{1}}} \cdot \exp\left(-\frac{\Delta E_{\underline{1},\underline{2}}}{k_B T}\right) \quad (6)$$

Provided that the energy difference between both states is high enough when compared to $k_B T$ (and the degeneracy of the upper state is not much larger than this of the lower state, whereby both conditions are typically fulfilled in electronic and vibrational spectroscopy), it can be concluded that the occupation of $\underline{1}$ is much larger than the occupation of $\underline{2}$. Thus, the rate of absorption far exceeds the rate of stimulated and spontaneous emission, so that absorption is the predominant process upon irradiation of a thermally equilibrated sample.

Experimentally, the absorption properties of a substance are often quantified in terms of the optical density (also called absorbance or extinction), $OD(\tilde{\nu})$, which is defined by Equation (7).^[129,132] The calculation of this quantity requires a measurement of the light intensity transmitted by a sample containing this substance, $I_s(\tilde{\nu})$, and a reference intensity, $I_r(\tilde{\nu})$. The reference intensity is usually recorded under identical conditions (i.e. using the same spectrometer, measuring cell and solvent (where applicable)) in absence of the compound of interest.

$$OD(\tilde{\nu}) = -\log_{10}\left(\frac{I_s(\tilde{\nu})}{I_r(\tilde{\nu})}\right) \quad (7)$$

According to the Lambert-Beer law (8),^[129,132] the optical density is proportional to the concentration of the substance, c , and the optical path length, d , of the sample. The constant of proportionality is called molar, decadic extinction coefficient, $\epsilon(\tilde{\nu})$, which is dependent on the frequency of the light, the molecule, and external conditions, e.g. the temperature, the pressure, and the solvent.

$$OD(\tilde{\nu}) = \epsilon(\tilde{\nu}) \cdot c \cdot d \quad (8)$$

In real spectra, each transition gives rise to an absorption band of finite width around the resonance frequency $\tilde{\nu}_0$ instead of an infinitely sharp peak at this frequency. Moreover, different absorption bands may have distinct band widths. For this reason, the extinction coefficient is often insufficient in order to specify the total 'absorption strength' of a transition. A more accurate quantification can be provided in terms of the frequency-integrated extinction coefficient, α_a , which can be obtained from experimental spectra via Equation (9).^[129] On the part of the theoretical description, the square of the magnitude of the transition dipole moment between the lower and upper state involved in an excitation, $|\mu_{\underline{1},\underline{2}}|^2$ (Equation (10); there, * indicates the complex conjugate), is used in quantum mechanics to calculate the absorption strength.^[133] It is obtained from the wavefunctions of both states, $\Psi_{\underline{1}}$ and $\Psi_{\underline{2}}$, under application of the electric dipole operator, $\vec{\mu}$, and integration over the coordinates of the three-dimensional space, \vec{r} . Moreover, in electronic spectroscopy, the oscillator strength, f_{osc} , is a frequently applied measure.^[129] It can be demonstrated that these three quantities and the Einstein coefficient of the absorption are all proportional (Equation (11)).^[129,134]

$$\alpha_a = \int \epsilon(\tilde{\nu}) d\tilde{\nu} \quad (9)$$

$$|\mu_{\underline{1},\underline{2}}|^2 = \left| \int \Psi_{\underline{1}}^* \vec{\mu} \Psi_{\underline{2}} d\vec{r} \right|^2 \quad (10)$$

$$\alpha_a \propto f_{osc} \propto |\mu_{\underline{1},\underline{2}}|^2 \propto \mathcal{B}_{\underline{1},\underline{2}} \quad (11)$$

On the basis of the transition dipole moment, a very fundamental statement regarding the oscillator strength of a transition can be made from a consideration within the framework of group theory:^[133,135] Given that $\Gamma_{\underline{1}}$ and $\Gamma_{\underline{2}}$ are the irreducible representations of the wavefunctions of both states, a light-induced transition between them will be possible only, if the product $\Gamma_{\underline{1}} \otimes \Gamma_{\underline{2}}$ is identical with (or contains) the irreducible representation of either of the three dipole components of the light (in x -, y -, or z -direction, cf. Equation (12)). Transitions are categorized as *dipole-allowed* or *dipole-forbidden*, depending on whether they fulfill this selection rule or not.

$$\Gamma_{\underline{1}} \otimes \Gamma_{\underline{2}} \begin{cases} = \Gamma_x \vee \Gamma_y \vee \Gamma_z \rightarrow |\mu_{\underline{1},\underline{2}}|^2 \geq 0 \rightarrow \text{dipole-allowed transition} \\ \neq \Gamma_x \wedge \Gamma_y \wedge \Gamma_z \rightarrow |\mu_{\underline{1},\underline{2}}|^2 = 0 \rightarrow \text{dipole-forbidden transition} \end{cases} \quad (12)$$

2.1.2 Electronic and Vibrational Spectroscopy

Electronic absorption spectroscopy probes the transitions of the electronic wavefunction from one eigenstate of the time-independent Schrödinger equation to a higher one.^[136] Often, these transitions are modeled by (combinations of) promotions of a single electron from one molecular orbital (one-electron wavefunction) to another one.^[136,137] Their resonance bands cover the electromagnetic spectrum starting from the near-infrared (nIR) (2500 nm–770 nm), the visible (Vis) (770 nm–390 nm), or the (near-)ultraviolet (UV) (390 nm–200 nm) region upwards in energy, depending on the molecule.^[128,138] At room-temperature, molecules occupy almost exclusively their electronic ground state because the thermal energy $k_B T$ (ca. 207 cm⁻¹ at 25°C) is much lower than the energy of the first excited state (cf. Equation (6)). Moreover, electronic excitations are often accompanied by simultaneous vibrational excitations, as the latter require typically much less energy than the former (see below). As a result of a manifold of possible vibrational excitations, the line widths of absorption bands in electronic spectroscopy are generally much larger than those of purely vibrational transitions^[128] and often larger than the spectral spacing between two bands.

Vibrational absorption spectroscopy rests on the excitation of the normal modes of the nuclear motional degrees of freedom.^[129,138] These vibrational normal modes are, beside the translational and rotational ones, eigenvectors of the mass-weighted Hessian matrix, which contains the second derivatives of the energy w.r.t. the nuclear coordinates,^[139,140] i.e. the force constants. The energy E_{v_a} of a vibrational state a of quantum number v_a is given by Equation (13) within the harmonic approximation of the potential energy surface, or Equation (14) if anharmonicity is considered. In general, the harmonic frequency, $\tilde{\nu}_a$, increases with the force constants along the associated normal mode and decreases with the masses of the

displaced nuclei. For example, the harmonic frequency, $\tilde{\nu}_{YZ}$, of the stretching mode of a diatomic molecule (Y-Z) is given by Equation (15) and depends on the force constant of the Y-Z bond, κ_{YZ} , and the reduced mass, \bar{m}_{YZ} , that is based on the masses of the nuclei, m_Y and m_Z , for its part.

$$E_{v_a} = \left(v_a + \frac{1}{2}\right) h c_0 \tilde{\nu}_a \quad (13)$$

$$E_{v_a} = \left(v_a + \frac{1}{2}\right) h c_0 \tilde{\nu}_a + \left(v_a + \frac{1}{2}\right)^2 \chi_{a,a} h c_0 \tilde{\nu}_a + \sum_{b \neq a} \left(v_a + \frac{1}{2}\right) \left(v_b + \frac{1}{2}\right) \chi_{a,b} h c_0 \tilde{\nu}_a \quad (14)$$

$$\tilde{\nu}_{YZ} = \frac{1}{2\pi c_0} \sqrt{\frac{\kappa_{YZ}}{\bar{m}_{YZ}}}, \quad \bar{m}_{YZ} = \frac{m_Y \cdot m_Z}{m_Y + m_Z} \quad (15)$$

Equation (14) demonstrates that the energy difference between two neighboring states of one mode is not constant but changes with the quantum number v_a due to the diagonal anharmonicity, quantified by the constant $\chi_{a,a}$. In addition, there are off-diagonal anharmonicities, depending each on the quantum number of a different normal mode b , v_b , and the anharmonicity constant $\chi_{a,b}$. In a substantial majority of cases, anharmonicity decreases the energy difference with increasing quantum number.

Many vibrational normal modes are localized at particular functional groups of a molecule. Furthermore, because the transition dipole moments, force constants and atomic masses are highly specific of these functional groups, the resulting resonance frequencies and absorption strengths are as well.^[129,138] As a consequence, an analysis of a vibrational absorption spectrum allows valuable conclusions regarding the molecular structure of the underlying species. Vibrational excitations tend to exhibit smaller absorption strengths and require typically lower photon energies than electronic transitions. The resonance frequencies of molecular vibrations are typically located in the mid-infrared (mIR) ($2.5 \mu\text{m}$ – $25 \mu\text{m}$, 4000 cm^{-1} – 400 cm^{-1}) and far-infrared (fIR) ($25 \mu\text{m}$ – 1 mm , 400 cm^{-1} – 10 cm^{-1}) spectral region.^[129,138] In more detail, most stretching (or valence) vibrations and deformation modes involving a displacement of hydrogen atoms absorb in the mIR region, whereas the absorptions of most other deformation modes are found in the fIR region. Regarding the high-frequency modes, molecules are solely residing in their ground state ($v = 0$) at room-temperature. Consequently, only the $v = 0 \rightarrow v = 1$ (*fundamental*) transitions contribute noteworthy to their absorption spectra.^[128,138] In contrast, excited states of modes having sufficiently low frequencies are significantly populated under ambient conditions. For fundamental vibrational transitions, the selection rule from Equation (12) can be rephrased to Equation (16).^[135] The fundamental excitation of a vibrational normal mode a is dipole-allowed, if the irreducible representation of this mode, Γ_a , equals the one of either of the three dipole components of the light.

$$\Gamma_a \begin{cases} = \Gamma_x \vee \Gamma_y \vee \Gamma_z \rightarrow |\mu_{\underline{1},\underline{2}}|^2 \geq 0 \rightarrow \text{dipole-allowed transition} \\ \neq \Gamma_x \wedge \Gamma_y \wedge \Gamma_z \rightarrow |\mu_{\underline{1},\underline{2}}|^2 = 0 \rightarrow \text{dipole-forbidden transition} \end{cases} \quad (16)$$

2.1.3 Time-Resolved Spectroscopy

If the investigated system is not stationary, e.g. during a chemical reaction, the concentrations of some species and, consequently, the optical density will be time-dependent. In all applications in this work, the initialization of time-dependent processes is realized by a (in comparison to the examined processes) short UV- or Vis-laser pulse, the *excitation pulse* or *pump pulse*, whose moment of impact at the system defines the zero point of the time axis, t_0 . On this basis, the delay, τ , between the impact of the excitation pulse and a measurement occurring at time t_m is defined via Equation (17).

$$\tau = t_m - t_0 \quad (17)$$

If the measurement is implemented in the form of another short but broadband laser pulse, the *probe pulse*, the technique is called *pump-probe* spectroscopy,^[141,142] which is applied in order to excess delays from tens of femtoseconds to several microseconds. On the other hand, conventional spectroscopic methods might be used for measurements on longer timescales instead.^[143–145] Furthermore, in time-resolved spectroscopy, it has proved to be convenient to consider the differential optical density,^[146] $\Delta\text{OD}(\tilde{\nu}, \tau)$, instead of the optical density itself. $\Delta\text{OD}(\tilde{\nu}, \tau)$ is defined as the difference between the optical density at the delay τ during the reaction, i.e. with the pump pulse, $\text{OD}_{wp}(\tilde{\nu}, \tau)$, and the optical density of the unperturbed system, i.e. without the pump pulse, $\text{OD}_{wop}(\tilde{\nu})$, according to Equation (18).

$$\begin{aligned} \Delta\text{OD}(\tilde{\nu}, \tau) &= \text{OD}_{wp}(\tilde{\nu}, \tau) - \text{OD}_{wop}(\tilde{\nu}) \\ &= -\log_{10} \left(\frac{I_{s,wp}(\tilde{\nu}, \tau)}{I_r(\tilde{\nu})} \right) + \log_{10} \left(\frac{I_{s,wop}(\tilde{\nu})}{I_r(\tilde{\nu})} \right) = -\log_{10} \left(\frac{I_{s,wp}(\tilde{\nu}, \tau)}{I_{s,wop}(\tilde{\nu})} \right) \end{aligned} \quad (18)$$

As Equation (18) demonstrates, $\Delta\text{OD}(\tilde{\nu}, \tau)$ does not require knowledge of the reference intensity spectrum, $I_r(\tilde{\nu})$, anymore, but only of the intensity spectrum of the sample without, $I_{s,wop}(\tilde{\nu})$, and with excitation, $I_{s,wp}(\tilde{\nu}, \tau)$.

Since $\Delta\text{OD}(\tilde{\nu}, \tau)$ is a quantity dependent on two variables, the delay τ and the frequency $\tilde{\nu}$, graphic representations often display extracts in which one of these variables is set constant. In doing so, an extract of the differential optical density at a constant delay in dependence on the frequency, $\Delta\text{OD}(\tilde{\nu}, \tau = \text{const.})$, is called *transient spectrum*. An extract at constant frequency in dependence on the delay, $\Delta\text{OD}(\tilde{\nu} = \text{const.}, \tau)$, is referred to as *kinetic trace*.

The principle of time-resolved spectroscopy is sketched in the form of energy level diagrams in Figure 2(a) and 2(b) (for Vis detection) and 2(c) and 2(d) (for IR detection).^[141,142] In each case, the former and latter figure represent the situation at a pump-probe delay before and after the pump, respectively. Figure 2(e) and 2(f) illustrate schematic spectra for both pump-probe delays in terms of the optical density and differential optical density, respectively. As discussed before, almost all molecules (black circles) reside in their electronic and vibrational ground state in the thermal equilibrium present before the pump pulse. Thus, a measurement before the excitation yields the absorption spectrum of the ground state (dotted, black line in

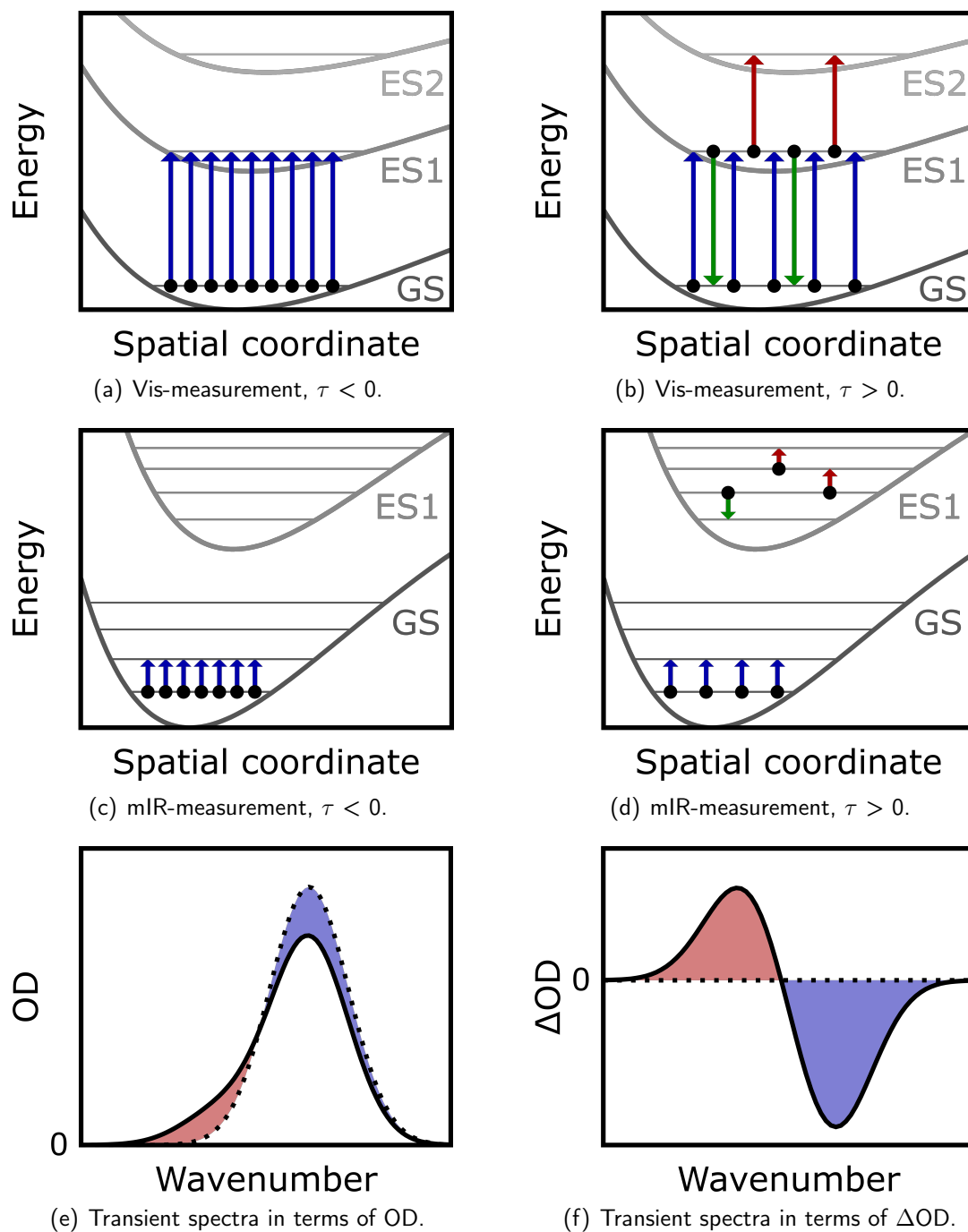


Figure 2: Illustrations of the working principle of time-resolved spectroscopy after UV/Vis-excitation. (a) - (d): Schematic energy level diagrams illustrating the transitions involved in Vis- and mIR-measurements before ($\tau < 0$) and after ($\tau > 0$) the pump pulse, as indicated by the subtitles. Gray curves represent the potential energy surfaces of the electronic ground state (GS) and excited state(s) (ES1 and ES2). Vibrational states are included as horizontal lines. Black circles symbolize individual molecules and colored arrows their transitions between quantum states: blue - ground state absorption, green - stimulated emission, red - excited state absorption. (e) & (f) Schematic transient spectra resulting from measurements before (dotted, black line) and after (solid, black line) the excitation in terms of the optical density and differential optical density, respectively. The red area emphasized a transient absorption, the blue one a transient bleaching.

Figure 2(e)), which becomes the zero line of the ΔOD axis in Figure 2(f). In the following, the pump pulse will promote some of the molecules to an excited electronic state, changing the absorption spectrum of the system. The new spectrum (solid, black line) expressed in terms of the differential optical density will exhibit positive and negative features arising from several contributions. Signals of negative amplitude are referred to as *transient bleaching* (blue area) and occur at the resonance frequencies of the parent's ground state, as indicated by the blue arrows in the energy level diagrams. The reduced optical density at these frequencies is a result of the depopulation of the ground state, effectively lowering its concentration. In addition, if the probe pulse triggers stimulated emission from a populated excited state (green arrows), the intensity of light at the corresponding resonance frequencies will be increased, resulting in a reduced optical density, too. On the other hand, positive signal contributions (red area), called *transient absorptions*, originate from molecules occupying excited electronic or vibrational states, whose absorption spectra deviate from this of the ground state (transitions indicated by red arrows, only electronically excited molecules are represented in the figures). In the case of vibrational resonances, these *excited state absorption* (ESA) are most often shifted to lower frequencies because of anharmonicity (see below and section 2.1.2) or due to a reduced bond strength in excited electronic states.^[147,148] Furthermore, the signatures of newly formed chemical species, generated via photoinduced reactions, give rise to absorptive features.

Beside the formation of photoproducts, another possible fate of the excited molecules is a return to the electronic and vibrational ground state, referred to as *ground state recovery* (GSR). In this context, the fraction of molecules avoiding the GSR and converted to photoproducts, $n(\text{converted})$, w.r.t. the amount of molecules initially excited, $n(\text{excited})$, is called *primary quantum yield*, Φ . Experimentally, this quantity is determined from the ratio of the amplitudes (or alternatively the integral) of a bleaching signal at quasi-infinite pump-probe delay and at $\tau = 0$, according to Equation (19).

$$\Phi = \frac{n(\text{converted})}{n(\text{excited})} = \frac{\Delta OD_{\text{bleach}}(\tilde{\nu}, \infty)}{\Delta OD_{\text{bleach}}(\tilde{\nu}, 0)} \quad (19)$$

Another process observed frequently in time-resolved spectroscopy is the spectral shift of signals due to *vibrational energy relaxation* (VER).^[149,150] For IR-probe spectroscopy, the underlying mechanism is illustrated in Figure 3. Subfigure (a) shows the energy level diagram of an hypothetical system having two vibrational modes, the high-frequency mode a and the low-frequency mode b . The total state of the system is described by two quantum numbers: $|v_a, v_b\rangle$. Again, the black circles symbolize individual molecules. At a delay shortly after the pump pulse (left panel), the excitation energy is distributed over the vibrations a and b of the molecule (as though they were in an environment of high temperature, 'in a hot state'). In contrast, the solvent molecules have not been affected at this early time yet, because intramolecular energy dissipation is faster than intermolecular energy dissipation.^[150,151] Still, while many excited states of mode b are accessed, (nearly) all molecules occupy the ground state

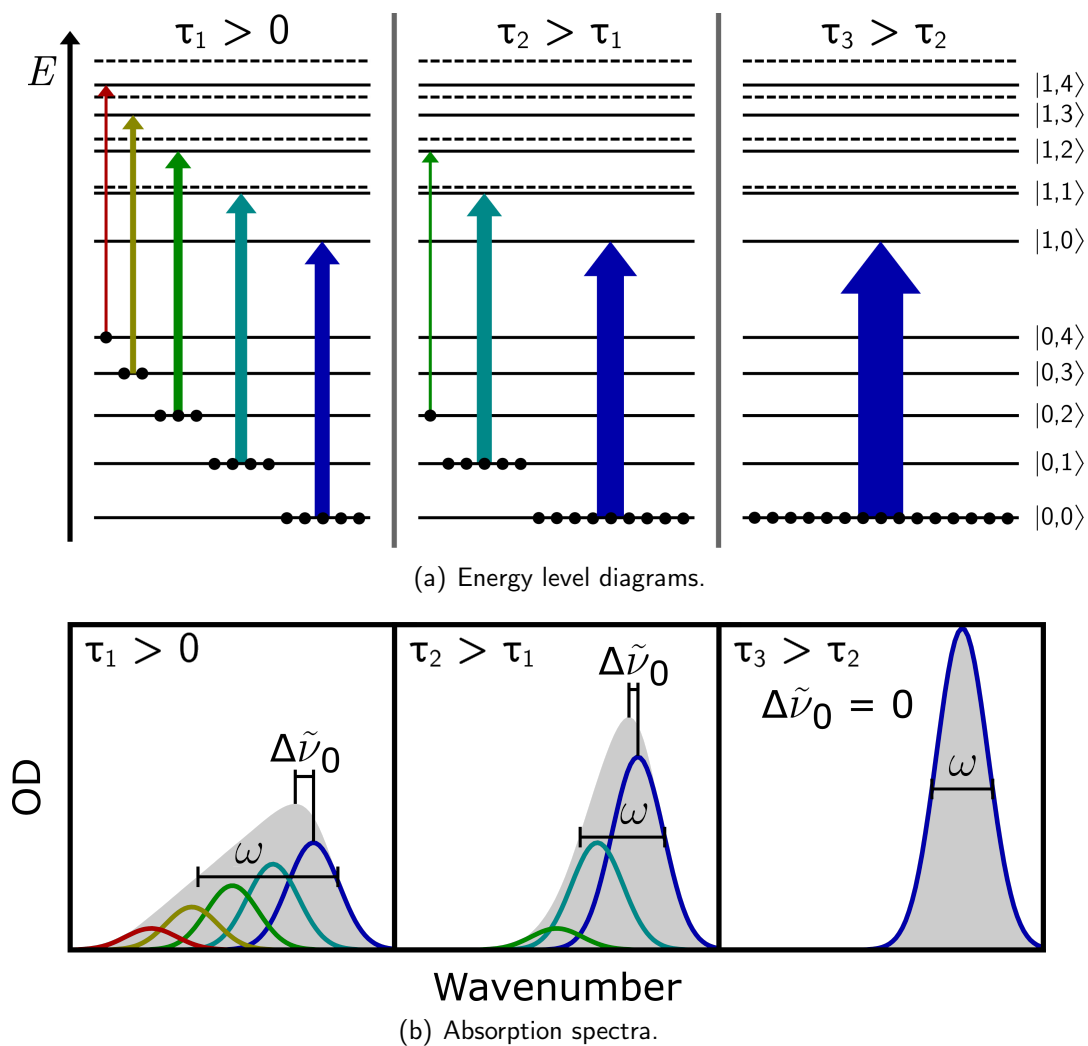


Figure 3: Schematic visualization of a vibrational energy relaxation. (a) Energy level diagrams. Solid lines represent vibrational states characterized by the two quantum numbers on the right. Dashed lines represent the hypothetical energies of these states in the absence of off-diagonal anharmonicity. Filled black circles symbolize molecules occupying the states. Colored arrows symbolize transitions absorbing the probe pulse, whose energy decreases from blue to red. The arrows' line widths encode the total absorbance of the transitions. (b) Resulting absorption spectra. Colored lines represent the individual signals corresponding to the transitions from the upper panel. The gray area equals the sum of all five signals. In both subfigures, the left, center, and right panel show the situation at three different delays after the photoexcitation in increasing order.

of mode a , because the energy of the molecule is not sufficient to populate the excited state of a significantly. A probe pulse in the region of the resonance frequency of mode a will now be absorbed by all excitations $|0, v_b\rangle \rightarrow |1, v_b\rangle$ of different v_b (colored arrows in the figure). Due to off-diagonal anharmonicity, all these excitations have slightly different energies. More precisely, they usually become less energetic the higher v_b is.^[146,150] The figure emphasized this by the solid lines, representing the real energy of the $|1, v_b\rangle$ states, which are lower than the sum of the energies of the states $|0, v_b\rangle$ and $|1, 0\rangle$ (dashed lines). The resulting spectrum is

a superposition of the signals of all these individual transitions (colored curves in the subfigure (b)). As their line widths are larger than their spacing, they give rise to a broad, asymmetric band, whose maximum is shifted to lower frequencies (red-shifted) w.r.t. this of the fundamental $|0,0\rangle \rightarrow |0,1\rangle$ transition by $\Delta\tilde{\nu}_0$.

With increasing delay, the molecules will undergo intermolecular energy dissipation ('vibrational cooling'), i.e. transfer their excess energy to the solvent and return steadily to lower states of mode b (central panel). Finally, thermal equilibrium will be reached, in which almost all molecules reside in $|0,0\rangle$ (right panel). As a consequence, the observed absorption band of the ensemble contracts, i.e. the bandwidth ω is reduced, and its maximum shifts to higher frequency (blue-shift).

Obviously, this model system presents a high simplification of reality, in which high-frequency modes couple to a multitude of low-frequency modes, all potentially excited to a certain degree. Still, the approach can be extended to a level allowing a description of the spectro-temporal evolution of vibrational excited, gradually relaxing molecules in practice. For instance, combination of an anharmonic coupling model, DFT calculations and second-order vibrational perturbation theory, applied in ref. [152], were able to reproduce the vibrational relaxation dynamics of an azidocobalt(II) complex with astonishing precision.

Despite only discussed in detail for IR-probe spectroscopy here, VER affects the shape of transient UV-Vis spectra similarly, too,^[153–155] due to the presence of vibronic coupling.^[129]

2.1.4 Spectral Line Shapes

The evaluation of spectroscopic data requires the determination of the strength (amplitude or integral), width and position of the occurring signals in a quantitative way. This can be achieved by fitting of suitable regression functions to the experimental spectra. From line shape theory, it is known that signals adopt in limiting cases either the shape of a Lorentzian function (20), $L(\tilde{\nu})$,^[129,156] or a Gaussian function (21), $G(\tilde{\nu})$.^[157,158]

$$L(\tilde{\nu}) = \frac{2A}{\pi} \cdot \frac{\omega}{4(\tilde{\nu} - \tilde{\nu}_0)^2 + \omega^2} \quad (20)$$

$$G(\tilde{\nu}) = \frac{2A}{\omega} \cdot \sqrt{\frac{\ln(2)}{\pi}} \cdot \exp\left(-4\ln(2) \left(\frac{\tilde{\nu} - \tilde{\nu}_0}{\omega}\right)^2\right) \quad (21)$$

Here, ω represents the full width at half maximum (FWHM), $\tilde{\nu}_0$ the frequency of the maximum (which is identical to the center frequency in both cases), and A the integral. Which line shape a signal will adopt depends on the predominant broadening mechanism. The finite radiative lifetime of an excited state gives rise to a *homogeneous broadening* (affecting all molecules equally). If this mechanism is decisive, a Lorentzian line shape will be found.^[129,156] On the other hand, *heterogeneous broadening* originates from varying environmental effects on distinct molecules, and will cause a Gaussian-type line shape, if predominant.^[129,146,156] More generalized, the line shape can be expressed by means of a Voigt function, $V(\tilde{\nu})$, which

is the convolution of a Lorentzian function and a Gaussian function according to Equation (22).^[156,159] Often, however, a simple, approximate pseudo-Voigt function (23), $V_p(\tilde{\nu})$, representing a superposition of a Lorentzian and a Gaussian function having the same FWHM and center frequency, and weighted by the parameter η ,^[160,161] is applied in practice instead of using $V(\tilde{\nu})$ itself.

$$V(\tilde{\nu}) = \int G(\tilde{\nu} - x)L(\tilde{\nu})dx \quad (22)$$

$$V_p(\tilde{\nu}) = \eta L(\tilde{\nu}) + (1 - \eta) G(\tilde{\nu}) \quad (23)$$

Although an experimental spectrum could in principle be described as a sum of Voigt functions, this is in practice not always feasible. For example, in the case of an ensemble of molecules in various excited vibrational states discussed in the previous section, an accurate analysis of the asymmetric line shape, taking into account all relevant, individual transitions, is extremely demanding.^[152] Commonly, in order to extract information from such bands in an easier way, they are described phenomenologically by a simple approximation function. In this context, the log-normal distribution $O(\tilde{\nu})$ (Equation (24))^[162] has proved to provide an appropriate description of asymmetric absorption bands in both electronic^[162–164] and vibrational spectroscopy.^[165,166] The additional parameter ρ is referred to as skewness and quantifies the asymmetry of the function.

$$O(\tilde{\nu}) = \begin{cases} \frac{A}{\sqrt{2\pi} \mathcal{L} (j-\tilde{\nu})} \cdot \exp\left(\frac{\mathcal{L}^2}{2}\right) \cdot \exp\left(-\frac{1}{2\mathcal{L}^2} \left(\ln\left(\frac{j-\tilde{\nu}}{\mathcal{K}}\right)\right)^2\right) & \text{if } \tilde{\nu} < j \\ 0 & \text{if } \tilde{\nu} \geq j \end{cases}$$

$$j = \tilde{\nu}_0 + \omega \frac{\rho}{\rho^2 - 1}$$

$$\mathcal{K} = \omega \frac{\rho}{\rho^2 - 1} \cdot \exp\left(\mathcal{L}^2\right)$$

$$\mathcal{L} = \frac{\ln(\rho)}{\sqrt{2 \ln(2)}} \quad (24)$$

2.1.5 Kinetic Equations

In order to quantify the rates of chemical reactions, the change of the concentrations of the involved species over time (or over the pump-probe delay τ) needs to be considered. Here, for the sake of simplicity, all reactions will be assumed to be irreversible. The most simple case is an unimolecular reaction, as shown in the generalized Equation (4), in which a single reactant molecule (R) is transformed into a product molecule (P). Reactions of this type obey usually a rate law of first order, according to Equation (25).^[167] This differential equation can be solved to obtain delay-dependent expressions of the concentrations $c_{R/P}(\tau)$ in the form of exponential functions (26,27). The rate is characterized by the rate constant, k_u , or by its reciprocal value, the time constant, $\mathcal{T} = k_u^{-1}$. $c_{R/P}(0)$ denotes the concentration of a species at the beginning of the reaction, $\tau = 0$. Examples of processes following this rate law

are i.a. internal conversions^[168] or some ligand dissociation reactions^[169] (although the latter case results in the formation of two products out of one reactant).



$$\frac{dc_R(\tau)}{d\tau} = -\frac{dc_P(\tau)}{d\tau} = -k_u c_R(\tau) \quad (25)$$

$$c_R(\tau) = c_R(0) \exp(-k_u \tau) = c_R(0) \exp\left(-\frac{\tau}{T}\right) \quad (26)$$

$$c_P(\tau) = c_P(0) + c_R(0) (1 - \exp(-k_u \tau)) = c_P(0) + c_R(0) \left(1 - \exp\left(-\frac{\tau}{T}\right)\right) \quad (27)$$

$$\begin{aligned} \Xi_N(\tau) &= \Delta OD(\tilde{\nu}, \infty) + \sum_{i=1}^N \Delta OD(\tilde{\nu}, 0)_i \cdot \exp(-k_{u,i} \tau) \\ &= \Delta OD(\tilde{\nu}, \infty) + \sum_{i=1}^N \Delta OD(\tilde{\nu}, 0)_i \cdot \exp\left(-\frac{\tau}{T_i}\right) \end{aligned} \quad (28)$$

Since the optical density, $OD(\tilde{\nu}, \tau)$, is proportional to the concentration of a chemical species according to Equation (8), and, consequently, the differential optical density, $\Delta OD(\tilde{\nu}, \tau)$, is proportional to the change of its concentration w.r.t. the state before the reaction, the rate constant can be extracted directly from an exponential regression of the spectroscopic data. However, in some cases, $\Delta OD(\tilde{\nu}, \tau)$ needs to be described by a sum of N exponential functions, $\Xi_N(\tau)$ according to Equation (28), instead of a single one. This situation may occur, if more than one chemical species, all of which are subjected to individual reactions having distinct rate constants, absorb at the same frequency $\tilde{\nu}$. Moreover, it is possible that the same product is generated from more than one distinct reactant at different rates. In Equation (28), $\Delta OD(\tilde{\nu}, 0)_i$ represents the amplitude of an individual exponential term i and $\Delta OD(\tilde{\nu}, \infty)$ denotes an asymptotic offset for $\tau \rightarrow \infty$.

The rate of a bimolecular reaction of the reactants R_1 and R_2 to the product(s) P_1 (and P_2), as shown in Equation (5), can (but does not need to) follow a rate law of second order described by Equation (29) (with $j = 1, 2$ and rate constant k_v).^[167] Examples of this type of reaction are i.a. some intermolecular electron transfer reactions and ligand substitutions following the associative mechanism.^[170] The general solution of this differential equation is the expression given in Equation (30),^[167] which can be further rephrased to (31-33) (given that $\Delta c_R(0) = c_{R_1}(0) - c_{R_2}(0) \neq 0$).



$$\frac{dc_{R_j}(\tau)}{d\tau} = -\frac{dc_{P_j}(\tau)}{d\tau} = -k_v c_{R_1}(\tau) c_{R_2}(\tau) \quad (29)$$

$$\frac{c_{R_1}(\tau)}{c_{R_2}(\tau)} = \frac{c_{R_1}(0)}{c_{R_2}(0)} \exp(\Delta c_R(0) k_v \tau) \quad (30)$$

$$c_{R_1}(\tau) = \frac{-\Delta c_R(0)}{\frac{c_{R_2}(0)}{c_{R_1}(0)} \exp(-\Delta c_R(0) k_v \tau) - 1} \quad (31)$$

$$c_{R_2}(\tau) = \frac{\Delta c_R(0)}{\frac{c_{R_1}(0)}{c_{R_2}(0)} \exp(\Delta c_R(0) k_v \tau) - 1} \quad (32)$$

$$c_{P_j}(\tau) = c_{P_j}(0) + c_{R_1}(0) - c_{R_1}(\tau) = c_{P_j}(0) + c_{R_2}(0) - c_{R_2}(\tau) \quad (33)$$

There are two special cases worth mentioning, which reduce the complexity of this solution significantly. First, if one of the two reactants exists in a vast excess (here: R_2), its concentration can be approximated as constant. Then, the rate law is equivalent to a rate law of first order (25) and yields the monoexponential solutions (26,27), only depending on c_{R_1} , again. This approximate rate law is referred to as *pseudo*-first order. Second, if the concentrations of both reactants are identical throughout the entire considered delay range, $c_{R_1}(\tau) = c_{R_2}(\tau)$, the more simple Equations (34,35) become solutions of Equation (29). Naturally, if R_1 and R_2 are the same molecule, this condition will always be fulfilled. Under these conditions, kinetic traces can be described by $\Lambda_R(\tau)$ (Equation (36)), for signals of reactants, or $\Lambda_P(\tau)$ (Equation (37)), for signals of products.

$$c_{R_j}(\tau) = \left(\frac{1}{c_{R_j}(0)} + k_v \tau \right)^{-1} \quad (34)$$

$$c_{P_j}(\tau) = c_{P_j}(0) + c_{R_j}(0) - \left(\frac{1}{c_{R_j}(0)} + k_v \tau \right)^{-1} \quad (35)$$

$$\Lambda_R(\tau) = \Delta OD(\tilde{\nu}, \infty) + \left(\frac{1}{\Delta OD(\tilde{\nu}, 0) - \Delta OD(\tilde{\nu}, \infty)} + k_v \tau \right)^{-1} \quad (36)$$

$$\Lambda_P(\tau) = \Delta OD(\tilde{\nu}, \infty) + \left(\frac{1}{\Delta OD(\tilde{\nu}, 0) - \Delta OD(\tilde{\nu}, \infty)} - k_v \tau \right)^{-1} \quad (37)$$

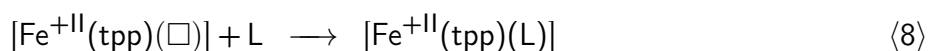
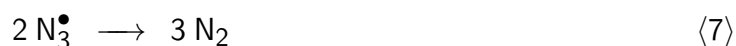
2.2 Chemical Background

2.2.1 Photochemistry of Azido Complexes

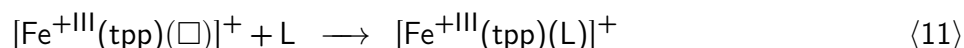
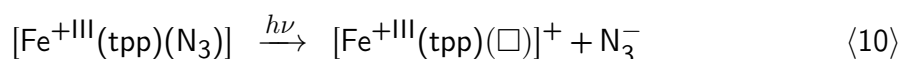
The photochemistry of azide-containing compounds has been intensively investigated in the past and is well described in the literature.^[171–176] Here, only potential reactions of the considered complex **[1]** ($[(\text{tpp})\text{Fe}-\text{N}_\alpha^\ominus-\text{N}_\beta^\oplus \equiv \text{N}_\gamma]$) will be discussed in more detail. As known from studies on other transition metal azido complexes, there are essentially three possible photochemical reactions.^[115,121,125,126] In addition, presumable secondary reactions following these primary pathways will be considered.

The first feasible decomposition pathway of **[1]** is the cleavage of a trinitrogen molecule, also known as azidyl radical, N_3^\bullet , as shown in Equation (6). The product complex is (5,10,15,20-tetraphenylporphyrin-21,23-diido)iron(+II), $[\text{Fe}^{\text{II}}(\text{tpp})(\square)]$ (**[3_{red}]**), which exhibits an unoccupied binding site (\square) in its ligand sphere. This reaction requires a homolytic breakage of the $\text{Fe}-\text{N}_\alpha$ bond and, while the total charge of the complex is preserved, causes the oxidation

state of the iron center to be decreased by one. For this reason, this reaction is referred to as *photoreduction* or *photoreductive pathway*.^[111–113,118–120,177,178] Its occurrence upon irradiation of [1] in organic solvents has already been verified by EPR spectroscopy in an earlier work.^[179] In principle, this reaction is reversible as a recombination of the two fragments has been observed experimentally after photolysis of other azido complexes.^[113,118] This recombination could occur either as so called *geminate* (or 'in-cage') recombination directly after their separation, i.e. while both products are still confined in the same solvent cage, or on later timescales by a diffusion driven, *non-geminate* mechanism.^[118] Regarding the detached N_3^\bullet fragment, it has to be mentioned that this molecule is metastable because of the highly exergonic self-quenching $\langle 7 \rangle$ converting it to dinitrogen.^[119,177,180,181] The reduced metal containing fragment, on the other hand, has the opportunity to undergo a secondary reaction, filling its vacant binding site. In many cases, a solvent molecule was observed to serve as ligand (L, see Equation $\langle 8 \rangle$), given that it has a sufficiently high tendency to form coordination compounds, e.g. acetonitrile or dimethyl sulfoxide.^[118–120,182] Alternatively, [3_{red}] might get oxidized in the presence of molecular oxygen,^[55,183,184] following Equation $\langle 9 \rangle$, or a similarly strong oxidizing agent to the corresponding iron(+III) complex.



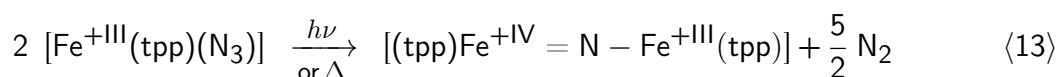
The second possible decomposition pathway is called *redox-neutral*^[115,116,182] and is depicted in Equation $\langle 10 \rangle$. As the name implies, the oxidation state of the iron center is preserved during this reaction. Accordingly, the Fe–N $_{\alpha}$ bond is cleaved in a heterolytic fashion generating an azide anion, N_3^- , and a complex of (5,10,15,20-tetraphenylporphyrin-21,23-diido)iron(+III), $[\text{Fe}^{+\text{III}}(\text{tpp})(\square)]^+$ ([3]), which carries a by one higher total charge and an empty binding site in its coordination sphere. As before, this vacancy can be filled either by recombination with an azide anion, so that this decomposition is reversible, too, or by coordination of a solvent molecule (Equation $\langle 11 \rangle$).^[115,116,182] However, in contrast to azidyl radicals, azide anions are considerably more stable and do not undergo a reaction to dinitrogen without an additional oxidizing agent under ambient conditions.^[185] The redox-neutral pathway can be assumed to become less likely with decreasing polarity of the solvent, since it requires a separation of charges. To the best of the author's knowledge, there are no reports of [1] in particular undergoing redox-neutral N_3^- release so far.



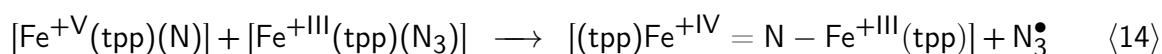
Lastly, [1] can release a dinitrogen fragment via heterolytic breakage of the $N_{\alpha}-N_{\beta}$, as shown in Equation (12). Such reactions are a common route towards high-valent nitrido complexes,^[111,113,115–117,126,186,187] including [2],^[104,105,108] applied frequently in previous studies on these compounds. Since dinitrogen is a stable and very inert molecule, it does not undergo any secondary reactions, nor is this pathway reversible.^[188] The electronic structure of the product complex [2] is quite intricate and will be discussed in more detail in section 2.2.3. In brief and simplified, the $Fe\equiv N_{\alpha}$ bond has a bond order of 2.5, connecting an iron(+V) ion and a terminal nitrido ligand (N^{3-}). Because of the increase of the oxidation state of the iron center by two in the course of reaction (12), it is referred to as *photooxidation* or *photooxidative pathway*.



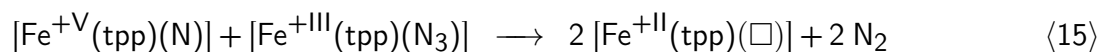
The stability and reactivity of nitridometal complexes depend strongly on the nature of the complex.^[10,13,15,89] In this case, although thermo- and photolysis of [1] in liquid solution are assumed to yield initially [2], it is well known that their final product is the dinuclear, mixed-valent, μ -N-bridged complex μ -nitrido-bis((5,10,15,20-tetraphenylporphyrin-21,23-diido)iron(+III,+IV)), $[Fe^{+III,+IV}(tpp)]_2N$ ([8]), as shown in Equation (13).^[109,110]



Despite that, there is still uncertainty regarding the mechanism of its formation. An early consideration on this topic was published by Cohen et al., who suggested two reaction schemes to explain the thermolysis of azido(porphyrindiido)iron(+III) complexes,^[109] the first of which is given in Equation (14). It assumes a nucleophilic attack of the nitrido ligand at the iron center of another complex of [1] as second reaction step. This generates directly the observed product complex [8] and releases the azido ligand as N_3^{\bullet} radical, which will be converted ultimately to N_2 by reaction (7).



Their second scheme, proceeding via the reactions specified in Equations (15) and (16), was later supported by investigations of Buchler et al..^[109,110] Here, the nitrido ligand is assumed to attack the azido group of [1], yielding eventually two N_2 molecules and two [3_{red}] complexes (Equation (15)). Gradually, this process will lower the concentration of [1], while [3_{red}] will accumulate if the solution is irradiated or heated continuously. Thus, it becomes more likely for complex [2] to react with [3_{red}] to the dinuclear product [8] via Equation (16) over time.



Interestingly, although both schemes explain Equation (13) validly, they differ entirely in the stoichiometry of [2] and [1]. While in the former mechanism, each complex of [2] reacts with exactly one complex of [1], each three complexes of [2] consume only a single complex of [1] in the latter one. In principle, this would allow a discrimination between the different schemes given that all reaction steps could be resolved.

In general, the occurrence of the three primary pathways is not mutually exclusive as there are several examples of compounds subjected to more than one of them at the same time.^[113–116,122] A priori, the result of a photolysis experiment of an azido transition metal complex can hardly be predicted since it depends on many parameters. As it will be discussed further in section 2.2.3, the d-electron count of the metal center and the symmetry of its ligand sphere play decisive roles in this regard. In brief, while photooxidation is commonly observed for tetragonal azido complexes of transition metals of groups 6 and 7,^[3] this reaction is rarely found for complexes of group 9 metals, which have a higher d-electron count.^[13,17] In addition, the spin state of the metal center was revealed to exert a crucial influence. For instance, the group of Roithová reported the spin state dependent photodissociation of a tetragonal azidoiron(+III) complex. Their model compound showed temperature-dependent yields of photooxidation and -reduction, which correlated positively with the population of its doublet and sextet state, respectively.^[122] The same tendency was found for complexes bearing the redox-innocent 1,4,8,11-tetraazacyclotetradecane-1-acetate (cyclam-ac) ligand. While the complex $[\text{Fe}^{\text{III}}(\text{cyclam-ac})(\text{N}_3)]^+$, having a doublet ground state, is capable of dissociation via photooxidation,^[115] the tri-methylated derivative $[\text{Fe}^{\text{III}}(\text{Me}_3\text{cyclam-ac})(\text{N}_3)]^+$ exhibits a sextet ground state and releases N_3^\bullet radicals exclusively.^[120,189] Another important aspect is the wavelength of the irradiated light. For example, the complex $[\text{Fe}(\text{cyclam})(\text{N}_3)_2]^+$ follows mostly the redox-neutral pathway at 532 nm and 355 nm excitation and predominantly the photooxidative pathway at 266 nm excitation.^[116] Similarly, $[\text{Fe}(\text{cyclam-ac})(\text{N}_3)]^+$ is subjected to redox-neutral decomposition, photoreduction and photooxidation in order of decreasing excitation wavelength.^[115]

Finally, environmental factors, such as the nature of the solvent or the temperature, need to be considered, especially in regard to bimolecular reaction steps, relying on the mobility of the reactants. For instance, geminate recombination (reverse reactions (6) and (10)) is favored in frozen matrices compared to liquid solutions, because molecular motions such as cage-escape are prevented.^[113] In contrast, the formation of dinuclear complexes like [8] is impeded there.^[114]

2.2.2 Quenching Reactions

Due to the possibility of three different reaction pathways following photoexcitation of [1], methods need to be established to verify their occurrence and quantify their relative yields. This can be achieved by probing for strong and characteristic IR signatures of the involved species. For example, the resonance band of the antisymmetric azide stretching vibration ($\nu_{\text{as}}(\text{N}_3)$) of [1] can serve as IR marker because of its large peak extinction coefficient of

ca. $2150 \text{ M}^{-1} \text{ cm}^{-1}$ and its spectral position at a frequency of 2056 cm^{-1} (in DCM, cf. section 4.1), i.e. within a spectral region free of absorption bands of common solvents^[190] and the atmosphere.^[191] Similarly, the free azide anion shows a comparably strong IR signal at somewhat lower frequencies^[182,192–194] (2006 cm^{-1} in DCM) allowing an easy inspection of the occurrence of the redox-neutral pathway. In addition, since quantitative stationary absorption spectra of both substances are precisely known (cf. Figure A2), the fractional yield of this pathway can be quantified. To this end, the signal strength of the transient absorption of the formed azide anions has to be set in relation to the depletion of the $\nu_{\text{as}}(\text{N}_3)$ band of [1].

Unfortunately, the photooxidative and -reductive pathways do not offer an equally simple way of verification. Neither of the arising products exhibits unambiguous IR signatures detectable by the means applied in this work. The dinitrogen molecule is entirely IR-silent^[195] and the azidyl radical has only small peak extinction coefficients.^[118,120] Although porphyrin-diido ligands exhibit in principle IR marker bands sensitive to the oxidation and spin state of the metal center,^[196,197] these signals are only of moderate amplitude. Furthermore, some of them are located at frequencies below 1000 cm^{-1} and, hence, are not accessible by means of the experimental techniques applied here.² The same holds true for the characteristic absorption band of the $\text{Fe}\equiv\text{N}$ stretching vibration of [2], which appears at 876 cm^{-1} according to the RR spectra published by Nakamoto et al..^[104]

For this reason, the verifications will be conducted in an indirect way using quenching experiments in this work. The working principle of these experiments is the addition of another substance, the *quencher*, to the photolyzed solution. Ideally, this substance reacts quantitatively and selectively with exactly one of the primary photoproducts to a specific secondary product, which exhibits an IR marker band. Furthermore, it is important that the quencher does not react with the parent compound, nor absorbs the excitation pulse by itself.

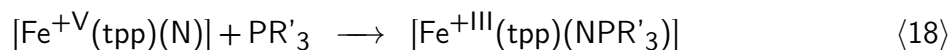
To identify the photoreductive pathway, iodide anions (I^-) have been established as simple and reliable quencher.^[120,178,198] The underlying reaction is a one-electron transfer converting the generated azidyl radical to an azide anion (Equation (17)).^[180,199] Then, as mentioned before, N_3^- anions can be detected easily via IR spectroscopy. The redox potentials of the redox pairs $\text{N}_3^\bullet/\text{N}_3^-$ and $\text{I}_2^\bullet/2\text{I}^-$ in aqueous solution are well-known and amount to $+1.33 \text{ V}$ ^[200] and $+1.03 \text{ V}$ vs. SHE,^[201] respectively. Although both potentials are naturally very dependent on the environment, it was shown that the oxidation of iodide by azidyl radicals is feasible in other commonly used solvents as well.^[202] Moreover, iodide anions can be introduced easily in solvents of different polarity by choosing the counter-cation appropriately. Still, this approach suffers from the fact that the redox reaction has to compete with the fast self-quenching of azidyl radicals (7) discussed in the previous section. Probably for this reason, the reduction to azide anions is inefficient and requires an excess of iodide to become quantitative.^[178]



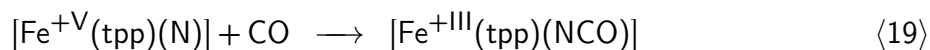
² This spectral region is obscured by absorptions of the CaF_2 windows of the measuring cell (cf. section 3.2) and many common solvents.^[190]

When quenching reactions shall be applied, it needs to be considered if, besides this desired reaction, the quencher can interact with other photoproducts or the reactant as well. Here, two options are conceivable: a coordination of the iodide to an iron complex and a redox reaction of both. The former option is unlikely since iodide is a weak ligand according to the spectrochemical series^[203,204] and the latter will occur only if the redox potential of a $[\text{Fe}(\text{tpp})(\text{L})_x]^q/[\text{Fe}(\text{tpp})(\text{L})_x]^{q-1}$ pair is larger than that of the $\text{I}_2^\bullet^-/2\text{I}^-$ pair (where $x = 0, 1, \text{ or } 2$, q is the charge, and L is an arbitrary ligand). Since the potential of the $[\text{Fe}^{\text{III}}(\text{tpp})]^+ / [\text{Fe}^{\text{II}}(\text{tpp})]$ pair was found to be -0.08 V (in benzonitrile)^[55] and it can be expected that an additional axial ligand stabilizes the iron(+III) state even more, an oxidation of iodide from low-valent complexes seems improbable. On the other hand, highly oxidized metal centers as in [2] could possibly be reduced by I^- ,^[198,205] potentially impeding other secondary reactions.

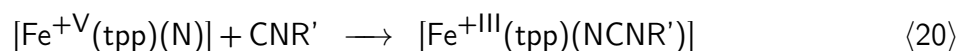
To validate the occurrence of the photooxidative pathway, several reaction partners for the generated nitrido complex are eligible.^[10,11,89,92–94] Here, only three of them, which have been used frequently in the past, shall be mentioned. (Again, the shown reaction equations will demonstrate them exemplary for the complex relevant for this work, [2].) There are many reports of the successful addition of phosphines (PR'_3 , with organic substituent R') to a nitrido complex yielding a phosphoraniminato ligand (NPR'_3 , see Equation (18)),^[7,11,89,90] whose $\text{P}=\text{N}$ stretching vibration absorbs strongly around 1200 cm^{-1} .^[115,116,206] Unfortunately, there are some cases known in which a reaction with phosphines does not occur.^[207]



An alternative reaction partner for [2] is carbon monoxide (CO), whose addition (Equation (19)) can be verified experimentally via detection of the characteristic absorption band of the $\text{N}=\text{C}=\text{O}$ antisymmetric stretching vibration of the resulting isocyanato ligand. This band has an absorption strength similar to the band of $\nu_{\text{as}}(\text{N}_3)$ and occurs typically in a frequency range from 2180 cm^{-1} to 2240 cm^{-1} .^[91,92,197,207,208]

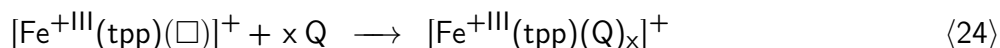
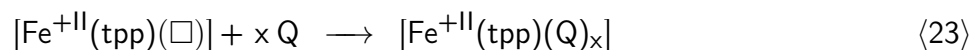
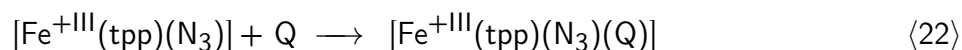
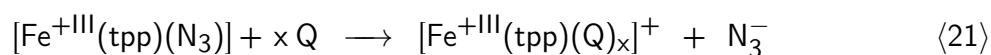


In the same way, an isonitrile (CNR') can react with a nitrido complex under formation of a carbodiimido complex, according to Equation (20).^[92–94,207] The absorption band of both the quencher and the product are reported to be located in the range from 2090 cm^{-1} to 2170 cm^{-1} , whereby the latter has a strong dependence on the properties of metal center.^[92,94,207,209–212] Compared to CO , isonitriles have some advantages. First, because of the organic substituent R' , their solubility in non-polar solvents is large, whereas CO dissolves well only in polar liquids.^[213,214] Second, these compounds are liquid (for small substituents R')^[215–218] rather than gaseous, making the preparation of their solutions simpler. Third, for the same reason, it is easily feasible to set their concentration precisely.



Interestingly, there is one example in which a subsequent ligand exchange of an isonitrile for the carbodiimido ligand is observed.^[92] In that study, the signal of a free carbodiimide anion was detected (2253 cm^{-1} for $t\text{BuNCN}^-$ in tetrahydrofuran solution).

Unfortunately, ligand substitutions are not limited to the products of the quenching reactions, but can affect all other complexes as well. For this reason, it has to be examined carefully, whether a quencher (Q) reacts with the parent compound or changes the light-induced primary reactions by coordination to it, as considered in Equations $\langle 21 \rangle$ and $\langle 22 \rangle$ ($x = 1, 2$), respectively. This holds true for isonitriles, carbon monoxide and phosphines since all of them are strongly coordinating molecules.^[204] Furthermore, other product complexes can be subjected to coordination of these molecules, too. In the case of the photoreductive or redox-neutral pathway, it is conceivable that recombination of the photoproducts could be prevented due to the occupation of the binding sites by a quencher, as shown in Equations $\langle 23 \rangle$ and $\langle 24 \rangle$, respectively.



2.2.3 Electronic Structure Considerations

Besides being important catalysts occurring widespread throughout nature, metalloporphyrins and related compounds are strong and flexible coloring agents,^[219] whose absorption properties have been the topic of empirical and theoretical considerations for a long time.^[220] An archetypal visible absorption spectrum of a metalloporphyrin consists of an exceptionally intensive absorption band in the range from 380 nm to 450 nm, the so-called *B-* or *Soret-band*, and up to four bands in the range from 500 nm to 700 nm, which are at least by an order of magnitude weaker than the B-band and referred to as *Q-bands*.^[221–225] For instance, the stationary UV-Vis absorption spectrum of (porphin-21,23-diido)zinc(+II) ($[\text{Zn}^{+\text{II}}(\text{p}^{2-})]$), adopted from ref. [226], is reproduced in Figure 4(a). The enormous oscillator strengths and low excitation energies stem from the extended π -electron system of the macrocyclic ligand, whose accurate description is a challenge theoretical chemists took up already in the 1950s.^[227–233] These early considerations culminated in the famous *four-orbital model* of porphyrins proposed by M. Gouterman,^[221] describing their low-energy excitations based on their two highest occupied (HOMO) and two lowest unoccupied molecular orbitals (LUMO). Although originally calculated within Hückel theory, the quantum mechanical description of these compounds was developed further using higher levels of theory with increasing computational capacities over

the following decades.^[51,108,222,234–239] Nevertheless, the 'shape' of the eponymous four orbitals remained qualitatively unchanged since their original introduction, and so did the essence of their interpretation.

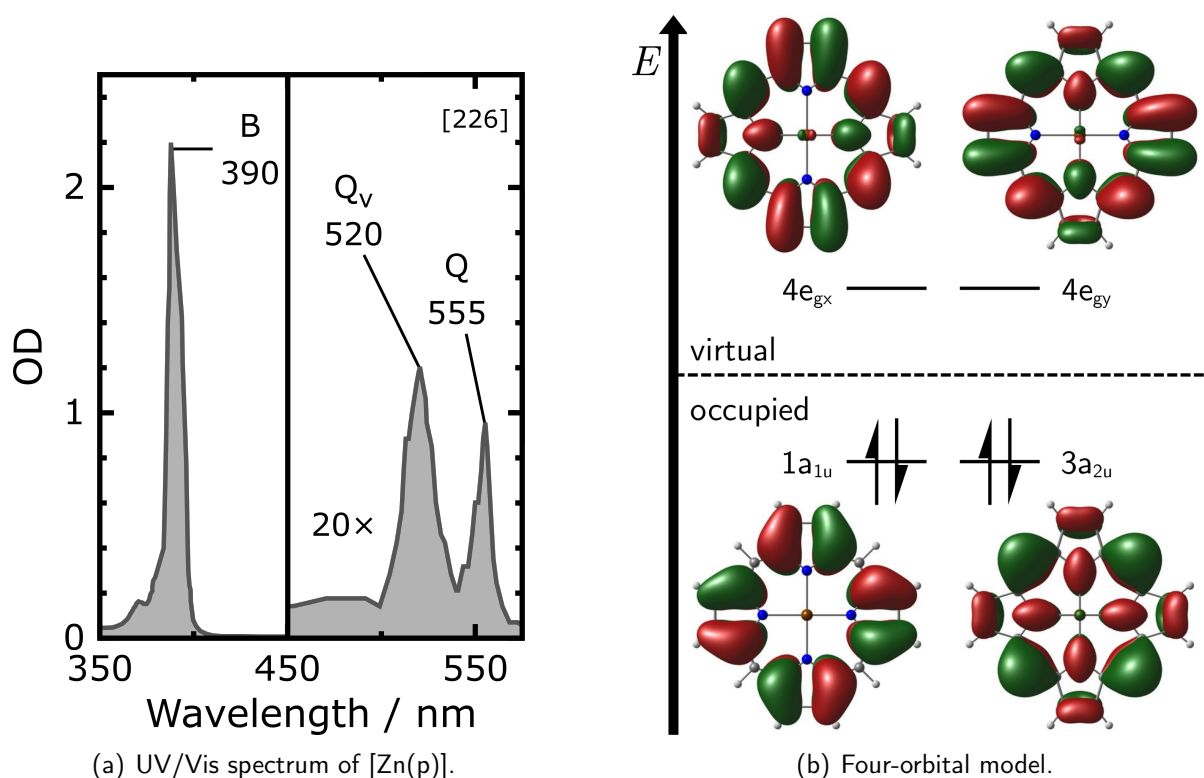


Figure 4: (a) Stationary UV-Vis absorption spectrum of [Zn(p)] in room-temperature *n*-octane solution, adopted from ref. [226]. The numbers indicate peak positions in nm. Note that the spectrum is scaled up by a factor of 20 above a wavelength of 450 nm. (b) Schematic energy level diagram of the frontier orbitals (Gouterman-orbitals) of [Zn(p)], including ball-and-stick models of the complex and isosurface plots of the orbitals. Isovalues: ± 0.02 . Harpoons pointing upwards and downwards represent α - and β -electrons, respectively. Labels designate the orbitals according to their irreducible representation within D_{4h} symmetry. Atomic color coding: H - white, C - gray, N - blue, Zn - brown.

A generic energy level diagram including Gouterman-orbitals of [Zn(p)], calculated by the methods described in section 3.3 and within D_{4h} ($\frac{4}{m} \frac{2}{m} \frac{2}{m}$) symmetry, is shown in Figure 4(b). All four frontier orbitals are π -orbitals and delocalized over the entire porphyrin macrocycle. While the two LUMOs are a set of degenerated orbitals of e_g -symmetry ($4e_g$), the two occupied orbitals, $1a_{1u}$ and $3a_{2u}$, belong to different irreducible representations, but are coincidentally almost degenerated as well. According to Gouterman's theory, the four possible one-electron excitations between these orbitals are subjected to strong configuration interactions.^[221,222,232,240,241] As a result, they split up into two high-energy excitation, which have high transition dipole moments and are responsible for the B-band, and two excitations of lower energy and transition dipole moment, giving rise to a single Q-band. In addition, the Q-band is often found to be accompanied by another band ca. 1250 cm^{-1} higher in wavenumber. This band was explained by the simultaneous excitation of a vibrational mode having this frequency and strongly coupled

to the electronic transition (a 'vibronic satellite' Q_V).^[222,241–243] Naturally, many metalloporphyrins deviate from D_{4h} symmetry because of substituents at the macrocycle, axial ligands bound to the metal, or intrinsic distortions.^[183,244–247] A lowering of the symmetry causes especially the Q-band to split up into two distinct bands, Q_x and Q_y ,^[220,221,232,248] resulting combined with the vibronic satellites in up to four distinct bands. Despite the four frontier orbitals having different designations depending on symmetry group of a complex, their shape remains recognizable regardless.^[221,236,237,249,250] For this reason and the sake of simplicity, these orbitals will be designated according to their irreducible representations within the point group D_{4h} throughout this work, although all complexes considered here belong to groups of lower symmetry. Moreover, the initial counting number will be omitted, leading to the notations: a_{1u} , a_{2u} , and e_g ($e_{g,x}$ and $e_{g,y}$).

It has to be mentioned that the energies of the a_{1u} - and the a_{2u} -orbital are dependent on the substitution of the metalloporphyrin. In more detail, substituents in pyrrole- β -position (like in 2,3,7,8,12,13,17,18-octaethylporphyrin-21,23-diido (oep²⁻) complexes) influence predominantly the a_{1u} -orbital, whereas those in *meso*-position (e.g. in tpp²⁻) affect mostly the a_{2u} -orbital.^[12,35,251,252] Moreover, electron-withdrawing and electron-donating groups lower and raise the energy of the affected orbital, respectively.

The electronic structure of $[Zn(p)]$ is in fact one of the most simple examples among the metalloporphyrins, because the central zinc(+II) ion is a d^{10} -system and, hence, does not contribute noteworthy to the low-energy excitations of the complex.^[253,254] In contrast, all complexes considered in this work contain open-shell iron centers. As it will be discussed in section 4.2, this causes the absorption spectrum of complex **[1]** to deviate significantly from the Gouterman model and to require a more sophisticated description.^[222,239,255] Here, a short overview of the contribution of the iron centers and axial ligands to the electronic structure of the relevant complexes shall be provided.

In general, the 4s-, three 4p-, and five 3d-orbitals of an iron atom contribute substantially to molecular bonding. Thereby, the former two sets overlap stronger with the orbitals of the adjacent atoms of the ligands than the latter set. As a consequence, the 4s- and 4p-orbitals are merged into σ - and σ^* -orbitals, subjected to a larger energy splitting. These orbitals have energies far apart from the pivotal range around the HOMO-LUMO gap^[121,204,256] and are therefore of subordinate importance in this consideration. In contrast, due to the smaller or (for symmetry reasons) absent overlap with orbitals of the ligands, the 3d-orbitals are typically found as the main contributions of weakly antibonding or non-bonding molecular orbitals. These orbitals are located in the relevant energetic range and will be discussed further here.

Schematic energy level diagrams of the five 3d-orbitals of the iron centers of the complexes **[3_{red}]**, **[1]**, and **[2]** are displayed in Figure 5. The energetic orders are based on references [253, 257], [255], and [108], which are (with one exception, see below) in agreement with the results of the calculations made in this work.

In complex **[3_{red}]**, the d_{xy} -orbital is lowest in energy, followed first by the d_{z^2} -orbital, then by the degenerated d_{xz} - and d_{yz} -orbital, as opposed to the expectations from simple

ligand field theory,^[121,204,256] which predicts the reverse order. This deviation is a result of an increased antibonding character of the latter three orbitals. Especially π -interactions between the d_{xz} - and d_{yz} -orbital and the π -orbitals of the porphyrindiido ligand,^[253] which are neglected in ligand field theory, raise their energies. As expected, the $d_{x^2-y^2}$ -orbital is significantly more up-shifted in energy due to a strong σ -antibonding interaction with the lone-pairs of the pyrrole-N-atoms. Since **[3_{red}]** is a d^6 -system, the distribution of electrons according to the Aufbau-principle indicates it to have a triplet ground state, which was in fact experimentally confirmed.^[258–261]

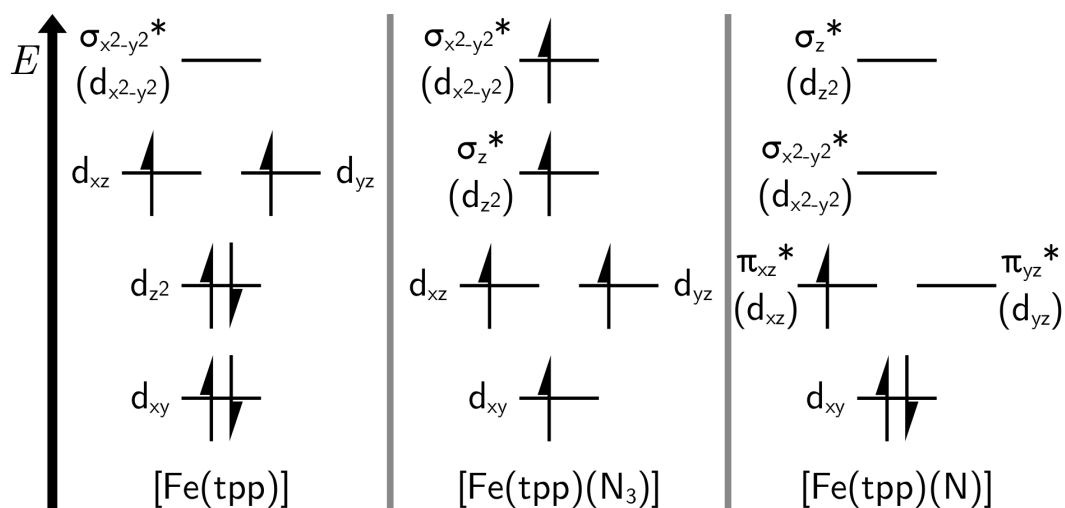


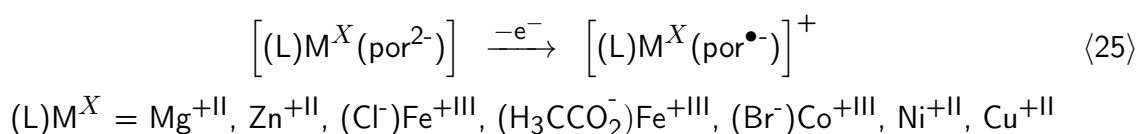
Figure 5: Schematic energy level diagrams of the 3d-orbitals of the iron atoms in the complexes **[3_{red}]** (left panel), **[1]** (central panel), and **[2]** (right panel). Harpoons pointing upwards and downwards represent α - and β -electrons, respectively.

Going to complex **[1]**, the introduction of the additional, axial azido ligand increases predominantly the relative energy of the d_{z^2} -orbital and, to a smaller extent, those of the d_{xz} - and d_{yz} -orbital. The electronic ground state of **[1]** was verified to be a high-spin, sextet state by a measurement of its magnetic susceptibility.^[262] The same holds true for related, square pyramidal tp^2 - complexes, carrying different anionic ligands^[255], e.g. the chlorido complex chlorido(5,10,15,20-tetraphenylporphyrin-21,23-diido)iron(+III), $[\text{Fe}^{\text{III}}(\text{tp})(\text{Cl})]$ (**[6]**).

Substitution of a nitrido ligand for the azido ligand raises the energy of the d_{z^2} -orbital even more, due to the smaller axial Fe–N bond length. According to the theoretical study from reference [108], it is located even above the $d_{x^2-y^2}$ -orbital. In contrast, the DFT calculations performed in this work predict the reverse order of those two orbitals. Notwithstanding this, the most intriguing feature of the electronic structure of complex **[2]** is the formation of π -bonding and -antibonding orbitals from the p_x - and p_y -orbital of the nitrido ligand and the d_{xz} - and d_{yz} -orbital of the iron atom. A description of a transition metal-nonmetal multiple bond was first introduced by Ballhausen et al. in 1962 on the example of the vanadyl cation,^[263] and later applied to a variety of other oxido- and nitridometal complexes.^[264–270] In essence, this model allows an explanation for the low stability and high reactivity of high-valent iron complexes. In a ligand sphere of tetragonal symmetry, as in **[2]**, all valence orbitals of the metal center participate in the formation of σ - and π -bonds to the ligands, except for the

d_{xy} -orbital. All bonding orbitals arising from these interactions are always filled with electrons formally contributed from the ligands. This allows in principle for a M–X (M = metal, X = O, N) bond order of three. However, depending on the number of d-electrons of the metal center, first the non-bonding d_{xy} -orbital, then the antibonding $\pi_x^*(d_{xz})$ - and $\pi_y^*(d_{yz})$ -orbital might become occupied. Consequently, a high d-electron count gives rise to a weakening of the M–X bond, explaining the experimental finding that oxido- and nitridometal complexes become continuously more reactive going from early to late transition metals.^[17,271,272] Nitrido complex [2] was proven to have a doublet (low-spin) ground state in frozen DCM solution,^[108] which means that a single electron occupies one of the $\pi^*(\text{FeN})$ orbitals, resulting in a Fe≡N bond order of 2.5.

In general, the four Gouterman-orbitals and the d-orbitals of the metal center are of similar energy but interact only marginally.^[232,235,253,273] Hence, the total energy level diagrams around the HOMO-LUMO gap of [1], [3_{red}], most other low-valent metalloporphyrins, and also [2] are essentially a sum of the individual diagrams of iron center and ligand. In contrast, the situation is very different for high-valent metal complexes other than [2]. Electrochemical one-electron oxidation of neutral porphyrindiido complexes of Zn^{+II}, Mg^{+II} as well as Fe^{+III}, Co^{+III}, Ni^{+II}, and Cu^{+II} results in an electron abstraction from the π -system of the macrocyclic ligand according to Equation <25>,^[55,274–277] although the latter metal ions possess d-electrons and could be further oxidized



The reason for this outcome is the fact that the a_{2u} - and a_{1u} -orbital of the porphyrin moiety are of similar energy as the d-orbitals of the metal center.^[235,253,273,278,279] With increasing oxidation state of the metal atom, its d-orbitals shift to lower energies, until they are located below the porphyrin's HOMO, so that the next oxidation will remove an electron from the latter. Such oxidized complexes are often called 'π-cation radicals',^[44,55,247,280,281] referring to the unpaired electron in the π -system of the porphyrinidyl ligand and their total positive charge. Unfortunately, this term is used very loosely in the literature, and many publications apply the expression 'π-cation radical' to the porphyrinidyl ligand (instead of the entire complex),^[27,28,282,283] ignoring the fact that the ligand still carries one negative formal charge after the electron abstraction. In this respect, the designation as 'cation' is highly misleading. For this reason, the expression 'π-radical' will be used in the rest of this work to refer to such electronic structures.

Interestingly, π -radicals can be categorized into two groups showing different absorption spectra,^[52,247,274–277,283–286] as it will be discussed in the following section. The distinction is based on the symmetry of the singly occupied molecular orbital (SOMO) of the porphyrinidyl π -radical ($\text{por}^{\bullet-}$), which might be either the a_{2u} -orbital or the a_{1u} -orbital. As mentioned above, which of both is higher in energy and, consequently, will be singly occupied after oxidation,

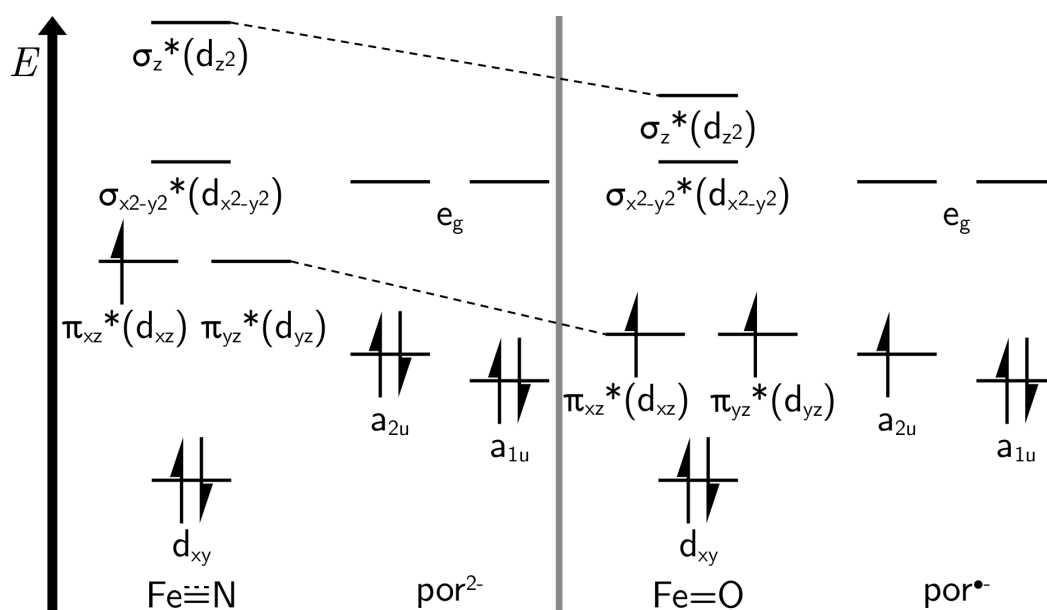


Figure 6: Schematic energy level diagram of the frontier orbitals of [2] (left panel) and [7] (right panel). Harpoons pointing upwards and downwards represent α - and β -electrons, respectively. The dashed lines indicate the relative energy shift of the Fe–X (X = N, O) antibonding orbitals by replacing an oxido for the nitrido ligand.

depends on the electronic effects and positions of substituents. Hence, 5,10,15,20-tetraphenylporphiridyl ($\text{tpp}^{\bullet-}$) complexes adopt usually an a_{2u} -type configuration and 2,3,7,8,12,13,17,18-octaethylporphiridyl ($\text{oep}^{\bullet-}$) complexes an a_{1u} -type configuration.^[37,274,275,283,285] In special cases, however, if both orbitals are nearly degenerated, an admixture of both configurations in the electronic ground state will be possible.^[275,285,287–289] Another feature of these structures is the opportunity of spin coupling between the porphiridyl ligand and the metal center, given that the latter is an open-shell ion.^[37,40,247,290–292] In this regard, both the strength and the character of the coupling (ferromagnetic vs. antiferromagnetic) appear to be very dependent on a variety of factors, e.g. the environment, the axial ligand, the counter-anion and substituents.^[40,245,247,291,293]

Besides electrochemical oxidation, another method of generating π -radicals is chemical oxidation accompanied by introduction of an oxido ligand.^[34,35,40,44,280,281,284,294,295] In fact, oxidoiron complexes bearing porphyrin ligands, e.g. the biocatalytically active Compound I or artificial model complexes like oxido(5,10,15,20-tetraphenylporphiridyl)iron(+IV), $[\text{Fe}^{+IV}(\text{tpp}^{\bullet-})(\text{O}^{2-})]^+$ ([7]), the oxido analog of [2], adopt in general a π -radical configuration.^[12,33,37,45,49,51,296,297] *meso*-substituted complexes like [7] were found to favor an overall quartet ground state, arising from local triplet state of the iron(+IV) ion strongly ferromagnetically coupled to the unpaired electron occupying the a_{2u} -orbital.^[43,44,298] Following the argumentation above, the Fe=O bond of these complexes is therefore best described as double bond. Considering this, it might be surprising that the seemingly isoelectronic nitridoiron complex [2] is an iron(+V) complex carrying a closed-shell porphyrindiido ligand and not a π -radical. This remarkable contrast is a consequence of the higher covalent character of the Fe \equiv N bond compared to the Fe=O bond,^[16] resulting in a larger energy splitting of

the π - and π^* -orbital from the Ballhausen model. Hence, the $\pi_x^*(d_{xz})$ - and $\pi_y^*(d_{yz})$ -orbital in [2] are higher in energy relative to the a_{2u} -orbital than in the case of [7],^[108] as sketched in Figure 6, impeding the formation of a π -radical.

Finally, another electron configuration which shall be mentioned here are porphyrin-centered triplet states (which will be abbreviated as 'triplet porphyrin states' in this work). These states are realized by promotion of an electron from an occupied $\pi(\text{por})$ -orbital to either of the e_g -orbitals and reversion of its spin orientation. Also here, distinctions between a_{1u} -type and a_{2u} -type states as well as between ferro- and antiferromagnetically coupled states can be made. Although these triplet porphyrin states are high in energy and are never the electronic ground state of a metalloporphyrin, they can occur as metastable states of considerable lifetime after photoexcitation, see also section 2.2.5.^[299–302]

2.2.4 Structure-Sensitive, Spectroscopic Characteristics of Metalloporphyrins

Naturally, both the variable functional groups, i.e. the metal center, substituents and axial ligand(s), as well as the multifarious electron configurations of metalloporphyrins manifest themselves in characteristic spectral signatures. For example, the presence of an axial ligand gives rise to a strong UV absorption band peaking around 370 nm.^[279,303,304] Moreover, Vis absorption characteristics of the various electronic structures were proposed based on spectra of electronically excited metalloporphyrins recorded by UV/Vis-pump/Vis-probe spectroscopy. A summary of these signatures was provided in the references [299, 300]:

- ◆ (Local) singlet $\pi(\text{por}) \rightarrow \pi^*(\text{por})$ states:
 - Reduced absorbance of the B-band compared to the ground state spectrum.
 - A strong absorption band between 450 nm and 650 nm, having a distinct maximum between 450 nm and 500 nm.
 - A broad, structureless, weak absorption band reaching from 700 nm up to the nIR.
- ◆ (Local) triplet $\pi(\text{por}) \rightarrow \pi^*(\text{por})$ states:

They have essentially the same spectral features as singlet $\pi(\text{por}) \rightarrow \pi^*(\text{por})$ states, but an additional, distinct band between 700 nm and 850 nm.
- ◆ $d(\text{metal}) \rightarrow d(\text{metal})$ states:

Their visible absorption spectra are red-shifted by 15-20 nm, but otherwise very similar to that of the electronic ground state, because the pivotal π - and π^* -orbitals of the porphyrindiido ligand are hardly affected by metal-centered excitations.
- ◆ $\pi(\text{por}) \rightarrow d(\text{metal})$ ligand-to-metal charge transfer (LMCT) states:
 - Reduced absorbance, broadening, and often blue-shift of the B-band compared to the ground state spectrum.
 - Each a strong absorption band peaking between 450 nm and 500 nm and between 650 nm and 700 nm.

- A broad, structureless, weak absorption band in the Q-band region, red-shifted compared to the ground state spectrum.

Furthermore, porphyrin π -radicals exhibit the same spectral features as $\pi(\text{por}) \rightarrow d(\text{Fe})$ LMCT states.^[55,305–311] This finding is not surprising, because their electron configurations are indeed identical to those of $\pi(\text{por}) \rightarrow d(\text{Fe})$ LMCT states, differing merely by the fact that this configuration has become their electronic ground state. Strictly speaking, it would be reasonable to make a distinction between π -radicals of the a_{1u} - and the a_{2u} -type, since their distinct electron configurations result in different absorption spectra. Although there are reports in the literature comparing the UV-Vis spectra of both types of π -radicals,^[54,283,284] a critical inspection^[285] led to the conclusion that a categorization of π -radicals by means of UV-Vis spectroscopy is not reliable due to the adulteration of the spectra by the influence of geometric factors. In addition, a mixture of a_{2u} - and a_{1u} -radical character can hardly be diagnosed by this means. Instead, EPR,^[37,40,252,288,306,312] electron nuclear double resonance (ENDOR),^[313–315] and NMR^[34–36,274,316–318] spectroscopy asserted themselves as appropriate detection techniques to evaluate the electron configuration of a porphyrin ligand, since they allow a more direct insight into the localization of the spin density.

Similar to their UV-Vis spectra, the infrared (IR) spectra of metalloporphyrins were extensively studied in the past^[197,319–321] In this context, the underlying vibrations were characterized by normal mode analyses.^[320,322–324] Comparisons of the IR and RR spectra of various porphyrindiido complexes revealed a set of vibrational modes, whose resonance frequencies are sensitive to the element of the metal center, its oxidation and spin state, the axial ligand and substituents at the porphyrindiido ligand.^[196,197,321,325–328] Among those, the only IR-active band above a frequency of 1000 cm^{-1} , i.e. the only one accessible using the setups employed in this work (see section 3), is the $\nu_{41}(\text{por})$ resonance band (nomenclature according to the normal mode analysis by Li et al.^[322]), absorbing around 1340 cm^{-1} . In more detail, the group of K. Nakamoto has demonstrated that this band is sensitive to the metal center^[321] and its spin state.^[196] For instance, the frequency of the $\nu_{41}(\text{por})$ band of $[\text{Fe}^{+III}(\text{tpp})(\text{L}_1)(\text{L}_2)]$ complexes was observed to fall in the range from 1331 cm^{-1} to 1341 cm^{-1} for high-spin and 1343 cm^{-1} to 1349 cm^{-1} for low-spin iron(+III) centers.

Interestingly, π -radical structures reveal themselves in IR spectroscopy not only in terms of the spectral positions of signals but also through their absorption strengths. A series of metalloporphyrins of metal centers in oxidation state +II and +III was shown to exhibit new and strong IR absorption bands upon electrochemical one-electron oxidation to π -radicals, which were essentially absent in the parent porphyrindiido complexes.^[329] Even more intriguing, the spectral position of the strong band, i.e. which normal mode is subjected to an amplification of its transition dipole moment, depends on the molecular structure of the π -radical: While $\text{tpp}^{\bullet-}$ complexes absorb strongly at ca. 1280 cm^{-1} , $\text{oepp}^{\bullet-}$ complexes manifest themselves through an increased absorption around 1550 cm^{-1} . Over several years, this finding was confirmed by various following studies.^[247,274,290,293,309,330–333] Later, the possibility of two distinct IR signatures of π -radicals was explained by electronic effects rather than the molecular structure.

According to Hu and Spiro,^[286] the absorption strength of a vibrational normal mode will be amplified if its atomic displacement vectors are perpendicular to the nodal planes of the porphyrin's SOMO. In brief, this model predicts that a_{2u} -radicals exhibit an increased absorption strength at 1280 cm^{-1} and a_{1u} -radicals at 1550 cm^{-1} .

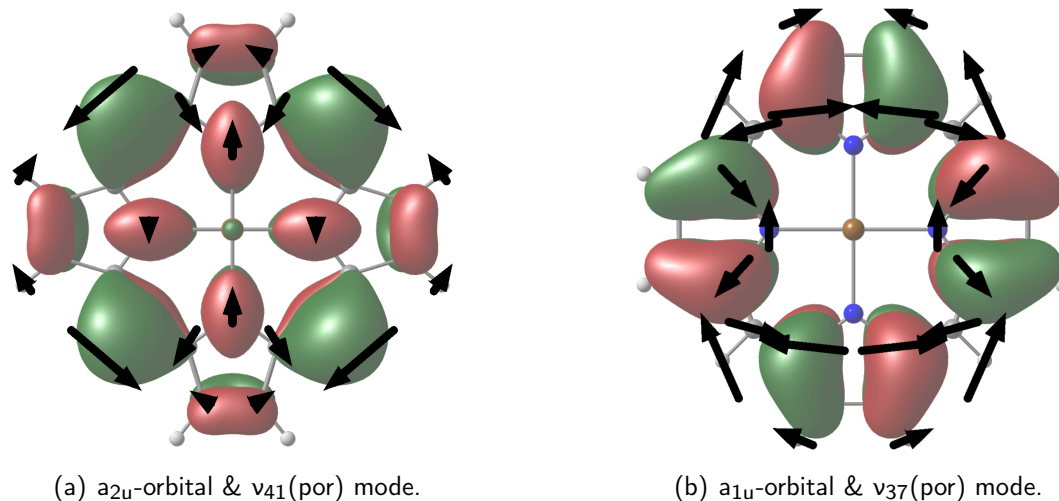


Figure 7: Ball-and-stick models of $[\text{Zn}(\text{p})]$, isosurface plots of (a) its $3a_{2u}$ -orbital and (b) its $1a_{1u}$ -orbital, and displacement vectors (black arrows) of the normal modes (a) $v_{41}(\text{por})$ and (b) $v_{37}(\text{por})$. According to reference [286], the transition dipole moments of these normal modes will get enhanced if the a_{2u} - or a_{1u} -orbital is single occupied, respectively, because their displacement vectors are perpendicular to the nodal planes of the respective orbital. Isovalues: ± 0.02 . Atomic color coding: H - white, C - gray, N - blue, Zn - brown.

As shown in Figure 7, the displacement vectors of the normal mode $v_{37}(\text{por})$, absorbing at ca. 1550 cm^{-1} , are perpendicular to the nodal planes of the a_{1u} -orbital. Similarly, the displacement vectors of the $v_{41}(\text{por})$ mode are perpendicular to the nodal planes of the a_{2u} -orbital. Moreover, the $v_{41}(\text{por})$ vibration was assigned to absorption bands peaking ca. 1280 cm^{-1} in that work. This is opposed to the commonly applied assignment, introduced by Li et al. for $[\text{Ni}(\text{tpp})]$,^[197,322] which associates this mode with signals located around 1340 cm^{-1} . In order to bring both studies in agreement, it needs to be assumed that the $v_{41}(\text{por})$ vibration is shifted by about -60 cm^{-1} upon π -radical formation. Such a change seems to be possible, as a similar shifts were reported for other modes in this region by RR spectroscopy.^[275,277,311,334,335]

Moreover, this model takes into account the possibility of mixed a_{1u}/a_{2u} -states, which were proposed to be the origin of an additional band at ca. 1600 cm^{-1} , besides the one at 1550 cm^{-1} , observed in some $\text{oe}p^{\bullet-}$ complexes. Since $\text{tpp}^{\bullet-}$ and $\text{oe}p^{\bullet-}$ complexes usually form a_{2u} - and a_{1u} -radicals, respectively, this theory predicts for most complexes the same IR signature as the previously suggested dependence of the porphyrin's substituents. Still, it has to be mentioned that exceptions for both explanations exist.^[286,329] Thus, the origin of the pronounced amplification of absorption strength of specific vibrations upon formation of a π -radical configuration is hitherto not fully understood.

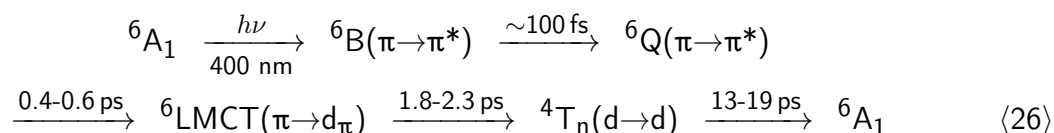
2.2.5 Photochemistry of Metalloporphyrins

Previous examinations on the photochemistry of metalloporphyrins have been conducted mainly by means of either visible transient absorption^[299,302,336–348] or fluorescence up-conversion spectroscopy, besides some other techniques.^[349–354] Comparing several studies, it becomes clear that the processes following photoexcitation are very dependent on the nature of system investigated.^[355–361] A detailed discussion of all de-excitation mechanisms of the various individual complexes^[336–341,356] exceeds the scope of this work. Hence, only a few findings shall be summarized here. In general, a distinction between, on the one hand, porphyrindiido complexes of the d^{10} -ion zinc(+II) and, on the other hand, metalloporphyrins of metal ions having open d-shells can be made. In zinc(+II) complexes, the lifetime of the B-state can reach up to a few picoseconds^[342,345,349–353,357,358,361,362] and the lifetime of the Q-state is in the order of 1-3 ns.^[299,351,358,361,363] Moreover, their lowest triplet state can be populated intermediately and lasts for up to a few milliseconds.^[301,362,364,365] On the other hand, the lifetime of the B-state in complexes of transition metals with open d-shell is limited to roughly 100 fs,^[337,358] and their ground state recovery occurs usually within tens to hundreds of picoseconds.^[302,336,338,339,341,346,347] This finding has been explained by the presence of the additional por \rightarrow metal charge transfer (CT) and metal-centered d \rightarrow d states between the electronic ground state, the Q-, and the B-state, which unlock alternative de-excitation pathways involving cascades of fast internal conversion (IC) and intersystem crossings (ISC).^[299,336–338,340,341,346,347,356,358] Still, triplet porphyrin states reach lifetimes of many microseconds even in these complexes.^[366,367]

The system probably most similar to [1] investigated so far is its chlorido analog [6]. The substitution of an chlorido ligand for the azido ligand can be expected to cause only marginal changes in the electronic structure. Hence, it will be assumed that the behaviour of [1] and [6] upon photoexcitation are essentially identical throughout this work.

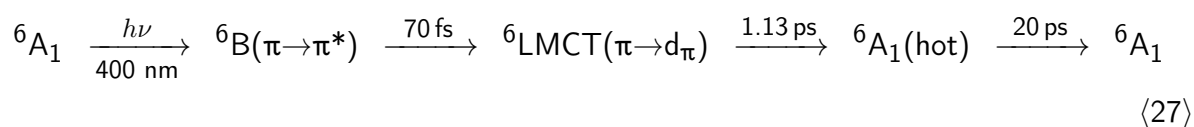
A picosecond UV-pump/Vis-probe experiment on complex [6] using 353 nm excitation pulses was already conducted in 1981^[368] and revealed two excited state absorptions at 445 nm and ca. 550 nm, declining with a time constant of 50 ± 20 ps. The authors assigned the underlying species to a triplet porphyrindiido complex and postulated this state to be populated by an ultrafast relaxation (< 100 fs) of the initially excited state, competing with an even faster direct ground state recovery. About thirty years later, the photoinduced dynamics of [6] were reinvestigated by A. S. Rury and R. J. Sension applying femtosecond 400 nm- and 520 nm-pump/Vis-probe spectroscopy.^[369] This study discovered the ultrafast processes to be dependent on the energy of the excitation pulses used: While complete GSR within ca. 100 ps was found at low pulse energies, excitation with higher energy yield a long-lived species. This observation indicated the occurrence of an additional de-excitation pathway initialized by two-photon absorption (TPA). Indeed, porphyrins are known to have exceptionally large cross-sections for both simultaneous^[345,359,360,370,371] and stepwise TPA.^[372–376] Besides that, the authors evaluated the spectro-temporal evolution observed after excitation with low-energy pulses by means of a global analysis. As they pointed out, the dynamics are well

described by a model featuring three exponential decay components with time constants of $\tau_1 = 0.4-0.6$ ps, $\tau_2 = 1.8-2.3$ ps and $\tau_3 = 13-19$ ps, depending on the solvent. Moreover, it was emphasized that a fourth, ultrafast (< 150 fs) relaxation process has to be preconnected because even the spectra at the earliest pump-probe delays are identical for both excitation wavelengths. Based on the results of a previous TD-DFT study on [6]^[239] and following the de-excitation mechanisms suggested for other metalloporphyrins, the authors developed a relaxation scheme summarized in Equation (26). Here, $\pi \rightarrow \pi^*$ refers to the mixed $a_{1u}/a_{2u} \rightarrow e_g$ excitations of the porphyrindiido ligand known from the Gouterman model.



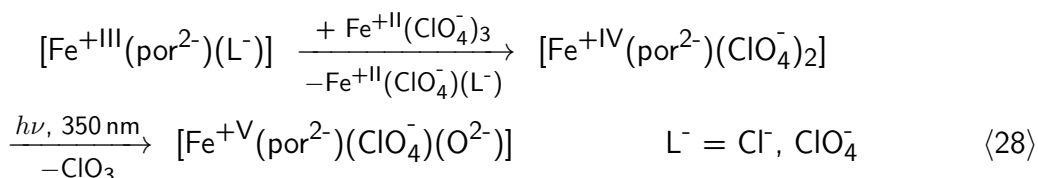
According to this, [6] undergoes an ultrafast (~ 100 fs) IC from the initially excited state (the B-state in the case of 400 nm excitation) to the Q-state, followed by a transition to a porphyrin-to-iron charge transfer state (${}^6\text{LMCT}(\pi \rightarrow d_\pi)$, with $d_\pi = d_{xz}/d_{yz}$) within ca. 0.5 ps. This state, for its part, has a lifetime of ca. 2 ps and relaxes further to a (presumably the lowest) quartet $d \rightarrow d$ state (4T_n), responsible for the absorption features observed at time delays of tens of picoseconds, in contrast to the earlier assignment to a triplet porphyrin state. Finally, [6] returns from this $d \rightarrow d$ state to its electronic ground state (6A_1) via an ISC. An alternative explanation for the spectro-temporal evolution involving pronounced effects of vibrational relaxation, as proposed for other complexes,^[338,344,346,347] was rejected in that work.

More recently, Vura-Weis and coworkers examined complex [6] by means of Vis-pump/ extreme UV-probe (XUV) spectroscopy,^[377] a technique mostly sensitive to the spin and oxidation state of the iron center, and proposed a remarkably different relaxation scheme, which is given in Equation (27). This group found strong XUV signals forming already within the earliest accessible pump-probe delays, indicative of a change of oxidation state of the iron center, and explained this finding by an ultrafast (70 fs) IC from the B-state directly to a LMCT state. Since these features were found to decay with $\tau_2 = 1.13$ ps to the much weaker signals of a 'nearly XUV-dark'^[377] state (maximal signal strength reduced to roughly one quarter), they proposed an IC to the vibrationally excited, electronic ground state, without an intermediate population of a $d \rightarrow d$ state, which is expected to yield stronger XUV responses than the observed ones. Also here, a process with a time constant in the range of ca. 20 ps was observed, which was, however, assigned to a VER on the ground state surface.



It has to be mentioned, that, although the electronic structures of [6] and [1] are presumably very similar to each other, there is a clear difference with regard to their possible reactivities.

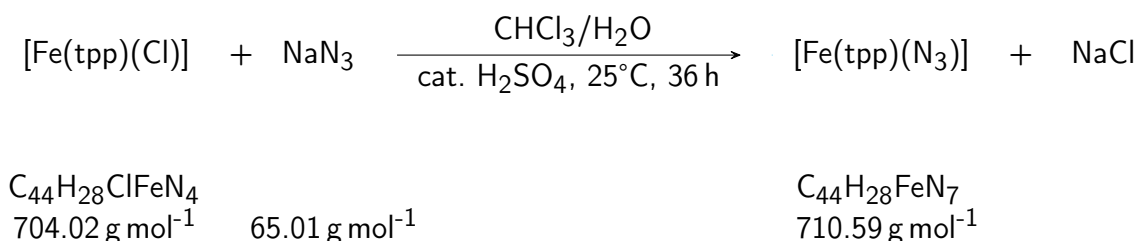
While photoreductive and redox-neutral photodissociations seem feasible in both cases, [6] cannot be converted directly to a high-valent complex similar to [2] via photooxidation. Yet, a comparable reactivity was observed for iron(+IV)(por²⁻) complexes carrying an axial perchlorato ligand, which are metastable compounds available from oxidation of the corresponding iron(+III) complexes with ferric perchlorate,^[64,378] cf. Equation (28). Upon irradiation, the photolabile perchlorato ligand undergoes a homolytic bond cleavage, thereby generating a high-valent oxidoiron complex^[60,64] reminiscent of Compound I and having a lifetime of some milliseconds.



Interestingly, measurements of this reaction by means of time-resolved absorption spectroscopy revealed that the high-valent product does not exhibit an UV-Vis spectrum typical of a π -radical, but instead a spectrum more similar to those of complexes bearing a closed-shell porphyrindiido ligands. Moreover, this intermediate was found to exhibit a much higher reactivity towards organic substrates than known π -radical oxidoiron(+IV) complexes,^[63] but similar to those of $[\text{Mn}^{+\text{V}}(\text{por}^{2-})(\text{O}^{2-})]^+$ ^[379,380] and $[\text{Fe}^{+\text{V}}(\text{cor}^{3-})(\text{O}^{2-})]$ complexes (cor = corrole).^[381] These results lead to the hypothesis that the primary product is an oxido(porphyrindiido)iron(+V) species, $[\text{Fe}^{+\text{V}}(\text{por}^{2-})(\text{O}^{2-})]^+$, i.e. an excited state of the oxido(porphirinidyl)iron(+IV) complex. In fact, the idea of a low-energy excited perferryl state has also been supported by subsequent theoretical calculations.^[51,56,58,249] Furthermore, this assumption offers an explanation for the discrepancy between the high reactivity of cytochrome P450 enzymes and the merely moderate reactivity of previous artificial model systems supposed to mimic them:^[61,63] The challenging C–H bond hydroxylations require the high-energy oxidoperferryl complex as catalytically active species instead of its oxidoferryl π -radical ground state. Yet, the short lifetime of this reactive state impeded earlier examinations on its reactivity, which were conducted mostly by means of the comparably slow stopped-flow mixing method.

3 Methods

3.1 Synthesis



Azido(5,10,15,20-tetraphenylporphyrin-21,23-diido)iron(+III) was prepared starting from its chlorido analog, [Fe(tpp)(Cl)], by substitution of an azido ligand for the chlorido ligand, as described by Adams et al. in the literature.^[382] 501 mg of [Fe(tpp)(Cl)] (Alfa Aesar, 0.712 mmol, 1.00 eq) were treated with 250 ml of chloroform (stab. with 0.6% ethanol, VWR Chemicals), a solution of 3.52 g of sodium azide (>99.0%, Sigma-Aldrich, 54.1 mmol, 76.0 eq) in 75 ml of water, and 8 drops of concentrated sulfuric acid (95-97%, Merck). The mixture was stirred at ambient temperature for 36 hours. During this time, small aliquots were extracted in order to measure their IR spectra. An optical density of about 0.06 at a frequency of 2056 cm⁻¹ and a layer thickness of 100 μm w.r.t. pure chloroform indicates the reaction to be completed. As soon as this criterion was fulfilled, the aqueous and organic phases were separated, and the latter was filtered, dried by addition of 370 mg of anhydrous sodium sulfate (≥99%, Carl Roth) and stirring for 3 hours, and filtered again. Afterward, the solvent was removed and the purple substance was dried for 8 hours under reduced pressure at 60 °C. The reaction yielded 412 mg (82 %) of the product complex.

IR: (DCM, 295 K): $\tilde{\nu} / \text{cm}^{-1}$ ($\epsilon / \text{M}^{-1} \text{cm}^{-1}$) = 1074 (330), 1179 (110), 1202 (220), 1340 (430), 1442 (380), 1488 (250), 1599 (180), 2056 (2150).

UV-Vis: (DCM, 295 K): λ / nm ($\log_{10}(\epsilon / \text{M}^{-1} \text{cm}^{-1})$) = 250 (4.32), 270 (4.30), 362 (4.81), 414 (5.09), 506 (4.20), 566 (3.67), 656 (3.52), 687 (3.61), 850 (2.74).

Elemental analysis³: (mass fraction / %)

Experimentally found: C – 72.78, H – 4.198, N – 13.25.

Anal. calc. for C₄₄H₂₈FeN₇: C – 74.37, H – 3.972, N – 13.80.

³ The elemental analysis was conducted on a Vario Micro Cube (Elementar).

3.2 Spectroscopic Methods

3.2.1 Stationary Spectroscopy

Stationary UV-Vis absorption spectra of the compounds of interest in liquid solution were recorded on a double-beam UV-160 spectrophotometer (Shimadzu) with a resolution of 3 nm and referenced against the spectra of the respective pure solvent, measured under identical conditions. To this end, both solutions and pure solvents were filled into 110-QS quartz cuvettes (Hellma), having an optical path length of 1 mm. Unless stated otherwise, stationary mIR absorption spectra were collected on a Nicolet 5700 Fourier-transform infrared (FTIR) spectrometer (Thermo Fisher) with a resolution of 1 cm^{-1} , again using the spectra of the respective pure solvent as reference, and corrected for artificial contributions arising from atmospheric water and carbon dioxide. For these measurements, solutions were filled into home-built cells consisting of two CaF_2 windows (4 mm thickness, Korth Kristalle GmbH) separated by $100\ \mu\text{m}$ polytetrafluoroethylene (PTFE) spacers and kept together by stainless steel holders. In all experiments, including those described in the following sections, DCM (99.8%, stabilized with amylene, Fisher Scientific) or deuterated dichloromethane (DCM-d_2) (99.6%, Deutero GmbH; for measurements in the spectral ranges from 1240 cm^{-1} to 1300 cm^{-1} and from 1405 cm^{-1} to 1435 cm^{-1}) were used as solvent.

3.2.2 Rapid-Scan Spectroscopy

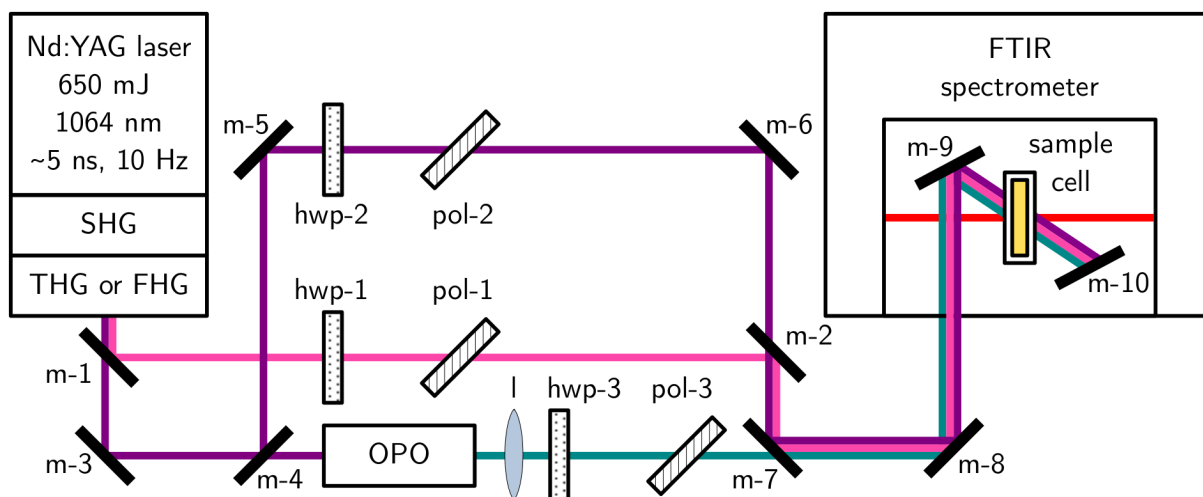


Figure 8: Schematic setup of the rapid-scan experiment. hwp - half-wave plate, l - convex lens, m - mirror, pol - thin film polarizer. Pink line - 266 nm beam, purple line - 355 nm beam, cyan line - 412 nm or 510 nm beam, red line - IR beam. The mirrors may be replaced or removed, depending on the chosen excitation wavelength. m-1 and m-2 are dichroic mirrors reflecting 266 nm light, whereas m-3 to m-6 are dichroic mirrors reflecting 355 nm light. m-7 to m-10 may be dichroic mirrors for either of these wavelengths or Ag mirrors.

Time-resolved mIR spectroscopy on timescales reaching from 10^1 ms to 10^1 s was performed using the rapid-scan mode of a commercial Vertex 70 FTIR spectrometer (Bruker), in conjunction with a Q-switched neodymium-doped yttrium aluminum garnet laser (Nd:YAG, Continuum, Surelite II-10), producing 650 mJ pulses centered at 1064 nm and a duration of ca. 5 ns at a repetition rate of 10 Hz.

Pump pulses centered at 266 nm and 355 nm were obtained by fourth- and third-harmonic generation (FHG; THG) of the fundamental frequency of the laser, respectively. The THG output was also used to drive an optical parametric oscillator (Surelite OPO Plus, Continuum) to provide pump pulses centered at 412 nm and 510 nm, which were collimated by a $f = +600$ mm lens. Independently of the center wavelength, the pulse energy was subsequently adjusted to 18 mJ by an appropriate half-wave plate and a thin film polarizer. Afterwards, the pump pulses were directed into the measuring cell in a way to spatially overlap with the IR beam of the spectrometer. In doing so, homogeneous illumination of the measured solution was ensured as the diameter of pump pulse (ca. 5 mm) was significantly larger than the diameter of the IR beam (1 mm). The setup is sketched in Figure 8.

In all rapid-scan experiments, solutions of [1] in DCM having a concentration of $c([1]) = 3.0$ mM were filled into home-built cells identical to those employed in the stationary FTIR measurements and described in section 3.2.1. When required, *tert*-butyl isonitrile (*t*BuNC) was added in equimolar amounts. In quenching experiment with tetra-*n*-butylammonium iodide (*n*Bu₄NI), its concentration was set to 3.0 mM, 10.5 mM, 30 mM, 105 mM, or 300 mM. Spectral and temporal resolution in these experiments amounted to 5 cm^{-1} and 72.5 ms, respectively.

3.2.3 UV/Vis-Pump/mIR-Probe Spectroscopy

Femtosecond UV/Vis-pump/mIR-probe experiments were driven by two ultrafast titanium-doped sapphire regenerative amplifiers (Ti:Sa, Solstice Ace, Newport Spectra-Physics), providing laser pulses having a duration of ca. 60 fs, an energy of > 4.5 mJ, and a center wavelength of 800 nm at a repetition rate of 1 kHz. Both lasers were seeded by a single, ultrafast, mode-locked Ti:sapphire oscillator (Mai Tai SP, Newport Spectra-Physics). The front-end output of the first laser system was divided into several fractions, one of which was used to drive a commercial optical parametric amplifier (OPA, TOPAS 800, Light Conversion) when required. Subsequently, pump pulses having center frequencies needed for the various pump-probe experiments were obtained by the following non-linear processes conducted in appropriately cut β -barium borate (β -Ba(BO₂)₂, BBO) crystals:

- ◆ 266 nm: Third-harmonic generation of the fundamental frequency (THG).
- ◆ 355 nm: Forth-harmonic generation of the TOPAS' signal output centered at 1420 nm (FHGS).

- ◆ 400 nm: Second-harmonic generation of the fundamental frequency (SHG).
- ◆ 510 nm: Sum frequency generation of the fundamental frequency and the TOPAS' signal output centered at 1410 nm (SFGS).

Thereafter, the pump beam was sent through a half-wave plate and a chopper disc, rotating synchronized to the laser's repetition rate to block every second pulse. Finally, the beam was focused by a fused silica lens ($f = +400$ mm) into the measuring cell, in which its diameter amounted to ca. 500 μ m. The pulse energy at the position of the measuring cell was adjusted as required.

The front-end output of the second laser system was used to drive another commercial optical parametric amplifier (TOPAS Prime, Light Conversion), whose signal- and idler-output were thereupon frequency down-converted in a type-I silver gallium sulfide (AgGaS_2) crystal via difference frequency generation (DFG) to mid-infrared pulses having a spectral bandwidth of roughly 200 cm^{-1} . Residual signal and idler light were removed by a germanium filter (Ge, Spectrogon) behind the crystal. The generated mIR-beam was then divided by a 50:50 beam splitter into two fractions, the probe and the reference beam, the former of which was sent two times through a silver-coated hollow-roof retroreflector (UBBR2.5-5S, Newport) mounted on a motorized translation stage (DL325, Newport). This setup allows a precise setting of the delay between pump and probe pulse in a range from roughly -500 ps to 3.5 ns. In the following, the powers of both beams were adjusted individually, each by a tunable half-wave plate and a polarizer. Thereafter, the beams were focused into the measuring cell by a gold-coated 90° off-axis parabolic mirror (OAP, $f_{eff} = +100$ mm) and afterwards recollimated by another, identical mirror. The diameter of both mIR beams inside the cell amounted to ca. 400 μ m, i.e. slightly smaller than that of the pump beam, guaranteeing homogeneous illumination of the measured fraction of solution. Behind the second OAP, the beams could optionally be attenuated further by IR reflective neutral density filters. Subsequently, they were focused by calcium fluoride lenses (CaF_2 , $f = +100$ mm), directed into a polychromator (iHR320, Horiba) and recorded by a 2×32 pixel, liquid-nitrogen cooled, mercury cadmium telluride (HgCdTe , MCT) array detector (MCT-13-1.0, Infrared Associates). The detector's electrical output was sent to a home-built 64 channel amplifier, digitalized by three data acquisition boards (DT 3016, Data Translation) and recorded by a homemade software.

The optical pathways were adjusted in a way that the spectral overlap of all three beams inside the measuring cell was guaranteed, the angles between pump and reference beam and pump and probe beam amounted to only 5°, and the reference pulse arrived at the cell ca. 1.5 ns before the pump pulse. Moreover, the polarization plane of the pump beam was set to the magic angle w.r.t. that of the probe beam to eliminate signal contributions caused by rotational diffusion.

The recorded spectra of the reference pulses were utilized to account for the shot-to-shot instability of the probe OPA, whereas the spectra of the probe pulses correspond alternatingly to the intensities $I_{s,wp}$ and $I_{s,wop}$ from Equation (18), depending on whether the pump pulse was blocked or permitted by the chopper disc, and were employed to calculate the differential

optical density.

During all measurements, the setup was purged with dry air to minimize absorption of the mIR pulses by atmospheric water. The measuring cell was a home-built flow cell, consisting of two CaF₂ windows (4 mm thickness, Korth Kristalle GmbH), held at a distance of 200 μm by an amalgamated lead spacer, and mounted together by an aluminum holder. The measured solutions of [1] in DCM or DCM-d₂ had a concentration of $c([1]) = 3.0 \text{ mM}$ and were circulated through a closed-looped PTFE tubing system, including a reservoir and the flow cell. Here, the flow was implemented by a gear pump (mini-gear pump 316/PTFE, Maprotec) and set to a rate of ca. 100 mL min⁻¹. Additionally, the cell was mounted to a motorized cell holder, allowing translation perpendicular to the pump beam during the measurements to avoid deposits of solid photoproducts on its windows. The entire setup is depicted in Figure 9.

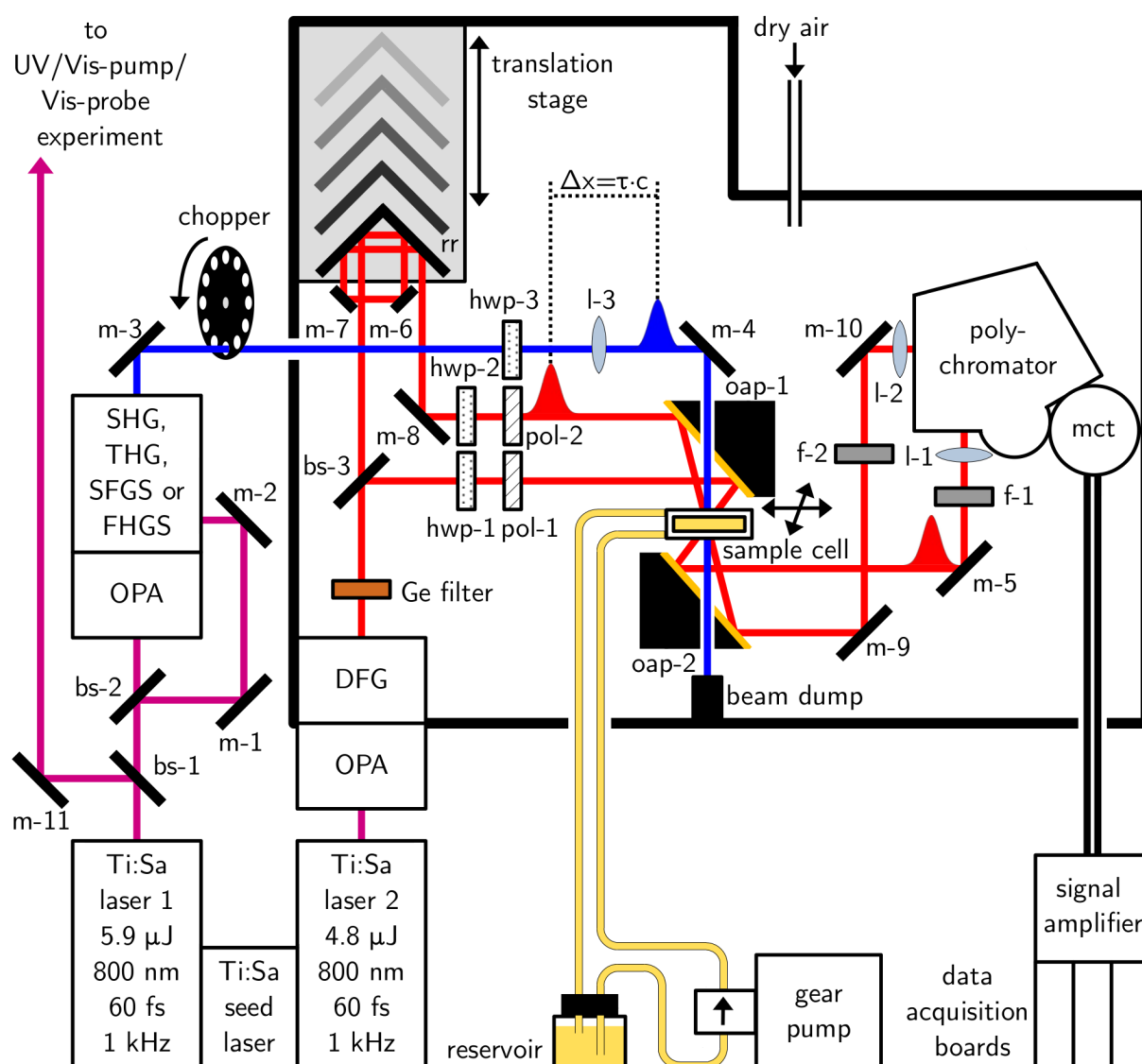


Figure 9: Schematic setup of the UV/Vis-pump/mIR- probe experiment. bs - beam splitter, f = IR filter, hwp - half-wave plate, l - convex lens, m - Ag mirror, mct - HgCdTe detector array, oap - Au-coated 90° off-axis parabolic mirror, pol - polarizer, rr - retroreflector. Pink line - 800 nm beam, blue line - pump beam, red line - mIR beam, yellow line - tubing filled with solution.

3.2.4 UV/Vis-Pump/Vis-Probe Spectroscopy

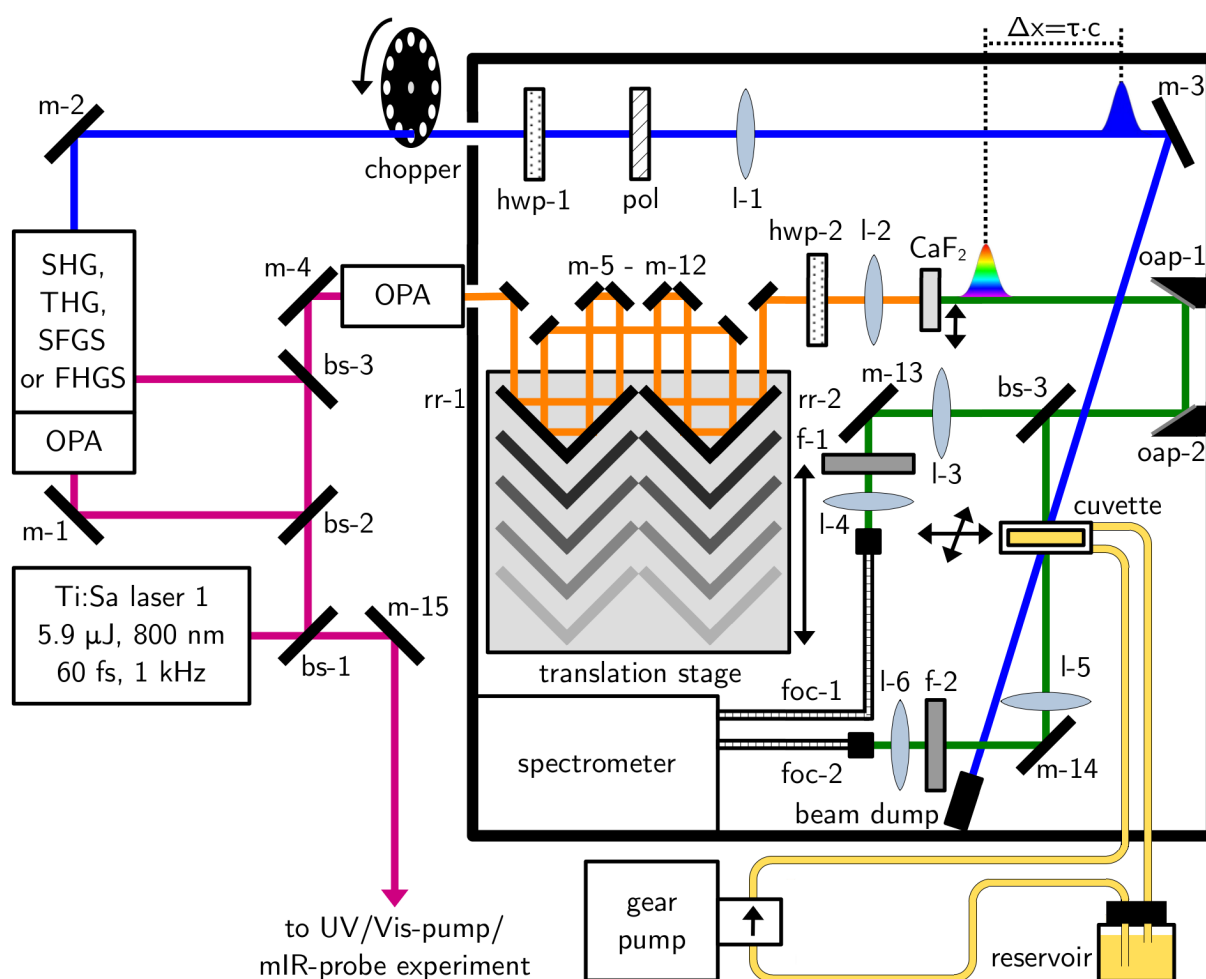


Figure 10: Schematic setup of the UV/Vis-pump/Vis-probe experiment. bs - beam splitter, f - neutral density filter, foc - fiber optic cable, hwp - half-wave plate, l - convex lens, m - Ag mirror, oap - Ag-coated 90° off-axis parabolic mirror, pol - polarizer, rr - retroreflector. Pink line - 800 nm beam, blue line - pump beam, orange line - signal beam, green line - white-light beam, yellow line - tubing filled with solution.

The femtosecond UV/Vis-pump/Vis-probe spectrometer (TAS, Newport/Spectra Physics), sketched in Figure 10, was powered by the same Ti:sapphire oscillator/regenerative amplifier front-end employed to generate pump pulses for the UV/Vis-pump/mIR-probe setup. A fraction of its output was converted to UV or Vis pump pulses by the same processes described in the previous section, using another commercial OPA (TOPAS Prime, Light Conversion) when required. The pump pulses traveled through a chopper disc, a half-wave plate setting their polarization plane to the magic angle w.r.t. that of the probe pulses, a $f = +75$ mm lens and were finally directed into the measuring cell. The pulse energy at the position of the cell was adjusted to $8.0 \mu\text{J}$ unless mentioned otherwise.

Another fraction of the laser's fundamental was used to drive a third TOPAS Prime to generate signal pulses centered at 1250 nm, which were first sent four times along a linear motorized translation stage (DLS 325, Newport) equipped with two silver-coated hollow-roof

retroreflectors (UBBR2.5-2I, Newport), allowing an adjustment of the pump-probe delay, and afterwards focused by a $f = +100$ mm quartz lens into a 3 mm calcium fluoride substrate moved by a motor during the measurements. In this substrate, a white-light supercontinuum was produced via self-phase modulation. Then, it was focused by two Ag-coated off-axis parabolic mirrors ($f_{eff} = +100$ mm), divided into a probe and a reference pulse, the former of which was spatially overlapped with the pump pulse inside the measuring the cell under an angle of ca. 10° . The diameters of the pump and probe beam inside the cell amounted to ca. $900 \mu\text{m}$ and ca. $500 \mu\text{m}$, respectively. Both probe and reference pulse were attenuated by neutral density filters and directed with fiber optic cables into a polychromator equipped with two diode arrays with 1024 pixels each. The entire setup and data acquisition was controlled by a homemade software. Thereby, the measuring principle is identical to this of the UV/Vis-pump/mIR-probe experiment.

The sample cell was a 1 mm quartz glass flow cell (QS, Hellma), attached to a tubing system identical to that described in section 3.2.3, and moved by two motors throughout the measurement. Solutions of **[1]** in DCM had a concentration of $c(\mathbf{[1]}) = 60 \mu\text{M}$.

3.3 Computational Methods

All quantum chemical calculations in this work were carried out within the framework of density functional theory (DFT) and its time-dependent extension (TD-DFT) using the program package TURBOMOLE V7.5.^[383–386] Chai's and Head-Gordon's functional ωB97X ,^[387] a range-separated hybrid version of Becke's GGA functional B97,^[388] was employing in conjunction with Ahlrichs' triple- ζ basis set, def2-TZVP,^[389,390] for all atoms of the porphyrin skeleton, iron atoms and the azido, chlorido, oxido, nitrido, isonitrilo, and carbodiimido groups of the axial ligands, whereas the smaller def2-SVP basis set^[389,391] was used for the atoms of the peripheral phenyl and *tert*-butyl groups. In order to compensate for the neglect of dispersion interaction of density functionals, Grimme's empirical dispersion correction, version 4 (D4)^[392,393] was added. Numerical integrations were performed on grids of the size 4 (internal nomenclature of the program). An implicit solvation model (conductor-like screening model, COSMO) was intentionally omitted as it caused issues in the convergence of frequency and TD-DFT calculations in some cases. Still, since experimental electronic absorption spectra of metalloporphyrins in the gas phase and in solution do not differ noteworthy,^[223,224] it can be assumed that results obtained under neglect of the solvation model are transferable to the systems in solution. If not stated otherwise, molecules were calculated within C_1 (1) symmetry, even though some of them could be assumed to adopt a higher symmetry group.

In more detail, single point calculations were considered to be converged if the difference of the total energy and the one-electron energy of two consecutive iteration steps were smaller than 10^{-7} and 10^{-4} , respectively. (All thresholds in atomic units.) Molecular geometries were optimized to a change of total energy of less than 10^{-6} between two successive steps, a

root mean square (rms) gradient and rms displacement of less than $5 \cdot 10^{-4}$, respectively, and a maximal gradient element and a maximal displacement element of 10^{-3} , respectively. The convergence of the electronic wavefunctions of the optimized structures were validated via stability analyses. All structures were confirmed to be true minima of the potential energy surface by analytic frequency calculations within the harmonic approximation and verifying that all eigenvalues of their hessian matrices are positive. The convergence criteria of frequency and excited state calculations were set to a maximal Euclidian residual norm of less than 10^{-5} and 10^{-7} , respectively. Other parameters equated to the default settings of the program. Vibrational frequencies were scaled by an empirical factor of 0.942 to account for the intrinsic overestimation made by hybrid density functionals. Population analyses were performed using the Löwdin method.

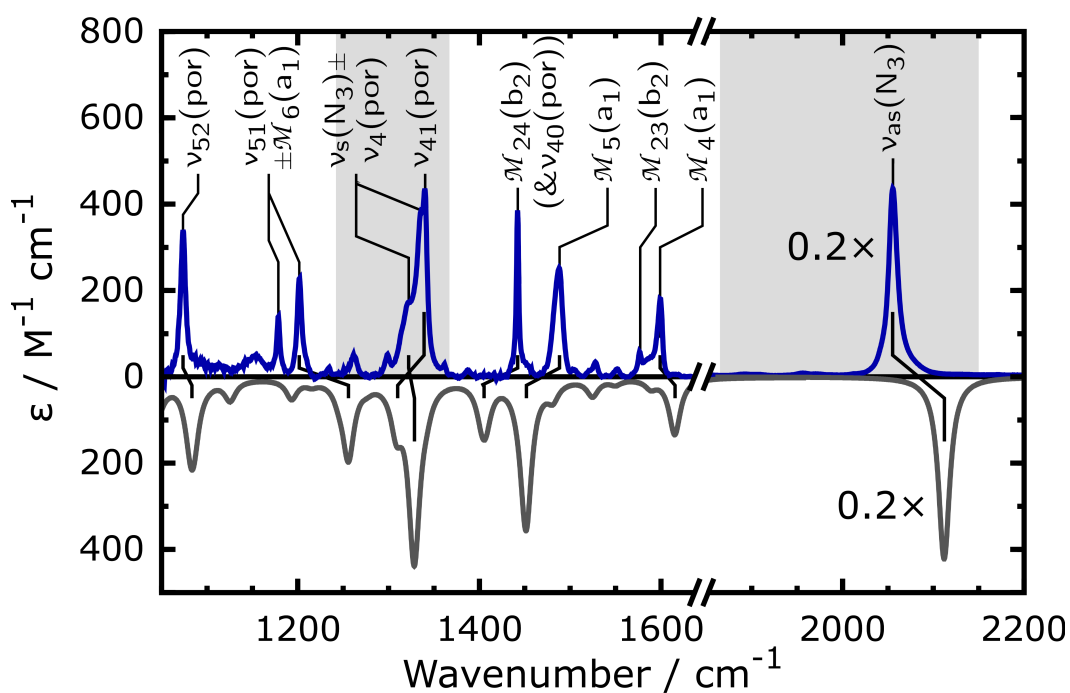
4 Stationary Spectroscopy

4.1 FTIR Spectroscopy

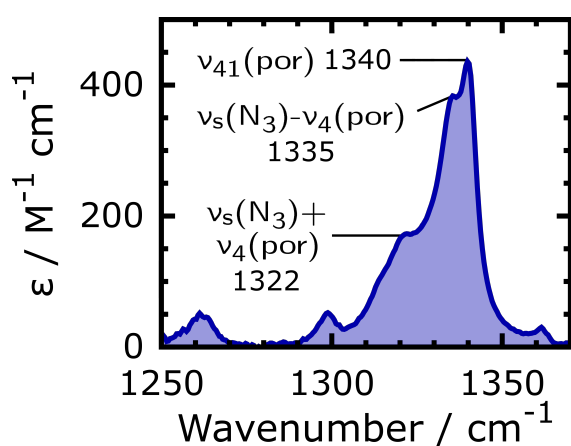
The stationary FTIR absorption spectrum of [1] in room-temperature DCM (DCM-d₂) solution in the spectral range from 1050 cm⁻¹ to 2200 cm⁻¹ is displayed in the upper panel of Figure 11(a). The spectrum consists of a variety of distinct signals, which will be assigned to molecular vibrationals in the following. To this end, the experimental spectrum of [1] is compared with spectra of related complexes and a theoretically predicted spectrum, shown in lower panel of Figure 11(a). As the figure demonstrates, the DFT calculation reproduces the experimental spectrum reasonably and, hence, justifies the application of the computed results in the interpretation.

Starting from the high-frequency border of the shown spectral range, a very pronounced signal, having a peak extinction coefficient of ca. 2150 M⁻¹ cm⁻¹, is observed at a frequency of 2056 cm⁻¹. A magnified representation of this signal is given in Figure 11(c). This band can be assigned unarguably to the antisymmetric stretching vibration of the N₃-ligand of [1], $\nu_{\text{as}}(\text{N}_3)$, since this vibration is, as already mentioned in section 2.2.2, a characteristic marker band of this functional group well known from other azido complexes.^[197,394] Moreover, the calculated spectrum of [1] features an intense resonance band in this spectral region, although 56 cm⁻¹ higher in wavenumber than the experimental value even after application of a scaling factor as typically done for frequencies obtained by hybrid-DFT methods. The corresponding, computed atomic displacement vectors of the underlying normal mode are depicted in Figure 11(f) and confirm the assignment to $\nu_{\text{as}}(\text{N}_3)$. The line shape of this signal complies well with a Lorentzian profile, except for a weak shoulder on its high-frequency flank, whose origin is undisclosed so far. It is worth mentioning that the resonance band of $\nu_{\text{as}}(\text{N}_3)$ of the bound N₃-ligand is blue-shifted by 50 cm⁻¹ with respect to the uncoordinated, free N₃⁻ anion in DCM solution (cf. Figure A2 in the appendix). In contrast, the absorption strength of this vibration is almost unaffected by coordination to the metal center. In fact, the ratio of the frequency-integrated extinction coefficients, α_a , of the $\nu_{\text{as}}(\text{N}_3)$ bands of [1] and N₃⁻ amounts to 0.95, differing only slightly from unity. For the purpose of time-resolved measurements of complex [1], probing this absorption band is an evident choice for several reasons. First, the signal exhibits a high absorption strength and, second, peaks in a region free of disruptive signals of the solvent or the atmosphere. Moreover, the signal is isolated from other bands of the complex, and localized on the reactive functional group. For all these reasons, time-resolved measurements of this band can be expected to yield results which are of high quality, contain valuable information, and are relatively easy to interpret.

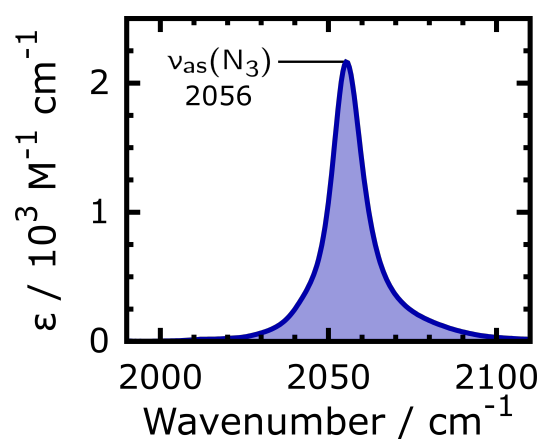
Going to lower frequencies, four bands at 1599 cm⁻¹, 1577 cm⁻¹, 1488 cm⁻¹, and 1442 cm⁻¹ are observed, whose extinctions coefficients range from 60 M⁻¹ cm⁻¹ to 400 M⁻¹ cm⁻¹. An expanded picture of this spectral region and representations of the underlying normal modes are given in Figure A1(b) and (f) - (j), respectively, in the appendix. All four signals match well-known resonance bands of monosubstituted phenyl groups, referred to as $\mathcal{M}_4(a_1)$,



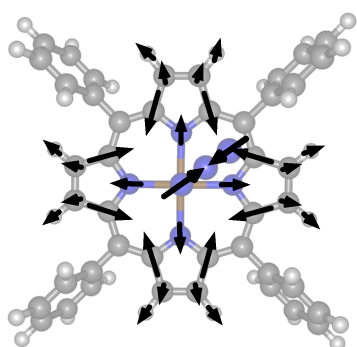
(a) Complete considered spectrum: 1050-2200 cm^{-1} .



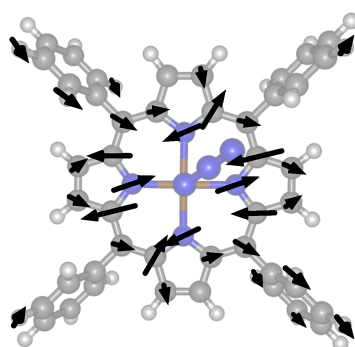
(b) Expanded 1250-1370 cm^{-1} region.



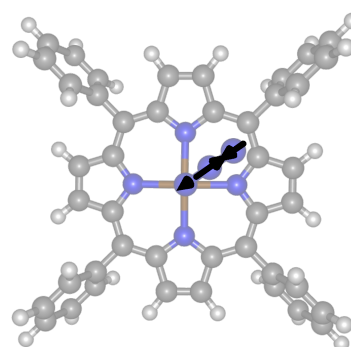
(c) Expanded 1990-2110 cm^{-1} region.



(d) $\nu_s(\text{N}_3)$ - $\nu_4(\text{por})$; 1335 cm^{-1} .



(e) $\nu_{41}(\text{por})$; 1340 cm^{-1} .



(f) $\nu_{as}(\text{N}_3)$; 2056 cm^{-1} .

Figure 11: Stationary FTIR absorption spectrum of [1] in room-temperature DCM (DCM-d_2) solution. (a) Upper panel: experimental spectrum (blue); regions probed in the fs-pump-probe experiments (light gray). Lower panel: inverted DFT-predicted spectrum (gray) obtained by convolution of the stick spectrum with a Lorentzian function having a FWHM of 20 cm^{-1} ; assignment of experimental and theoretical absorption bands (black lines and labels); above the axis intercept, the spectra are scaled by a factor of 0.2 for more clarity. (b) & (c) Expansions of the experimental spectrum in the spectral regions

important for this work, as specified in the subtitles. The numbers and labels indicate peak positions in cm^{-1} and their assignment. (d), (e) & (f) Ball-and-stick models of [1] and calculated atomic displacement vectors (black arrows) of the normal modes corresponding to the absorption bands shown in (b) and (c). The subtitles specify their notations and experimental resonance frequencies. Atomic color coding: H - white, C - gray, N - blue, Fe - brown.

$\mathcal{M}_{23}(b_2)$, $\mathcal{M}_5(a_1)$, and $\mathcal{M}_{24}(b_2)$, respectively, in the systematic Mulliken (Herzberg) nomenclature^[140,395] suggested by Wright and coworkers.^[396] Regarding the three high-frequency signals, this assignment is fully in line with the results of the DFT calculation. However, in the case of the band centered at 1442 cm^{-1} , the calculations predict an overlap and weak coupling of the $\mathcal{M}_{24}(b_2)$ vibration with the $\nu_{40}(\text{por})$ mode centered at the porphyrin moiety, both of which are essentially C–H rocking modes. Although both porphyrin and phenyl groups exhibit a resonance at this frequency, it can be assumed that the absorbance originates predominantly from the phenyl groups. A study by Hu and Spiro revealed that the analogous band of [Cu(tp)] changes its spectral position only upon deuteration of the phenyl rings, but not upon deuteration of the porphyrin skeleton.^[286] Regarding their sensitivity towards the electronic and molecular structure, a comparison to spectra of other metallo-tp complexes demonstrates all four bands to be hardly affected by the nature of the metal center and axial ligand.^[397,398] For this reason and because of their poor absorption strength, these signals are of subordinate importance in view of exploring the photoreactivity of [1].

At even lower frequencies, three overlapping bands are observed at 1340 cm^{-1} , 1335 cm^{-1} , and 1322 cm^{-1} (cf. Figure 11(b)), with extinction coefficients of $430\text{ M}^{-1}\text{ cm}^{-1}$, $380\text{ M}^{-1}\text{ cm}^{-1}$, and $170\text{ M}^{-1}\text{ cm}^{-1}$, respectively. The first signal can be assigned to the $\nu_{41}(\text{por})$ mode, an E_u -symmetric combination of the symmetric pyrrole half-ring stretching modes (in the idealized picture of the porphyrin ligand having D_{4h} symmetry),^[322] visualized in Figure 11(e). Moreover, the corresponding A_{1g} -symmetric combination ($\nu_4(\text{por})$) and the symmetric azide stretching vibration ($\nu_s(\text{N}_3)$) are known to have resonance frequencies in this spectral region.^[197,394] Both of these normal modes would be IR-silent if the N_3^- -ligand and tp^{2-} -ligand adopted the high symmetry group of their respective free anion ($D_{\infty h}$ and D_{4h} , respectively). Yet, because of the coordination to the metal center, the symmetry is lowered and $\nu_s(\text{N}_3)$ becomes IR-active. The DFT calculations predict $\nu_s(\text{N}_3)$ and $\nu_4(\text{por})$ to be strongly coupled, so that the resulting out-of-phase and in-phase combinations, $\nu_s(\text{N}_3)-\nu_4(\text{por})$ and $\nu_s(\text{N}_3)+\nu_4(\text{por})$, can be held responsible for the signals at 1335 cm^{-1} and 1322 cm^{-1} , respectively. The former normal mode is depicted in Figure 11(d).

It is worth mentioning that the good agreement of the computed and experimental spectrum in this region is merely a result of an error compensation. As shown in Figure A3 in the appendix, DFT predicts the weak band at 1322 cm^{-1} to originate from $\nu_{41}(\text{por})$. However, a comparison of the experimental spectra of [1] and the chlorido complex [6] reveals that only the band at 1340 cm^{-1} is preserved upon replacement of the azido ligand. Consequently, this signal must originate from a tp^{2-} -centered vibration, while the other two bands source

their absorption strength from the azido ligand. Hence, the correctly predicted spectrum is a corollary of, on the one hand, both the frequency and the oscillator strength of $\nu_{41}(\text{por})$ being underestimated and, on the other hand, both quantities being overestimated in the case of $\nu_5(\text{N}_3)$. Moreover, the harmonic frequency calculation does not reproduce the smaller signals observed at 1361 cm^{-1} , 1299 cm^{-1} , and 1261 cm^{-1} , which are therefore likely to originate from either overtones or combination modes of low-frequency vibrations.

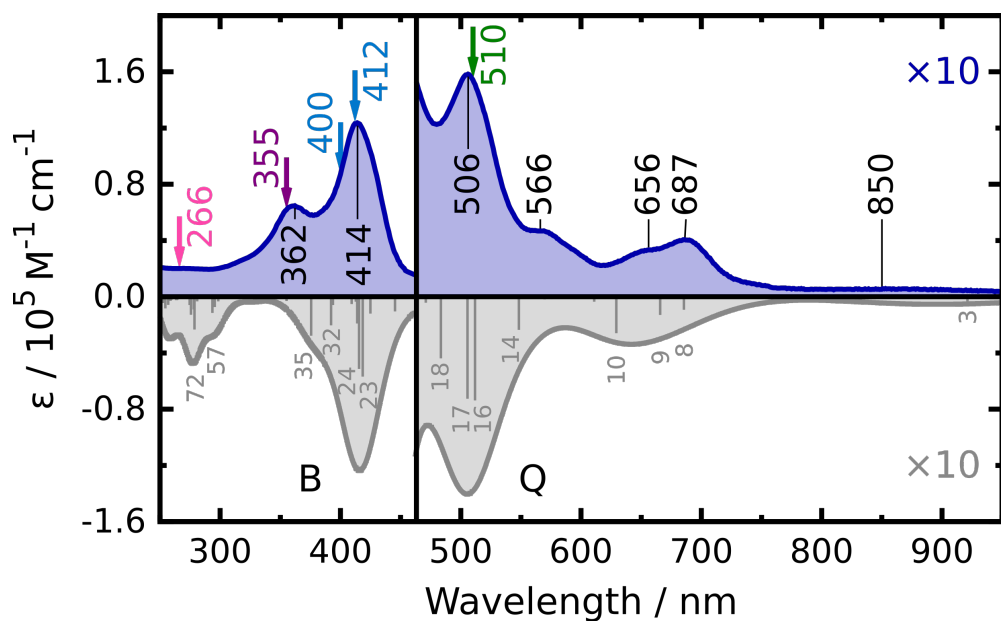
This spectral region is, besides the one around the $\nu_{\text{as}}(\text{N}_3)$ signal, a promising target for time-resolved experiments. First, the presence of the $\nu_5(\text{N}_3)$ resonance band allows in principle monitoring the photoreactivity of **[1]**, too, although it is less suited than the $\nu_{\text{as}}(\text{N}_3)$ resonance band due to its lower extinction coefficient. Second, the $\nu_{41}(\text{por})$ band is known to be a structure-sensitive marker band in general^[196] and especially diagnostic of the formation of a_{2u} -type π -radical configurations, as discussed in section 2.2.4. However, it has to be kept in mind that this electronic structure causes the $\nu_{41}(\text{por})$ band to shift to a frequency of about 1280 cm^{-1} . In brief, probing this spectral region might allow gathering information regarding the electronic structure of transient species and products.

Below this region, three additional bands are found at 1202 cm^{-1} , 1179 cm^{-1} , and 1074 cm^{-1} , having extinction coefficients between $100\text{ M}^{-1}\text{ cm}^{-1}$ and $350\text{ M}^{-1}\text{ cm}^{-1}$. An enlarged representation is given in Figure A1(a) in the appendix. These bands correspond to C–H rocking and scissoring modes involving both the phenyl groups and the porphyrin macrocycle ($\mathcal{M}_6(a_1)$, $\nu_{51}(\text{por})$, and $\nu_{52}(\text{por})$, Figure A1(c) - (e)).^[322,396] Similar to the signals in the range from 1400 cm^{-1} to 1620 cm^{-1} , these three signals are neither strong nor structure-sensitive,^[397,398] therefore unlikely to yield valuable information regarding the aims of this work, and will not be considered any further.

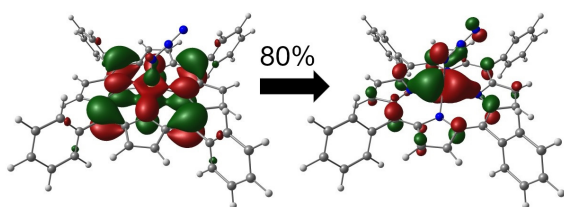
4.2 UV-Vis Spectroscopy

The stationary UV-Vis absorption spectrum of **[1]** is reproduced in Figure 12(a). As in the previous section, the experimentally observed absorption bands will be explained with regard to their underlying transitions, here between electronic states of complex **[1]**, based on information from the literature and quantum chemical calculations.

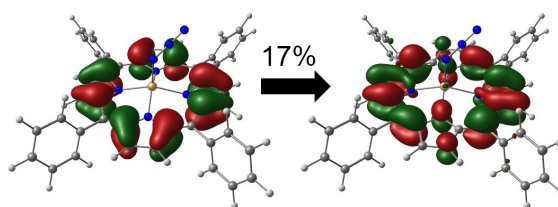
At first glance, the visible absorption spectrum of **[1]** seems to reflect all spectral features of a typical metalloporphyrin (cf. section 2.2.3): a pronounced B-band peaking at 414 nm ($\epsilon = 1.24 \cdot 10^5\text{ M}^{-1}\text{ cm}^{-1}$) and four weaker Q-bands at 506 nm ($\epsilon = 1.58 \cdot 10^4\text{ M}^{-1}\text{ cm}^{-1}$), 566 nm ($\epsilon = 4.7 \cdot 10^3\text{ M}^{-1}\text{ cm}^{-1}$), 656 nm ($\epsilon = 3.3 \cdot 10^3\text{ M}^{-1}\text{ cm}^{-1}$), and 687 nm ($\epsilon = 4.0 \cdot 10^3\text{ M}^{-1}\text{ cm}^{-1}$). Still, a closer inspection reveals these signals to deviate in both their spectral positions and relative amplitudes from the spectra of 'normal' metalloporphyrins described by the Gouterman model.^[222–224,279] This is because the Gouterman model takes into account only the four frontier orbitals of the porphyrindiido ligand under the assumption that orbitals of the metal center do not contribute to the low-energy excitations.^[221,232,233,255] While this prerequisite is reasonable for metal centers having an entirely full d-shell or no d-electrons at all,



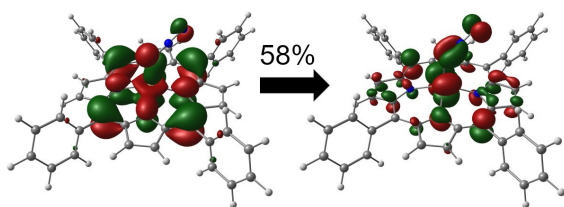
(a) Experimental and calculated UV-Vis absorption spectrum.



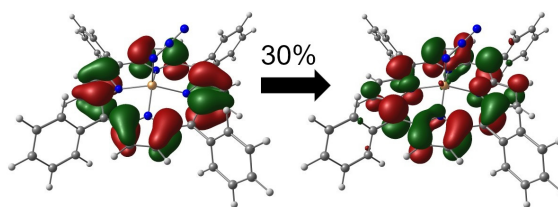
(b) Root 3, β -NTO pair 1.



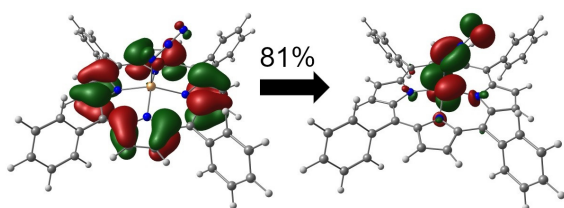
(c) Root 3, α -NTO pair 1.



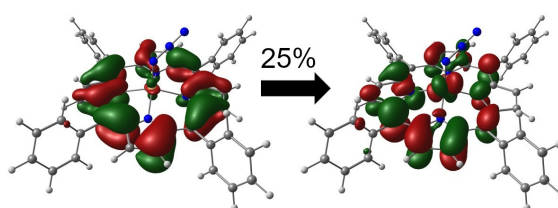
(d) Root 8, β -NTO pair 1.



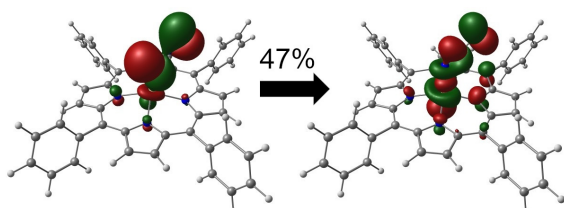
(e) Root 8, α -NTO pair 1.



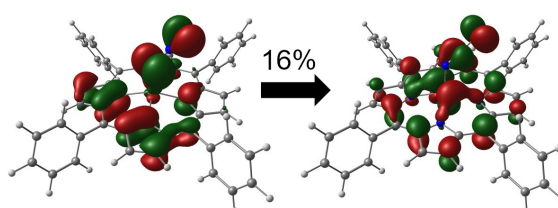
(f) Root 16, β -NTO pair 1.



(g) Root 24, β -NTO pair 1.



(h) Root 35, β -NTO pair 1.



(i) Root 35, β -NTO pair 2.

Figure 12: Stationary UV-Vis absorption spectrum of [1] in room-temperature DCM solution. (a) Upper panel: experimental spectrum (blue); the black numbers indicate peak positions in nm; labeled, colored arrows indicate the center wavelengths of the

pump pulses used in time-resolved experiments. Lower panel: inverted, TD-DFT-predicted spectrum (gray) obtained by frequency down-shift of the stick spectrum by 4000 cm^{-1} and convolution with a Gaussian function having a FWHM of 2000 cm^{-1} ; selected roots are labeled by the gray numbers. Black letters assign the spectral regions to the B- and Q-bands. Note that the spectra are scaled up by a factor of 10 above a wavelength of 460 nm. (b) - (e) Ball-and-stick models of [1] and isosurface plots of the natural transition orbital pairs of highest eigenvalues of selected roots from the TD-DFT calculation. The subtitles indicate the corresponding root and the spin function of a NTO pair, while the numbers above the arrows specify their contributions to the total excitations. Isovalues: ± 0.03 . Atomic color coding: H - white, C - gray, N - blue, Fe - brown.

e.g. Zn^{+II} (d^{10}) and Mg^{+II} , respectively, metal atoms having a partially occupied d-shell and especially those having unpaired electrons show spectra strongly differing from the predictions of this simple model.^[222-224] The differences originate from admixtures of the purely porphyrin-centered $\pi \rightarrow \pi^*$ transitions and metal-centered $d \rightarrow d$, metal-to-ligand charge transfer (MLCT), and ligand-to-metal charge transfer (LCMT) transitions, including those involving orbitals centered at axial ligands if those are present.^[222,255,278,399,400] For instance, Kobayashi et al. reported UV-Vis spectra of various $[\text{Fe}^{+III}(\text{tpp})(\text{L})]$ complexes, carrying different, monoanionic, axial ligands L, and pointed out that the lowest excited states need to be described by superpositions of the $\pi(\text{por}) \rightarrow \pi(\text{por})^*$ and $\pi(\text{por}) \rightarrow d(\text{Fe})$ CT transitions.^[255] Not surprisingly, those spectra are nearly equivalent to the spectrum of [1] measured in this work. In the more recent study,^[239] Lehnert and coworkers reproduced the absorption spectrum of the chlorido complex [6] well by means of TD-DFT calculations and supported this proposal.

Similarly, the TD-DFT calculation of [1] conducted in this work yield a spectrum as shown in gray in Figure 12(a), which is essentially in line with the experimental spectrum. At the same time, an evaluation of the theoretical results by means of a natural transition orbital (NTO) analysis corroborates the findings of Kobayashi et al. and Lehnert et al., and, in doing so, underpins the assumption that the electronic structures of [1] and [6] are indeed highly comparable. NTOs and detailed assignments of the all roots up to the ones corresponding to the B-band (root 23 and 24) and selected roots in the ultraviolet region are presented in section 8.2. For the sake of clarity, only NTOs of root 3, 8, and 16, contributing to the signal observed at 850 nm, 687 nm, and 506 nm, respectively, are exemplarily included in Figures 12(b) - (f). Indeed, root 3, 8, 16, and most other computed excitations of significant oscillator strength in the Q-band region ($> 450\text{ nm}$) exhibit predominantly $\pi(\text{por}) \rightarrow d(\text{Fe})$ CT character, and, in some instances, a smaller contribution of the $a_{1u} \rightarrow e_g$ transition. These excitations give rise to the absorption bands centered at 506 nm, 656 nm, and 687 nm, as well as the weak tail maximal at ca. 850 nm and reaching up to the nIR region. In contrast, the 'true' Q-bands of [1], i.e. the mixed $a_{1u}/a_{2u} \rightarrow e_g$ transitions according to the Gouterman model (although even those show a small degree of CT character), exhibit negligible oscillator strengths. Interestingly, they are predicted to be split into two distinct subsets, root 6 and 7, located around 800 nm, and root 1 and 2, located above a wavelength of 1000 nm. Note also that there is

no participation of purely iron-centered excitations, as the high-spin d^5 -configuration does not offer spin-allowed $d \rightarrow d$ transitions.

As opposed to the Q-band region, the pronounced B-band of [1] at 414 nm is in fact well described by the classic superposition of $a_{1u}/a_{2u} \rightarrow e_g$ transitions, with only minor contributions of orbitals centered at the iron atom or azido group. An exemplary NTO pair is depicted in Figure 12(g).

Azide-to-iron CT transition are predicted to absorb, on the one hand, in the Q-band region, yet having small oscillator strengths. The only exception is root 14, the $\pi_x^{nb}(N_3) \rightarrow d_{yz}(Fe)$ transition, which can be hold responsible for the absorption band at 566 nm. On the other hand, $N_3 \rightarrow Fe$ transitions are the predominant contributions to the strong absorption band peaking at 362 nm ($\epsilon = 6.48 \cdot 10^4 M^{-1} cm^{-1}$, cf. Figure 12(h) & (i)). This result is in agreement with a previous study, which assigned the intensive bands of (porphyrindiido)iron complexes in this region to LMCT transitions from the axial ligand.^[304] This proposal was based on the observation that photolysis experiments under selective excitation at this wavelength induced a heterolytic Fe-L bond cleavage.

Even deeper in the ultraviolet, a region of nearly uniform absorbance around an extinction coefficient of $2.0 \cdot 10^4 M^{-1} cm^{-1}$ is observed. The TD-DFT calculation predicts a multitude of electronic transitions contributing to this band, whose descriptions require each numerous NTO pairs. Furthermore, many of those NTOs cannot be assigned unequivocally to a specific functional group of the complex. Experimentally, it is known that both phenyl-centered $\pi \rightarrow \pi^*$ transitions^[138,401] and porphyrin-centered $\pi \rightarrow \pi^*$ transitions (N and L band),^[224,240,248,303] involving orbitals beyond the four-orbital model, absorb in this region. Furthermore, the assumption of additional por \leftrightarrow Fe CT^[222] and $N_3 \rightarrow Fe$ CT transitions occurring there is justified.^[120,125] As before, coupling of these different types of transitions is presumably possible. Hence, due to its high complexity, an assignment of this absorption band is not feasible here.

The fact that the absorption bands of [1] cover a very broad spectral range raises the question, which excitation wavelength is most suited to induce the desired photooxidation to [2]. The currently available information leave this question unanswered. On the one hand, the previous studies on [2] utilized light of wavelengths between 406.7 nm and 514.5 nm for this purpose.^[104,105,108] On the other hand, $N_3 \rightarrow Fe$ CT transitions, presumably activating the azido ligand, are achieved most easily by pumping around 362 nm.^[304,369] And lastly, photooxidation of azidoiron(+III) complexes with redox-innocent auxiliary ligands was revealed to become efficient only for excitation around 266 nm, but not for longer wavelengths.^[115,116] Considering this, it is not possible to predict the outcome of a photolysis of [1] at a given wavelength a priori. For this reason, the first aim of this work, which will be the topic of the following section, is to identify the excitation wavelength most appropriate to produce the high-valent nitrido complex [2].

5 Time-Resolved Spectroscopy

5.1 Quantum Yield of Photoconversion and Distribution of the Products

In the beginning of the investigations on the photolysis of [1], the primary quantum yield (Φ) of photoconversion and the nature and fractional yields of the generated products were determined. The results on this topic are published in the following research article:

S. Flesch, P. Vöhringer, *Chem. Eur. J.* **2023**, *29*, e202301207.

DOI: <https://doi.org/10.1002/chem.202301207>

The full article and supporting information (SI) are attached in the appendix, section 8.10. Their contents and essential results are summarized in the following, whereat the individual contributions of the first author (and author of this doctoral thesis), Stefan Flesch, and the second author of the article, Prof. Dr. Peter Vöhringer, are specified.

As discussed in section 2.2.1, three distinct reaction pathways can be distinguished in the photolysis of transition metal azido complexes:^[115,116,121]

- ◆ The release of N₂ under formation of a nitrido complex, referred to as *photooxidation*, cf. Equation <12>.
- ◆ The *redox-neutral* cleavage of azido anions, creating a vacancy in the ligand sphere of the metal center, cf. Equation <10>.
- ◆ The generation of an azidyl radical and a reduced metal complex, likewise bearing a vacancy (*photoreduction*), cf. Equation <6>.

The individual quantum yields of all three processes depend on the complex, the excitation wavelength and the environment.^[115,116,121] In the case of [1], the occurrence of both the photoreductive and photooxidative pathway were reported.^[109,110,179,304] However, quantitatively accurate quantum yields and their dependence on the excitation wavelength have not been determined so far. Knowledge of the distribution of the products is nevertheless highly valuable in order to interpret data produced by ultrafast time-resolved measurements. Therefore, the quantum yields of the three aforementioned reactions were experimentally determined in liquid DCM solution by UV/Vis-pump/mIR-probe and rapid-scan spectroscopy at four different excitation wavelengths: 510 nm, 400/412 nm, 355 nm and 266 nm.

All experimental contributions to this work, i.e. synthesis of [1], stationary FTIR and UV-Vis, rapid-scan FTIR and UV/Vis-pump/mIR-probe measurements, as well as all DFT calculations were performed by Stefan Flesch, who evaluated their results and wrote the original manuscript. Peter Vöhringer revised and validated the analysis, improved the writing and the

evaluation of the kinetic traces by means of linear regressions.

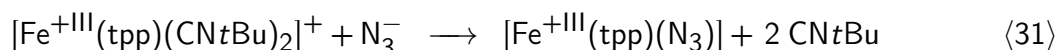
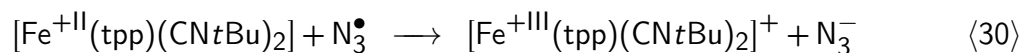
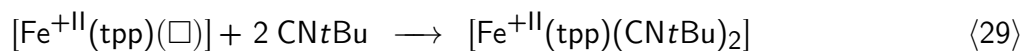
In the first section of the article, the stationary UV-Vis absorption spectrum of [1] and the stationary FTIR spectrum of [1], N_3^- (already discussed in section 4), and *t*BuNC in the range from 1900 cm^{-1} to 2200 cm^{-1} are presented. Here, it is emphasized that the frequency-integrated extinction coefficients (the absorption strength), α_a , of the $\nu_{\text{as}}(\text{N}_3)$ resonance bands of the free and coordinated N_3^- anion are approximately the same. Consequently, the formation of azide anions via the redox-neutral pathway can easily be verified and quantified by detection of its resonance band at 2006 cm^{-1} . Because this band is observed neither in the fs-pump-probe nor in the rapid-scan spectra regardless of the excitation wavelength, the occurrence of the redox-neutral decomposition of [1] can be excluded.

Obtaining spectroscopic evidence of the photooxidation and -reduction is more challenging as none of their products exhibits strong and characteristic absorptions in the accessible spectral range. Thus, these reaction pathways are verified in an indirect fashion by chemical conversion of the primary photoproducts (quenching, cf. section 2.2.2). In the second part of the article, the quenching of azidyl radicals, originating from photoreduction and tracked by stationary difference spectroscopy, is discussed. Following Equation (17), N_3^\bullet molecules can be converted to N_3^- anions via a one-electron transfer reaction with iodide anions, I^- .^[120,178,180,198] Still, this reaction has to compete with the self-quenching of N_3^\bullet to N_2 .^[119,177,178] For this reason, the former reaction requires a large excess of I^- up to a hundredfold w.r.t. [1] in order to proceed quantitatively. In this asymptotic limit, the fractional yield of the photoreduction, f_{red} , i.e. the ratio of N_3^\bullet molecules (or [3_{red}] complexes) generated per decomposed complex of [1], is calculated from the ratio of the integrals of the N_3^- resonance band and the parent's bleaching signal and the known ratio of these signals from the stationary spectra. f_{red} amounts to 0.6, 0.4, and 0.5 for 510 nm, 412 nm, and 355 nm excitation, respectively. For 266 nm excitation, this quenching reaction is not feasible as I^- absorbs at this wavelength as well (see SI).

By process of elimination, it has to be concluded that the remaining fraction of decomposition, f_{ox} , proceeds via photooxidation. Yet, in order to provide an experimental proof of the formation of [2], another quenching reaction is performed by addition of *tert*-butyl isonitrile (*t*BuNC, cf. Equation (20)). Various previous studies on the reactivity of nitrido complexes have demonstrated them to react with isonitriles to carbodiimido complexes, whose NCN-antisymmetric stretching vibration gives rise to a strong signal between 2100 cm^{-1} and 2200 cm^{-1} .^[7,92,94,207,209] And indeed, a strong band at 2121 cm^{-1} , attributed to the complex *tert*-butylcarbodiimido(5,10,15,20-tetraphenylporphyrin-21,23-diido)iron(+III), $[\text{Fe}^{\text{+III}}(\text{tpp})(\text{NCN}t\text{Bu})]$ ([4]), is found in the rapid-scan spectra after photolysis of a solution of [1] and one equivalent of *t*BuNC, unequivocally proving the formation of [2].

Interestingly, besides this band, two additional transient absorptions at 2006 cm^{-1} and 2200 cm^{-1} are observed, both of which decay entirely within ca. 10 s. At the same time, the bleaching signals of [1] and *t*BuNC decline partially. An analysis of the peak positions and integral ratios leads to the conclusion that the signal at 2200 cm^{-1} originates from

the complex bis(*tert*-butylisonitrilo)(5,10,15,20-tetraphenylporphyrin-21,23-diido)iron(+III), $[\text{Fe}^{\text{+III}}(\text{tpp})(\text{CN}t\text{Bu})_2]^+$ (**[5]**), which recombines with an N_3^- anion (absorbing at 2006 cm^{-1}) to **[1]** and under release of two *t*BuNC molecules, according to Equation (31). This bimolecular reaction follows second order kinetics and has a rate constant of $k_v = (2.03 \pm 0.35) \cdot 10^4\text{ M}^{-1}\text{s}^{-1}$ at room-temperature.



The existence of **[5]** is explained by a fast complexation of the photoreduction product **[3_{red}]** by two *t*BuNC molecules, forming the complex bis(*tert*-butylisonitrilo)(5,10,15,20-tetraphenylporphyrin-21,23-diido)iron(+II), $[\text{Fe}^{\text{+II}}(\text{tpp})(\text{CN}t\text{Bu})_2]$ (**[5_{red}]**), as described in Equation (29). This species is assumed to undergo a subsequent one-electron transfer with an N_3^\bullet radical to **[5]** and N_3^- , according to Equation (30).

Finally, the primary quantum yields of photooxidation and -reduction are determined by evaluation of ($12\ \mu\text{J}$) fs-UV/Vis-pump/mlR-probe kinetic traces of the bleaching signal of **[1]**. To this end, the kinetic traces for all four excitation wavelengths are fitted as monoexponential functions, giving time constants of around 20 ps. While, the photoconversion turns out to be very inefficient at 510 nm excitation ($\Phi = 0.8\%$), pump pulses centered at the lower wavelengths give rise to considerable quantum yields: 7.4% for 400 nm, 5.7% for 355 nm, and 7.1% for 266 nm. Multiplying these values with the fractional yields of photooxidation and -reduction gives the primary quantum yields of both processes.

In summary, the work presented in this article delivers the following information regarding the photolysis of **[1]** in liquid, room-temperature DCM solution:

- ◆ The primary yield of photoconversion is $< 1\%$ for 510 nm excitation and 5.5–7.5% for excitation wavelengths $\leq 400\text{ nm}$.
- ◆ Photolysis of **[1]** proceeds via photooxidation to **[2]** and -reduction to **[3_{red}]** in roughly equal amounts, which are only slightly dependent on the excitation wavelength.
- ◆ The former process can be verified by a reaction of the high-valent nitrido product **[2]** with an isonitrile to a carboddimido complex (**[4]**), whereas the latter can be evidenced by conversion of N_3^\bullet radicals to N_3^- anions by addition of I^- .

Judging by the results obtained here, pump pulses with center wavelengths around 400 nm are best suited to generate the nitrido complex **[2]**. Hence, subsequent experiments, discussed in the rest of this work, focus on excitation with light of exactly this wavelength.

5.2 Primary Processes after Photoexcitation – Low-Energy Excitation

5.2.1 Dependence on the Pump Pulse Energy

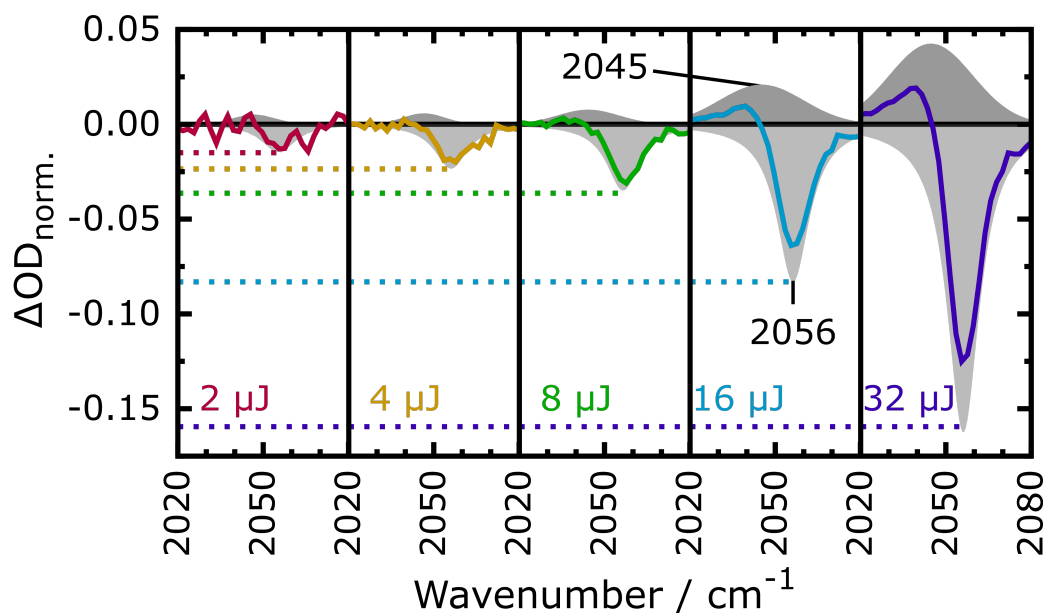
It is crucial to mention that the primary quantum yields specified in the previous section are comparable with each other only because the applied pump pulses of varying center wavelengths have the same energy density, i.e. the energy of a pulse, E_{pump} , divided by its area. In fact, repetitions of the 400 nm-pump/mIR-probe experiments in the spectral region around the $\nu_{\text{as}}(\text{N}_3)$ resonance band using pump pulses of different pulse energies (at constant beam diameter) revealed Φ to be highly dependent on this parameter. This effect is pictured in Figure 13(a), which shows transient spectra recorded in these experiments at a pump-probe delay of 200 ps, i.e. after completion of the primary photoinduced processes, as it will be demonstrated later. To enhance comparability, each spectrum is normalized to the amplitude of the initial bleaching contribution $\Delta\text{OD}_{\text{bleach}}(2056 \text{ cm}^{-1}, 0 \text{ ps}, E_{\text{pump}})$, recorded with the same E_{pump} , as stated in Equation (38). This approach appears justified because the early transient spectra of different E_{pump} do not differ in shape, but merely in magnitude. As Figure 13(a) reveals, the normalized residual signals and, consequently, the primary quantum yield increase significantly with the energy of the pump pulse.

$$\Delta\text{OD}_{\text{norm.}}(\tilde{\nu}, \tau, E_{\text{pump}}) = \frac{\Delta\text{OD}(\tilde{\nu}, \tau, E_{\text{pump}})}{\Delta\text{OD}_{\text{bleach}}(2056 \text{ cm}^{-1}, 0 \text{ ps}, E_{\text{pump}})}, \quad (\tau = 200 \text{ ps}) \quad (38)$$

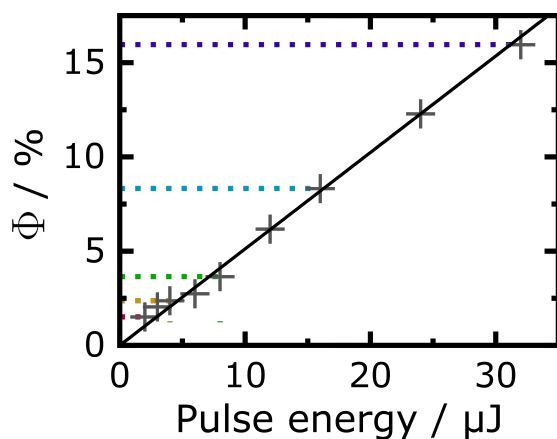
In order to provide a more accurate determination of the primary quantum yield, the transient spectra were fitted as superpositions of two functions: a Lorentzian profile, describing the transient bleaching, and a log-normal distribution or Gaussian function, describing the transient absorption at early and late delays, respectively (see also section 5.2.2). As demonstrated in Figure 13(b), the correlation of the primary quantum yield on the energy of the pump pulse reflects a proportional function. This finding is in agreement with the publication of Rury and Sension,^[369] who reported the observation of a long-lived excited species after 400 nm excitation of [6] by fs-Vis-probe spectroscopy and attributed its formation to processes following TPA.

In fact, if the reactive channel was accessible from absorption of a single photon (SPA) instead, the quantum yield would be expected to be independent of the pulse energy. This is because, in this scenario, an enhanced pulse energy, i.e. a larger number of photons, raises the number of excited complexes in a proportional fashion,^[402] but does not change the subsequent processes each individual excited complex is subjected to. Hence, a higher pulse energy scales up the amplitudes of all transient signals at any pump-probe delay by a constant factor, which cancels out in the calculation of Φ .

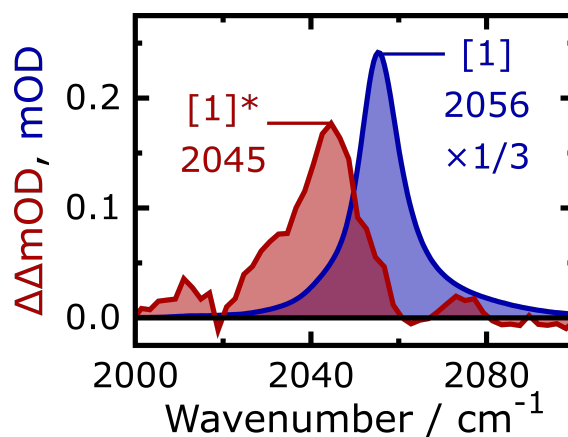
In contrast, the probability of a molecule absorbing two photons successively increases with the square of the pulse energy.^[371,402] Consequently, if the generation of photoproducts is triggered by such a TPA, the amplitude of a residual bleaching signal will show a quadratic



(a) Transient spectra at $\tau = 200$ ps, normalized to the initial bleaching signal.



(b) Primary quantum yield in dependence on the pump pulse energy.



(c) Product spectrum after $12 \mu\text{J}$, 400 nm -excitation and scaled, stationary FTIR spectrum of **[1]**.

Figure 13: Dependence of the late 400 nm -pump/ $1900\text{--}2100 \text{ cm}^{-1}$ -probe spectra of **[1]** in room-temperature DCM solution on the energy of the pump pulse. (a) Transient spectra recorded 200 ps after photoexcitation, normalized to the initial bleaching signal, for several pump pulse energies, as specified by the colored numbers. The light gray areas represent Lorentzian functions describing the bleaching contributions, the dark gray areas Gaussian functions describing the transient absorptions. The black numbers indicate peak positions in cm^{-1} . The dotted, colored lines emphasize the amplitude of the bleaching contribution, which is, due to the normalization of the spectra, equal to the negative primary quantum yield. (b) Primary quantum yields determined for various pump pulse energies (gray crosses) and proportional regression function (black line). (c) Product spectrum after $12 \mu\text{J}$, 400 nm -excitation of **[1]** in the spectral region around the $\nu_{\text{as}}(\text{N}_3)$ resonance band, averaged over delays from 150 ps to 3.5 ns (red), and stationary FTIR spectrum of **[1]** (blue), scaled to the magnitude applied to calculate the product spectrum. The numbers indicate peak positions in cm^{-1} .

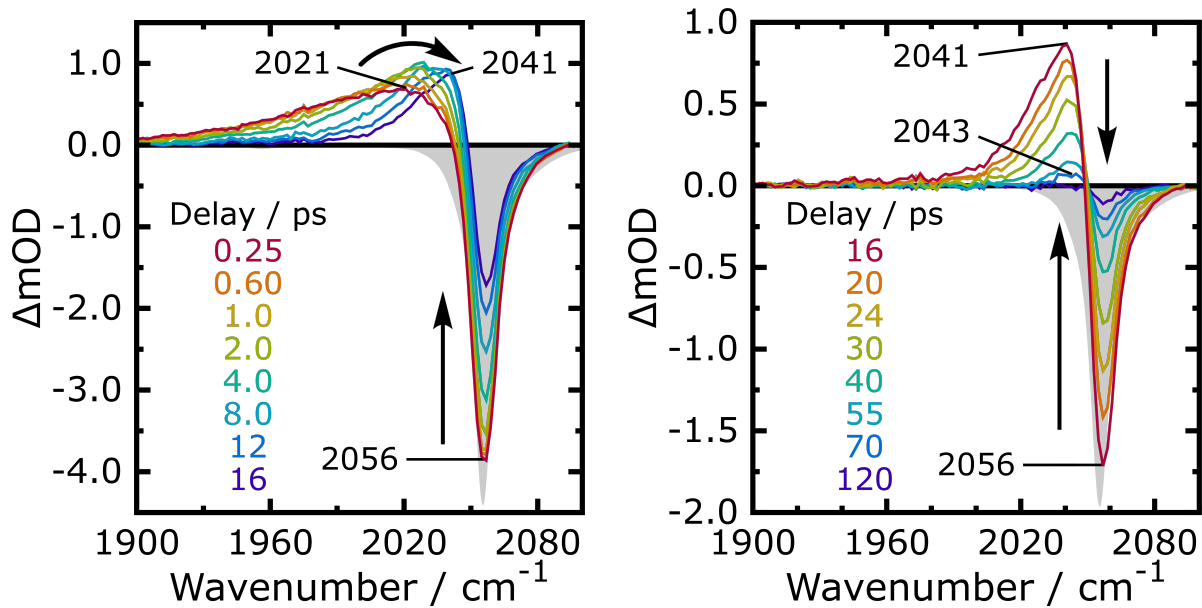
growth as well. However, the strength of the initial bleaching signal might still scale proportionally with the pulse energy even if significant TPA occurs, given that the two photons are absorbed subsequently ('resonant TPA') rather than simultaneously. This is because the transient bleaching is indicative of the depopulation of the ground state, which is not affected by the absorption of a second photon by the already excited molecules. Based on these scaling behaviors and Equation (19), Φ will depend proportionally on the pulse energy, exactly as experimentally observed here. Moreover, this result provides an explanation of the extremely low efficiency of the photoconversion of [1] to [2] reported in earlier studies, which relied on low-power light sources.^[105,108,110]

Interestingly, the late pump-probe spectra in Figure 13(a) exhibit, besides the residual bleaching signal, a transient absorption centered around 2040 cm^{-1} . Due to the significant overlap of both signals, the absorption band is better viewed in terms of a purely absorptive product spectrum, i.e. after removal of the bleaching contribution by subtracting the inverted, properly scaled FTIR spectrum of the parent complex from the transient spectra. The product spectrum, shown in red in Figure 13(c), demonstrates the signal's peak frequency to be actually located at 2045 cm^{-1} . Considering the spectral position, the absorption cannot be associated with either of the two known photoproducts, [3_{red}] and [2], but rather indicates the formation of another azide species. In addition, an assignment to the free azide anion can be excluded as well, since its resonance band is located at a distinctly smaller frequency (2006 cm^{-1}). It has to be mentioned that this signal remains unchanged over the entire available time range of the pump-probe experiment up to 3.5 ns, but is absent in the earliest rapid-scan spectrum recorded 72.5 ms after photoexcitation. This implies a limited, but here not exactly determined lifetime of the underlying species. Considering all this, the underlying species is presumably a long-lived excited state of the parent complexes itself, [1]*. Judging by the integral ratio of absorption and bleaching signal, and under the assumption that the $\nu_{\text{as}}(\text{N}_3)$ band has a similar absorption strength in this excited state and in the ground state, it can be estimated that about a third of the converted complexes are channeled into this state. This means, combined with the results of the quenching experiments, that the photoconversion of [1] yields the three species, [1]*, [2], and [3_{red}] in roughly even amounts (1:1:1), all of which originate from TPA.

The nature of the excited state [1]* will be the topic of further discussion in section 5.3. The next section, however, will be devoted to the elucidation of the primary events following the photoexcitation of [1].

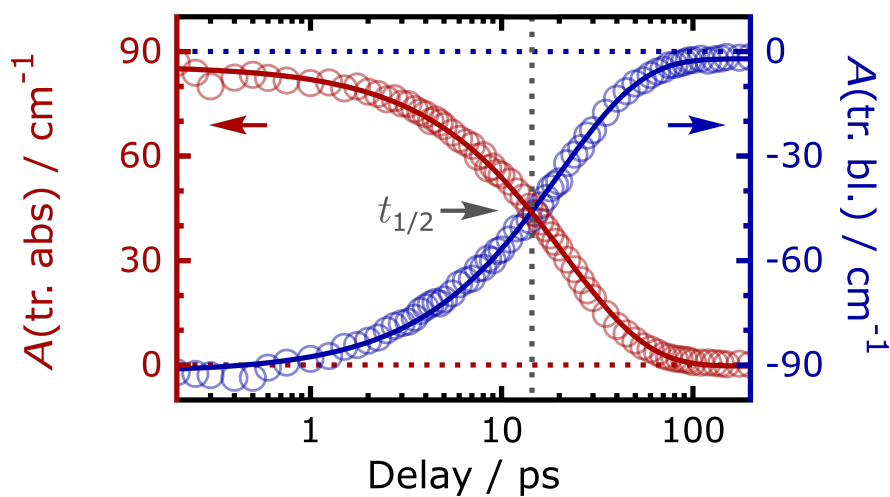
5.2.2 400 nm-Pump/1900-2100 cm^{-1} -Probe Experiment

In detail, this section focuses on the consideration of a $3\text{ }\mu\text{J}$, 400 nm-pump/1900-2100 cm^{-1} -probe experiment of [1], which allows an evaluation of the processes following SPA, since the contributions of TPA are negligibly small at this low pump pulse energy. Transient spectra at selected pump-probe delays are displayed in Figure 14 (corresponding spectra recorded after $12\text{ }\mu\text{J}$ (high-energy), 400 nm excitation are given in Figure A5 in the appendix).

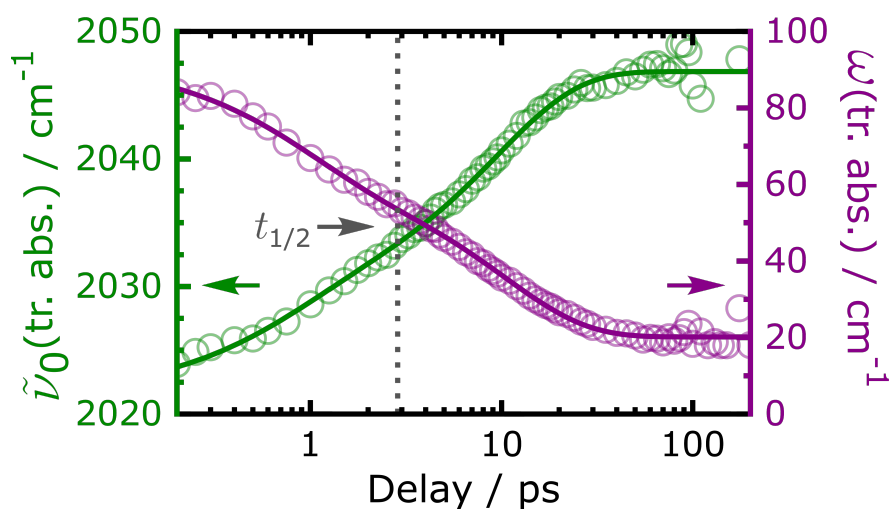


(a) Transient spectra, $0.25 \text{ ps} \leq \tau \leq 16 \text{ ps}$.

(b) Transient spectra, $16 \text{ ps} \leq \tau \leq 120 \text{ ps}$.



(c) Time dependence of the band integrals.



(d) Time dependence of the peak frequency and bandwidth of the transient absorption.

Figure 14: (a) & (b) Transient $3 \mu\text{J}$, 400 nm -pump/ $1900\text{-}2100 \text{ cm}^{-1}$ -probe spectra of [1] in room-temperature DCM solution at various pump-probe delays, as specified in the

legends. The gray areas represent the inverted, properly scaled, stationary FTIR spectrum of [1]. Black numbers indicate peak positions in cm^{-1} and black arrows emphasize the spectro-temporal evolution. (c) Band integrals of the transient bleaching (blue circles) and the transient absorption (red circles) obtained by fitting of the individual transient spectra at each pump-probe delay as superposition of a Lorentzian function and a log-normal distribution. Note that the right ordinate applies to the former, the left ordinate to the latter data. The blue and red line represent monoexponential fit functions. Colored, dotted lines emphasize the respective zero line. The labeled, gray, dotted line highlights the half-life period of the decay. (d) Bandwidth (purple circles) and peak frequency (green circles) of the transient absorption obtained by the fits mentioned in (c). Note that the right ordinate applies to the former, the left ordinate to the latter data. The colored lines represent biexponential fit functions. The labeled, gray, dotted line highlights the half-life period of the VER (mean value of the two fits).

Immediately after photoexcitation ($\tau = 0.25$ ps), a pronounced transient bleaching signal is observed at a frequency of 2056 cm^{-1} , coinciding with the absorption of the $\nu_{\text{as}}(\text{N}_3)$ vibration of [1]. This signal is the spectral manifestation of the depopulation of the ground state of [1] due to promotion to an excited state under the absorption of a photon. These excited complexes, for their part, give rise to a broad transient absorption band red-shifted compared to the bleaching signal, having a maximum at 2021 cm^{-1} . Again, the spectral position of this band evidences it to originate from a $\nu_{\text{as}}(\text{N}_3)$ vibration mode. Moreover, its asymmetric, broad band shape is characteristic of a manifold of vibrationally excited states, indicating that parts of the pump energy are dispensed over the vibrational modes of the complex within the time-resolution of the experiment.

In the following ca. 100 ps, both transient absorption and bleaching decline almost completely, demonstrating [1] to be highly photostable and returning fully to its equilibrium state after single-photon excitation. The small permanent bleaching signal observed after this time window, equivalent to a primary quantum yield of $\Phi = 2.0\%$, is attributed to the processes triggered by TPA, not fully suppressed at this pump energy (cf. section 5.2.1). The spectro-temporal evolution within the first 100 ps can be subdivided into two stages. In the first stage (Figure 14(a)) from 0.25 ps to roughly 16 ps, the transient absorption is subjected to a pronounced spectral shift from 2021 cm^{-1} to 2041 cm^{-1} and strong decrease of its bandwidth, both of which are typical signatures of a VER process. At the same time, both transient absorption and bleaching decay to about half of their initial strength, indicating a recovery of the ground state of [1]. The remaining half of the excited complexes undergoes GSR within the second stage, starting at ca. 16 ps (Figure 14(b)), during which the band shapes of both signals are nearly unaltered.

In order to quantify the underlying kinetics accurately, the individual transient spectra are first fitted as superpositions of a Lorentzian function and a log-normal distribution, describing the transient bleaching and transient absorption, respectively. Figure 14(c) depicts the temporal evolution of the band integrals, $A(\text{tr. bl.})$ and $A(\text{tr. abs.})$, obtained from these fits. While the former integral is indicative of the degree of ground state depopulation at a given pump-probe delay, the latter integral allows insight into the situation of the azido ligand in the

excited state. This is because both bands originate from $\nu_{\text{as}}(\text{N}_3)$ vibrations and the absorption strength of this normal mode is largely preserved independently of the environment, but given that the anionic character of the azide moiety is retained. In contrast, a neutral azidyl ligand, possibly generated by a $\text{N}_3 \rightarrow \text{Fe}$ CT excitation, would not exhibit any absorptions in this spectral region^[118,120,403] and, thus, would decrease the value of $A(\text{tr. abs.})$. Yet, as it becomes apparent from Figure 14(c), $A(\text{tr. abs.})$ is roughly as large as $A(\text{tr. bl.})$ at any pump-probe delay. Hence, it needs to be concluded that the anionic azido ligand remains essentially intact over the entire considered time frame.

Regarding the kinetics, the decays of $A(\text{tr. abs.})$ and $A(\text{tr. bl.})$, i.e. the GSR, are found both to proceed strictly monoexponentially with time constants of 21.5 ± 0.3 ps and 20.0 ± 0.3 ps, respectively. The good agreement of both time constants and the shape stability of the transient spectra during the second phase of their decay highly indicates the GSR to proceed via a direct state-to-state conversion starting from a single excited state. As a consequence, the final spectral position of the transient absorption at ca. 2046 cm^{-1} can be viewed as the resonance frequency of this excited state of [1]. Note that this band must not be confused with the signature of the long-lived excited state observed after high pulse energy excitation, discussed in the previous section. Although both states have nearly the same $\nu_{\text{as}}(\text{N}_3)$ resonance frequency, their very distinct lifetimes identify them as different species.

The interpretation is (at the current state) in line with the work on complex [6] by Rury and Sension, who attributed a process occurring with $\mathcal{T} = 18.5$ ps to a conversion from a quartet $d(\text{Fe}) \rightarrow d(\text{Fe})$ state to the ground state.^[369] In contrast, Vura-Weis et al. assigned the same process to a VER on the ground state surface.^[377] However, this second interpretation cannot be applied to explain the pump-probe spectra of [1] presented here for the following reason: If the transient absorption band originated from the vibrationally, but not electronically excited parent complex, the VER and the GSR would be directly connected. For its part, the VER is characterized by the shift of the peak frequency $\tilde{\nu}_0(\text{tr. abs.})$ and the decrease of the bandwidth $\omega(\text{tr. abs.})$ of the transient absorption. Both parameters can be extracted from the same spectral fits as the band integrals mentioned above. Their evolutions are graphically represented in Figure 14(d) and can be described phenomenologically as biexponential functions. Yet, to provide a straightforward comparison of their kinetics to those of the band integrals, it is expedient to consider the half-life period, $t_{1/2}$, of all processes. While, $t_{1/2} = \ln(2) \mathcal{T} \approx 14.4$ ps for the decay of the band integrals, the half-life period of the shift of $\tilde{\nu}_0(\text{tr. abs.})$ amounts to 3.4 ps and the change of $\omega(\text{tr. abs.})$ proceeds with $t_{1/2} = 2.3$ ps. Thus, the VER is roughly a factor of five faster than the GSR, excluding a direct connection of both processes.

Instead, the spectral shift and narrowing of the transient absorption are assigned to a VER on the energy surface of an excited electronic state, since they take place within a time frame in which the electronic ground state has not been significantly replenished yet. Although another VER on the ground state surface subsequent to the electronic de-excitation cannot be excluded here (and is in fact likely), this process can be expected to occur at a similar

rate as the VER in the upper electronic state. As a consequence, it could not be observed independently by means of the experiment employed here.

Finally, it remains the question regarding the nature of the excited state decaying with a time constant of ca. 20 ps. Answering this question is hardly possible by means of vibrational spectroscopy only, but requires the application of a method more sensitive to the electronic structure. For this reason, complementary Vis-probe spectra will be presented and considered in the following section.

5.2.3 400 nm-Pump/Vis-Probe Experiment

Just like in the mIR-probe experiments, 400 nm-pump/Vis-probe spectra recorded at late delays (> 100 ps) show a pronounced dependence on the energy of the pump pulse. Permanent transient signals persisting for at least 3.5 ns, as displayed in Figure A12(a) in the appendix, are observed only for high pulse energies. Not surprisingly, the spectrum matches the one reported by Sension et al. for photolysis of [6] under comparable conditions.^[369] Again, the signal strengths are found to increase proportionally with the pump pulse energy when referenced against the amplitude of the initial signals (cf. Figure A12(b)), verifying their origin to be TPA.

As before, the evaluation will be focused on excitations with pump pulses of low energy, causing TPA to be negligible. Transient Vis-spectra following 8 μ J, 400 nm excitation are presented in Figure 15. Note that, due to the larger diameter of the pump pulse in the Vis-probe setup compared to this of the mIR-probe setup (ca. 0.9 mm vs. ca. 0.5 mm), the energy densities applied in both experiments are roughly equivalent. The transient spectra at delays immediately after photoexcitation are characterized by an intense negative signal at 415 nm, arising from the bleaching of the parent's B-band, and a strong transient absorption peaking at roughly 450 nm. Moreover, the Q-band region up to the nIR is covered by net-positive differential optical density, featuring indentations corresponding to the bleaching contributions of the ground state of [1]. Remarkably, the early transient spectra are essentially independent of the excitation wavelength, as demonstrated in Figure A11, which shows complementary spectra following 266 nm, 355 nm, and 510 nm excitation. A priori, it is expected that excitations using different photon energies yield initially distinct spectra, as different excited states are populated. Hence, the invariance of the early spectra w.r.t. the photon energy implies that all originally excited states relax within the time resolution of the experiment to the same energetically lower state, responsible for the observed spectra after 0.1 ps.

The subsequent evolution can, as before, be divided into two phases: A first phase ranging from 0.1 ps to ca. 16 ps, in which significant shifts of the band maxima and decay of the signals take place (Figure 15(a)), and a second phase, in which the decline continues, yet, under shape stability of the spectra, as emphasized by the presence of several isosbestic points (Figure 15(b)). However, compared to the 1900-2100 cm^{-1} -probe spectra, a larger fraction of the signal decay occurs already within the first phase. More precisely, both the B-band bleaching and the absorption band in the Q-band region decline to about 3/4 within 16 ps, whereas the

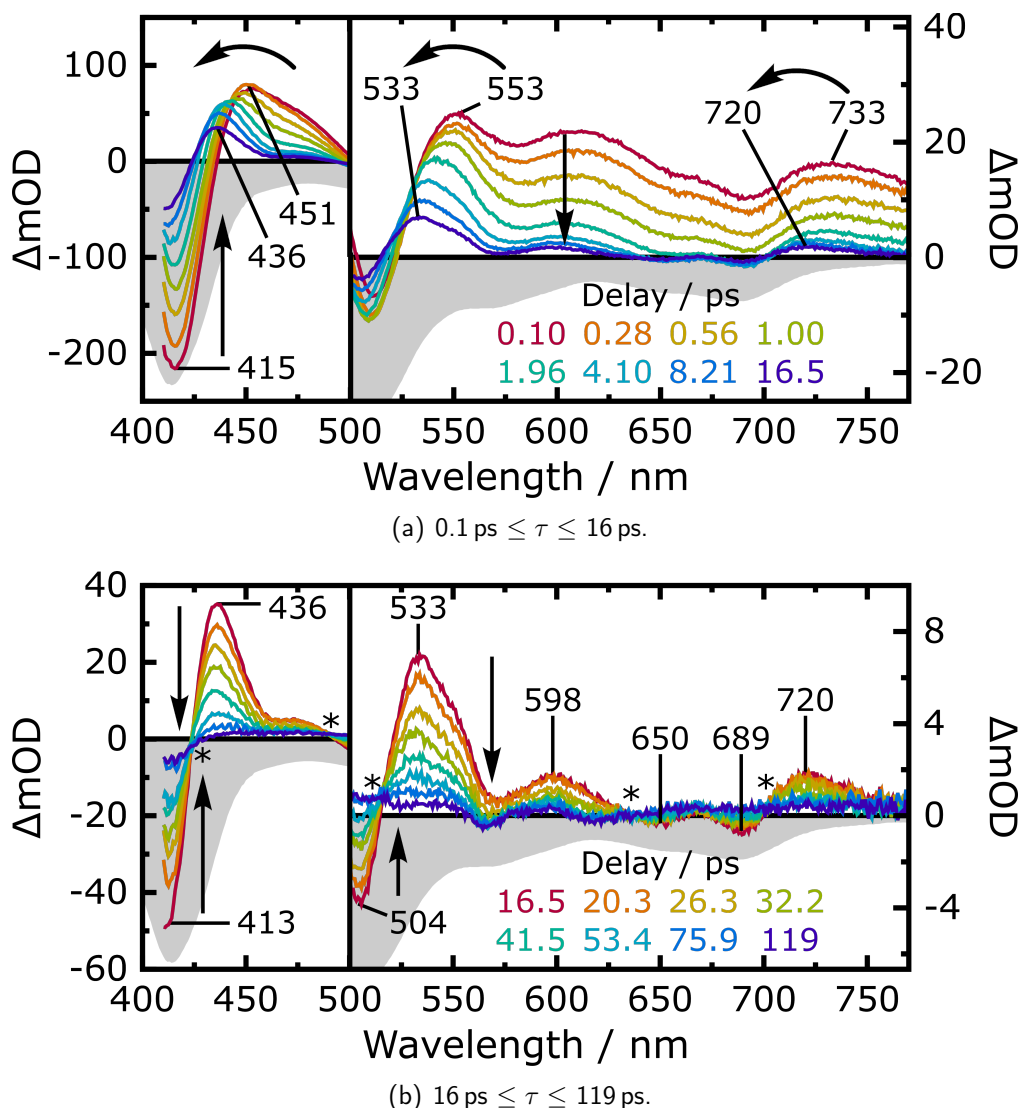


Figure 15: Transient $8 \mu\text{J}$, 400 nm -pump/Vis-probe spectra of [1] in room-temperature DCM solution, at various pump-probe delays as specified in the legends. (a) Early delays ($0.1\text{-}16 \text{ ps}$), (b) late delays ($16\text{-}119 \text{ ps}$). Note that the energy density of the pump pulses applied in this experiment is roughly equivalent to that of the $1900\text{-}2100 \text{ cm}^{-1}$ -probe experiment, due to a larger beam diameter at the position of the sample. The gray areas represent the inverted, properly scaled, stationary UV-Vis spectrum of [1]. Black numbers indicate peak positions in nm, black arrows emphasize the spectro-temporal evolution, and asterisk label isosbestic points. Note that the scaling of the ordinate changes above a wavelength of 500 nm .

signals in the mIR regress only to roughly $1/2$ within the same time. After ca. 100 ps , the electronic ground state is replenished almost completely, except of some minor signals, again attributed to the pathway following TPA.

Due to the multitude of strongly overlapping signals in the Vis-region, an analysis of the kinetics by first applying a simple regression model to the transient spectra, followed by an evaluation of the fit parameters in the time domain, as conducted for the $1900\text{-}2100 \text{ cm}^{-1}$ -probe spectra, is not feasible here. Instead, the kinetic traces at all probe wavelengths are fitted and evaluated individually. Most kinetic τ traces turn out to be well described by a

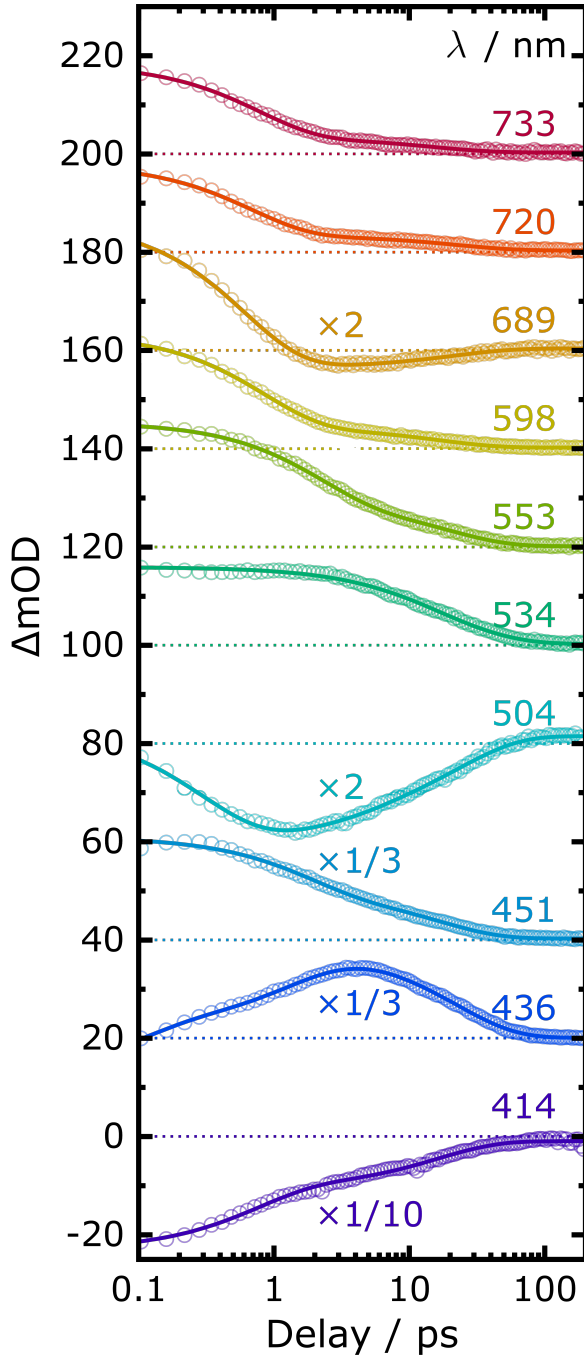


Table 1: Bi- or triexponential fit parameters of selected $8\mu\text{J}$, 400nm -pump/Vis-probe kinetic traces of the [1] in room-temperature DCM solution.

λ / nm	$\Delta\text{mOD}(0)_i$	τ_i / ps	$\Delta\text{mOD}(\infty)$
733	15.0	0.77	0.3
	3.0	15.1	
720	14.6	0.68	0.4
	0.3	22.5	
689	14.9	0.62	0.2
	-2.0	21.5	
598	19.1	0.84	0.2
	4.1	16.6	
553	16.5	2.1	0.2
	8.7	19.8	
534	7.6	11.9	0.3
	8.1	30.6	
504	11.5	0.32	0.8
	-2.3	4.2	
	-8.5	24.3	
451	45.4	1.7	1.3
	37.1	17.2	
436	-40.7	0.09	0.5
	-63.4	1.5	
	71.8	22.7	
414	-125.7	0.73	-9.4
	-95.4	16.4	

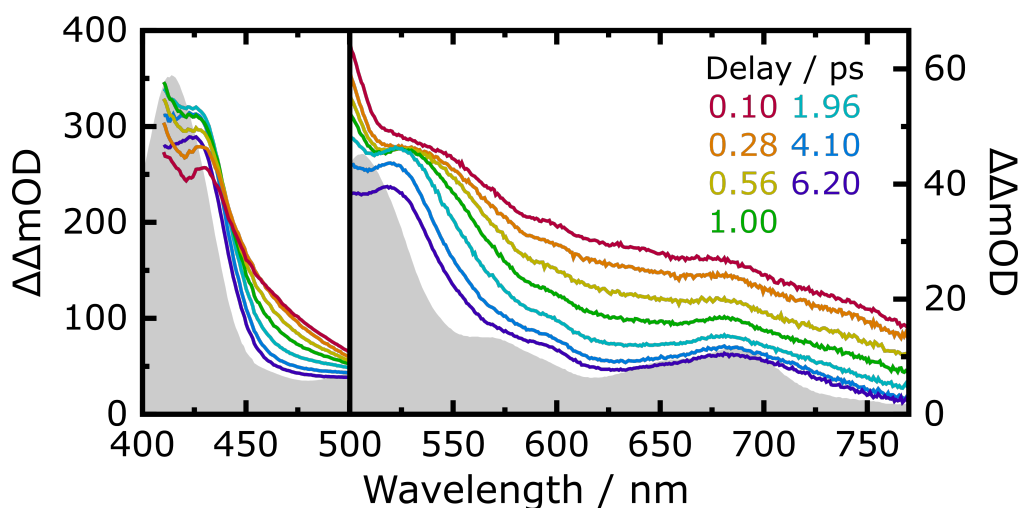
Figure 16: $8\mu\text{J}$, 400nm -pump/Vis-probe kinetic traces of the [1] in room-temperature DCM solution at selected probe wavelengths (circles), as specified in the legend. Solid lines represent bi- or triexponential fit functions. For clarity, the individual traces are vertically shifted. The zero line of each trace is indicated by a dotted line.

biexponential fit function, while a minority, falling into regions around the shifting maxima, requires a triexponential description. Some exemplary kinetic traces are depicted in Figure 16 and their fit parameters are listed in Table 1. (A summary of the fit parameters of all traces is given in Figure A13 in the appendix.) In general, the obtained time constants are distributed mostly within two distinct ranges between 0.6 ps and 1.0 ps and between 13 ps and 30 ps. The latter match qualitatively the time constants extracted from evaluation of the transient $\nu_{\text{as}}(\text{N}_3)$ signals. Yet, as opposed to the publication on the photolysis of [6], in which 'well defined exponential decay components'^[369] are reported, indicating the occurrence of direct state-to-state conversions only, the individual time constants found here are largely spread. This finding underpins the assumption that the excited complexes are subjected to VER, at least within the first few picoseconds, during which the spectra lack isosbestic points.

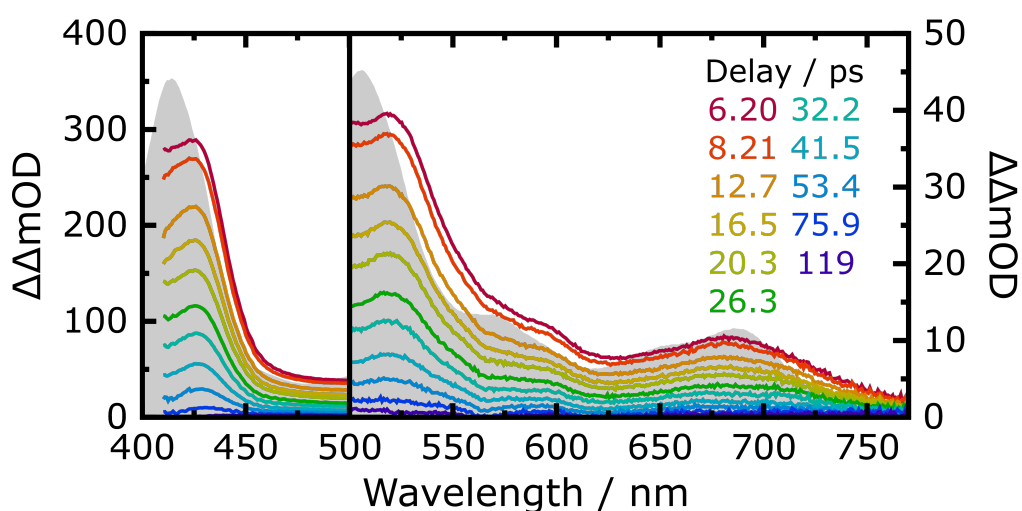
In order to obtain a better view on the properties of the excited complexes, purely absorptive product spectra are calculated and displayed in Figure 17. These spectra are generated under the assumption that the GSR takes place monoexponentially with a time constant of 20.7 ps (cf. section 5.2.2). As emphasized in Figure 17(a), the product spectrum consists of a single, structureless band, maximal in ΔOD at about 425 nm but reaching up to the nIR during the early delays (< ca. 2 ps). Within this time window, the absorbance in the B-band region increases at the expense of absorbance in the Q-band region. In total, this means a blue-shift of absorption strength, which is characteristic of a vibrational cooling process.

Roughly estimated from the shifts of the maxima in the transient Vis-spectra, the VER has a half-life period of 1-2 ps, which is smaller than the value extracted from the 1900-2100 cm^{-1} -probe spectra. At first glance, it might seem counterintuitive that the VER of the same complex occurs at different rates depending on the considered spectral region. Yet, it shall be reminded that the spectral narrowing and frequency upshift of a monitored absorption band of a high-energy transition is caused by the coupling to highly excited, but gradually relaxing low-frequency vibrational modes. However, these various modes transfer their excess energy to the solvent at distinct rates. Since the electronic B- and Q-excitations and the $\nu_{\text{as}}(\text{N}_3)$ vibration of [1] are likely to be coupled to different low-frequency vibrations, the rates of VER extracted from probing their individual resonance bands are non-uniform.

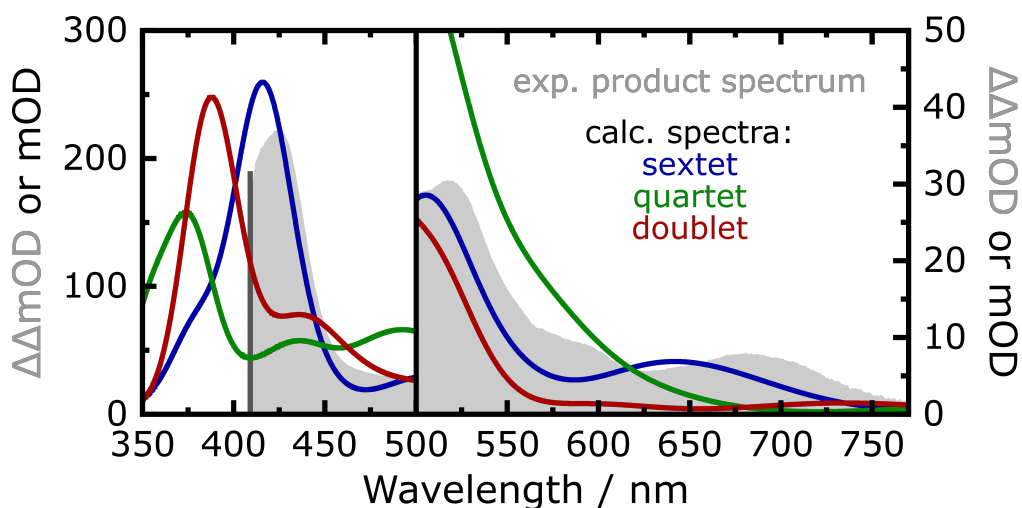
It is worth mentioning that both references [369] and [377] attribute the process occurring within 1-2 ps to a conversion from a por \rightarrow Fe CT state to a lower-lying electronic state instead (for [6]). In fact, the weakened B-band and increased absorbance in the Q-band region are features which indicate, according to the criteria suggested by Holten et al. (cf. section 2.2.4),^[299,300] the presence of such a LMCT state. Still, due to the influence of the VER occurring on this timescale, it is infeasible to revise, whether there is an additional conversion between electronic states taking place simultaneously, by inspection of the transient Vis-spectra recorded here. However, the monoexponential progressions of the transient signals in the 1900-2100 cm^{-1} -probe spectra imply that only a single, excited electronic state is monitored in that experiment. Hence, the lifetime of any higher-lying states, if populated at all, must be



(a) $0.10 \text{ ps} \leq \tau \leq 6.2 \text{ ps}$.



(b) $6.2 \text{ ps} \leq \tau \leq 119 \text{ ps}$.



(c) Averaged product spectrum ($\tau = 10\text{-}15 \text{ ps}$) and calculated spectra of $d \rightarrow d$ states of [1].

Figure 17: (a) & (b) Product spectra obtained from the $8 \mu\text{J}$, 400 nm -pump/Vis-probe spectra of [1] in room-temperature DCM solution, at various pump-probe delays as specified in the legends. The gray area represents the properly scaled, stationary UV-Vis spectrum of [1]. (c) Product spectrum averaged over pump-probe delays from 10 ps to 15 ps (gray area) and properly scaled, TD-DFT-predicted spectra of the

lowest sextet, quartet, and doublet state of [1] (colored lines), as specified in the legend. Note that the scaling of the ordinate changes above a wavelength of 500 nm.

limited to the time resolution of the mIR-probe setup of 200 fs, which is much smaller than the lifetime of the LMCT state proposed in the literature (2.3 ps^[369]; 1.13 ps^[377]).

After ca. 6 ps, the product spectra are stable in shape and decline completely within tens of picoseconds, as shown in Figure 17(b). These spectra feature distinct signals in the Q-band region and match essentially the stationary UV-Vis spectrum of the parent complex, yet red-shifted by roughly 10 nm. Based on this trait and following Holten's criteria, Rury and Sension assigned the underlying state to an iron-centered $d \rightarrow d$ state, presumably the lowest quartet state of the parent complex (there: [6]). However, as shown in Figure 17(c), TD-DFT calculations of complex [1] in different spin states predict both the lowest quartet and doublet state (both are $d(\text{Fe}) \rightarrow d(\text{Fe})$ states) to exhibit each a B-band blue-shifted compared to that of the sextet ground state, as opposed to the proposal by Holten et al.. Furthermore, their computed absorption spectra in the Q-band region are qualitatively in disagreement with the experimental product spectrum on this timescale. Hence, an assignment of the underlying species to either of these states appears inadequate.

Having the $d(\text{Fe}) \rightarrow d(\text{Fe})$ states excluded, the question arises, which alternative excited state of [1] is responsible for the absorption bands present at timescales of tens of picoseconds. In principle, there are three possible candidates, the first of which are vibrationally excited states, already suggested by Vura-Weis et al..^[377] However, this option has already been rejected in the argumentation in section 5.2.2. Considering excited electronic states, porphyrin-centered $\pi(\text{por}) \rightarrow \pi^*(\text{por})$ states and $\text{por} \rightarrow \text{Fe}$ CT states come into question. Unfortunately, an assessment of the spectral signatures of these states by means of computational chemistry is impeded by the high demand of excited state calculations. Nevertheless, there are two arguments in favor of an association with a $\pi(\text{por}) \rightarrow \pi^*(\text{por})$ state: First, the TD-DFT calculation of ⁶[1] predicts the degenerated roots 1 and 2 to be $Q(\pi \rightarrow \pi^*)$ states, located below an energy of 10000 cm^{-1} . In contrast, the $\text{por} \rightarrow \text{Fe}$ CT states lowest in energy are root 3, 4, and 5, located roughly at 15000 cm^{-1} . Hence, it is more likely that [1] resides longest in the less energetic $Q(\pi \rightarrow \pi^*)$ states before returning to the ground state. This idea complies with Kasha's rule,^[404] which rests on the assumption that the lifetime of the lowest excited electronic state of a given spin multiplicity is much larger than those of higher excited states. Second, Vura-Weis and coworkers found in their XUV-probe experiments rather weak transient signals on this timescale.^[377] This indicates the underlying excited state to have an iron center in the same oxidation state as the ground state. While (pure) $\pi(\text{por}) \rightarrow \pi^*(\text{por})$ states fulfill this criterion, a $\text{por} \rightarrow \text{Fe}$ charge transfer lowers the oxidation state of the iron center by one. Based on these arguments, the product spectrum shown in Figure 17(c) is assigned to a ⁶ $Q(\pi \rightarrow \pi^*)$ state, the first (and second) excited sextet state of [1], and the exponential decay component of 20.7 ± 0.3 ps to the GSR from this state.

5.2.4 De-excitation Scheme

At this point, the results on the processes following single-photon excitation of [1] shall be summarized briefly. These findings are illustrated in the form of a de-excitation scheme in Figure 18 and compared to the previously proposed schemes (for the analogous chlorido complex [6]) there.

400 nm excitation of [1] promotes the complex from its ground state into the porphyrin-centered ${}^6B(\pi \rightarrow \pi^*)$ state (root 23 and 24 in the TD-DFT calculation). Due to the invariance of even the earliest Vis-probe spectra on the excitation wavelength, it can be concluded that [1] converts from the ${}^6B(\pi \rightarrow \pi^*)$ state and other high-energy states within less than 100 fs to the same lower-lying state. Whether this conversion proceeds via interjacent excited states, as suggested by Rury and Sension,^[369] cannot be verified here because of the limited time resolution of the applied experiments.

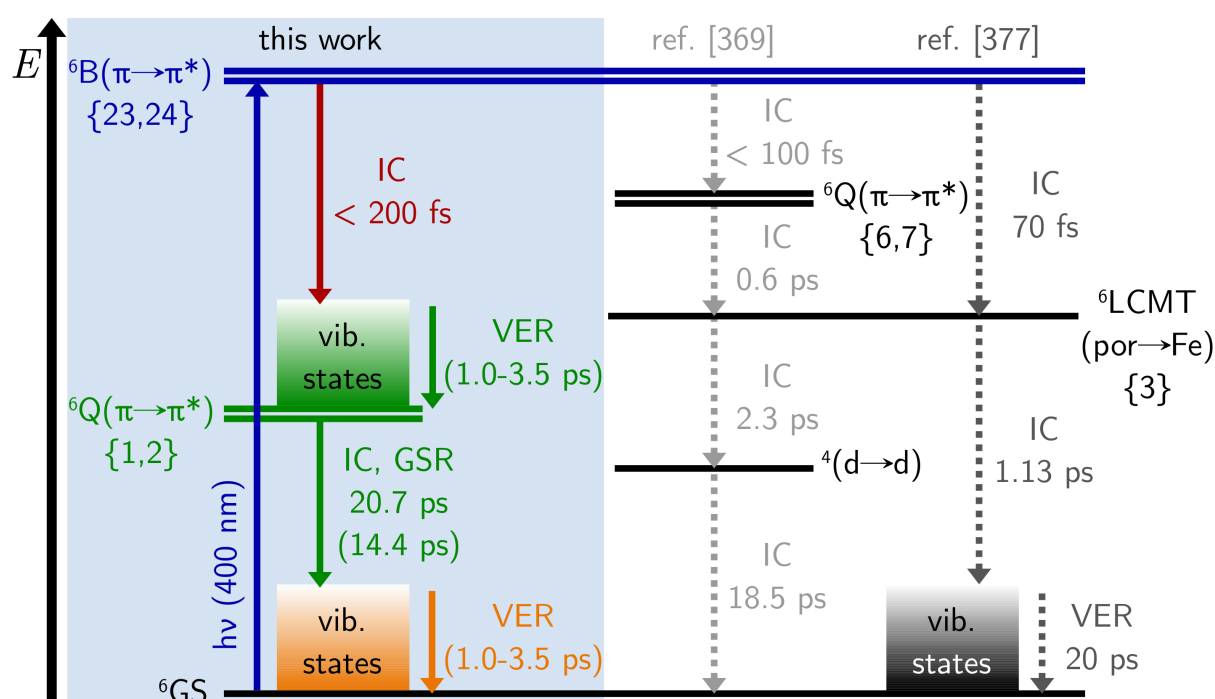


Figure 18: De-excitation scheme of [1] following SPA developed in this work (blue box). Horizontal lines symbolize electronic states of [1], assigned by the adjacent labels, and colored areas represent multitudes of vibrational states, in a qualitative energy level diagram. The numbers in curly brackets indicate the corresponding roots from the TD-DFT calculation. The blue arrow represents the excitation triggered by a 400 nm-photon. Other colored arrows represent de-excitation processes. Their labels specify their time constants or half-life periods (in parentheses). Color coding: green - directly observed in this work, red - indirectly derived from the experimental data, orange - not evidenced but highly likely. Dotted arrows represent the de-excitation pathways suggested previously by Rury and Sension (light gray)^[369] and Vura-Weis et al. (dark gray)^[377] for analogous complex [6].

From 200 fs on, both the transient absorption and bleaching band associated with $\nu_{as}(N_3)$ vibrations decline strictly monoexponentially to zero, implying a direct and complete state-to-state conversion from a single excited state to the ground state. This excited state exhibits

a Vis spectrum similar to that of the ground state, but red-shifted by ca. 10 nm, a $\nu_{as}(\text{N}_3)$ resonance band at ca. 2046 cm^{-1} , and decays with a time constant of $\tau_2 = 20.7 \pm 0.3\text{ ps}$ (half-life period: 14.4 ps). Moreover, the pronounced blue-shifts and spectral narrowing of the transient absorptions in both the mIR- and the Vis-probe spectra evidence the occurrence of a vibrational energy relaxation. The half-life period of this process falls into a range from 1.0 ps to 3.5 ps. Since this process is much faster than the GSR, it is concluded that the VER takes place on the potential energy surface of an excited electronic state. This interpretation is opposed to the previous work on [6] by Vura-Weis et al., who proposed the electronic ground state to be replenished already after ca. 2 ps and assigned a decay component of ca. 20 ps to a VER on the ground state energy surface. In fact, another VER on the ground state energy surface cannot be excluded here and is indeed very likely. Yet, it occurs presumably with a rate similar to that of the VER in the excited electronic state, and, hence, cannot be tracked here.

The monitored excited state, present on timescales of a few tens of picoseconds, is assigned to the lowest excited sextet state of [1], a porphyrin-centered ${}^6\text{Q}(\pi \rightarrow \pi^*)$ state (root 1 and 2). The alternative assignment to an iron-centered $d \rightarrow d$ state, suggested by Rury and Sension,^[369] is rejected here, because the TD-DFT-predicted Vis absorption spectra of the lowest quartet and doublet ($d(\text{Fe}) \rightarrow d(\text{Fe})$) states of [1] are in stark disagreement with the experimental product spectrum. Also, no evidence for the population of a por \rightarrow Fe CT state (e.g. root 3) during the first 1-2 picoseconds, as proposed in both references [369] and [377], is obtained in this work. Therefore, this state is not included in the de-excitation model developed here. If such a LMCT state is intermediately populated, its lifetime must be below the time resolution of the mIR-probe experiment (200 fs), because its presence and conversion to the lower-lying ${}^6\text{Q}(\pi \rightarrow \pi^*)$ state would manifest themselves in the transient mIR spectra otherwise.

5.3 Electronic Structures of the Photoproducts – High-Energy Excitation

5.3.1 400 nm-Pump/1410-1500 cm^{-1} -Probe and -1550-1620 cm^{-1} -Probe Experiments

Up to this point of this work, the investigations on the photolysis of [1] have been focused on detection of either the visible spectral range or the $\nu_{as}(\text{N}_3)$ resonance band in the mid-infrared. These experiments yielded valuable insight into the ultrafast processes following the photoexcitation and the chemical nature of the products. Despite that, they did not allow any conclusions concerning the electronic structure of the generated photoproducts. In order to gather information in this regard, measurements of different probe regions in the mIR had to be conducted. As mentioned in section 2.2.4, π -radical porphyrins exhibit characteristic absorption bands at either ca. 1280 cm^{-1} or ca. 1550 cm^{-1} , depending on the symmetry of the SOMO. Moreover, the $\nu_{41}(\text{por})$ resonance band located around 1340 cm^{-1} functions as spin state marker of the iron center, given that the porphyrin ligand has a closed-shell configuration.

Hence, probing in the spectral region from 1250 cm^{-1} to 1650 cm^{-1} appears to be a promising approach.

If not mentioned otherwise, all pump-probe experiments discussed in this and the following sections were performed using pump pulses of high pulse energy, since photoproducts were demonstrated to be formed in detectable amounts only under this condition.

Figure A6 in the appendix displays $12\text{ }\mu\text{J}$, 400 nm -pump/mIR-probe spectra in the ranges from 1410 cm^{-1} to 1500 cm^{-1} and 1550 cm^{-1} to 1620 cm^{-1} . Despite the high pump pulse energy, all transient signals observed in these ranges decline essentially to zero within ca. 100 ps . This finding is not surprising, because all bands of [1] in this region are associated with normal modes centered at the phenyl rings, which are insensitive to the changes occurring at the iron center and axial ligand upon photoexcitation. Besides those features, no transient signals were found in the spectral range from 1370 cm^{-1} to 1850 cm^{-1} within delays up to 3.5 ns . In particular, an absorption band at ca. 1550 cm^{-1} , indicative of an a_{1u} -type π -radical, has not been detected. The absence of such a signal is not unexpected either, since complexes of tpp^{2-} are known to favor the a_{2u} -radical configuration (cf. section 2.2.3).

In contrast, measurements in the range from 1240 cm^{-1} to 1370 cm^{-1} revealed themselves to comprise some intriguing spectral features, which will be the topic of discussion in the rest of this section.

5.3.2 400 nm-Pump/1300-1370 cm^{-1} -Probe Experiment

Transient $16\text{ }\mu\text{J}$, 400 nm -pump/ $1300\text{-}1370\text{ cm}^{-1}$ -probe spectra of [1] are displayed in Figure 19(a). Immediately after the impact of the pump pulse, three transient signals are observed: A bleaching band centered at 1340 cm^{-1} , coinciding with the peak frequency of the strongest signal of [1] in this region, and two overlapping transient absorptions at 1312 cm^{-1} and 1328 cm^{-1} . In addition, as the negative signal is much narrower than the stationary absorption band of [1], it is clear that both transient absorptions overcompensate the bleaching contribution in the region below 1335 cm^{-1} . While these spectral features change only slightly during the first few picoseconds, a pronounced decay of all three signals is observed on timescales of tens of picoseconds, which is completed after ca. 100 ps . Thereafter, the spectra remain essentially unchanged up to 3.5 ns . Again, the temporal evolution of these spectra is quantified by multiexponential fits of all individual kinetic traces, here within the range from 1306 cm^{-1} to 1350 cm^{-1} and 0.1 ps to 500 ps . Selected kinetic traces and fit functions are depicted in Figure 19(c), and the fit parameters of all kinetic traces are listed in Table A3. In brief, the obtained time constants fall into three regions. First, a small time constant of $< 3\text{ ps}$, which is found for traces in the range from 1330 cm^{-1} to 1345 cm^{-1} . In this region, the transient absorption originally peaking 1328 cm^{-1} is subjected to a small spectral shift towards 1331 cm^{-1} . The shift and the time constant describing its effect on the kinetic traces are attributed to the VER already discussed in the previous sections. Second, the decline of the bleaching signal and the absorption at 1331 cm^{-1} occur with time constants in the range from 17 ps to 35 ps , i.e. at roughly the same rate as the internal conversion from the ${}^6\text{Q}(\pi\rightarrow\pi^*)$ state to the ground state, and,

hence, are assigned to this process. Interestingly, the low-frequency band centered at 1312 cm^{-1} decays with a distinctly smaller time constant of 9-14 ps. The occurrence of this new time constant indicates that the underlying process is not included in the de-excitation scheme developed for SPA of [1] in section 5.2.4. In fact, in a complementary pump-probe experiment using $3\text{ }\mu\text{J}$ (low-energy) pump pulses, cf. Figure A7, the band at 1312 cm^{-1} is essentially absent,

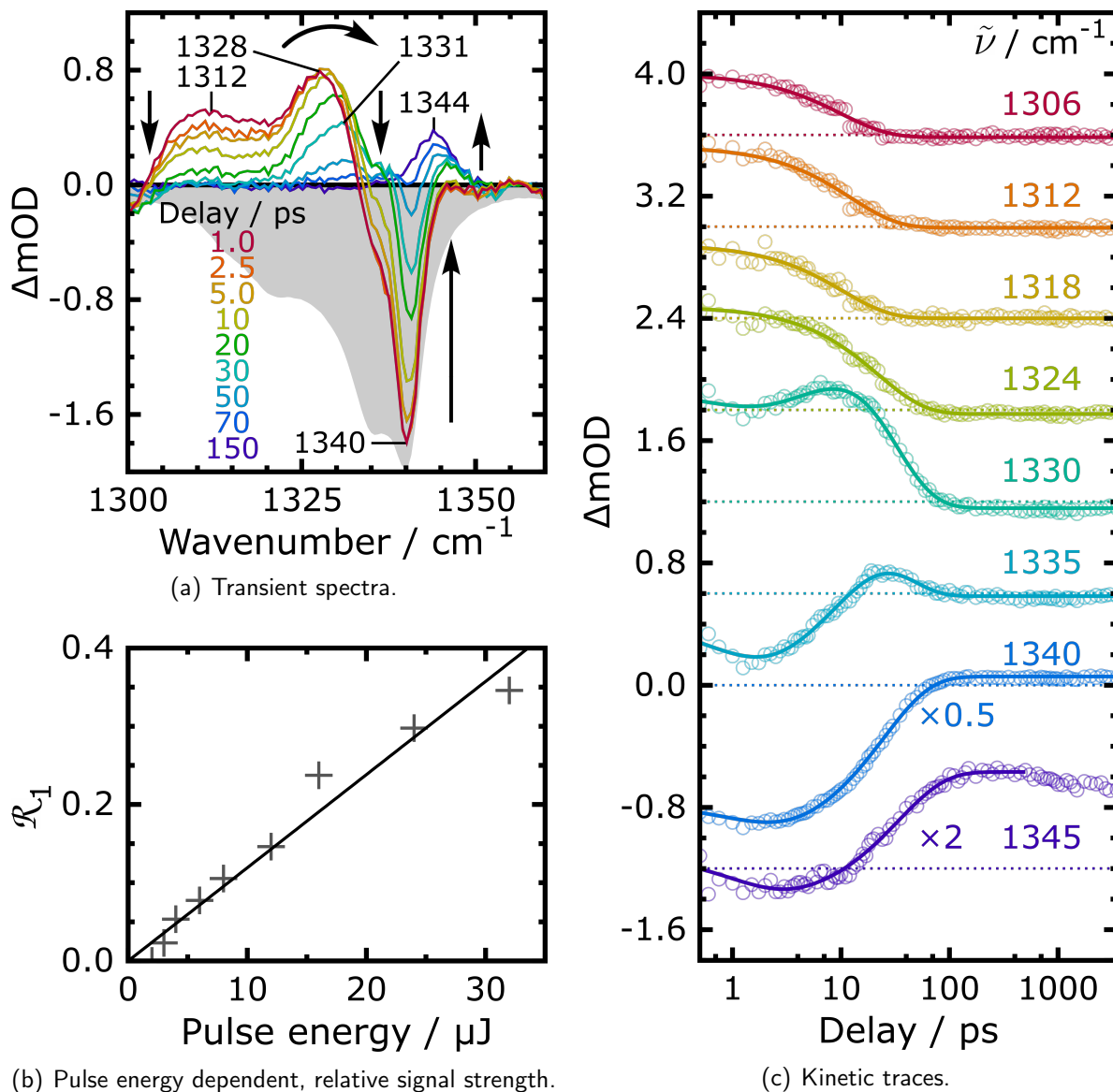


Figure 19: (a) Transient $16\text{ }\mu\text{J}$, 400 nm -pump/ 1300 - 1370 cm^{-1} -probe spectra of [1] in room-temperature DCM solution at various pump-probe delays, as specified in the legend. The gray area represents the inverted, properly scaled, stationary FTIR spectrum of [1]. Black numbers indicate peak positions in cm^{-1} and black arrows emphasize the spectro-temporal evolution. (b) Ratio of the amplitudes of the residual transient absorption band ($\Delta\text{OD}(1344\text{ cm}^{-1}, 200\text{ ps}, E_{\text{pump}})$) and the initial bleaching signal ($\Delta\text{OD}(1340\text{ cm}^{-1}, 1\text{ ps}, E_{\text{pump}})$) in dependence on the energy of the pump pulse (gray crosses) and proportional fit function (black line). (c) Kinetic traces at various frequencies as specified in the legend. Circles and solid lines represent experimental data and (multi)exponential fit functions, respectively. For clarity, the individual traces are vertically shifted. The zero line of each trace is indicated by a dotted line.

whereas the other spectral features remain unchanged. Thus, it can be assumed that this band originates from a transient species generated by TPA and having a different lifetime than the ${}^6Q(\pi \rightarrow \pi^*)$ state populated by SPA. Besides those signals, another transient absorption is found at 1344 cm^{-1} , which emerges from the declining bleaching signal and persists until the end of the considered delay range of 3.5 ns (dark blue kinetic trace in Figure 19(c)). Although a slight decrease of ΔOD at this frequency after 500 ps might imply a finite lifetime of the underlying species, the limitation to the measured temporal window does not allow a verification of this hypothesis. Just like all residual transient absorptions detected previously, this signal is absent in transient spectra recorded after low-energy excitation (see Figure A7). As before, the origin of the signal is assigned to either SPA or TPA by investigation of its amplitude, $\Delta\text{OD}(1344\text{ cm}^{-1}, 200\text{ ps}, E_{\text{pump}})$, compared to the amplitude of the initial bleaching signal, $\Delta\text{OD}(1340\text{ cm}^{-1}, 1\text{ ps}, E_{\text{pump}})$. The ratio of the two differential optical densities, \mathcal{R}_1 (cf. Equation (39)) is plotted against the applied pump pulse energy in Figure 19(b). Again, the proportional correlation confirms the origin of the responsible species to be TPA.

$$\mathcal{R}_1 = -\frac{\Delta\text{OD}(1344\text{ cm}^{-1}, 200\text{ ps}, E_{\text{pump}})}{\Delta\text{OD}(1340\text{ cm}^{-1}, 1\text{ ps}, E_{\text{pump}})} \quad (39)$$

This band's most striking property is its high absorption strength. Given that the initial bleaching signal in this region has an estimated amplitude of ca. $-2\Delta\text{mOD}$ and Φ is roughly 8% at $16\text{ }\mu\text{J}$, 400 nm excitation, the residual bleaching signal after 150 ps has an amplitude of ca. $-0.16\Delta\text{mOD}$. However, a negative contribution of this magnitude is not observed in the late transient spectra, as it is entirely overcompensated by the transient absorption. Moreover, in spite of the mutual compensation of both signals, ΔmOD reaches a value of $+0.4$ at 1344 cm^{-1} . Thus, it must be concluded that the signal strength of the transient absorption exceeds that of the parent's residual bleaching band by more than a factor of three. An assignment of this extraordinary absorption band will be provided in section 5.3.5 and 5.3.6.

5.3.3 400 nm-Pump/1240-1310 cm^{-1} -Probe Experiment

Pump-probe spectra of [1] in the region from 1240 cm^{-1} to 1310 cm^{-1} , likewise recorded after $16\text{ }\mu\text{J}$, 400 nm excitation, are reproduced in Figure 20(a). Note that this experiment had to be conducted in deuterated DCM because this spectral region is obscured by a solvent absorption in DCM of natural isotope distribution. In general, deuteration of the solvent molecules can change the rate of energy transfer between them and the solute significantly.^[149,405,406] Hence, the kinetics extracted from this experiment might deviate from those of the previous measurements. However, a complementary $1300\text{-}1370\text{ cm}^{-1}$ -probe experiment in DCM- d_2 , whose results are summarized in Figure A8 and Table A4 in the appendix, reveals the spectro-temporal evolution in both solvents to proceed with nearly identical rates.

As shown in Figure 20(a), although [1] exhibits each a weak absorption band at 1299 cm^{-1} and 1261 cm^{-1} , a bleaching signal is only observed at the former frequency. This is because the low-frequency bleaching contribution is overcompensated by an approximately twice as

strong transient absorption, giving rise to a net-positive feature maximal at 1265 cm^{-1} . Just as the signals in other probe regions, both this absorption and the parent's bleaching signal decay within tens of picoseconds. Yet, no measurable shift of peak positions indicative of VER is found in these spectra. At the same time as the initial signals decline, a new transient absorption emerges around a frequency of 1282 cm^{-1} , reaches its final strength after ca. 100 ps and persists for delays of at least 3.5 ns.

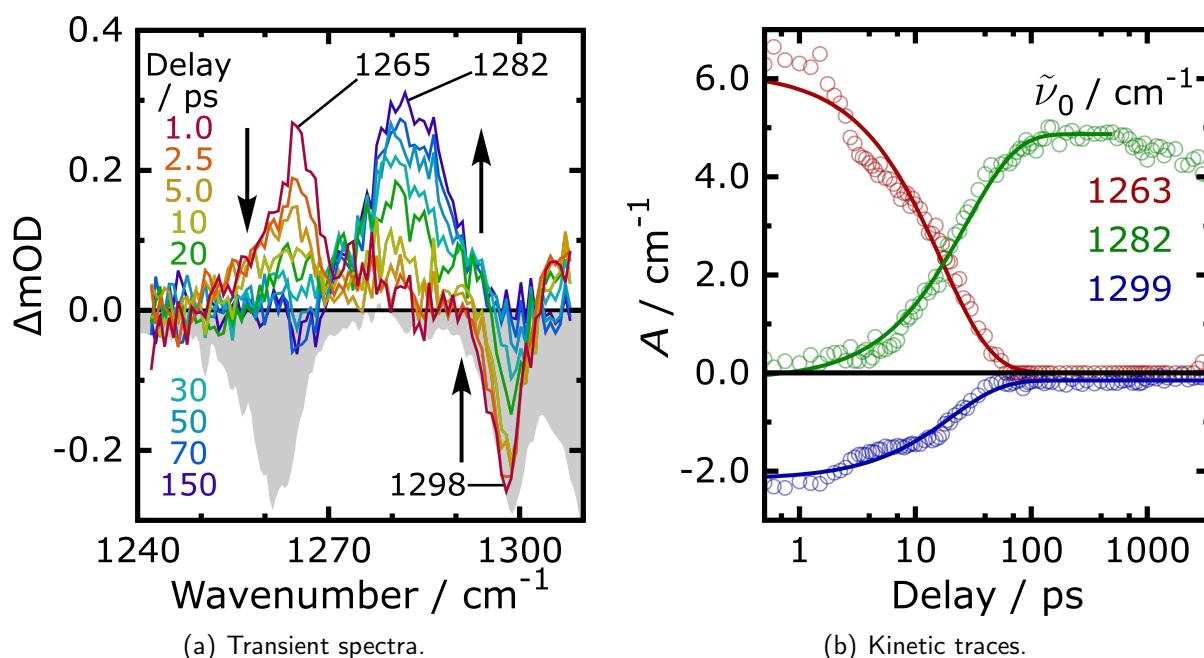


Figure 20: (a) Transient $16\text{ }\mu\text{J}$, 400 nm -pump/ $1240\text{--}1310\text{ cm}^{-1}$ -probe spectra of [1] in room-temperature DCM- d_2 solution at various pump-probe delays, as specified in the legend. The gray area represents the inverted, properly scaled, stationary FTIR spectrum of [1]. Black numbers indicate peak positions in cm^{-1} and black arrows emphasize the spectro-temporal evolution. (b) Kinetic traces of the signals peaking at the spectral positions stated in the legend. The integrals (circles) were determined by fitting of the individual transient spectra as a superposition of four pseudo-Voigt functions of fixed shape (see also Figure A9, Table A5, and Table A6). The lines represent monoexponential fit functions.

In order to describe the temporal evolution of these signals accurately despite the small signal-to-noise ratio, the individual transient spectra are fitted by a superposition of four pseudo-Voigt functions of fixed shape and position, obtained by the following procedure: First, the stationary FTIR spectrum of [1] is described by two functions, whose relative amplitudes are fixed in the following. Second, purely absorptive product spectra are calculated, as already described in section 5.2.1. In doing so, the spectra in the temporal windows from 0.1 ps to 2.0 ps and 150 ps to 3.5 ns , showing the initial and the final absorption band at 1263 cm^{-1} and 1282 cm^{-1} , respectively, are averaged to improve the signal-to-noise ratio. This proceeding appears justified because the changes during these time frames are sufficiently small. Both product spectra are fitted as pseudo-Voigt functions as well. All three spectra, including regression functions, are shown in Figure A9 in the appendix and the fit parameters are listed in Table A5. The integrals of these functions obtained by fitting of the transient spectra for

all recorded pump-probe delays are displayed in Figure 20(b) and fitted as monoexponential functions for their part. (Application of biexponential functions does not result in a significant improvement of the description.) Again, the GSR is found to occur with a time constant of 20.6 ± 0.9 ps, consistent with the analyses of other probe regions. Likewise, the transient absorption at about 1263 cm^{-1} decays at a similar rate ($\tau = 17.0 \pm 0.7$ ps) and is therefore assigned to a resonance band of the ${}^6\text{Q}(\pi \rightarrow \pi^*)$ state. In contrast, the band peaking at 1282 cm^{-1} rises with a distinctly larger time constant of 27.3 ± 0.9 ps, implying this process to be unconnected to the GSR. Thus, the underlying species is presumably a product generated by TPA. Similarly to the transient absorption found at 1344 cm^{-1} , this signal is strikingly strong compared to the expected residual bleaching after 100 ps and appears to decay on timescales of many nanoseconds.

A product spectrum averaged over the delay range from 150 ps to 3.5 ns, incorporating all three residual transient absorptions observed after high-energy excitation (at 1282 cm^{-1} , 1344 cm^{-1} , and 2045 cm^{-1}), is displayed in Figure 21. This spectrum was corrected for the adulterating effect of different energies of the applied pump pulses in the measurements of the three individual probe regions. Moreover, the spectrum is converted from the differential optical density to estimated extinction coefficients, $\epsilon(\text{est.})$, based on a comparison to the amplitude of the residual $\nu_{\text{as}}(\text{N}_3)$ bleaching signal after $16 \mu\text{J}$ excitation, and under the assumption that exactly one of the three primary product complexes ($[\mathbf{1}]^*$, $[\mathbf{2}]$, and $[\mathbf{3}_{\text{red}}]$) is responsible for each signals. (Conveniently, the three product complexes are formed in nearly equivalent amounts, cf. section 5.2.1.) Given that this prerequisite is correct, resonance bands of presumably porphyrin-centered vibrational modes exhibit extinction coefficients of around $2000 \text{ M}^{-1} \text{ cm}^{-1}$. The reason for the unusually large absorption strengths of these signals and their assignment requires a deeper consideration, given in the following sections.

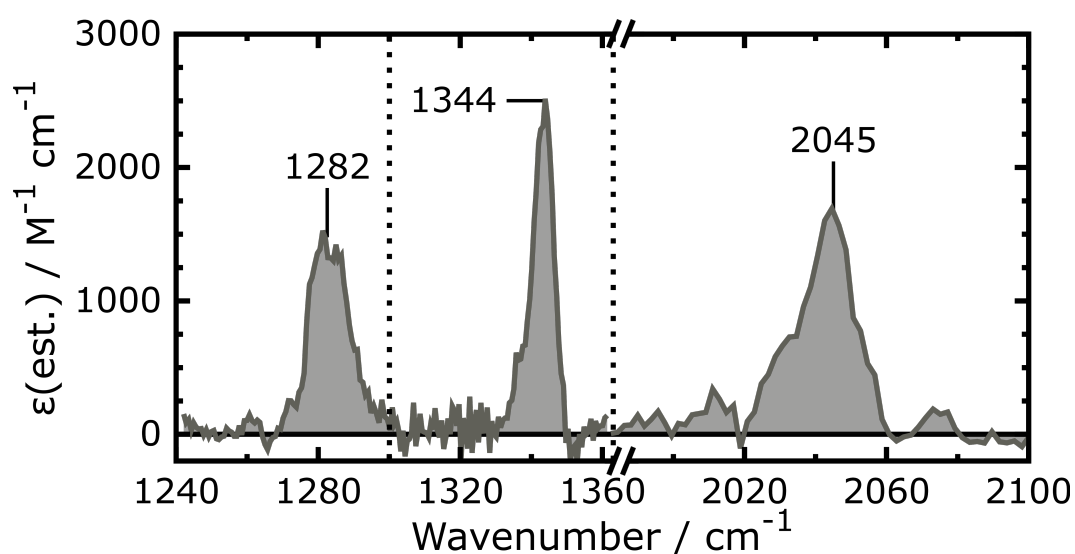


Figure 21: mIR product spectrum of the photolysis of $[\mathbf{1}]$ with $16 \mu\text{J}$, 400 nm-pump pulses in room-temperature DCM- d_2 (left panel) and DCM solution (central & right panel), averaged over pump-probe delays from 150 ps to 3500 ps. The numbers indicate peak positions in cm^{-1} .

5.3.4 Notation of Electron Configurations

In the upcoming evaluation, different electronic structures of metalloporphyrins will be considered, including porphyrin ligands having a closed-shell, π -radical or triplet configuration (cf. section 2.2.3). In order to distinguish the various structures, a specification of the overall spin multiplicity of a complex is not sufficient anymore. For example, there are five fundamentally different configurations giving rise to an overall quartet state of [1], schematically displayed in Figure 22:

- ◆ an intermediate-spin iron(+III) (d^5) center and a closed-shell porphyrindiido ligand
- ◆ a high-spin iron(+II) (d^6) center and an antiferromagnetically coupled π -radical porphyrinidyl ligand
- ◆ an intermediate-spin iron(+II) (d^6) center and a ferromagnetically coupled π -radical porphyrinidyl ligand
- ◆ a high-spin iron(+III) (d^5) center and an antiferromagnetically coupled triplet porphyrindiido ligand
- ◆ a low-spin iron(+III) (d^5) center and a ferromagnetically coupled triplet porphyrindiido ligand

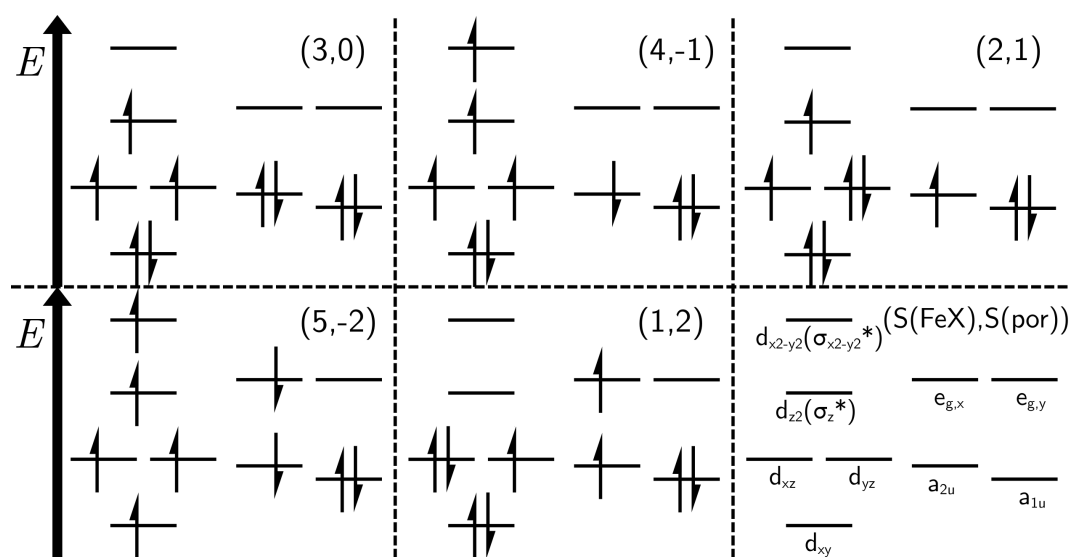


Figure 22: Schematic energy level diagrams of the frontier orbitals of [1]. The individual panels show different electron configurations of an overall quartet multiplicity. Harpoons pointing upwards and downwards represent α - and β -electrons, respectively. The label in the top right of each panel represents a shorthand notation. The lower right panel assigns the energy levels to molecular orbitals.

To differentiate between these structures properly, a set of two numbers is introduced here, $S(\text{FeX})$ and $S(\text{por})$, stating the number of unpaired electrons localized at the iron atom and its axial ligand (X), on the one hand, and the porphyrin ligand, on the other hand. The spin coupling of the two moieties is given by the signs of these numbers: ferromagnetic coupling if the

signs are identical, antiferromagnetic coupling if they are opposite. Hereafter, these numbers will be written in parentheses behind the complex as the following: [complex]($S(\text{FeX}), S(\text{por})$). For example, the five structures listed above are abbreviated as [1](3,0), [1](4,-1), [1](2,1), [1](5,-2), and [1](1,2), respectively.

In order to classify an electronic structure calculated by a DFT method, $S(\text{FeX})$ and $S(\text{por})$ can be estimated by means of a population analysis (here, the Löwdin method was applied). This analysis assigns a (fractional) number of unpaired electrons, $s_c(i)$, to each atom i . The computed numbers of unpaired electrons at the iron atom and axial ligand, $S_c(\text{FeX})$, and the porphyrin ligand, $S_c(\text{por})$, are obtained by summation of $s_c(i)$ over the corresponding atoms according to Equations (40) and (41). Note that only the atoms of the porphyrin ligand contributing to its extended π -system are included in the definition of $S_c(\text{por})$, i.e. its carbon and nitrogen atoms, but neither the hydrogen atoms nor the atoms of the phenyl rings.

$$S_c(\text{FeX}) = s_c(\text{Fe}) + \sum_i^{\text{axial ligand}} s_c(i) \quad (40)$$

$$S_c(\text{por}) = \sum_i^{\text{C,N(por)}} s_c(i) \quad (41)$$

Strictly speaking, another distinction could be made between the a_{2u} - and the a_{1u} -type of π -radical and triplet porphyrin ligands, which cannot be expressed by this notation scheme. Nevertheless, since all complexes considered here are *meso*-tetraphenyl-substituted, they will be assumed to adopt exclusively the a_{2u} -type in both open-shell cases in the following. In fact, in all DFT calculations of π -radical and triplet porphyrin structures, the a_{2u} -orbital is singly occupied rather than the a_{1u} -orbital (given that this distinction is feasible, see below). Moreover, the energetically lowest possible configuration of d-electrons at the iron center will be assumed for each local spin state.

5.3.5 Quantum Chemical Calculations & Interpretation – Part 1: π -Radical Porphyrin States

As discussed in previous sections, the following newly formed species are present in the solution within the time frame from 100 ps to 3.5 ns after two-photon excitation of [1]: N_3^\bullet , N_2 , [3_{red}], [2], and [1]*. The IR-spectra of the former three molecules are experimentally known and do not include strong spectral features at frequencies in the range from 1250 cm^{-1} to 1400 cm^{-1} .^[118,120,195,403,407] Regarding [2], DFT-predicted spectra of its global minimum structures in different spin states (doublet, quartet, and sextet, shown in Figure 24) do not comprise absorption bands comparable to the experimentally observed ones, either. In fact, the absorption strengths of both [2] and [3_{red}] (see Figure 25) in this spectral region are predicted to be even lower than the absorption strength of [1] (see Figure 23), which originates partially from the $\nu_s(\text{N}_3)$ vibration absent in both product complexes. The possibility of [1]* being responsible for the signals at issue will be considered in the following.

According to the literature, the presence of a pronounced absorption band in a very narrow spectral window around a frequency of 1280 cm^{-1} indicates the formation of a complex having an a_{2u} -type π -radical configuration (cf. section 2.2.4). For example, the product of the one-electron oxidation of chlorido complex **[6]** is the π -radical complex chlorido(5,10,15,20-tetraphenylporphyrinidyl)iron(+III), $[\text{Fe}^{\text{III}}(\text{tpp})(\text{Cl})]^+$ (**[6_{ox}]**), which consists of a high-spin iron center and an antiferromagnetically coupled $\text{tpp}^{\bullet-}$ -ligand, i.e. **[6_{ox}](5,-1)**, and absorbs strongly at 1280 cm^{-1} .^[247,274,293]

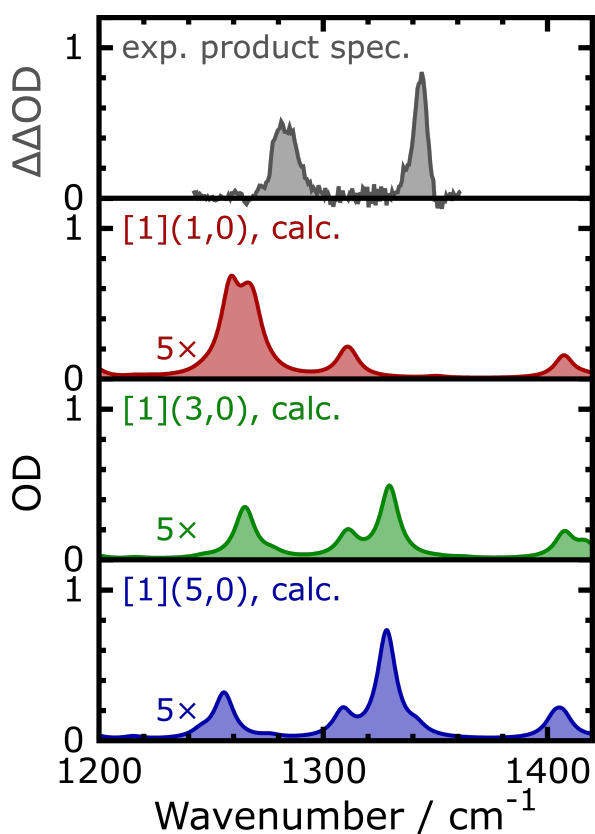


Figure 23: Upper panel: mIR product spectrum of the photolysis of **[1]** with $16\ \mu\text{J}$, 400 nm -pump pulses in room-temperature DCM/DCM- d_2 solution, averaged over delays from 150 ps to 3.5 ns . Other panels: DFT-predicted IR absorption spectra of **[1]($n,0$)** ($n = 1, 3, 5$, as specified by the labels), obtained by convolution of the stick spectra with a Lorentzian function ($\text{FWHM} = 10\text{ cm}^{-1}$). In all panels, an optical density of one is equivalent to an estimated extinction coefficient of $3000\text{ M}^{-1}\text{ cm}^{-1}$. Note that the calculated spectra are scaled up by a factor of five.

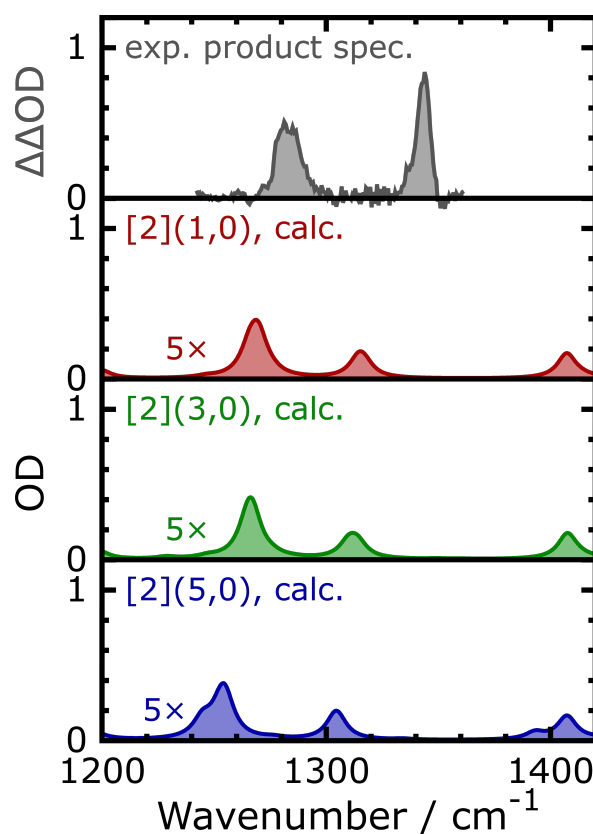


Figure 24: Upper panel: mIR product spectrum of the photolysis of **[1]** with $16\ \mu\text{J}$, 400 nm -pump pulses in room-temperature DCM/DCM- d_2 solution, averaged over delays from 150 ps to 3.5 ns . Other panels: DFT-predicted IR absorption spectra of **[2]($n,0$)** ($n = 1, 3, 5$, as specified by the labels), obtained by convolution of the stick spectra with a Lorentzian function ($\text{FWHM} = 10\text{ cm}^{-1}$). In all panels, an optical density of one is equivalent to an estimated extinction coefficient of $3000\text{ M}^{-1}\text{ cm}^{-1}$. Note that the calculated spectra are scaled up by a factor of five.

While this hints towards an explanation of the low-frequency absorption, the signal observed at 1344 cm^{-1} is located far beyond this characteristic spectral window and, hence, cannot be explained by an a_{2u} -type π -radical complex. As a matter of fact, no reports regarding an outstandingly intensive absorption band of metalloporphyrins in this spectral region could be found. However, a careful inspection of the previous studies on the IR-spectra of π -radical metalloporphyrins reveals all complexes considered there to bear metal ions in an oxidation

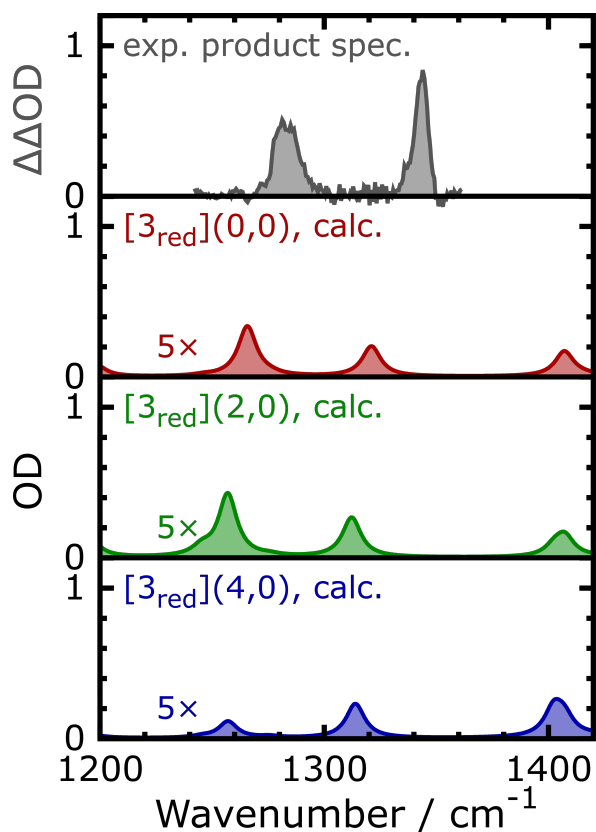


Figure 25: Upper panel: mIR product spectrum of the photolysis of [1] with $16\text{ }\mu\text{J}$, 400 nm -pump pulses in room-temperature DCM/DCM- d_2 solution, averaged over delays from 150 ps to 3.5 ns . Other panels: DFT-predicted IR absorption spectra of $[3_{\text{red}}](n,0)$ ($n = 0, 2, 4$, as specified by the labels), obtained by convolution of the stick spectra with a Lorentzian function ($\text{FWHM} = 10\text{ cm}^{-1}$). In all panels, an optical density of one is equivalent to an estimated extinction coefficient of $3000\text{ M}^{-1}\text{ cm}^{-1}$. Note that the calculated spectra are scaled up by a factor of five.

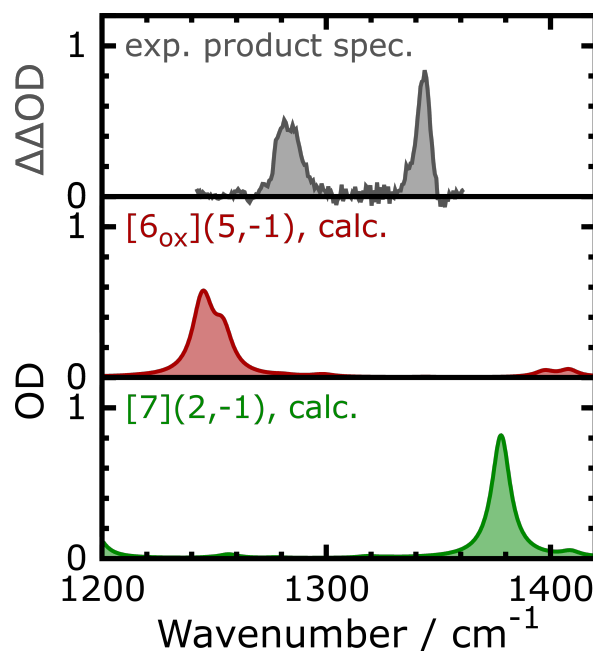


Figure 26: Upper panel: mIR product spectrum of the photolysis of [1] with $16\text{ }\mu\text{J}$, 400 nm -pump pulses in room-temperature DCM/DCM- d_2 solution, averaged over delays from 150 ps to 3.5 ns . Central and lower panel: DFT-predicted IR absorption spectra of $[6_{\text{ox}}](5,-1)$ (red) and $[7](2,-1)$ (green), obtained by convolution of the stick spectra with a Lorentzian function ($\text{FWHM} = 10\text{ cm}^{-1}$). In all panels, an optical density of one is equivalent to an estimated extinction coefficient of $3000\text{ M}^{-1}\text{ cm}^{-1}$.

state of either +II or +III.^[247,274,285,286,290,293,331,332,408,409] As opposed to that and to the best of the author's knowledge, the IR spectra of high-valent metalloporphyrins have not been reported so far. Thus, it is unknown which effect an increase of the oxidation state of the iron center above +III might cause.

In order to investigate this issue, additional DFT calculations are performed, as described in detail in section 8.5. First, it is verified that the employed level of theory is capable of reproducing the known IR spectrum of complex **[6_{ox}]** reasonably. In agreement with the experimental finding, the theory predicts the (5,-1) (a_{2u} -type π -radical) configuration to be the electronic ground state of the complex. At the same time, the calculated spectrum of **[6](5,-1)**, displayed in Figure 26, features a pronounced signal in the expected spectral region.

Having confirmed the theory to be reliable in this regard, the calculations are extended to the high-valent oxidoiron(+IV) complex **[7]**, which is likewise known to be a π -radical.^[57,410] DFT predicts the (2,-1) configuration of **[7]** to be the electronic ground state and yields an IR absorption spectrum as shown in Figure 26 (similar spectra are obtained for the alternative configurations, (2,1), (4,1), and (4,-1), as demonstrated in Figure A14). And in fact, complex **[7]** is predicted to exhibit a pronounced absorption band at 1378 cm^{-1} , instead of a signal around 1280 cm^{-1} .

At this point, a short explanation about the reason for the remarkable difference between the predicted IR spectra of **[7]** (iron(+IV)($tpp^{\bullet-}$)) and **[6_{ox}]** (iron(+III)($tpp^{\bullet-}$)) seems requisite. According to reference [286], the symmetry of the porphyrin's SOMO dictates, which vibrational mode of a π -radical metalloporphyrin will be subjected to an increase of absorption strength. As shown in Figure 27, the SOMO of **[6_{ox}]** is a typical a_{2u} -orbital, known from the Gouterman model, which gives rise to an intense band at 1280 cm^{-1} according to that work. In contrast, the SOMO of **[7]** can neither be identified as pure a_{2u} - nor as pure a_{1u} -orbital. In fact, the $\pi(\text{por})$ spin orbitals of **[7]** around the HOMO-LUMO gap in both the α - and the β -subset adopt the shapes of 'twisted' a_{1u} and a_{2u} -orbitals, indicating a substantial mixing of both orbital. This finding can be explained as follows: With increasing oxidation state of the iron center, the energy of the a_{2u} -orbital decreases, as it has large orbital lobes towards this atom. In contrast, the energy of the a_{1u} -orbital remains nearly unchanged, because its nodal planes intersect at the iron atom. At the high oxidation state of +IV, the normally higher lying a_{2u} -orbital is lowered in energy to an extent, that causes both orbitals to be almost degenerated. This situation forces the complex to undergo a pseudo-Jahn-Teller distortion, giving rise to a pattern of alternately increased and decreased bond lengths in the porphyrin backbone (see Figure A15 in the appendix) and a mixing of the a_{2u} - and the a_{1u} -orbital to new orbitals of lower symmetry. In this distorted structure, the displacement vectors, resonance frequencies, and absorption strengths of the vibrational modes vary from those of more symmetric π -radicals like **[6_{ox}]**, yielding the noticeably different absorption spectrum. Yet, a simple correlation between the displacement vectors of the affected normal mode and the nodal planes of the SOMO, as suggested in ref. [286], could not be found here. Thus, a conclusive reason to question, why the normal mode of **[7]** absorbing at 1378 cm^{-1} in particular is raised

in absorption strength, cannot be given at this point.

At first glance, the decent agreement between the calculated spectrum of [7] and the measured band at 1344 cm^{-1} seems to imply this complex as possible origin of this signal. And in fact, a reaction of the primary photoproducts of [1] with molecular oxygen was already verified in reference [109], in which the $\mu\text{-O}$ bridged complex $[\text{Fe}^{\text{III}}(\text{tpp})]_2\text{O}$ was identified as by-product of this photolysis, besides the main product $[\text{Fe}^{\text{III},+\text{IV}}(\text{tpp})]_2\text{N}$ ([8]), especially if the initial concentration of [1] was low ($> 1.4\text{ mM}^{-1}$). Based on this finding, the occurrence of [7] as intermediate is thinkable (albeit not evidenced). Still, even if a reaction of either [3_{red}] or [2] with dioxygen to [7] is assumed, such a reaction will be bimolecular in nature and, thus, will have a rate limited by diffusion. Typically, diffusion controlled reactions in room-temperature solution take place on timescales of many nanoseconds to microseconds.^[411] As opposed to that, the species absorbing at 1344 cm^{-1} is formed fully within 100 ps, thus excluding an assignment to [7].

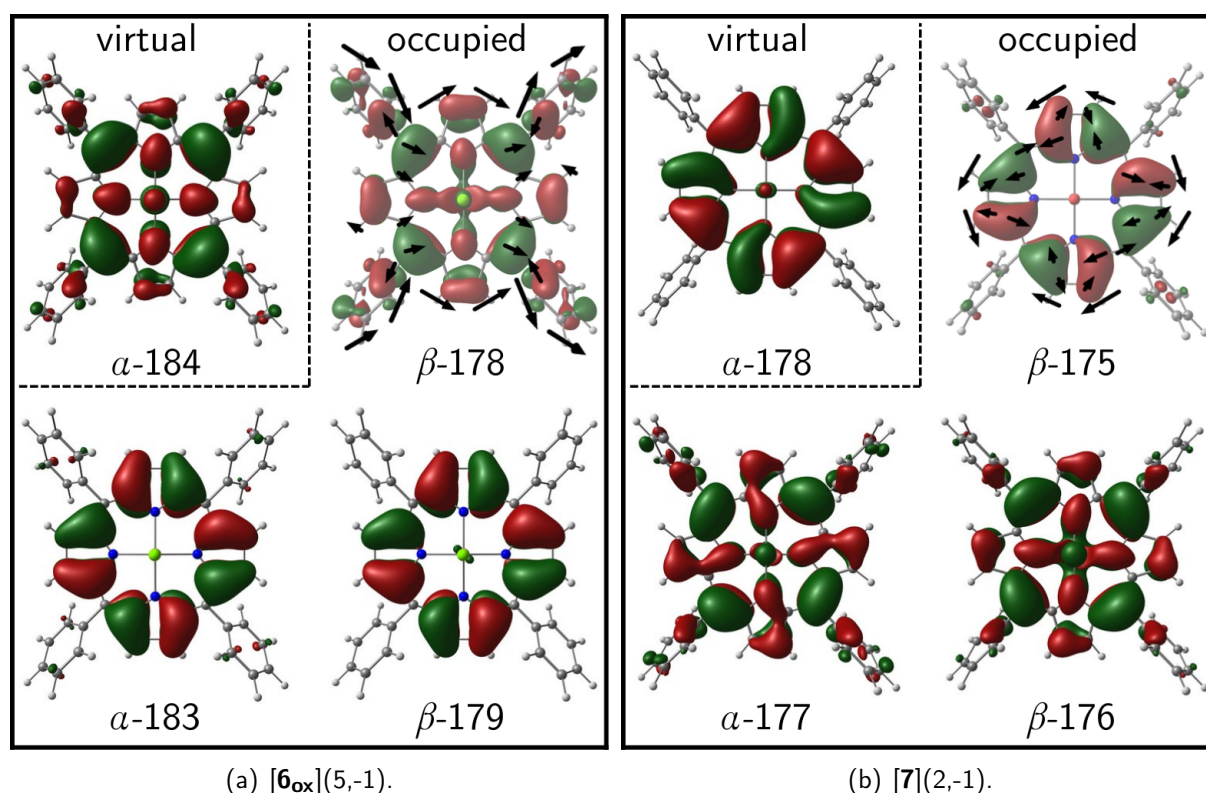


Figure 27: Ball-and-stick models of (a) $[\mathbf{6}_{\text{ox}}](5,-1)$ and (b) $[\mathbf{7}](2,-1)$ and isosurface plots of their lowest unoccupied and three highest occupied molecular spin orbitals, calculated via DFT. The labels specify the spin functions and the numbers of the orbitals (within a spin subset). The black arrows drawn on top of the SOMO show the displacement vectors of the normal mode having an unusually high absorption strength. Isovalues: ± 0.02 . Atomic color coding: H - white, C - gray, N - blue, O - red, Cl - green, Fe - brown.

Keeping this argument in mind, the species responsible for all observed transient absorptions must belong to the primary photoproducts. Yet, none of the three complexes ([1], [2], and [3_{red}]) exhibits such absorption bands, according to the theoretical predictions shown in Fig-

ures 23-25, neither in their electronic ground state nor in the lowest $d(\text{Fe}) \rightarrow d(\text{Fe})$ states of other spin multiplicities. Therefore, it has to be concluded that a higher-lying excited state is the origin of those signals. The presence of a long-lived excited state of [1] has already been confirmed in section 5.2.1. Regarding [3_{red}] and [2], it has not been evidenced yet whether they are formed directly in their electronic ground state or if they populated intermediately an excited state, too. For instance, it is entirely conceivable that [2] is formed in a low-lying, excited π -radical ($\text{por} \rightarrow \text{Fe}$ CT) state, reminiscent of the ground state of [7] and, hence, likely absorbing around 1350 cm^{-1} , before it relaxes to its ground state. In particular, this hypothesis seems justified because of the previous studies, which pointed to [7] undergoing a similar conversion during its photolytic formation (despite the energetic order of the π -radical and closed-shell ligand states is inverted there). Following this idea, the second signal, centered at 1282 cm^{-1} , would need to be assigned to a $\text{por} \rightarrow \text{Fe}$ CT state of either [1], [3_{red}], or both, which can be expected to absorb strongly at this frequency since they represent 'normal' π -radicals of low-valent metal centers.

Still, there are two arguments contradicting this hypothesis. First, complementary pump-probe experiments of the chlorido complex [6] yield a product spectrum (Figure A10), showing two spectral features almost identical to those obtained after photoexcitation of [1] (see Figure 21). As [6] is incapable of generating a high-valent iron complex comparable to [7] in a direct, unimolecular reaction upon photoexcitation, the band at 1344 cm^{-1} cannot be explained by the presence of such a complex in that case. Second, all efforts to identify energetically low-lying $\text{por} \rightarrow \text{Fe}$ CT states of [1], [2], or [3_{red}], potentially suited to cause those absorptions, by means of computational chemistry remained unsuccessful (see section 8.5 for details). In all three complexes and different spin multiplicities, $\text{por} \rightarrow \text{Fe}$ CT states are high in energy, as summarized in Table A9, and can be assumed to have rather short lifetimes. In this context, it shall be reminded that the lowest LMCT of [1], earlier proposed to contribute to its relaxation pathway,^[369,377] cannot have a lifetime of more than 200 fs, as discussed in section 5.2. In the cases of [1] and [3_{red}], the reason for the high energy of these states is the low oxidation state of their iron atoms (see section 2.2.3). Regarding [2], a delocalization of the unpaired electrons over the nitrido ligand was previously found to be very efficient^[108,297] and, hence, favored over π -radical formation. Also, it is noteworthy that the majority of π -radical complexes reported in the literature bears a total positive charge,^[247,274,285,286,290,293,331,332,408,409] as opposed to [1] and its two photoproducts. While the total charge has not been considered as relevant parameter on this matter so far, it can be surmised that it affects the stability of π -radical configurations as well.

To sum up, although experimental and/or DFT-predicted spectra of π -radical metalloporphyrins match either of the two observed signals at 1282 cm^{-1} and 1344 cm^{-1} , complexes having such electron configurations are found to be an inappropriate explanation for the occurrence of these bands.

5.3.6 Quantum Chemical Calculations & Interpretation – Part 2: Triplet Porphyrin States

Despite π -radicals are unlikely to be the reason for the strong signals in the experimental product spectrum, the idea of an amplification of absorption strength of certain vibrational modes by the presence of unpaired electrons at the porphyrin ligand appears to be conclusive. Other configurations fulfilling this criterion are porphyrin-centered triplet states. These state have been proven experimentally to be surprisingly long-lived intermediates in the photochemistry of various metalloporphyrins, living for up to milliseconds.^[301,362,364,365,367] Although they are comparably short-lived if the metal center is an iron atom,^[366] lifetimes of at least several nanoseconds seem plausible even in those cases.

Furthermore, in contrast to the π -radical porphyrin configurations, triplet porphyrin configurations can be optimized by (ground state!) DFT and represent local energy minima, despite being located in an energetically high range between 10000 cm⁻¹ and 23000 cm⁻¹ above the respective global minimum (cf. Table A8). Details of these calculations are given in section 8.5 in the appendix. In brief, there are seventeen distinct system (molecular structure + electron configuration) relevant to this evaluation. They arise from the possibility of the iron centers in each of the considered complexes, [1], [2], and [3_{red}], adopting either a low-, intermediate-, or high-spin configuration, which can couple either ferro- or antiferromagnetically with the unpaired electrons of the triplet porphyrindiido ligand (except for the low-spin iron(+II) d⁶-configuration in [3_{red}], which is a local singlet). The optimization of those high-energy structures is challenging due to their very poor convergence behavior. In total, eleven of those seventeen systems could be converged successfully in this work.

Notwithstanding this, it might seem surprising that triplet porphyrin states have long lifetimes and can be computationally optimized by ground state DFT, in stark contrast to π -radical porphyrin states, although both types of configurations are similarly high in energy. The reason for this differences lies presumably in their equilibrium geometries. A consideration of the molecular structures of the calculated complexes (cf. Figure A15) reveals that 'normal' π -radicals (with non-degenerated a_{2u}- and a_{1u}-orbital) are only slightly distorted compared to complexes with closed-shell tpp²⁻-ligands. In contrast, complexes with a triplet porphyrin configuration show a pronounced change of their structural parameters, also involving a reduction of their symmetry. These variations are a consequence of a Jahn-Teller distortion, enforced by the occupation of one of the degenerated e_g-orbitals. Apparently, the closed-shell porphyrin configuration is raised above the triplet configuration in this highly distorted geometry. A conversion from the local minimum structure of the triplet porphyrin state to the global minimum is presumably impeded by an energetic barrier. As opposed to that, the π -radical porphyrin configurations represent excited states even at their own equilibrium geometry because this geometry is rather similar to that of the closed-shell porphyrin state and does not increase the energy of the latter sufficiently.

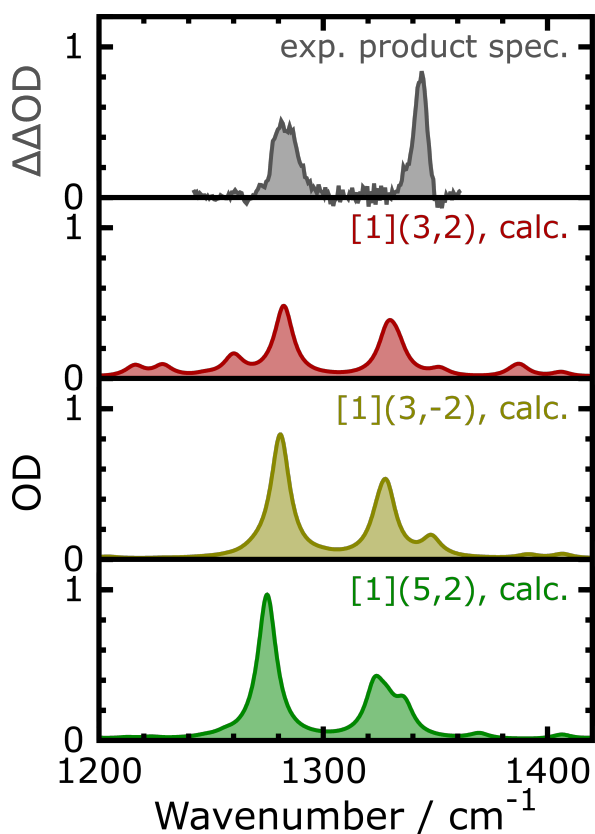


Figure 28: Upper panel: mIR product spectrum of the photolysis of **[1]** with 16 μJ , 400 nm-pump pulses in room-temperature DCM/DCM- d_2 solution, averaged over delays from 150 ps to 3.5 ns. Other panels: DFT-predicted IR absorption spectra of **[1](3,2)** (red), **[1](3,-2)** (yellow), and **[1](5,2)** (green), obtained by convolution of the stick spectra with a Lorentzian function ($\text{FWHM} = 10 \text{ cm}^{-1}$). In all panels, an optical density of one is equivalent to an estimated extinction coefficient of $3000 \text{ M}^{-1} \text{ cm}^{-1}$.

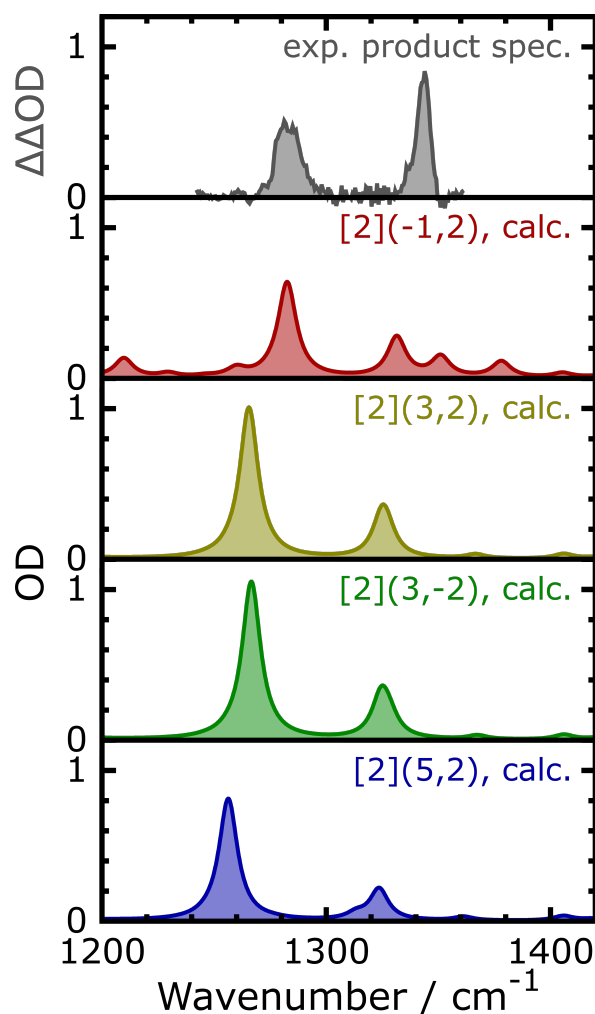


Figure 29: Upper panel: mIR product spectrum of the photolysis of **[1]** with 16 μJ , 400 nm-pump pulses in room-temperature DCM/DCM- d_2 solution, averaged over delays from 150 ps to 3.5 ns. Other panels: DFT-predicted IR absorption spectra of **[2](-1,2)** (red), **[2](3,2)** (yellow), **[2](3,-2)** (green), and **[2](5,2)** (blue), obtained by convolution of the stick spectra with a Lorentzian function ($\text{FWHM} = 10 \text{ cm}^{-1}$). In all panels, an optical density of one is equivalent to an estimated extinction coefficient of $3000 \text{ M}^{-1} \text{ cm}^{-1}$.

The success of some calculations of triplet porphyrin complexes allows a comparison of their DFT-predicted IR absorption spectra with the experimental product spectrum. Figures 28, 29, and 30 display the computed spectra of the converged triplet porphyrin states of **[1]**, **[2]**, and **[3_{red}]**, respectively. As it becomes apparent, all of those systems exhibit each a pronounced

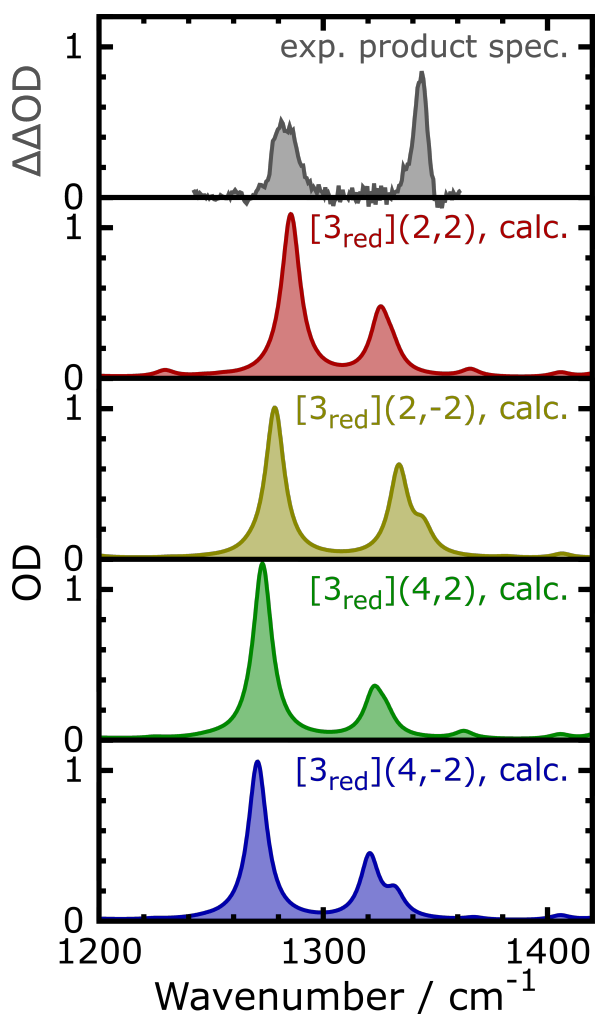


Figure 30: Upper panel: mIR product spectrum of the photolysis of **[1]** with 16 μJ , 400 nm-pump pulses in room-temperature DCM/DCM- d_2 solution, averaged over delays from 150 ps to 3.5 ns. Other panels: DFT-predicted IR absorption spectra of $[\mathbf{3}_{\text{red}}](n, \pm 2)$ ($n = 2, 4$), as specified by the labels, obtained by convolution of the stick spectra with a Lorentzian function (FWHM = 10 cm^{-1}). In all panels, an optical density of one is equivalent to an estimated extinction coefficient of 3000 $\text{M}^{-1} \text{cm}^{-1}$.

absorption band in the ranges from 1255 cm^{-1} to 1285 cm^{-1} and from 1320 cm^{-1} to 1350 cm^{-1} , independently of the oxidation and spin state of the metal center and the presence and nature of an axial ligand. Moreover, the theoretical spectra reflect qualitatively the large, estimated extinction coefficients of the experimental spectrum. The rough agreement supports the assumption made in that estimation, that only one of the three product species is responsible for the permanent absorptions. Still, the predicted absorption strengths deviate quantitatively from the measured ones, as the relative magnitudes of the two absorption bands are opposed there. Experimentally, the ratio of the absorption strengths, $\alpha_a(1344 \text{ cm}^{-1} \text{ band})/\alpha_a(1280 \text{ cm}^{-1} \text{ band})$, amounts to 1.25, whereas this quantity ranges from 0.31 to 0.87 in the theoretical results.

Despite this mismatch, the computed spectra and the experimental product spectrum are overall in good agreement. This finding and the previously reported long lifetimes of complexes having triplet porphyrin ligands highly suggest such a species to be the origin of the two absorption bands peaking at 1282 cm^{-1} and 1344 cm^{-1} . Combined with the information that an excited state of the parent complex, $[\mathbf{1}]^*$, is present during the same time frame (deduced from the additional, transient $\nu_{\text{as}}(\text{N}_3)$ absorption band at 2045 cm^{-1} , cf. section 5.2.1), it has to be concluded that **[1]** populates intermediately an a_{2u} -type triplet porphyrin state after TPA, although its exact electron configuration cannot be identified at this point. Moreover, because the two low-frequency bands of all considered triplet porphyrin states of **[1]**, **[2]**, and $[\mathbf{3}_{\text{red}}]$ are very akin, it appears

justified to suspect these two spectral features to be characteristic marker bands of the a_{2u} -type triplet porphyrin configuration. Yet, this proposal requires further verification by future investigations. As a downside of the consistency of the predicted spectra of all three complexes and due to the rather poor accuracy of the predicted absorption strengths, it is unfeasible to determine whether triplet porphyrin states of [2] and [3_{red}] contribute to the signals at 1280 cm^{-1} and 1344 cm^{-1} , too. Hence, it cannot be verified whether the two product complexes are formed directly in their respective electronic ground state or if they populate an excited state in the first few nanoseconds after their generation.

Finally, the underlying normal modes responsible for the remarkably strong signals in the calculated spectra and whether they are in line with the theory of Hu and Spiro^[286] shall be discussed briefly. Since both, the porphyrin-centered SOMOs and the relevant normal modes are similar in all calculated systems, they will be considered explicitly only for the exemplary complex [3_{red}](2,2) here. The displacement vectors of the strongly absorbing vibrations and isosurface plots of the SOMOs of this system are illustrated in Figure 31. As expected, the two SOMOs of the tpp^{2-} -ligand show the typical shapes of an a_{2u} - and an $e_{g,x}$ -orbital. Regarding the vibrational modes, there is a single one responsible for the band centered around 1280 cm^{-1} , whereas there are two modes contributing to the band centered at about 1340 cm^{-1} . In essence, these latter two normal modes are the $\nu_{41}(\text{por})$ vibrations in x - and y -direction, whose degeneracy is lifted as a result of the distorted molecular geometry. Hu and Spiro suggested the resonance bands of these vibrational modes to be frequency down-shifted to ca. 1280 cm^{-1} in π -radical porphyrin complexes. As opposed to that, the theoretical calculations done here predict them to absorb at ca. 1340 cm^{-1} , i.e. at roughly the same wavenumber as in the closed-shell porphyrin state. It remains unclear at this point whether this discrepancy is due to the spectral shift being exclusive to π -radical porphyrin configurations (but absent in the triplet porphyrin configurations considered here), or due to the normal mode assignment in either ref. [286] or this work being erroneous. In the case of the triplet porphyrin states of [1], there is an additional, third contribution from the $\nu_5(\text{N}_3)$ vibration to the band at ca. 1340 cm^{-1} . The absorption strength of this vibration is nearly unaltered compared to the closed-shell porphyrin complexes and similarly large as each of those of the two $\nu_{41}(\text{por})$ vibrations in the triplet porphyrin complexes.

The band at ca. 1280 cm^{-1} originates from the E_u -symmetric combination of the antisymmetric pyrrole half-ring stretching modes ($\nu_{44}(\text{por})$). This mode absorbs only poorly and at a frequency of about 1000 cm^{-1} in complexes with closed-shell tpp^{2-} -ligands. Interestingly, only the vibration with displacement vectors in x -direction is predicted to give rise to the pronounced absorption band. As opposed to that, the vibration in y -direction remains weakly IR-active and is frequency up-shifted only to $1160\text{--}1210\text{ cm}^{-1}$ upon triplet porphyrin formation. As demonstrated in Figure 31, the normal modes $\nu_{44}(\text{por})_x$, $\nu_{41}(\text{por})_x$, and $\nu_{41}(\text{por})_y$ follow the proposal made in ref. [286], that normal modes with displacement vectors perpendicular to the nodal planes of the SOMOs are amplified in absorption strength. In particular, many of the atomic displacement vectors of the $\nu_{44}(\text{por})_x$ mode intersect the nodal planes of the a_{2u} -

and the $e_{g,x}$ -orbital under large angles. In the cases of the $\nu_{41}(\text{por})$ vibrations, this condition is still mostly fulfilled, yet the angles of intersection are on average smaller. According to Hu's model, this suggests lower absorption strengths for these modes compared to the $\nu_{44}(\text{por})_x$ mode, which is in fact experimentally observed. However, judging by the same model but in contrast to the computed results, the absorption strength of the $\nu_{44}(\text{por})_y$ should be increased significantly as well, because its displacement vectors are likewise oriented almost perpendicular to the SOMO's nodal planes (cf. Figure A16). This mismatch might hint towards the alternative explanation, that geometric factors, i.e. the distortions inflicted by triplet or π -radical porphyrin configurations, are pivotal for the rise of vibrational absorption strength,^[329] rather than the electronic structure itself (see also section 2.2.4). Hence, it has to be emphasized again, that the reason for the increased absorption strength in metalloporphyrins having certain electron configurations is not fully understood yet.

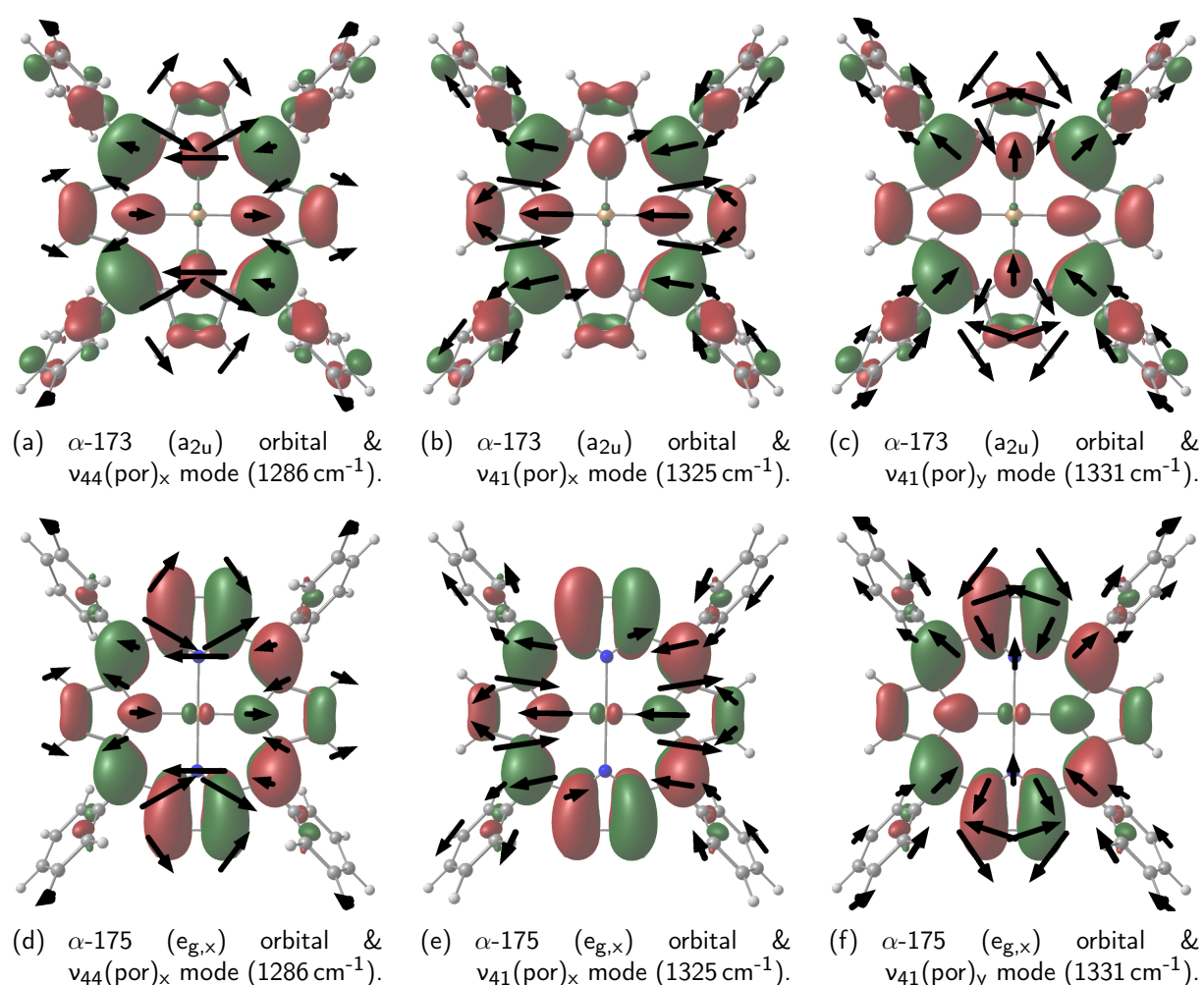


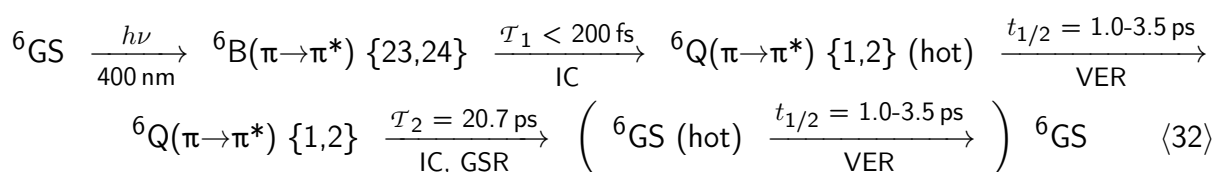
Figure 31: Ball-and-stick models of $[\mathbf{3}_{\text{red}}](2,2)$, isosurface plots of its porphyrin-centered SOMOs, and displacement vectors of the normal modes having unusually high absorption strengths (black arrows), calculated via DFT. The subtitles specify the spin functions, the numbers of the orbitals (within a α -spin subset), and their assignments according to the Gouterman model as well as the assignments of the normal modes (according to ref. [322]) and their computed resonance frequencies. Isovalues: ± 0.02 . Atomic color coding: H - white, C - gray, N - blue, Fe - brown.

6 Summary and Outlook

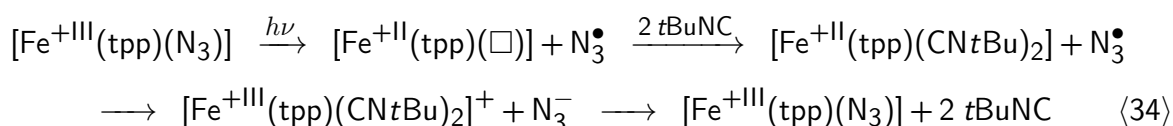
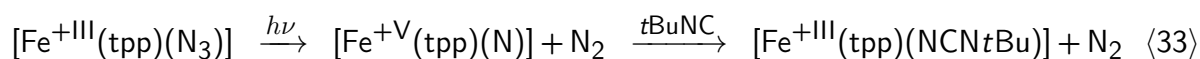
In summary, the photolysis of the archetypal model complex azido(5,10,15,20-tetraphenylporphyrin-21,23-diido)iron(+III) ($[\text{Fe}^{\text{III}}(\text{tpp})(\text{N}_3)]$, **[1]**) was investigated in liquid, room-temperature DCM (DCM-d_2) solution in this work. In earlier studies, complex **[1]** has already been employed as precursor of the high-valent nitrido complex $[\text{Fe}^{\text{V}}(\text{tpp})(\text{N})]$ (**[2]**),^[104,105,108] reminiscent of the reactive intermediate in the catalytic cycles of many oxidative metalloenzymes, Compound I, but only by means of matrix isolation techniques. In contrast, examinations in liquid solution have previously been impeded by the low stability of the photoproducts. Here, a conjunction of (ultra-)fast time-resolved infrared and visible spectroscopy, chemical quenching reactions and calculations based on density functional theory allowed, for the first time, a systematic exploration of the processes following the photoexcitation of **[1]** and the occurring intermediates.

Complex **[1]** is found to be remarkably photostable, as significant photoconversion is observed only under usage of pump pulses of high energies. In detail, the primary quantum yield scales proportionally with the pulse energy, giving evidence that the reactive channel is available exclusively after two-photon absorption. Single-photon absorption, on the other hand, results in a complete ground state recovery. Moreover, excitation wavelengths of 400 nm and below allow a decomposition by an order of magnitude more efficient than 510 nm excitation.

The relaxation mechanism of **[1]** after single-photon excitation can be outlined as shown in Equation (32) (numbers in curly brackets represent the underlying roots from a TD-DFT calculation, see also Figure 18) and described in the following: First, **[1]** is converted from the initially excited state, e.g. the porphyrin-centered ${}^6\text{B}(\pi \rightarrow \pi^*)$ state after 400 nm excitation, to one of the lowest two excited sextet states, a degenerated pair of dark, low-energy, porphyrin-centered ${}^6\text{Q}(\pi \rightarrow \pi^*)$ states, within less than 200 fs (\mathcal{T}_1). Whether this conversion is direct or proceeds via intermediate population of interjacent electronic states, for instance a porphyrin-to-iron charge transfer state, could not be determined here. Next, the complex undergoes a vibrational energy relaxation within a few picoseconds (half-life period $t_{1/2} = 1.0\text{-}3.5$ ps) while in the ${}^6\text{Q}(\pi \rightarrow \pi^*)$ state. Finally, it returns to its electronic ground state with a time constant of $\mathcal{T}_2 = 20.7 \pm 0.3$ ps. Alternative assignments of the last process to a vibrational relaxation on the potential energy surface of the ground state or the decay of the lowest $d(\text{Fe}) \rightarrow d(\text{Fe})$ quartet state, as suggested for the analogous chlorido complex $[\text{Fe}^{\text{III}}(\text{tpp})(\text{Cl})]$ (**[6]**) in earlier studies,^[369,377] are rejected here. These proposals could not be brought in line with the kinetics observed in this work or the results of TD-DFT calculations, respectively. Despite that, another VER on the ground state surface is likely, but proceeds presumably with a similar rate as in the ${}^6\text{Q}(\pi \rightarrow \pi^*)$ state.



The excitation of [1] with high-energy pulses yields primarily three product species, an excited state of the parent complex ([1]*), the nitrido complex [2] via photooxidative cleavage of N₂, and the iron(+II) complex [Fe^{+II}(tpp)(□)] ([3_{red}]) via photoreductive release of N₃[•]. These three species are generated in roughly equal amounts, only slightly dependent on the excitation wavelength. The formation of [2] is verified by addition of *t*BuNC, resulting in a reaction to the carbodiimido complex [Fe^{+III}(tpp)(NCN*t*Bu)] ([4], cf. Equation (33)), and detection of the characteristic IR absorption of the NCN-antisymmetric stretching vibration at 2121 cm⁻¹. In addition, the diisonitrilo complex [Fe^{+III}(tpp)(CN*t*Bu)₂]⁺ ([5], ν_{as}(C≡N) = 2200 cm⁻¹) and N₃⁻ anions are generated in this experiment, which replenish the reactants on the timescale of seconds (*k_v* = (2.03 ± 0.35) · 10⁴ M⁻¹ s⁻¹). The formation of these species is attributed to a complexation of [3_{red}] by two *t*BuNC molecules, followed by a one-electron transfer to an azidyl radical (cf. Equation (34)). A more direct evidence and quantification of the photoreductive pathway is achieved by quenching of the byproduct, N₃[•], with large excesses (100:1 w.r.t. [1]) of iodide to N₃⁻.



Furthermore, two pronounced, permanent transient absorptions are detected at 1344 cm⁻¹ and 1282 cm⁻¹. By comparison with DFT-predicted spectra obtained from ground state calculations of various complexes having different electron configurations, these signals are assigned to a complex bearing a porphyrindiido ligand in a local triplet state, rather than a π-radical metalloporphyrin. The additional occurrence of a ν_{as}(N₃) resonance band at 2045 cm⁻¹ suggests the excited state of the parent complex mentioned above, [1]*, to be the origin of these absorption bands.

Despite this work has delivered many valuable results, it leaves some questions unanswered and raises further issues, whose disclosure requires additional investigations:

- ◆ In this work, many bimolecular reactions have been proposed to explain the results of the rapid-scan and stationary IR difference spectra, but not directly observed because they take place on timescales not covered by the applied techniques. This included:
 - 1) The formation of the dinuclear, μ-N bridged complex [8] out of [2] and [1].
 - 2) The quenching of N₃[•] to N₃⁻ by iodide.
 - 3) The quenching of [2] to the carbodiimido complex [4] by *t*BuNC.
 - 4) The conversion of [3_{red}], N₃[•] and *t*BuNC to the diisonitrilo complex [5] and N₃⁻.
 - 5) The return of the triplet porphyrindiido complexes to their electronic ground state.
 Solid evidence of these processes, determination of their rates and discovery of their mechanisms requires complementary examinations by means of transient spectroscopy on the timescales of nano- to microseconds.

- ◆ While the relaxation mechanism of [1] after single-photon absorption has been discussed thoroughly, the primary events following two-photon excitation, yielding ultimately all photoproducts, remained widely undisclosed. The only information in this regard obtained here is the decay of a transient absorption located at 1312 cm^{-1} with $\tau_3 \approx 10\text{ ps}$ and the rise of the transient absorption at 1282 cm^{-1} with $\tau_4 \approx 27\text{ ps}$. Both time constants deviate significantly from those observed after SPA.
- ◆ The exact electron configuration of the complex [1]*, carrying a triplet porphyrindiido ligand, including the spin state of the iron center and its spin coupling to the ligand, could not be determined here. Moreover, it remains unclear whether triplet porphyrin states of the complexes [3_{red}] and [2] are formed as well and contribute to the signals at 1282 cm^{-1} and 1344 cm^{-1} . In this context, complex [1] appears to be a rather inconvenient model system to elucidate the properties of triplet porphyrindiido complexes, due to its multifarious photoreactivity and the variety of possible spin states of iron cations. Hence, future studies on such electronic states should focus (at least for the near term) on complexes showing a simpler electronic structure and photochemistry, for instance [Zn(tp)] and [Mg(tp)].

Research efforts on all of these topics will highly benefit from the results of this work, in which substantial parts of photochemistry of [1] have already been discovered and important correlations between the electronic structures and the IR absorption spectra of metalloporphyrins have been pointed out.

7 Bibliography

- [1] R. Zhang, S. Klaine, C. Alcantar, F. Bratcher, *J. Inorg. Biochem.* 2020, 212, 111246.
- [2] A. R. McDonald, L. Que Jr., *Coord. Chem. Rev.* 2013, 257, 414–428.
- [3] R. A. Eikey, M. M. Abu-Omar, *Coord. Chem. Rev.* 2003, 243, 83–124.
- [4] J. Hohenberger, K. Ray, K. Meyer, *Nat. Commun.* 2012, 3, 720–732.
- [5] S. P. de Visser, J.-U. Rohde, Y.-M. Lee, J. Cho, W. Nam, *Coord. Chem. Rev.* 2013, 257, 381–393.
- [6] A. Gunay, K. H. Theopold, *Chem. Rev.* 2010, 110, 1060–1081.
- [7] J. M. Smith, D. Subedi, *Dalton Trans.* 2012, 41, 1423–1429.
- [8] K. Nakamoto, *J. Mol. Struct.* 1997, 408–409, 11–16.
- [9] C. T. Saouma, J. C. Peters, *Coord. Chem. Rev.* 2011, 255, 920–937.
- [10] K. Dehnicke, J. Strähle, *Angew. Chem. Int. Ed. Engl.* 1981, 20, 413–426.
- [11] K. Dehnicke, J. Strähle, *Angew. Chem. Int. Ed. Engl.* 1992, 31, 955–978.
- [12] Y. Watanabe, H. Fujii in *Metal-Oxo and Metal-Peroxo Species in Catalytic Oxidations*, (Ed.: B. Meunier), Springer, Berlin, Heidelberg, 2000, pp. 61–89.
- [13] J. F. Berry, *Comments Inorg. Chem.* 2009, 30, 28–66.
- [14] W. P. Griffith, *Coord. Chem. Rev.* 1970, 5, 459–517.
- [15] W. P. Griffith, *Coord. Chem. Rev.* 1972, 8, 369–396.
- [16] J. F. Berry, S. DeBeer George, F. Neese, *Phys. Chem. Chem. Phys.* 2008, 10, 4361–4374.
- [17] J. R. Winkler, H. B. Gray in *Molecular Electronic Structures of Trans. Metal Complexes I, Structure & Bonding*, (Eds.: D. M. P. Mingos, P. Day, J. P. Dahl), Springer, Berlin, Heidelberg, 2012, pp. 17–28.
- [18] D. J. Ferraro, L. Gakhar, S. Ramaswamy, *Biochem. Biophys. Res. Commun.* 2005, 338, 175–190.
- [19] M. Costas, K. Chen, L. Que Jr., *Coord. Chem. Rev.* 2000, 200–202, 517–544.
- [20] M. Costas, M. P. Mehn, M. P. Jensen, L. Que Jr., *Chem. Rev.* 2004, 104, 939–986.
- [21] M. Sono, M. P. Roach, E. D. Coulter, J. H. Dawson, *Chem. Rev.* 1996, 96, 2841–2887.
- [22] L. Que Jr., W. B. Tolman, *Nature* 2008, 455, 333–340.
- [23] E. Torres, M. Ayala in *Comprehensive Inorganic Chemistry II (Second Edition)*, Vol. 6, (Eds.: J. Reedijk, K. Poeppelemeier), Elsevier, Amsterdam, 2013, Chapter 6.24, pp. 685–735.
- [24] M. M. Martin, *Industrial Chemical Process Analysis and Design*, Elsevier, Boston, 2016.
- [25] J. A. Moulijn, M. Makkee, A. E. van Diepen, *Chemical Process Technology*, Vol. 2, Wiley, 2013.
- [26] P. R. O. de Montellano, *Cytochrome P450: Structure, Mechanism, and Biochemistry*, 4th ed., Springer, New York, 2015.
- [27] E. G. Hrycaj, S. M. Bandiera, *Arch. Biochem. Biophys.* 2012, 522, 71–89.
- [28] I. G. Denisov, T. M. Makris, S. G. Sligar, I. Schlichting, *Chem. Rev.* 2005, 105, 2253–2277.
- [29] B. Meunier, S. P. de Visser, S. Shaik, *Chem. Rev.* 2004, 104, 3947–3980.
- [30] I. Schlichting, J. Berendzen, K. Chu, A. M. Stock, S. A. Maves, D. E. Benson, R. M. Sweet, D. Ringe, G. A. Petsko, S. G. Sligar, *Science* 2000, 287, 1615–1622.
- [31] W. Nam in *Comprehensive Coordination Chemistry II*, (Eds.: J. A. McCleverty, T. J. Meyer), Pergamon, Oxford, 2003, pp. 281–307.
- [32] S. N. Dhuri, S. S. Harmalkar in *Advances in Biological Science Research*, (Eds.: S. N. Meena, M. M. Naik), Academic Press, 2019, pp. 363–380.
- [33] T. M. Makris, K. v. Koenig, I. Schlichting, S. G. Sligar, *J. Inorg. Biochem.* 2006, 100, 507–518.
- [34] H. Fujii, K. Ichikawa, *Inorg. Chem.* 1992, 31, 1110–1112.
- [35] H. Fujii, *J. Am. Chem. Soc.* 1993, 115, 4641–4648.
- [36] H. Fujii, T. Yoshimura, H. Kamada, *Inorg. Chem.* 1997, 36, 6142–6143.
- [37] H. Fujii, *Coord. Chem. Rev.* 2002, 226, 51–60.
- [38] Z. Cong, T. Kurahashi, H. Fujii, *Angew. Chem. Int. Ed.* 2011, 50, 9935–9939; *Angew. Chem.* 2011, 123, 10109–10113.
- [39] T. Murakami, K. Yamaguchi, Y. Watanabe, I. Morishima, *Bull. Chem. Soc. Jpn.* 1998, 71, 1343–1353.
- [40] H. Fujii, T. Yoshimura, H. Kamada, *Inorg. Chem.* 1996, 35, 2373–2377.
- [41] J. T. Groves, Y. Watanabe, *J. Am. Chem. Soc.* 1988, 110, 8443–8452.
- [42] A. Gold, K. Jayaraj, P. Doppelt, R. Weiss, G. Chottard, E. Bill, X. Ding, A. X. Trautwein, *J. Am. Chem. Soc.* 1988, 110, 5756–5761.
- [43] D. Mandon, R. Weiss, K. Jayaraj, A. Gold, J. Turner, E. Bill, A. X. Trautwein, *Inorg. Chem.* 1992, 31, 4404–4409.
- [44] E. Bill, X.-Q. Ding, E. L. Bominaar, A. X. Trautwein, H. Winkler, D. Mandon, R. Weiss, A. Gold, K. Jayaraj, W. E. Hatfield, M. L. Kirk, *Eur. J. Biochem.* 1990, 188, 665–672.
- [45] D. Dolphin, *Isr. J. Chem.* 1981, 21, 67–71.
- [46] J. Rittle, M. T. Green, *Science* 2010, 330, 933–937.
- [47] T. H. Yosca, M. T. Green, *Isr. J. Chem.* 2016, 56, 834–840.
- [48] T. Egawa, H. Shimada, Y. Ishimura, *Biochem. Biophys. Res. Commun.* 1994, 201, 1464–1469.
- [49] Y. Watanabe, *J. Biol. Inorg. Chem.* 2001, 6, 846–856.
- [50] R. Weiss, V. Bulach, A. Gold, J. Turner, A. X. Trautwein, *J. Biol. Inorg. Chem.* 2001, 6, 831–845.
- [51] H. Chen, J. Song, W. Lai, W. Wu, S. Shaik, *J. Chem. Theory Comput.* 2010, 6, 940–953.
- [52] L. K. Hanson, C. K. Chang, M. S. Davis, J. Fajer, *J. Am. Chem. Soc.* 1981, 103, 663–670.
- [53] S. Shaik, D. Kumar, S. P. de Visser, A. Altun, W. Thiel, *Chem. Rev.* 2005, 105, 2279–2328.
- [54] D. Dolphin, A. Forman, D. C. Borg, J. Fajer, R. H. Felton, *Proc. Natl. Acad. Sci. U.S.A.* 1971, 68, 614–618.
- [55] A. Wolberg, J. Manassen, *J. Am. Chem. Soc.* 1970, 92, 2982–2991.

- [56] H. Isobe, K. Yamaguchi, M. Okumura, J. Shimada, *J. Phys. Chem. B* 2012, *116*, 4713–4730.
- [57] T.-H. Chen, N. Asiri, K. W. Kwong, J. Malone, R. Zhang, *Chem. Commun.* 2015, *51*, 9949–9952.
- [58] M. Radoń, E. Broclawik, K. Pierloot, *J. Chem. Theory Comput.* 2011, *7*, 898–908.
- [59] K. W. Kwong, D. Patel, J. Malone, N. F. Lee, B. Kash, R. Zhang, *New J. Chem.* 2017, *41*, 14334–14341.
- [60] Z. Pan, Q. Wang, X. Sheng, J. H. Horner, M. Newcomb, *J. Am. Chem. Soc.* 2009, *131*, 2621–2628.
- [61] M. Newcomb, R. E. P. Chandrasena, *Biochem. Biophys. Res. Commun.* 2005, *338*, 394–403.
- [62] M. Newcomb, R. Zhang, Z. Pan, D. N. Harischandra, R. E. P. Chandrasena, J. H. Horner, E. Martinez II, *Catal. Today* 2006, *117*, 98–104.
- [63] Z. Pan, R. Zhang, M. Newcomb, *J. Inorg. Biochem.* 2006, *100*, 524–532.
- [64] Z. Pan, R. Zhang, L. W.-M. Fung, M. Newcomb, *Inorg. Chem.* 2007, *46*, 1517–1519.
- [65] X. Sheng, J. H. Horner, M. Newcomb, *J. Am. Chem. Soc.* 2008, *130*, 13310–13320.
- [66] M. J. Merrick, R. A. Edwards, *Microbiol. Rev.* 1995, *59*, 604–622.
- [67] N. V. Bhagavan, C.-E. Ha, *Essentials of Medical Biochemistry*, 2nd ed., Academic Press, San Diego, 2015, pp. 227–268.
- [68] R. Dixon, D. Kahn, *Nat. Rev. Microbiol.* 2004, *2*, 621–631.
- [69] R. Bjornsson, F. Neese, R. R. Schrock, O. Einsle, S. DeBeer, *J. Biol. Inorg. Chem.* 2015, *20*, 447–460.
- [70] D. C. Rees, F. A. Tezcan, C. A. Haynes, M. Y. Walton, S. Andrade, O. Einsle, J. B. Howard, *Philos. Trans. R. Soc. A* 2005, *363*, 971–984.
- [71] B. M. Hoffman, D. Lukoyanov, Z.-Y. Yang, D. R. Dean, L. C. Seefeldt, *Chem. Rev.* 2014, *114*, 4041–4062.
- [72] J. C. Peters, M. P. Mehn in *Activation of Small Molecules: Organometallic and Bioinorganic Perspectives*, (Ed.: W. B. Tolman), Wiley-VCH, Weinheim, 2006, Chapter 3, pp. 81–119.
- [73] J. L. Crossland, D. R. Tyler, *Coord. Chem. Rev.* 2010, *254*, 1883–1894.
- [74] C. Smith, A. K. Hill, L. Torrente-Murciano, *Energy Environ. Sci.* 2020, *13*, 331–344.
- [75] L. E. Apodaca, *NITROGEN (FIXED)—AMMONIA*, U. S. Geological Survey, 2023, <https://www.usgs.gov/centers/national-minerals-information-center/nitrogen-statistics-and-information>.
- [76] T. Kandemir, M. E. Schuster, A. Senyshyn, M. Behrens, R. Schlögl, *Angew. Chem. Int. Ed.* 2013, *52*, 12723–12726; *Angew. Chem.* 2013, *125*, 12955–12959.
- [77] J. Qian, Q. An, A. Fortunelli, R. J. Nielsen, W. A. Goddard III, *J. Am. Chem. Soc.* 2018, *140*, 6288–6297.
- [78] *Nitrogen Fixation, Topics in Organometallic Chemistry, Vol. 60*, (Ed.: Y. Nishibayashi), Springer Nature, Cham, 2017.
- [79] P. Müller, C. Fruit, *Chem. Rev.* 2003, *103*, 2905–2919.
- [80] K. Arashiba, Y. Miyake, Y. Nishibayashi, *Nat. Chem.* 2011, *3*, 120–125.
- [81] J. M. Smith in *Progress in Inorganic Chemistry, Vol. 58*, (Ed.: K. D. Karlin), WILEY, Hoboken, 2014, pp. 417–470.
- [82] J. S. Figueroa, N. A. Piro, C. R. Clough, C. C. Cummins, *J. Am. Chem. Soc.* 2006, *128*, 940–950.
- [83] B. A. MacKay, M. D. Fryzuk, *Chem. Rev.* 2004, *104*, 385–401.
- [84] C. E. Laplaza, C. C. Cummins, *Science* 1995, *268*, 861–863.
- [85] B. Askevold, J. T. Nieto, S. Tussupbayev, M. Diefenbach, E. Herdtweck, M. C. Holthausen, S. Schneider, *Nat. Chem.* 2011, *3*, 532–537.
- [86] J. J. Scepaniak, J. A. Young, R. P. Bontchev, J. M. Smith, *Angew. Chem. Int. Ed.* 2009, *48*, 3158–3160; *Angew. Chem.* 2009, *121*, 3204–3206.
- [87] D. V. Yandulov, R. R. Schrock, *Science* 2003, *301*, 76–78.
- [88] D. V. Yandulov, R. R. Schrock, *Inorg. Chem.* 2005, *44*, 1103–1117.
- [89] J. Strähle, *Comments Inorg. Chem.* 1985, *4*, 295–321.
- [90] J. J. Scepaniak, M. D. Fulton, R. P. Bontchev, E. N. Duesler, M. L. Kirk, J. M. Smith, *J. Am. Chem. Soc.* 2008, *130*, 10515–10517.
- [91] S. D. Brown, J. C. Peters, *J. Am. Chem. Soc.* 2005, *127*, 1913–1923.
- [92] J. J. Scepaniak, R. P. Bontchev, D. L. Johnson, J. M. Smith, *Angew. Chem. Int. Ed.* 2011, *50*, 6630–6633; *Angew. Chem.* 2011, *123*, 6760–6763.
- [93] X.-Y. Yi, Y. Liang, C. Li, *RSC Adv.* 2013, *3*, 3477–3486.
- [94] H.-K. Kwong, W.-L. Man, J. Xiang, W.-T. Wong, T.-C. Lau, *Inorg. Chem.* 2009, *48*, 3080–3086.
- [95] R. L. Gdula, M. J. A. Johnson, N. W. Ockwig, *Inorg. Chem.* 2005, *44*, 9140–9142.
- [96] R. L. Gdula, M. J. A. Johnson, *J. Am. Chem. Soc.* 2006, *128*, 9614–9615.
- [97] A. M. Geyer, R. L. Gdula, E. S. Wiedner, M. J. A. Johnson, *J. Am. Chem. Soc.* 2007, *129*, 3800–3801.
- [98] L. K. Woo, J. G. Goll, *J. Am. Chem. Soc.* 1989, *111*, 3755–3757.
- [99] L. K. Woo, J. G. Goll, D. J. Czapla, J. A. Hays, *J. Am. Chem. Soc.* 1991, *113*, 8478–8484.
- [100] F. L. Neely, L. A. Bottomley, *Inorg. Chem.* 1997, *36*, 5432–5434.
- [101] L. A. Bottomley, F. L. Neely, *J. Am. Chem. Soc.* 1989, *111*, 5955–5957.
- [102] L. A. Bottomley, F. L. Neely, *Inorg. Chem.* 1997, *36*, 5435–5439.
- [103] H.-X. Wang, L. Wu, B. Zheng, L. Du, W.-P. To, C.-H. Ko, D. L. Phillips, C.-M. Che, *Angew. Chem. Int. Ed.* 2021, *60*, 4796–4803; *Angew. Chem.* 2021, *133*, 4846–4853.
- [104] W.-D. Wagner, K. Nakamoto, *J. Am. Chem. Soc.* 1988, *110*, 4044–4045.
- [105] W.-D. Wagner, K. Nakamoto, *J. Am. Chem. Soc.* 1989, *111*, 1590–1598.
- [106] C. Calle, R.-A. Eichel, C. Finazzo, J. Forrer, J. Granwehr, I. Gromov, W. Groth, J. Harmer, M. Kälin, W. Lämmler, L. Liesum, Z. Mádi, S. Stoll, S. V. Doorslaer, A. Schweiger, *Chimia* 2001, *55*, 763–766.
- [107] P. Gütllich, E. Bill, A. X. Trautwein, *Mössbauer spectroscopy and transition metal chemistry: Fundamentals and applications*, Springer Berlin Heidelberg, 2011.
- [108] H.-C. Chang, B. Mondal, H. Fang, F. Neese, E. Bill, S. Ye, *J. Am. Chem. Soc.* 2019, *141*, 2421–2434.
- [109] D. A. Summerville, I. A. Cohen, *J. Am. Chem. Soc.* 1976, *98*, 1747–1752.
- [110] J. W. Buchler, C. Dreher, *Z. Naturforsch.* 1984, *B 39*, 222–230.
- [111] J. F. Berry, E. Bill, E. Bothe, S. DeBeer George, B. Mienert, F. Neese, K. Wieghardt, *Science* 2006, *312*, 1937–1941.
- [112] K. Meyer, J. Bendix, N. Metzler-Nolte, T. Weyhermüller, K. Wieghardt, *J. Am. Chem. Soc.* 1998, *120*, 7260–7270.
- [113] C. A. Grapperhaus, B. Mienert, E. Bill, T. Weyhermüller, K. Wieghardt, *Inorg. Chem.* 2000, *39*, 5306–5317.

- [114] K. Meyer, E. Bill, B. Mienert, T. Weyhermüller, K. Wieghardt, *J. Am. Chem. Soc.* **1999**, *121*, 4859–4876.
- [115] H. Vennekate, D. Schwarzer, J. Torres-Alacan, P. Vöhringer, *J. Am. Chem. Soc.* **2014**, *136*, 10095–10103.
- [116] J. Torres-Alacan, U. Das, A. C. Filippou, P. Vöhringer, *Angew. Chem. Int. Ed.* **2013**, *52*, 12833–12837; *Angew. Chem.* **2013**, *125*, 13067–13071.
- [117] J. Torres-Alacan, J. Lindner, P. Vöhringer, *ChemPhysChem* **2015**, *16*, 2289–2293.
- [118] H. Vennekate, D. Schwarzer, J. Torres-Alacan, O. Krahe, A. C. Filippou, F. Neese, P. Vöhringer, *Phys. Chem. Chem. Phys.* **2012**, *14*, 6165–6172.
- [119] J. Torres-Alacan, O. Krahe, A. C. Filippou, F. Neese, D. Schwarzer, P. Vöhringer, *Chem. Eur. J.* **2012**, *18*, 3043–3055.
- [120] J. Torres-Alacan, P. Vöhringer, *Chem. Eur. J.* **2017**, *23*, 6746–6751.
- [121] J. Torres-Alacan, P. Vöhringer, *Int. Rev. Phys. Chem.* **2014**, *33*, 521–553.
- [122] E. Andris, R. Navrátil, J. Jašik, G. Sabenya, M. Costas, M. Srncic, J. Roithová, *Angew. Chem. Int. Ed.* **2017**, *56*, 14057–14060; *Angew. Chem.* **2017**, *129*, 14245–14248.
- [123] D. Bégué, G. G. Qiao, C. Wentrup, *J. Am. Chem. Soc.* **2012**, *134*, 5339–5350.
- [124] S. Flesch, P. Vöhringer, *Angew. Chem. Int. Ed.* **2022**, *61*, e202205803; *Angew. Chem.* **2022**, *134*, e202205803.
- [125] L. I. Domenianni, R. Fligg, A. Schäfermeier, S. Straub, J. Beerhues, B. Sarkar, P. Vöhringer, *Phys. Chem. Chem. Phys.* **2019**, *21*, 20393–20402.
- [126] P. Formentin, M. Álvaro, H. García, E. Palomares, M. J. Sabater, *New J. Chem.* **2002**, *26*, 1646–1650.
- [127] M. Sasikala, S. Mohan, S. Swarnakumari, *Int. J. Life Sci. Pharm. Res.* **2021**, *11*, P136–P145.
- [128] D. Harvey, *Analytical Chemistry 2.0, Vol. 1*, LibreTexts libraries, 2009.
- [129] J. M. Hollas, *Modern Spectroscopy*, 4th ed., WILEY, 2004.
- [130] H. Abramczyk, *Introduction to Laser Spectroscopy*, Elsevier Science, Amsterdam, 2005.
- [131] S. M. Blinder, *Introduction to Quantum Mechanics (Second Edition)*, Academic Press, San Diego, 2021.
- [132] T. G. Mayerhöfer, S. Pahlow, J. Popp, *ChemPhysChem* **2020**, *21*, 2029–2046.
- [133] W. Demtröder, *Atoms, Molecules and Photons, An Introduction to Atomic-, Molecular- and Quantum Physics, Vol. 3*, Springer, Berlin, Heidelberg, 2018.
- [134] R. C. Hilborn, *Am. J. Phys.* **1982**, *50*, 982–986.
- [135] F. A. Cotton, *Chemical Applications of Group Theory, Vol. 3*, WILEY, New York, 1990.
- [136] F. Jensen, *Introduction to Computational Chemistry*, 3rd ed., WILEY, Chichester, 2017.
- [137] A. Szabo, N. S. Ostlund, *Modern Quantum Chemistry, Introduction to Advanced Electronic Structure Theory*, Dover Publications, New York, 1996.
- [138] M. Hesse, H. Meier, B. Zeeh, *Spektroskopische Methoden in der organischen Chemie, Vol. 8*, Thieme, 2011.
- [139] H. H. Nielsen, *Rev. Mod. Phys.* **1951**, *23*, 90–136.
- [140] G. Herzberg, *Molecular Spectra and Molecular Structure. II. Infrared and Raman Spectra of Polyatomic Molecules*, D. van Nostrand Company Inc., New York, 1945.
- [141] R. Berera, R. van Grondelle, J. T. M. Kennis, *Photosynth. Res.* **2009**, *101*, 105–118.
- [142] M. Chergui in *Comprehensive Biophysics, Vol. 1*, (Ed.: E. H. Egelman), Elsevier, Amsterdam, 2012, pp. 398–424.
- [143] P. R. Griffiths, C. T. Foskett, R. Curbelo, *Appl. Spectrosc. Rev.* **1972**, *6*, 31–77.
- [144] C. J. Manning, R. A. Palmer, J. L. Chao, *Rev. Sci. Instrum.* **1991**, *62*, 1219–1229.
- [145] W. Uhlmann, A. Becker, C. Taran, F. Siebert, *Appl. Spectrosc.* **1991**, *45*, 390–397.
- [146] P. Hamm, M. T. Zanni, *Concepts and Methods of 2D Infrared Spectroscopy*, Cambridge University Press, 2011.
- [147] J. Laane, *Frontiers of Molecular Spectroscopy*, Elsevier, Amsterdam, 2009.
- [148] J. I. Zink, *Coord. Chem. Rev.* **2001**, *211*, 69–96.
- [149] J. C. Owruksy, D. Raftery, R. M. Hochstrasser, *Annu. Rev. Phys. Chem.* **1994**, *45*, 519–555.
- [150] P. Hamm, S. M. Ohline, W. Zinth, *J. Chem. Phys.* **1997**, *106*, 519–529.
- [151] W. Kaiser, A. Seilmeier in *Time-Resolved Vibrational Spectroscopy*, (Eds.: A. Laubereau, M. Stockburger), Springer, Berlin, Heidelberg, 1985, pp. 42–44.
- [152] S. Straub, J. Stubbe, J. Lindner, B. Sarkar, P. Vöhringer, *Inorg. Chem.* **2020**, *59*, 14629–14642.
- [153] T. Kühne, P. Vöhringer, *J. Chem. Phys.* **1996**, *105*, 10788–10802.
- [154] S. Straub, L. I. Domenianni, J. Lindner, P. Vöhringer, *J. Phys. Chem. B* **2019**, *123*, 7893–7904.
- [155] S. Sang, T. Unruh, S. Demeshko, L. I. Domenianni, N. P. van Leest, P. Marquetand, F. Schneck, C. Würtele, F. J. de Zwart, B. de Bruin, L. González, P. Vöhringer, S. Schneider, *Chem. Eur. J.* **2021**, *27*, 16978–16989.
- [156] K. S. Seshadri, R. N. Jones, *Spectrochim. Acta* **1963**, *19*, 1013–1085.
- [157] N. A. Nemkovich, A. N. Rubinov, V. I. Tomin in *Topics in Fluorescence Spectroscopy: Principles*, (Ed.: J. R. Lakowicz), Springer, Boston, 2002, pp. 367–428.
- [158] M. G. Zakaraya, G. G. Maisuradze, J. Ulstrup, *J. Raman Spectrosc.* **1989**, *20*, 359–365.
- [159] T. Sundius, *J. Raman Spectrosc.* **1973**, *1*, 471–488.
- [160] G. K. Wertheim, M. A. Butler, K. W. West, D. N. E. Buchanan, *Rev. Sci. Instrum.* **1974**, *45*, 1369–1371.
- [161] T. Ida, M. Ando, H. Toraya, *J. Appl. Cryst.* **2000**, *33*, 1311–1316.
- [162] D. B. Siano, D. E. Metzler, *J. Chem. Phys.* **1969**, *51*, 1856–1861.
- [163] H. Marciniak, S. Lochbrunner, *Chem. Phys. Lett.* **2014**, *609*, 184–188.
- [164] M. Maroncelli, G. R. Fleming, *J. Chem. Phys.* **1987**, *86*, 6221–6239.
- [165] B. Wezislá, J. Lindner, U. Das, A. C. Filippou, P. Vöhringer, *Angew. Chem. Int. Ed.* **2017**, *56*, 6901–6905; *Angew. Chem.* **2017**, *129*, 7005–7009.
- [166] S. Straub, P. Brünker, J. Lindner, P. Vöhringer, *Phys. Chem. Chem. Phys.* **2018**, *20*, 21390–21403.
- [167] O. A. El Seoud, W. J. Baader, E. L. Bastos in *Encyclopedia of Physical Organic Chemistry*, WILEY, 2016, pp. 1–68.
- [168] M. Sauer, J. Hofkens, J. Enderlein, *Handbook of Fluorescence Spectroscopy and Imaging: From Single Molecules to Ensembles*, WILEY-VCH, 2011.
- [169] L. Helm, A. E. Merbach, *Chem. Rev.* **2005**, *105*, 1923–1959.
- [170] R. W. Hay, *Reaction Mechanisms of Metal Complexes*, Woodhead Publishing, 2000.

- [171] W. P. Fehlhammer, W. Beck, *Z. Anorg. Allg. Chem.* **2013**, *639*, 1053–1082.
- [172] P. C. Samartzis, A. M. Wodtke, *Phys. Chem. Chem. Phys.* **2007**, *9*, 3054–3066.
- [173] J. Šima, *Coord. Chem. Rev.* **2006**, *250*, 2325–2334.
- [174] N. P. Gritsan, M. S. Platz in *Advances in Physical Organic Chemistry*, Vol. 36, Academic Press, **2001**, pp. 255–304.
- [175] N. P. Gritsan, M. S. Platz, *Chem. Rev.* **2006**, *106*, 3844–3867.
- [176] J. Kubicki, Y. Zhang, J. Xue, H. Ling Luk, M. Platz, *Phys. Chem. Chem. Phys.* **2012**, *14*, 10377–10390.
- [177] V. Balzani, L. Moggli, F. Scandola, V. Carassiti, *Inorg. Chim. Acta Rev.* **1967**, *1*, 7–34.
- [178] J. F. Endicott, M. Z. Hoffman, L. S. Beres, *J. Phys. Chem.* **1970**, *74*, 1021–1029.
- [179] D. Rehorek, T. Berthold, H. Hennig, T. J. Kemp, *Z. Chem.* **1988**, *28*, 72–73.
- [180] Z. B. Alfassi, A. Harriman, R. E. Huie, S. Mosseri, P. Neta, *J. Phys. Chem.* **1987**, *91*, 2120–2122.
- [181] M. Chase, NIST-JANAF Thermochemical Tables, 4th Edition, **1998**, <https://janaf.nist.gov/>.
- [182] S. Flesch, L. I. Domenianni, P. Vöhringer, *Phys. Chem. Chem. Phys.* **2020**, *22*, 25618–25630.
- [183] C. Hu, B. C. Noll, C. E. Schulz, W. R. Scheidt, *Inorg. Chem.* **2007**, *46*, 619–621.
- [184] A. D. Adler, F. R. Longo, F. Kampas, J. Kim, *J. Inorg. Nucl. Chem.* **1970**, *32*, 2443–2445.
- [185] B. L. Evans, *Proc. Royal Soc. A* **1958**, *246*, 199–203.
- [186] G. Sabenya, L. Lázaro, I. Gamba, V. Martin-Diaconescu, E. Andris, T. Weyhermüller, F. Neese, J. Roithova, E. Bill, J. Lloret-Fillol, M. Costas, *J. Am. Chem. Soc.* **2017**, *139*, 9168–9177.
- [187] J. J. Scepaniak, C. S. Vogel, M. M. Khusniyarov, F. W. Heinemann, K. Meyer, J. M. Smith, *Science* **2011**, *331*, 1049–1052.
- [188] O. Krahe, E. Bill, F. Neese, *Angew. Chem. Int. Ed.* **2014**, *53*, 8727–8731; *Angew. Chem.* **2014**, *126*, 8872–8876.
- [189] O. Krahe, F. Neese, M. Engeser, *ChemPlusChem* **2013**, *78*, 1053–1057.
- [190] SDBSWeb : <https://sdb.sdb.aist.go.jp> (National Institute of Advanced Industrial Science and Technology, 09.11.2023).
- [191] P. L. Hanst, *Fresenius Z. Anal. Chem.* **1986**, *324*, 579–588.
- [192] K. O. Christe, W. W. Wilson, R. Bau, S. W. Bunte, *J. Am. Chem. Soc.* **1992**, *114*, 3411–3414.
- [193] G. M. Sando, K. Dahl, J. C. Owrutsky, *J. Phys. Chem. B* **2007**, *111*, 4901–4909.
- [194] D. Czurlok, J. Torres-Alacan, P. Vöhringer, *J. Chem. Phys.* **2015**, *142*, 212402.
- [195] K. Sridharan, *Spectral Methods in Transition Metal Complexes*, Elsevier, **2016**, pp. 69–97.
- [196] H. Oshio, T. Ama, T. Watanabe, J. Kincaid, K. Nakamoto, *Spectrochim. Acta A Mol. Spectrosc.* **1984**, *40*, 863–870.
- [197] K. Nakamoto, *Infrared and Raman Spectra of Inorganic and Coordination Compounds Part B: Applications in Coordination, Organometallic and Bioinorganic Chemistry*, 6th ed., Wiley, **2009**.
- [198] G. Ferraudi, J. F. Endicott, *Inorg. Chem.* **1973**, *12*, 2389–2396.
- [199] P. Neta, R. E. Huie, A. B. Ross, *J. Phys. Chem. Ref. Data* **1988**, *17*, 1027–1284.
- [200] M. R. DeFelippis, M. Faraggi, M. H. Klapper, *J. Phys. Chem.* **1990**, *94*, 2420–2424.
- [201] H. A. Schwarz, B. H. J. Bielski, *J. Phys. Chem.* **1986**, *90*, 1445–1448.
- [202] M. E. Niyazymbetov, D. H. Evans, *J. Chem. Soc., Perkin Trans. 2* **1993**, 1333–1338.
- [203] R. Tsuchida, *Bull. Chem. Soc. Jpn.* **1938**, *13*, 388–400.
- [204] A. F. Holleman, E. Wiberg, N. Wiberg, *Lehrbuch der Anorganischen Chemie*, Vol. 102, de Gruyter, Berlin, **2007**.
- [205] S. I. Arshankow, A. L. Poznjak, *Z. Anorg. Allg. Chem.* **1981**, *481*, 201–206.
- [206] T. A. Betley, J. C. Peters, *J. Am. Chem. Soc.* **2004**, *126*, 6252–6254.
- [207] B. L. Tran, M. Pink, X. Gao, H. Park, D. J. Mindiola, *J. Am. Chem. Soc.* **2010**, *132*, 1458–1459.
- [208] J. S. Sílvia, C. C. Cummins, *J. Am. Chem. Soc.* **2009**, *131*, 446–447.
- [209] Y.-J. Kim, Y.-S. Kwak, Y.-S. Joo, S.-W. Lee, *J. Chem. Soc., Dalton Trans.* **2002**, 144–151.
- [210] G. Veneziani, S. Shimada, M. Tanaka, *Organometallics* **1998**, *17*, 2926–2929.
- [211] H. Herrmann, J. Lloret Fillol, H. Wadepohl, L. H. Gade, *Angew. Chem. Int. Ed.* **2007**, *46*, 8426–8430; *Angew. Chem.* **2007**, *119*, 8578–8582.
- [212] G. C. Blouin, J. S. Olson, *Biochemistry* **2010**, *49*, 4968–4976.
- [213] D. K. Matsumoto, C. N. Satterfield, *Ind. Eng. Chem. Proc. Des. Dev.* **1985**, *24*, 1297–1300.
- [214] U.-J. Jáuregui-Haza, E. J. Pardillo-Fontdevila, A. M. Wilhelm, H. Delmas, *Lat. Am. Appl. Res.* **2004**, *34*, 71–74.
- [215] SAFETY DATA SHEET - Butyl isocyanide, CAS-No.: 2769-64-4, Version 6.3, Sigma-Aldrich - Merck Group, 05.03.2021.
- [216] SAFETY DATA SHEET - tert-Butyl isocyanide, CAS-No.: 7188-38-7, Version 6.3, Sigma-Aldrich - Merck Group, 28.10.2022.
- [217] SAFETY DATA SHEET - Isopropyl isocyanide, CAS-No.: 598-45-8, Version 6.6, Sigma-Aldrich - Merck Group, 27.09.2022.
- [218] SAFETY DATA SHEET - Cyclohexyl isocyanide, CAS-No.: 931-53-3, Version 6.4, Sigma-Aldrich - Merck Group, 28.04.2022.
- [219] S. Thunell, *Scand. J. Clin. Lab. Invest.* **2000**, *60*, 509–540.
- [220] R. Giovannetti in *Macro To Nano Spectroscopy*, (Ed.: J. Uddin), InTech, **2012**, Chapter 6, pp. 87–108.
- [221] M. Gouterman, G. H. Wagnière, L. C. Snyder, *J. Mol. Spectrosc.* **1963**, *11*, 108–127.
- [222] M. Gouterman in *The Porphyrins*, Vol. III, (Ed.: D. Dolphin), Academic Press, **1978**, Chapter 1, pp. 1–165.
- [223] G. D. Dorough, J. R. Miller, F. M. Huennekens, *J. Am. Chem. Soc.* **1951**, *73*, 4315–4320.
- [224] L. Edwards, D. H. Dolphin, M. Gouterman, A. D. Adler, *J. Mol. Spectrosc.* **1971**, *38*, 16–32.
- [225] P. J. Spellane, M. Gouterman, A. Antipas, S. Kim, Y. C. Liu, *Inorg. Chem.* **1980**, *19*, 386–391.
- [226] G. W. Canters, G. Jansen, M. Noort, J. H. van der Waals, *J. Phys. Chem.* **1976**, *80*, 2253–2259.
- [227] W. T. Simpson, *J. Chem. Phys.* **1949**, *17*, 1218–1221.
- [228] H. C. Longuet-Higgins, C. W. Rector, J. R. Platt, *J. Chem. Phys.* **1950**, *18*, 1174–1181.
- [229] J. R. Platt, *J. Opt. Soc. Am.* **1953**, *43*, 252–257.
- [230] J. R. Platt, *Radiation Biology*, Chapter 2, Vol. III, (Ed.: A. Hollaender), McGraw-Hill, **1956**.

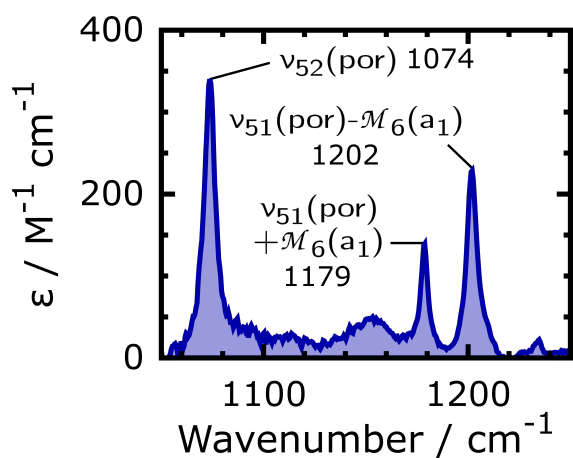
- [231] H. Kobayashi, *J. Chem. Phys.* **1959**, *30*, 1362–1363.
- [232] M. Gouterman, *J. Chem. Phys.* **1959**, *30*, 1139–1161.
- [233] M. Gouterman, *J. Mol. Spectrosc.* **1961**, *6*, 138–163.
- [234] Z.-L. Cai, M. J. Crossley, J. R. Reimers, R. Kobayashi, R. D. Amos, *J. Phys. Chem. B* **2006**, *110*, 15624–15632.
- [235] S. Chantrell, C. McAuliffe, R. Munn, A. Pratt, *Coord. Chem. Rev.* **1975**, *16*, 259–284.
- [236] T. Hashimoto, Y.-K. Choe, H. Nakano, K. Hirao, *J. Phys. Chem. A* **1999**, *103*, 1894–1904.
- [237] H. Ryeng, A. Ghosh, *J. Am. Chem. Soc.* **2002**, *124*, 8099–8103.
- [238] A. G. Skillman, J. R. Collins, G. H. Loew, *J. Am. Chem. Soc.* **1992**, *114*, 9538–9544.
- [239] F. Paulat, N. Lehnert, *Inorg. Chem.* **2008**, *47*, 4963–4976.
- [240] C. Weiss, H. Kobayashi, M. Gouterman, *J. Mol. Spectrosc.* **1965**, *16*, 415–450.
- [241] F. Adar in *The Porphyrins, Vol. III*, (Ed.: D. Dolphin), Academic Press, **1978**, Chapter 2, pp. 167–209.
- [242] A. T. Grudushko, K. N. Solov'ev, A. S. Starukhin, *Opt. Spectrosc.* **1976**, *40*, 267–271.
- [243] M. H. Perrin, M. Gouterman, C. L. Perrin, *J. Chem. Phys.* **1969**, *50*, 4137–4150.
- [244] N. Ehlinger, W. R. Scheidt, *Inorg. Chem.* **1999**, *38*, 1316–1321.
- [245] H. Song, C. A. Reed, W. R. Scheidt, *J. Am. Chem. Soc.* **1989**, *111*, 6865–6866.
- [246] F. A. Walker, H. Nasri, I. Turowska-Tyrk, K. Mohanrao, C. T. Watson, N. V. Shokhirev, P. G. Debrunner, W. R. Scheidt, *J. Am. Chem. Soc.* **1996**, *118*, 12109–12118.
- [247] P. Gans, G. Buisson, E. Duee, J. C. Marchon, B. S. Erler, W. F. Scholz, C. A. Reed, *J. Am. Chem. Soc.* **1986**, *108*, 1223–1234.
- [248] J. D. Petke, G. M. Maggiora, L. L. Shipman, R. E. Christoffersen, *J. Mol. Spectrosc.* **1978**, *71*, 64–84.
- [249] Q. M. Phung, K. Pierloot, *J. Chem. Theory Comput.* **2019**, *15*, 3033–3043.
- [250] T. Vangberg, R. Lie, A. Ghosh, *J. Am. Chem. Soc.* **2002**, *124*, 8122–8130.
- [251] R. A. Binstead, M. J. Crossley, N. S. Hush, *Inorg. Chem.* **1991**, *30*, 1259–1264.
- [252] J. Fajer, D. C. Borg, A. Forman, R. H. Felton, L. Vegh, D. Dolphin, *Ann. N.Y. Acad. Sci.* **1973**, *206*, 349–364.
- [253] M.-S. Liao, S. Scheiner, *J. Chem. Phys.* **2002**, *117*, 205–219.
- [254] K. A. Nguyen, R. Pachter, *J. Chem. Phys.* **2001**, *114*, 10757–10767.
- [255] H. Kobayashi, Y. Yanagawa, H. Osada, S. Minami, M. Shimizu, *Bull. Chem. Soc. Jpn.* **1973**, *46*, 1471–1479.
- [256] J. E. House, *Inorganic Chemistry (Second Edition)*, Academic Press, **2013**.
- [257] M. Tarrago, C. Römel, J. Nehrkorn, A. Schnegg, F. Neese, E. Bill, S. Ye, *Inorg. Chem.* **2021**, *60*, 4966–4985.
- [258] J. P. Collman, J. L. Hoard, N. Kim, G. Lang, C. A. Reed, *J. Am. Chem. Soc.* **1975**, *97*, 2676–2681.
- [259] H. Goff, G. N. La Mar, C. A. Reed, *J. Am. Chem. Soc.* **1977**, *99*, 3641–3646.
- [260] G. Lang, K. Spartaian, C. A. Reed, J. P. Collman, *J. Chem. Phys.* **1978**, *69*, 5424–5427.
- [261] P. D. W. Boyd, D. A. Buckingham, R. F. McMeeking, S. Mitra, *Inorg. Chem.* **1979**, *18*, 3585–3591.
- [262] Y. Zhang, W. A. Hallows, W. J. Ryan, J. G. Jones, G. B. Carpenter, D. A. Schweigart, *Inorg. Chem.* **1994**, *33*, 3306–3312.
- [263] C. J. Ballhausen, H. B. Gray, *Inorg. Chem.* **1962**, *1*, 111–122.
- [264] T. A. Betley, Q. Wu, T. Van Voorhis, D. G. Nocera, *Inorg. Chem.* **2008**, *47*, 1849–1861.
- [265] N. Aliaga-Alcalde, S. DeBeer George, B. Mienert, E. Bill, K. Wieghardt, F. Neese, *Angew. Chem. Int. Ed.* **2005**, *44*, 2908–2912; *Angew. Chem.* **2005**, *117*, 2968–2972.
- [266] A. Decker, J.-U. Rohde, L. Que Jr., E. I. Solomon, *J. Am. Chem. Soc.* **2004**, *126*, 5378–5379.
- [267] A. Decker, E. I. Solomon, *Angew. Chem. Int. Ed.* **2005**, *44*, 2252–2255; *Angew. Chem.* **2005**, *117*, 2292–2295.
- [268] A. Decker, M. D. Clay, E. I. Solomon, *J. Inorg. Biochem.* **2006**, *100*, 697–706.
- [269] H. B. Gray, C. R. Hare, *Inorg. Chem.* **1962**, *1*, 363–368.
- [270] S. Yamamoto, H. Kashiwagi, *Chem. Phys. Lett.* **1988**, *145*, 111–116.
- [271] R. H. Holm, *Chem. Rev.* **1987**, *87*, 1401–1449.
- [272] J. M. Mayer, *Comments Inorg. Chem.* **1988**, *8*, 125–135.
- [273] M. Zerner, M. Gouterman, *Theoret. Chim. Acta* **1966**, *4*, 44–63.
- [274] M. A. Phillippi, H. M. Goff, *J. Am. Chem. Soc.* **1982**, *104*, 6026–6034.
- [275] R. S. Czernuszewicz, K. A. Macor, X.-Y. Li, J. R. Kincaid, T. G. Spiro, *J. Am. Chem. Soc.* **1989**, *111*, 3860–3869.
- [276] J. Fajer, D. C. Borg, A. Forman, D. Dolphin, R. H. Felton, *J. Am. Chem. Soc.* **1970**, *92*, 3451–3459.
- [277] D. Kim, L. A. Miller, G. Rakhit, T. G. Spiro, *J. Phys. Chem.* **1986**, *90*, 3320–3325.
- [278] M. Zerner, M. Gouterman, H. Kobayashi, *Theoret. chim. Acta* **1966**, *6*, 363–400.
- [279] A. Antipas, J. W. Buchler, M. Gouterman, P. D. Smith, *J. Am. Chem. Soc.* **1978**, *100*, 3015–3024.
- [280] J. T. Groves, R. C. Haushalter, M. Nakamura, T. E. Nemo, B. J. Evans, *J. Am. Chem. Soc.* **1981**, *103*, 2884–2886.
- [281] A. L. Balch, L. Latos-Grazynski, M. W. Renner, *J. Am. Chem. Soc.* **1985**, *107*, 2983–2985.
- [282] B. Meunier, *Metal-Oxo and Metal-Peroxo Species in Catalytic Oxidations, Structure & Bonding, Vol. 97*, Springer, Berlin, Heidelberg, **2000**.
- [283] D. Dolphin, R. H. Felton, *Acc. Chem. Res.* **1974**, *7*, 26–32.
- [284] D. Dolphin, Z. Muljiani, K. Rousseau, D. C. Borg, J. Fajer, R. H. Felton, *Ann. N.Y. Acad. Sci.* **1973**, *206*, 177–200.
- [285] J. Turner, A. Gold, R. Weiss, D. Mandon, A. X. Trautwein, *J. Porphyrins Phthalocyanines* **2001**, *05*, 357–364.
- [286] S. Hu, T. G. Spiro, *J. Am. Chem. Soc.* **1993**, *115*, 12029–12034.
- [287] K. Jayaraj, J. Turner, A. Gold, D. A. Roberts, R. N. Austin, D. Mandon, R. Weiss, E. Bill, M. Müther, A. X. Trautwein, *Inorg. Chem.* **1996**, *35*, 1632–1640.
- [288] M. Satoh, Y. Ohba, S. Yamauchi, M. Iwaizumi, *Inorg. Chem.* **1992**, *31*, 298–303.
- [289] W. R. Scheidt, B. Cheng, K. Venugopal Reddy, K. E. Brancato, *J. Porphyrins Phthalocyanines* **2017**, *21*, 273–286.
- [290] B. S. Erler, W. F. Scholz, Y. J. Lee, W. R. Scheidt, C. A. Reed, *J. Am. Chem. Soc.* **1987**, *109*, 2644–2652.

- [291] G. Lang, B. Boso, B. S. Erler, C. A. Reed, *J. Chem. Phys.* **1986**, *84*, 2998–3004.
- [292] M. J. Benecy, J. E. Frew, N. Scowen, P. Jones, B. M. Hoffman, *Biochemistry* **1993**, *32*, 11929–11933.
- [293] W. F. Scholz, C. A. Reed, Y. J. Lee, W. R. Scheidt, G. Lang, *J. Am. Chem. Soc.* **1982**, *104*, 6791–6793.
- [294] J. T. Groves, Y. Watanabe, T. J. McMurry, *J. Am. Chem. Soc.* **1983**, *105*, 4489–4490.
- [295] J. T. Groves, *J. Inorg. Biochem.* **2006**, *100*, 434–447.
- [296] M. Radoń, E. Broclawik in *Computational Methods to Study the Structure and Dynamics of Biomolecules and Biomolecular Processes: From Bioinformatics to Molecular Quantum Mechanics (Second Edition)*, (Ed.: A. Liwo), Springer, Cham, **2019**, pp. 755–823.
- [297] A. Dey, A. Ghosh, *J. Am. Chem. Soc.* **2002**, *124*, 3206–3207.
- [298] W. R. Patterson, T. L. Poulos, D. B. Goodin, *Biochemistry* **1995**, *34*, 4342–4345.
- [299] J. Rodriguez, C. Kirmaier, D. Holten, *J. Am. Chem. Soc.* **1989**, *111*, 6500–6506.
- [300] D. Holten, M. Gouterman in *Optical Properties and Structure of Tetrapyrroles*, (Eds.: G. Blauer, H. Sund), De Gruyter, Berlin, Boston, **1985**, pp. 63–90.
- [301] L. Pekkarinen, H. Linschitz, *J. Am. Chem. Soc.* **1960**, *82*, 2407–2411.
- [302] C. D. Tait, D. Holten, M. Gouterman, *Chem. Phys. Lett.* **1983**, *100*, 268–272.
- [303] W. S. Caughey, R. M. Deal, C. Weiss, M. Gouterman, *J. Mol. Spectrosc.* **1965**, *16*, 451–463.
- [304] D. N. Hendrickson, M. G. Kinnaird, K. S. Suslick, *J. Am. Chem. Soc.* **1987**, *109*, 1243–1244.
- [305] J. H. Fuhrhop, D. Mauzerall, *J. Am. Chem. Soc.* **1969**, *91*, 4174–4181.
- [306] I. Fujita, L. K. Hanson, F. A. Walker, J. Fajer, *J. Am. Chem. Soc.* **1983**, *105*, 3296–3300.
- [307] S. Hashimoto, Y. Tatsuno, T. Kitagawa, *J. Am. Chem. Soc.* **1987**, *109*, 8096–8097.
- [308] L. Kaustov, M. E. Tal, A. I. Shames, Z. Gross, *Inorg. Chem.* **1997**, *36*, 3503–3511.
- [309] D. H. Jones, A. S. Hinman, *Can. J. Chem.* **2000**, *78*, 1318–1324.
- [310] M. Neumann-Spallart, K. Kalyanasundaram, *Z. Naturforsch. B* **1981**, *36*, 596–600.
- [311] W. A. Oertling, A. Salehi, Y. C. Chung, G. E. Leroi, C. K. Chang, G. T. Babcock, *J. Phys. Chem.* **1987**, *91*, 5887–5898.
- [312] R. Rutter, M. Valentine, M. P. Hendrich, L. P. Hager, P. G. Debrunner, *Biochemistry* **1983**, *22*, 4769–4774.
- [313] J. E. Roberts, B. M. Hoffman, R. Rutter, L. P. Hager, *J. Biol. Chem.* **1981**, *256*, 2118–2121.
- [314] J. E. Roberts, B. M. Hoffman, R. Rutter, L. P. Hager, *J. Am. Chem. Soc.* **1981**, *103*, 7654–7656.
- [315] B. M. Hoffman, *Acc. Chem. Res.* **1991**, *24*, 164–170.
- [316] I. Morishima, Y. Shiro, Y. Takamuki, *J. Am. Chem. Soc.* **1983**, *105*, 6168–6170.
- [317] I. Morishima, Y. Takamuki, Y. Shiro, *J. Am. Chem. Soc.* **1984**, *106*, 7666–7672.
- [318] I. Morishima, Y. Shiro, K. Nakajima, *Biochemistry* **1986**, *25*, 3576–3584.
- [319] L. J. Boucher, J. J. Katz, *J. Am. Chem. Soc.* **1967**, *89*, 1340–1345.
- [320] H. Ogoshi, Y. Saito, K. Nakamoto, *J. Chem. Phys.* **1972**, *57*, 4194–4202.
- [321] J. Kincaid, K. Nakamoto, *J. Inorg. Nucl. Chem.* **1975**, *37*, 85–89.
- [322] X.-Y. Li, R. S. Czernuszewicz, J. R. Kincaid, Y. O. Su, T. G. Spiro, *J. Phys. Chem.* **1990**, *94*, 31–47.
- [323] X. Y. Li, R. S. Czernuszewicz, J. R. Kincaid, P. Stein, T. G. Spiro, *J. Phys. Chem.* **1990**, *94*, 47–61.
- [324] T. S. Rush III, P. M. Kozlowski, C. A. Piffat, R. Kumble, M. Z. Zgierski, T. G. Spiro, *J. Phys. Chem. B* **2000**, *104*, 5020–5034.
- [325] Y. Ozaki, K. Iriyama, H. Ogoshi, T. Ochiai, T. Kitagawa, *J. Phys. Chem.* **1986**, *90*, 6105–6112.
- [326] G. Chottard, P. Battioni, J.-P. Battioni, M. Lange, D. Mansuy, *Inorg. Chem.* **1981**, *20*, 1718–1722.
- [327] T. Kitagawa, J. Teraoka, *Chem. Phys. Lett.* **1979**, *63*, 443–446.
- [328] J. Teraoka, T. Kitagawa, *J. Phys. Chem.* **1980**, *84*, 1928–1935.
- [329] E. T. Shimomura, M. A. Phillippi, H. M. Goff, W. F. Scholz, C. A. Reed, *J. Am. Chem. Soc.* **1981**, *103*, 6778–6780.
- [330] J. Chen, E. Wuttke, W. Polit, T. Exner, R. F. Winter, *J. Am. Chem. Soc.* **2013**, *135*, 3391–3394.
- [331] M. Li, T. J. Neal, G. R. A. Wyllie, C. E. Schulz, W. R. Scheidt, *Inorg. Chem.* **2010**, *49*, 8078–8085.
- [332] L. O. Spreer, A. C. Maliyackel, S. Holbrook, J. W. Otvos, M. Calvin, *J. Am. Chem. Soc.* **1986**, *108*, 1949–1953.
- [333] K. Itoh, K. Nakahasi, H. Toeda, *J. Phys. Chem.* **1988**, *92*, 1464–1468.
- [334] W. A. Oertling, A. Salehi, C. K. Chang, G. T. Babcock, *J. Phys. Chem.* **1989**, *93*, 1311–1319.
- [335] K. Prendergast, T. G. Spiro, *J. Phys. Chem.* **1991**, *95*, 9728–9736.
- [336] E. A. Morlino, M. A. J. Rodgers, *J. Am. Chem. Soc.* **1996**, *118*, 11798–11804.
- [337] M.-H. Ha-Thi, N. Shafizadeh, L. Poisson, B. Soep, *Phys. Chem. Chem. Phys.* **2010**, *12*, 14985–14993.
- [338] H. S. Eom, S. C. Jeoung, D. Kim, J.-H. Ha, Y.-R. Kim, *J. Phys. Chem. A* **1997**, *101*, 3661–3669.
- [339] D. Kim, C. Kirmaier, D. Holten, *Chem. Phys.* **1983**, *75*, 305–322.
- [340] C. D. Tait, D. Holten, M. Gouterman, *J. Am. Chem. Soc.* **1984**, *106*, 6653–6659.
- [341] H.-Z. Yu, J. S. Baskin, B. Steiger, C. Z. Wan, F. C. Anson, A. H. Zewail, *Chem. Phys. Lett.* **1998**, *293*, 1–8.
- [342] M. Andersson, J. Davidsson, L. Hammarström, J. Korppi-Tommola, T. Peltola, *J. Phys. Chem. B* **1999**, *103*, 3258–3262.
- [343] D. W. Dixon, C. Kirmaier, D. Holten, *J. Am. Chem. Soc.* **1985**, *107*, 808–813.
- [344] Y. Kholodenko, M. Volk, E. Gooding, R. M. Hochstrasser, *Chem. Phys.* **2000**, *259*, 71–87.
- [345] A. Lukaszewicz, J. Karolczak, D. Kowalska, A. Maciejewski, M. Ziolk, R. P. Steer, *Chem. Phys.* **2007**, *331*, 359–372.
- [346] J. Rodriguez, D. Holten, *J. Chem. Phys.* **1989**, *91*, 3525–3531.
- [347] C. M. Drain, S. Gentemann, J. A. Roberts, N. Y. Nelson, C. J. Medforth, S. Jia, M. C. Simpson, K. M. Smith, J. Fajer, J. A. Shelnutt, D. Holten, *J. Am. Chem. Soc.* **1998**, *120*, 3781–3791.
- [348] M. Inamo, C. Okabe, T. Nakabayashi, N. Nishi, M. Hoshino, *Chem. Phys. Lett.* **2007**, *445*, 167–172.
- [349] H. Chosrowjan, S. Taniguchi, T. Okada, S. Takagi, T. Arai, K. Tokumam, *Chem. Phys. Lett.* **1995**, *242*, 644–649.
- [350] G. G. Gurzadyan, T.-H. Tran-Thi, T. Gustavsson, *J. Chem. Phys.* **1998**, *108*, 385–388.

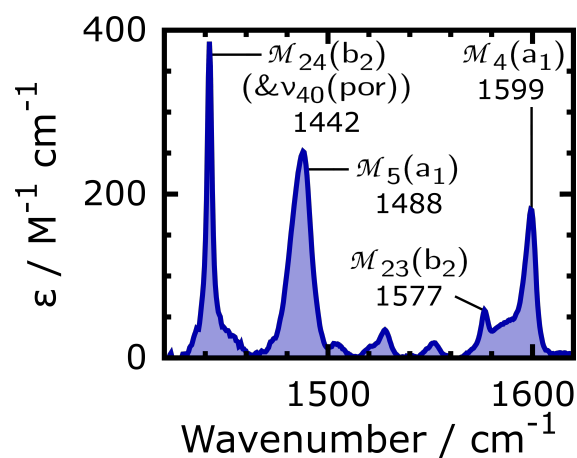
- [351] S. Akimoto, T. Yamazaki, I. Yamazaki, A. Osuka, *Chem. Phys. Lett.* **1999**, *309*, 177–182.
- [352] N. Mataga, Y. Shibata, H. Chosrowjan, N. Yoshida, A. Osuka, *J. Phys. Chem. B* **2000**, *104*, 4001–4004.
- [353] U. Tripathy, D. Kowalska, X. Liu, S. Velate, R. P. Steer, *J. Phys. Chem. A* **2008**, *112*, 5824–5833.
- [354] H.-Z. Yu, J. S. Baskin, A. H. Zewail, *J. Phys. Chem. A* **2002**, *106*, 9845–9854.
- [355] S. K. Karthick Kumar, V. Tiwari, T. Goswami, D. Goswami, *Chem. Phys. Lett.* **2009**, *476*, 31–36.
- [356] Y. Mizutani, Y. Uesugi, T. Kitagawa, *J. Chem. Phys.* **1999**, *111*, 8950–8962.
- [357] N. Shafizadeh, L. Krim, S. Sorgues, B. Soep, *Chem. Phys. Lett.* **2002**, *357*, 37–44.
- [358] S. Sorgues, L. Poisson, K. Raffael, L. Krim, B. Soep, N. Shafizadeh, *J. Chem. Phys.* **2006**, *124*, 114302.
- [359] S. Tobita, I. Tanaka, *Chem. Phys. Lett.* **1983**, *96*, 517–521.
- [360] S. Tobita, Y. Kaizu, H. Kobayashi, I. Tanaka, *J. Chem. Phys.* **1984**, *81*, 2962–2969.
- [361] J. Karolczak, D. Kowalska, A. Lukaszewicz, A. Maciejewski, R. P. Steer, *J. Phys. Chem. A* **2004**, *108*, 4570–4575.
- [362] L. Bajema, M. Gouterman, C. B. Rose, *J. Mol. Spectrosc.* **1971**, *39*, 421–431.
- [363] U. Even, J. Magen, J. Jortner, J. Friedman, H. Levanon, *J. Chem. Phys.* **1982**, *77*, 4374–4383.
- [364] A. Harriman, *J. Chem. Soc. Faraday Trans. 1* **1980**, *76*, 1978–1985.
- [365] M. P. Tsvirko, G. F. Stelmakh, V. E. Pyatosin, K. N. Solovyov, T. F. Kachura, *Chem. Phys. Lett.* **1980**, *73*, 80–83.
- [366] A. Harriman, *J. Chem. Soc. Faraday Trans. 1* **1981**, *77*, 369–377.
- [367] A. Harriman, *J. Chem. Soc. Faraday Trans. 1* **1982**, *78*, 2727–2734.
- [368] P. A. Cornelius, A. W. Steele, D. A. Chernoff, R. M. Hochstrasser, *Chem. Phys. Lett.* **1981**, *82*, 9–14.
- [369] A. S. Rury, R. J. Sension, *Chem. Phys.* **2013**, *422*, 220–228.
- [370] S. Tobita, Y. Kajii, I. Tanaka in *Porphyrins*, (Eds.: M. Gouterman, P. M. Rentzepis, K. D. Straub), ACS Symposium Series Vol. 321, American Chemical Society, **1986**, pp. 219–230.
- [371] Y. Kobayashi, K. Mutoh, J. Abe, *J. Photochem. Photobiol. C* **2018**, *34*, 2–28.
- [372] M. Drobizhev, A. Karotki, M. Kruk, A. Rebane, *Chem. Phys. Lett.* **2002**, *355*, 175–182.
- [373] M. Drobizhev, F. Meng, A. Rebane, Y. Stepanenko, E. Nickel, C. W. Spangler, *J. Phys. Chem. B* **2006**, *110*, 9802–9814.
- [374] T. C. Wen, L. C. Hwang, W. Y. Lin, C. H. Chen, C. H. Wu, *Chem. Phys.* **2003**, *286*, 293–302.
- [375] J. L. Humphrey, D. Kuciauskas, *J. Am. Chem. Soc.* **2006**, *128*, 3902–3903.
- [376] M. Kruk, A. Karotki, M. Drobizhev, V. Kuzmitsky, V. Gael, A. Rebane, *J. Lumin.* **2003**, *105*, 45–55.
- [377] E. S. Ryland, M.-F. Lin, M. A. Verkamp, K. Zhang, K. Benke, M. Carlson, J. Vura-Weis, *J. Am. Chem. Soc.* **2018**, *140*, 4691–4696.
- [378] Z. Pan, D. N. Harischandra, M. Newcomb, *J. Inorg. Biochem.* **2009**, *103*, 174–181.
- [379] R. Zhang, M. Newcomb, *J. Am. Chem. Soc.* **2003**, *125*, 12418–12419.
- [380] R. Zhang, J. H. Horner, M. Newcomb, *J. Am. Chem. Soc.* **2005**, *127*, 6573–6582.
- [381] D. N. Harischandra, R. Zhang, M. Newcomb, *J. Am. Chem. Soc.* **2005**, *127*, 13776–13777.
- [382] K. M. Adams, P. G. Rasmussen, W. R. Scheidt, K. Hatano, *Inorg. Chem.* **1979**, *18*, 1892–1899.
- [383] TURBOMOLE V7.5 2020, a development of University of Karlsruhe and Forschungszentrum Karlsruhe GmbH, 1989–2007, TURBOMOLE GmbH, since 2007; available from www.turbomole.com.
- [384] R. Ahlrichs, M. Bär, M. Häser, H. Horn, C. Kölmel, *Chem. Phys. Lett.* **1989**, *162*, 165–169.
- [385] O. Treutler, R. Ahlrichs, *J. Chem. Phys.* **1995**, *102*, 346–354.
- [386] M. Von Arnim, R. Ahlrichs, *J. Comput. Chem.* **1998**, *19*, 1746–1757.
- [387] J.-D. Chai, M. Head-Gordon, *J. Chem. Phys.* **2008**, *128*, 084106.
- [388] A. D. Becke, *J. Chem. Phys.* **1997**, *107*, 8554–8560.
- [389] F. Weigend, R. Ahlrichs, *Phys. Chem. Chem. Phys.* **2005**, *7*, 3297–3305.
- [390] A. Schäfer, C. Huber, R. Ahlrichs, *J. Chem. Phys.* **1994**, *100*, 5829–5835.
- [391] A. Schäfer, H. Horn, R. Ahlrichs, *J. Chem. Phys.* **1992**, *97*, 2571–2577.
- [392] E. Caldeweyher, C. Bannwarth, S. Grimme, *J. Chem. Phys.* **2017**, *147*, 034112.
- [393] E. Caldeweyher, S. Ehlert, A. Hansen, H. Neugebauer, S. Spicher, C. Bannwarth, S. Grimme, *J. Chem. Phys.* **2019**, *150*, 154122.
- [394] Z. Dori, R. F. Ziolo, *Chem. Rev.* **1973**, *73*, 247–254.
- [395] R. S. Mulliken, *J. Chem. Phys.* **1955**, *23*, 1997–2011.
- [396] A. M. Gardner, T. G. Wright, *J. Chem. Phys.* **2011**, *135*, 114305.
- [397] K. Ueno, A. E. Martell, *J. Phys. Chem.* **1956**, *60*, 934–938.
- [398] D. W. Thomas, A. E. Martell, *J. Am. Chem. Soc.* **1959**, *81*, 5111–5119.
- [399] M. Gouterman, L. K. Hanson, G.-E. Khalil, W. R. Leenstra, J. W. Buchler, *J. Chem. Phys.* **1975**, *62*, 2343–2353.
- [400] K. Stavrev, M. C. Zerner, *Chem. Phys. Lett.* **1995**, *233*, 179–184.
- [401] L. Doub, J. M. Vandenbelt, *J. Am. Chem. Soc.* **1947**, *69*, 2714–2723.
- [402] A. Horn, *The Physics of Laser Radiation-Matter Interaction: Fundamentals, and Selected Applications in Metrology*, Springer Nature, Cham, **2022**.
- [403] R. Tian, J. C. Facelli, J. Michl, *J. Phys. Chem.* **1988**, *92*, 4073–4079.
- [404] M. Kasha, *Discuss. Faraday Soc.* **1950**, *9*, 14–19.
- [405] S. Hume, G. Hithell, G. M. Greetham, P. M. Donaldson, M. Towrie, A. W. Parker, M. J. Baker, N. T. Hunt, *Chem. Sci.* **2019**, *10*, 6448–6456.
- [406] D. Czurlok, J. Gleim, J. Lindner, P. Vöhringer, *J. Phys. Chem. Lett.* **2014**, *5*, 3373–3379.
- [407] T. Watanabe, T. Ama, K. Nakamoto, *J. Phys. Chem.* **1984**, *88*, 440–445.
- [408] M. Ravikanth, A. Misra, D. Reddy, T. K. Chandrashekar, *J. Chem. Soc., Dalton Trans.* **1994**, 491–495.
- [409] Z. Gross, C. Barzilay, *Angew. Chem. Int. Ed. Engl.* **1992**, *31*, 1615–1617.
- [410] L. M. Proniewicz, I. R. Paeng, K. Nakamoto, *J. Am. Chem. Soc.* **1991**, *113*, 3294–3303.
- [411] A. F. Olea, J. K. Thomas, *J. Am. Chem. Soc.* **1988**, *110*, 4494–4502.

8 Appendix

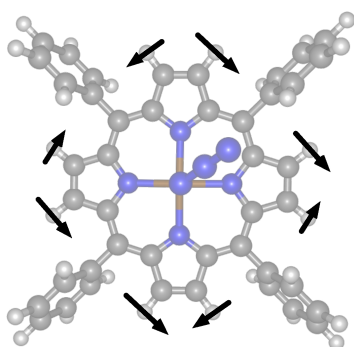
8.1 Additional Stationary FTIR Spectra



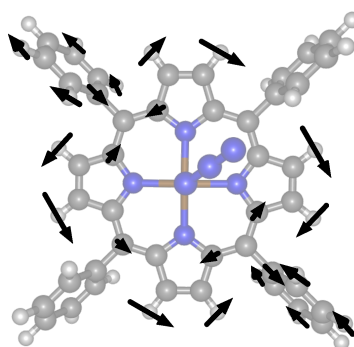
(a) Expanded 1050-1250 cm^{-1} region.



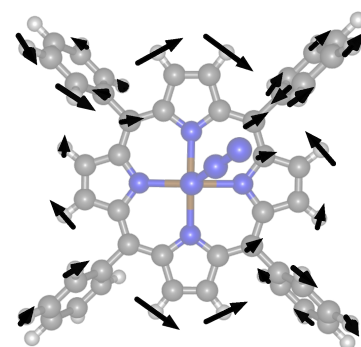
(b) Expanded 1420-1620 cm^{-1} region.



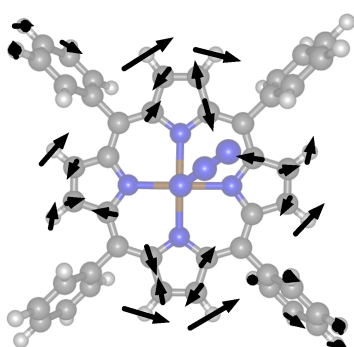
(c) $\nu_{52}(\text{por})$; 1074 cm^{-1} .



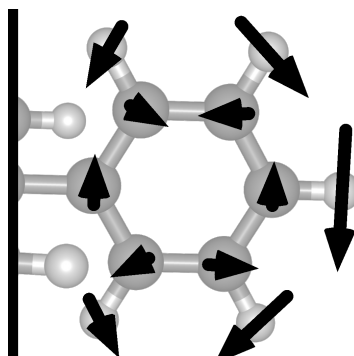
(d) $\nu_{51}(\text{por})+\mathcal{M}_6(a_1)$; 1179 cm^{-1} .



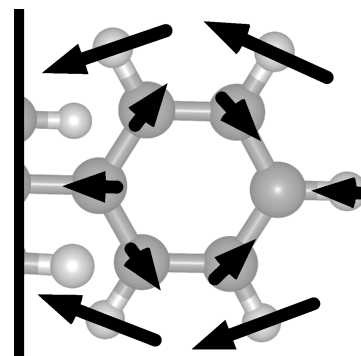
(e) $\nu_{51}(\text{por})-\mathcal{M}_6(a_1)$; 1202 cm^{-1} .



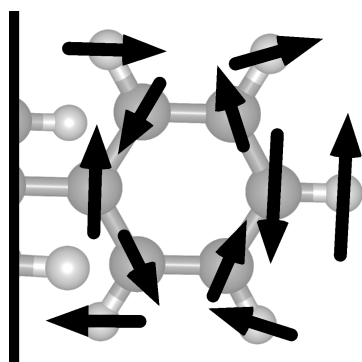
(f) $\nu_{40}(\text{por})$; 1442 cm^{-1} .



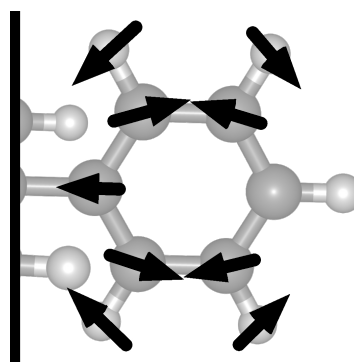
(g) $\mathcal{M}_{24}(b_2)$; 1442 cm^{-1} .



(h) $\mathcal{M}_5(a_1)$; 1488 cm^{-1} .



(i) $\mathcal{M}_{23}(b_2)$; 1577 cm^{-1} .



(j) $\mathcal{M}_4(a_1)$; 1599 cm^{-1} .

Figure A1: (a) & (b) Expansions of the stationary FTIR absorption spectrum of [1] in room-temperature DCM (DCM-d₂) solution, as specified in the subtitles. The numbers and labels indicate peak positions in cm⁻¹ and their assignment. (c) - (j) Ball-and-stick models of [1] and calculated atomic displacement vectors (black arrows) of the normal modes corresponding to the absorption bands shown in (a) and (b). The subtitles specify their notations and experimental resonance frequencies. Atomic color coding: H - white, C - gray, N - blue, Fe - brown.

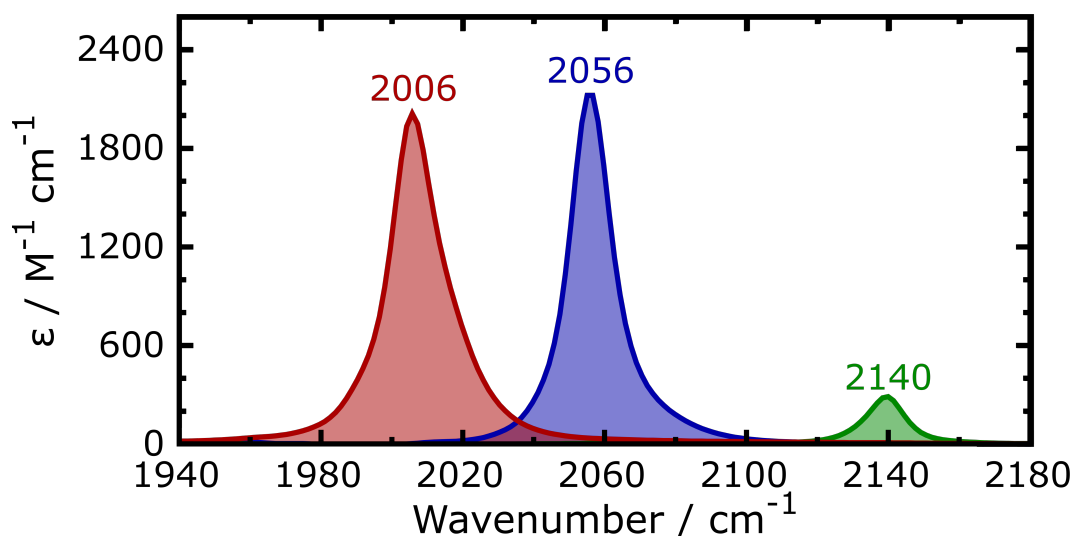


Figure A2: Stationary FTIR absorption spectra of [1] (blue) and N₃⁻ (red) in the region of the antisymmetric N₃-stretching vibration band and *t*BuNC (green) in the region of the C≡N-stretching vibration band. All spectra were recorded in room-temperature DCM solution.⁴ The numbers indicate peak positions in cm⁻¹.

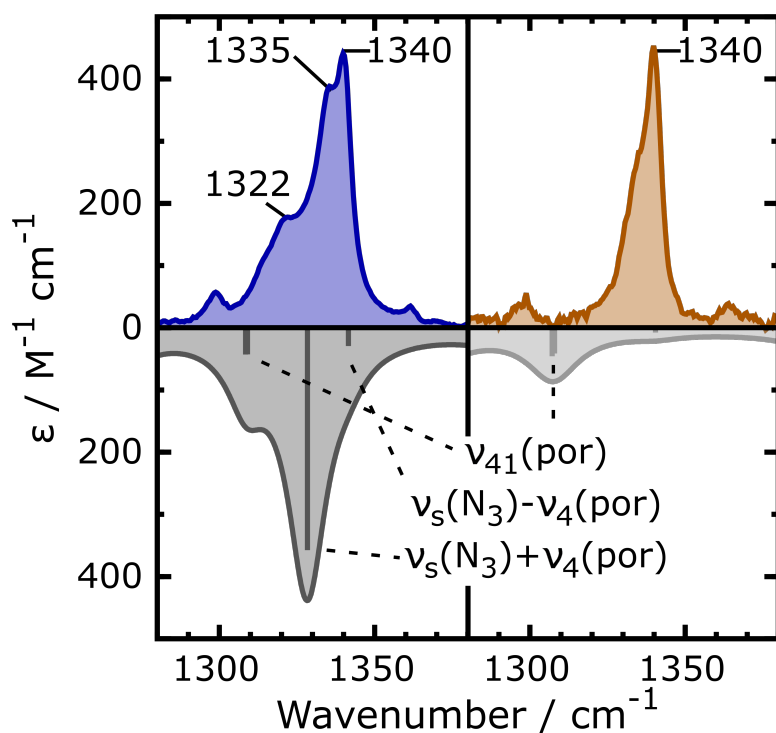


Figure A3: Experimental, stationary FTIR absorption spectra in room-temperature DCM solution and inverted, DFT-calculated IR spectra of [1] (blue and dark gray, respectively) and [6] (orange and light gray, respectively) in the region of the ν_{41} vibration band of the porphyrindiido ligand. The calculated spectra were obtained by convolution of the stick spectra with a Lorentzian function having a FWHM of 20 cm⁻¹. The numbers indicate peak positions in cm⁻¹. The labels assign the frequencies of the stick spectra to their underlying normal modes.

⁴ These spectra were recorded on the Vertex 70 spectrometer (Bruker) with a resolution of 5 cm⁻¹.

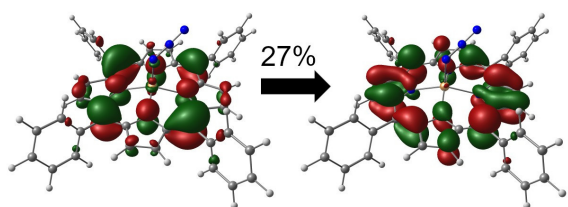
8.2 Natural Transition Orbitals and Excitation Energies

Table A1: Excitation energies, (dipole-length) oscillator strengths, assignment to experimentally observed absorption bands, and characterization of selected electronic transitions of [1](5,0), calculated by TD-DFT. Note that the calculated excitation energies, starting from root 3, have to be frequency down-shifted by 4000 cm⁻¹ to reproduce the experimental spectrum reasonably.

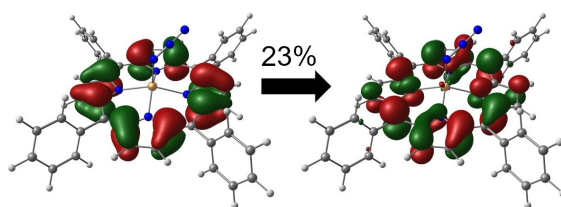
root	ΔE_{calc} / cm ⁻¹	f_{osc}	ΔE_{exp} / cm ⁻¹	λ_{exp} / nm	transitions
1	3279	0.00000463	n.a.	n.a.	Q (a _{1u} , a _{2u} → e _g)
2	3736	0.00000390	n.a.	n.a.	Q (a _{1u} , a _{2u} → e _g)
3	14856	0.00300889	11760	850	a _{2u} → d _{xy} /d _{xz} /d _{yz} (Fe) (β) + a _{1u} → e _g (α)
4	15226	0.00164812			a _{2u} → d _{xy} /d _{xz} /d _{yz} (Fe) (β) + a _{1u} → e _g (α)
5	15518	0.00167908			a _{2u} → d _{xy} /d _{xz} /d _{yz} (Fe) (β) + a _{1u} → e _g (α)
6	16255	0.00015919	n.a.	n.a.	Q (a _{1u} , a _{2u} → e _g)
7	16495	0.00042780	n.a.	n.a.	Q (a _{1u} , a _{2u} → e _g)
8	18589	0.00868976	14560	687	a _{2u} → d _{yz} (Fe) (β) + a _{1u} → e _g (α)
9	19021	0.01242581			a _{2u} → d _{xz} (Fe) (β) + a _{1u} → e _g (α) + π _y ^{nb} (N ₃) → d _{yz} (Fe) (β)
10	19890	0.02590952	15240	656	a _{2u} → d _{z²} (Fe) (β) + π _y ^{nb} → d _{yz} (Fe) (β)
11	20367	0.00311714	n.a.	n.a.	π _y ^{nb} (N ₃) → d _{xz} (Fe) (β)
12	21383	0.00188070	n.a.	n.a.	a _{1u} → d _{xy} (Fe) (β) + a _{2u} → d _{yz} (Fe) (β)
13	21551	0.00180091	n.a.	n.a.	a _{2u} → d _{z²} (Fe) (β) + a _{1u} → d _{xy} (Fe) (β) + π _y ^{nb} (N ₃) → d _{yz} (Fe) (β)
14	22238	0.02528765	17670	566	π _x ^{nb} (N ₃) → d _{yz} (Fe) (β)
15	23067	0.00083471	n.a.	n.a.	π _y ^{nb} (N ₃) → d _{xy} (Fe) (β)
16	23534	0.07340224	19760	506	a _{1u} → d _{yz} (Fe) (β)
17	23777	0.07111802			a _{1u} → d _{xz} (Fe) (β)
18	24684	0.04407340	n.a.	n.a.	a _{1u} → d _{z²} (Fe) (β)
19	25234	0.00292392	n.a.	n.a.	π _y ^{nb} (N ₃) → d _{z²} (Fe) (β)
20	25539	0.00099836	n.a.	n.a.	π _x ^{nb} (N ₃) → d _{xy} (Fe) (β)
21	26455	0.11116384	n.a.	n.a.	π _x ^{nb} (N ₃) → d _{xz} (Fe) (β) + π _y ^{nb} (N ₃) → d _{yz} (Fe) (β)
22	27539	0.11962126	n.a.	n.a.	a _{2u} → d _{x²-y²} (Fe) (β)
23	27898	0.56352751	24150	414	B (a _{1u} , a _{2u} → e _g) + π _x ^{nb} (N ₃) → d _{z²} (Fe) (β)
24	28075	0.51422949			B (a _{1u} , a _{2u} → e _g)
32	29494	0.20426323	n.a.	n.a.	π(por) → e _g
35	30622	0.28395945	27620	362	π _x ^{nb} (N ₃) → d _{z²} (Fe) (β) + π _y ^{nb} (N ₃) → d _{yz} (Fe) (β)
57	38068	0.11619441	>33300	<300	complex
72	39891	0.24102249	>33300	<300	complex
74	40275	0.13263516	>33300	<300	π(por) → d _{z²} (Fe) (β) + π _x ^{nb} (N ₃) → d _{x²-y²} (Fe) (β)

Table A2: Excitation energies and (dipole-length) oscillator strengths of the electronic transitions of [1](5,0) not mentioned in Table A1, calculated by TD-DFT. Note that the calculated excitation energies, starting from root 3, have to be frequency down-shifted by 4000 cm^{-1} to reproduce the experimental spectrum reasonably.

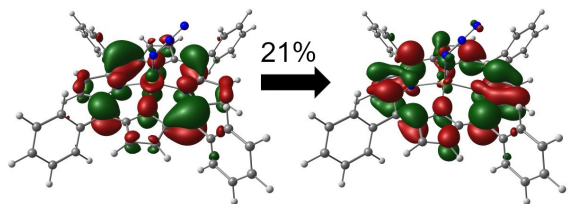
root	ΔE_{calc} / cm^{-1}	f_{osc}	root	ΔE_{calc} / cm^{-1}	f_{osc}	root	ΔE_{calc} / cm^{-1}	f_{osc}
25	28163	0.19041899	53	37503	0.03335636	82	41391	0.00430445
26	28176	0.00872473	54	37633	0.00275328	83	41408	0.00547780
27	28225	0.03594091	55	37840	0.07477187	84	41507	0.00106240
28	28278	0.00301415	56	37910	0.05536594	85	41599	0.00070289
29	28427	0.05245025	58	38154	0.00353659	86	41794	0.01775056
30	29148	0.00013947	59	38505	0.01205195	87	41827	0.02507625
31	29394	0.05902615	60	38717	0.00179415	88	41877	0.02863995
33	29913	0.00337858	61	38752	0.00134854	89	41964	0.02750789
34	30056	0.01886927	62	38824	0.00175144	90	42033	0.00040850
36	31760	0.01127982	63	38854	0.00073055	91	42124	0.01648903
37	32158	0.03145321	64	38889	0.00012313	92	42238	0.00653449
38	32262	0.01449099	65	38895	0.00013964	93	42286	0.01381483
39	32923	0.00041102	66	38938	0.00013533	94	42486	0.01210012
40	34038	0.00410870	67	38975	0.00365287	95	42557	0.02310605
41	34370	0.01635975	68	39031	0.00022752	96	42654	0.03151807
42	34611	0.01602781	69	39437	0.00002319	97	42714	0.02419405
43	34884	0.00377342	70	39494	0.00193812	98	42761	0.01392217
44	35194	0.00049208	71	39603	0.03403842	99	42939	0.05749169
45	35685	0.00830765	73	39949	0.09330138	100	43033	0.00946361
46	36061	0.00051694	75	40418	0.06231870	101	43230	0.01472741
47	36136	0.00009967	76	40564	0.01965041	102	43304	0.08110216
48	36425	0.01380733	77	40698	0.01321826	103	43519	0.04601485
49	36588	0.00456684	78	41022	0.00305071	104	43605	0.00597321
50	36796	0.01175710	79	41093	0.00456698	105	43675	0.01045384
51	37135	0.00287593	80	41130	0.00400757			
52	37365	0.01612827	81	41362	0.00108314			



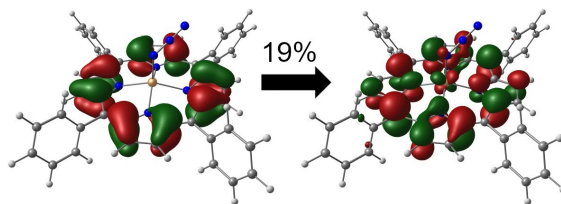
(a) Root 1, α -NTO pair 1.



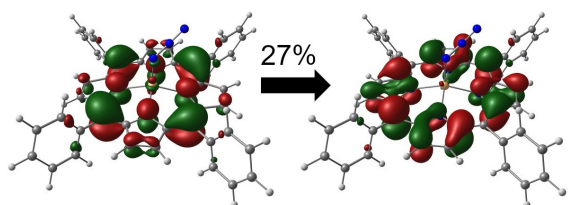
(b) Root 1, α -NTO pair 2.



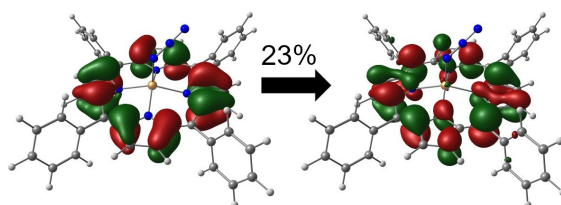
(c) Root 1, β -NTO pair 1.



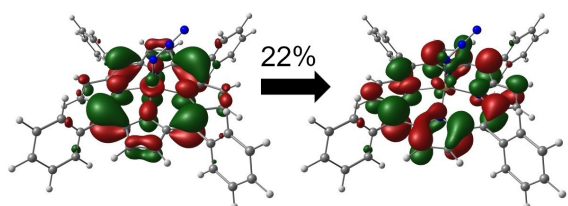
(d) Root 1, β -NTO pair 2.



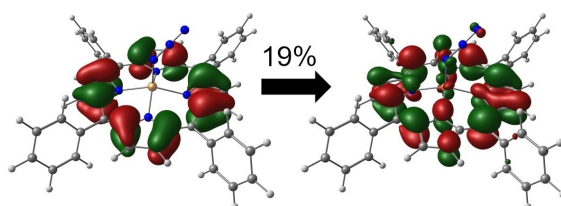
(e) Root 2, α -NTO pair 1.



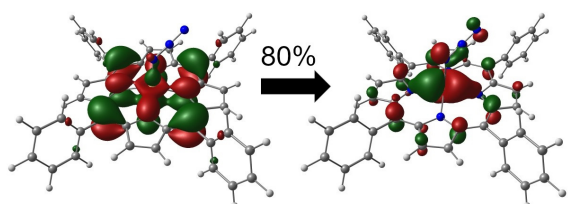
(f) Root 2, α -NTO pair 2.



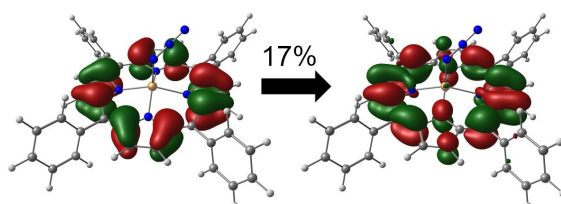
(g) Root 2, β -NTO pair 1.



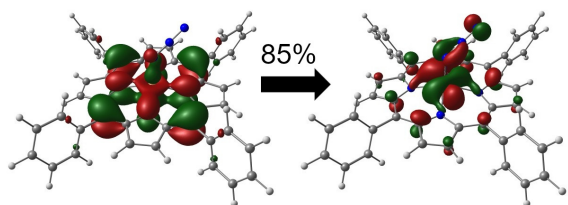
(h) Root 2, β -NTO pair 2.



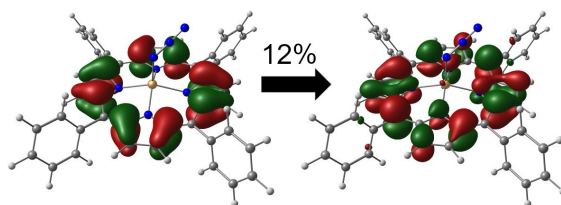
(i) Root 3, β -NTO pair 1.



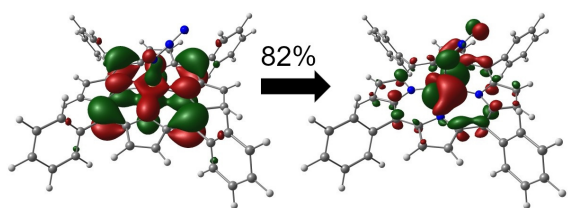
(j) Root 3, α -NTO pair 1.



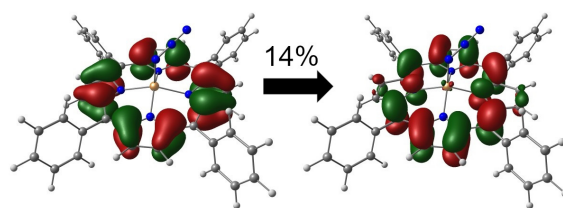
(k) Root 4, β -NTO pair 1.



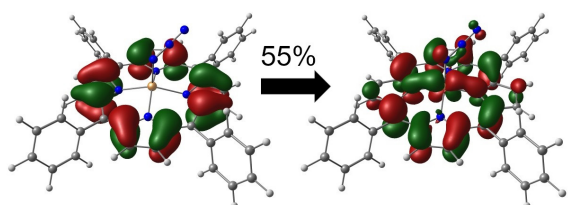
(l) Root 4, α -NTO pair 1.



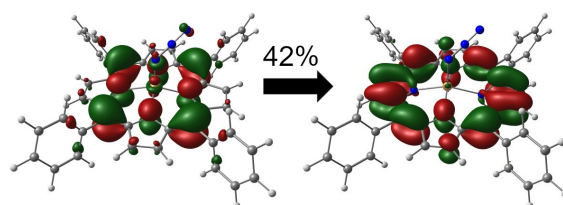
(m) Root 5, β -NTO pair 1.



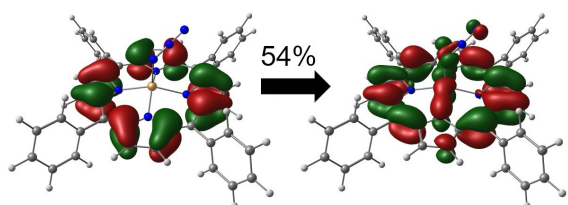
(n) Root 5, α -NTO pair 1.



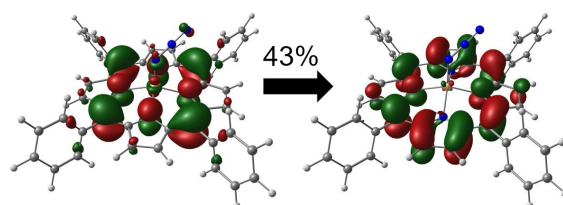
(o) Root 6, β -NTO pair 1.



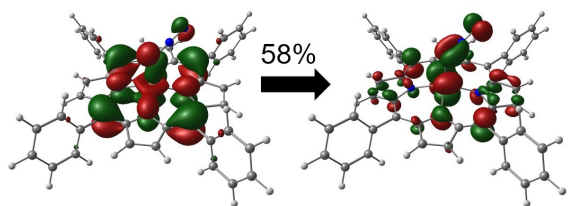
(p) Root 6, α -NTO pair 1.



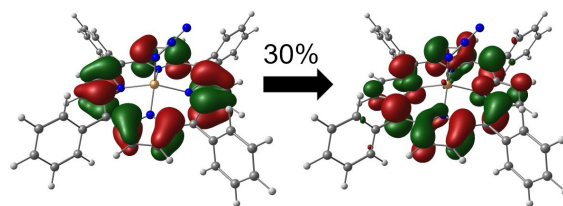
(q) Root 7, β -NTO pair 1.



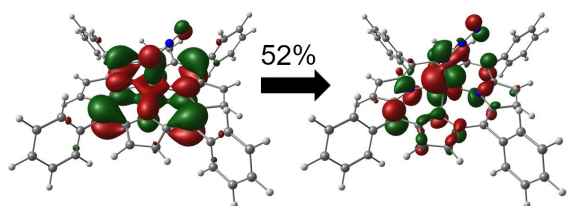
(r) Root 7, α -NTO pair 1.



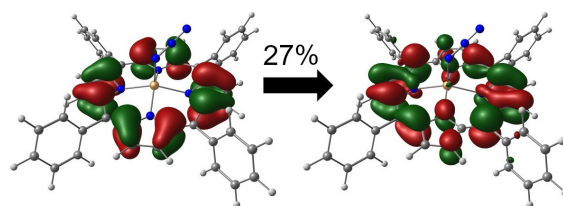
(s) Root 8, β -NTO pair 1.



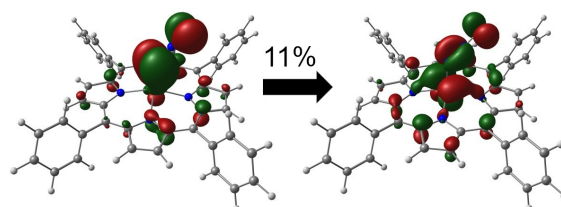
(t) Root 8, α -NTO pair 1.



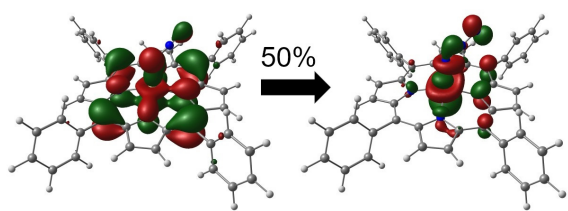
(u) Root 9, β -NTO pair 1.



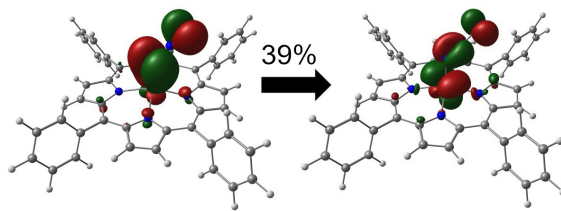
(v) Root 9, α -NTO pair 1.



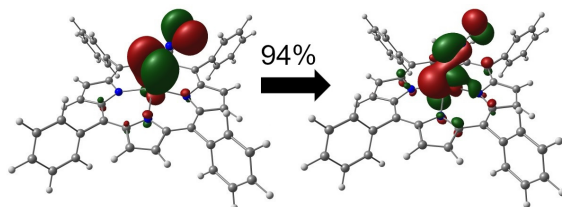
(w) Root 9, β -NTO pair 2.



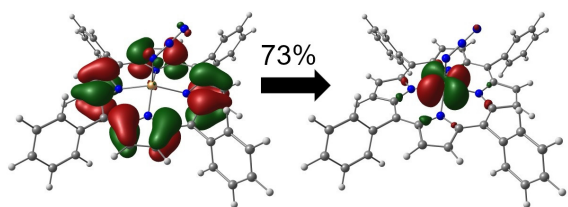
(x) Root 10, β -NTO pair 1.



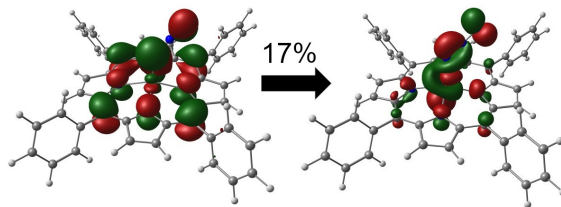
(y) Root 10, β -NTO pair 2.



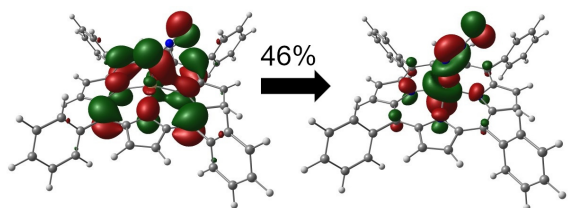
(z) Root 11, β -NTO pair 1.



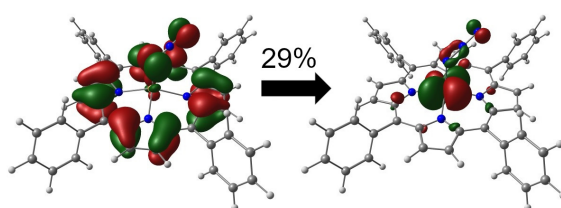
(aa) Root 12, β -NTO pair 1.



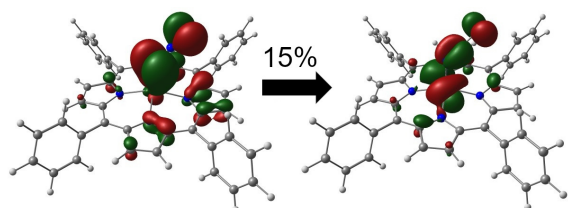
(ab) Root 12, β -NTO pair 2.



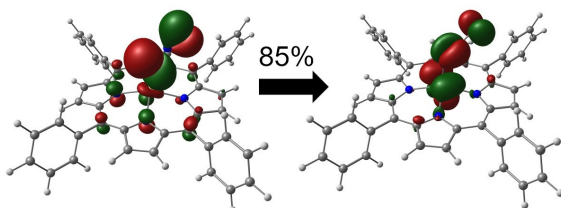
(ac) Root 13, β -NTO pair 1.



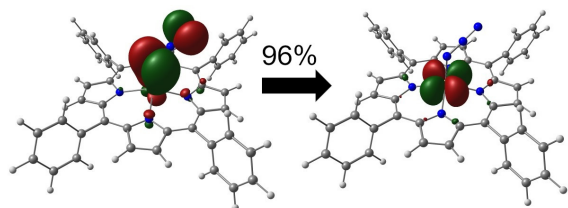
(ad) Root 13, β -NTO pair 2.



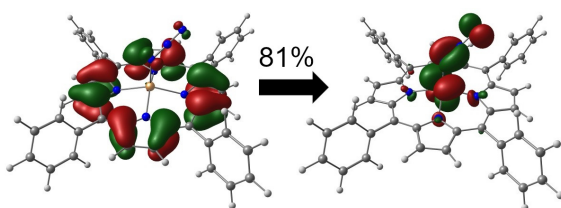
(ae) Root 13, β -NTO pair 3.



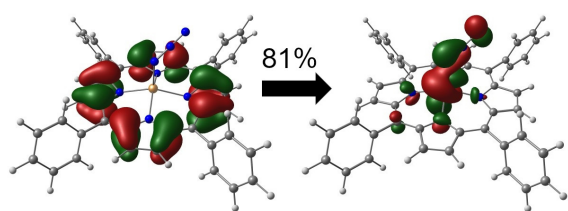
(af) Root 14, β -NTO pair 1.



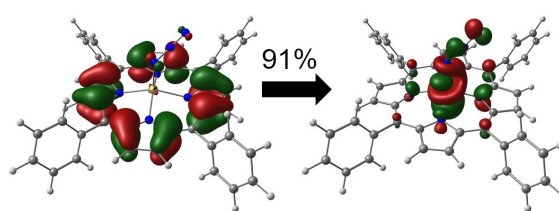
(ag) Root 15, β -NTO pair 1.



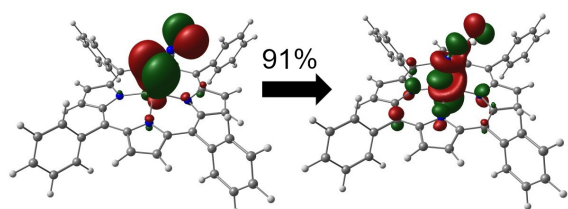
(ah) Root 16, β -NTO pair 1.



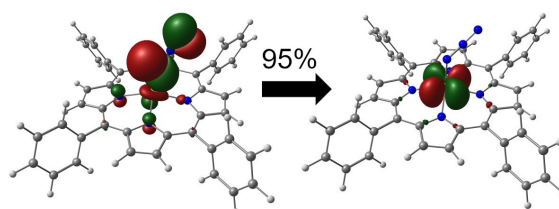
(ai) Root 17, β -NTO pair 1.



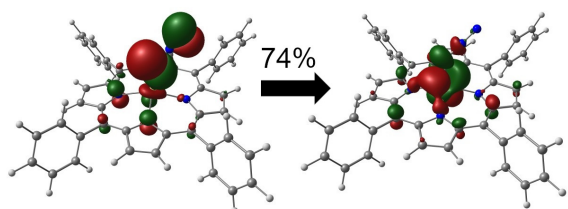
(aj) Root 18, β -NTO pair 1.



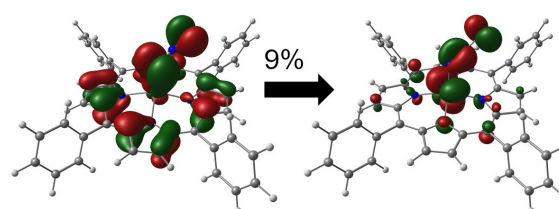
(ak) Root 19, β -NTO pair 1.



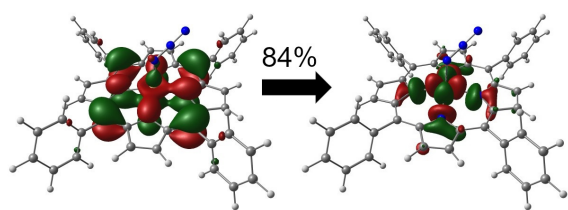
(al) Root 20, β -NTO pair 1.



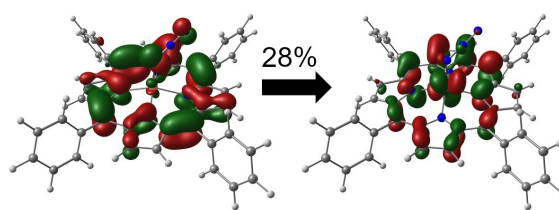
(am) Root 21, β -NTO pair 1.



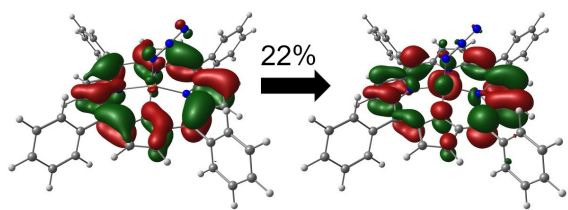
(an) Root 21, β -NTO pair 2.



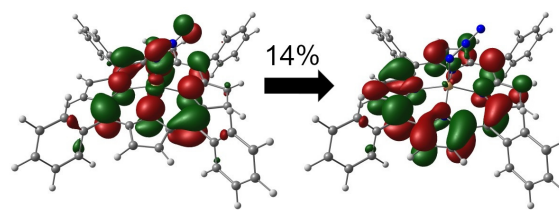
(ao) Root 22, β -NTO pair 1.



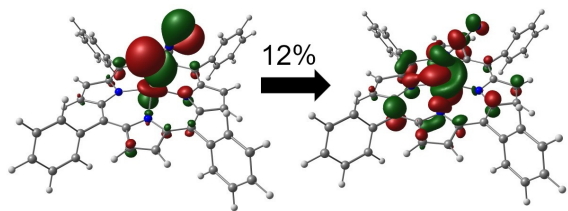
(ap) Root 23, β -NTO pair 1.



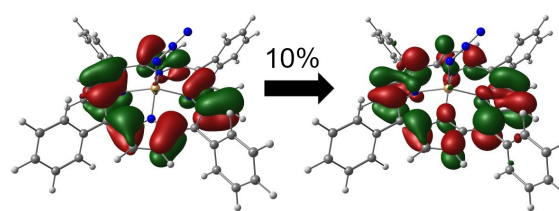
(aq) Root 23, β -NTO pair 2.



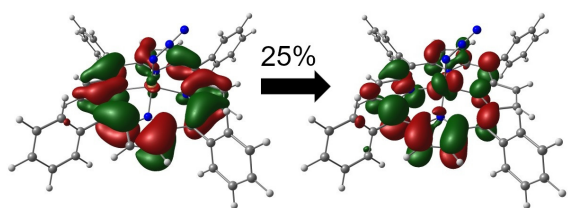
(ar) Root 23, α -NTO pair 1.



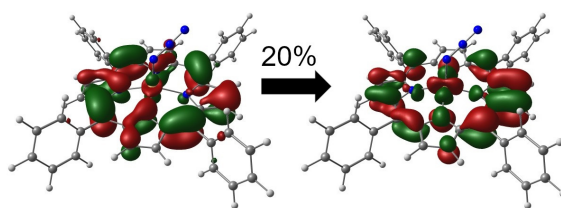
(as) Root 23, β -NTO pair 3.



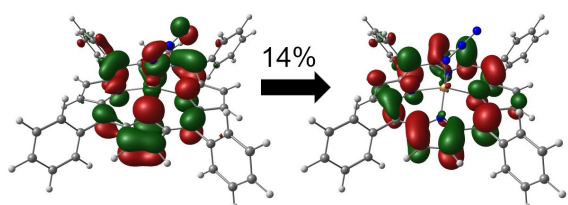
(at) Root 23, α -NTO pair 2.



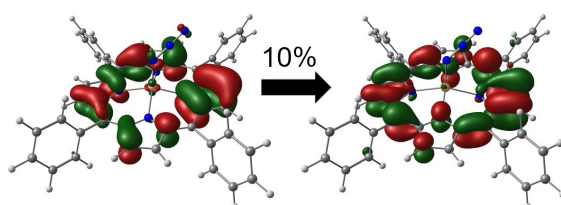
(au) Root 24, β -NTO pair 1.



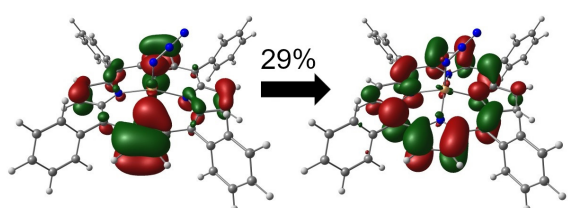
(av) Root 24, β -NTO pair 2.



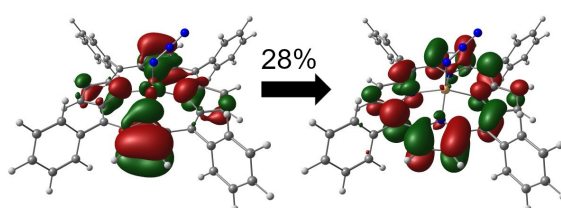
(aw) Root 24, α -NTO pair 1.



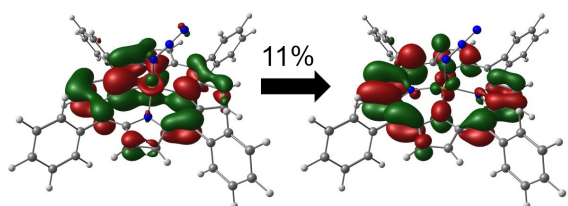
(ax) Root 24, α -NTO pair 2.



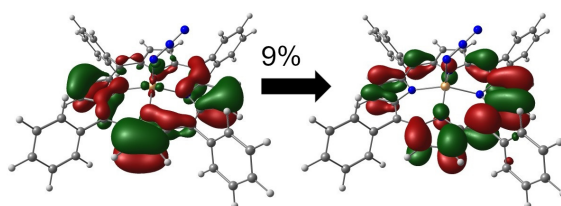
(ay) Root 32, β -NTO pair 1.



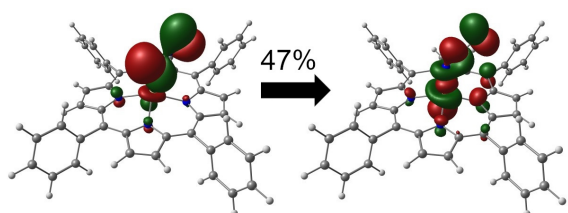
(az) Root 32, α -NTO pair 1.



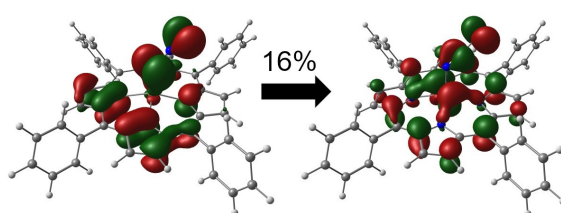
(ba) Root 32, β -NTO pair 2.



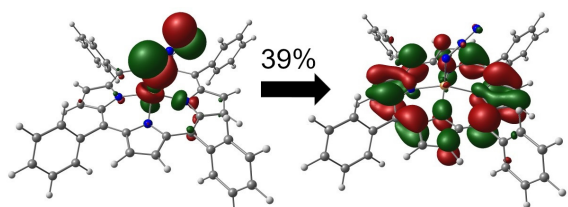
(bb) Root 32, α -NTO pair 2.



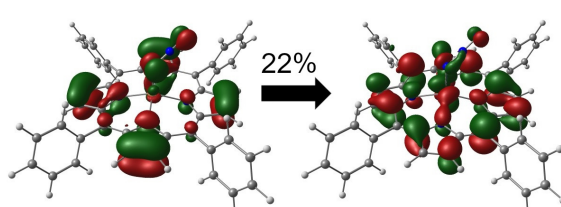
(bc) Root 35, β -NTO pair 1.



(bd) Root 35, β -NTO pair 2.



(be) Root 57, α -NTO pair 1.



(bf) Root 57, β -NTO pair 1.

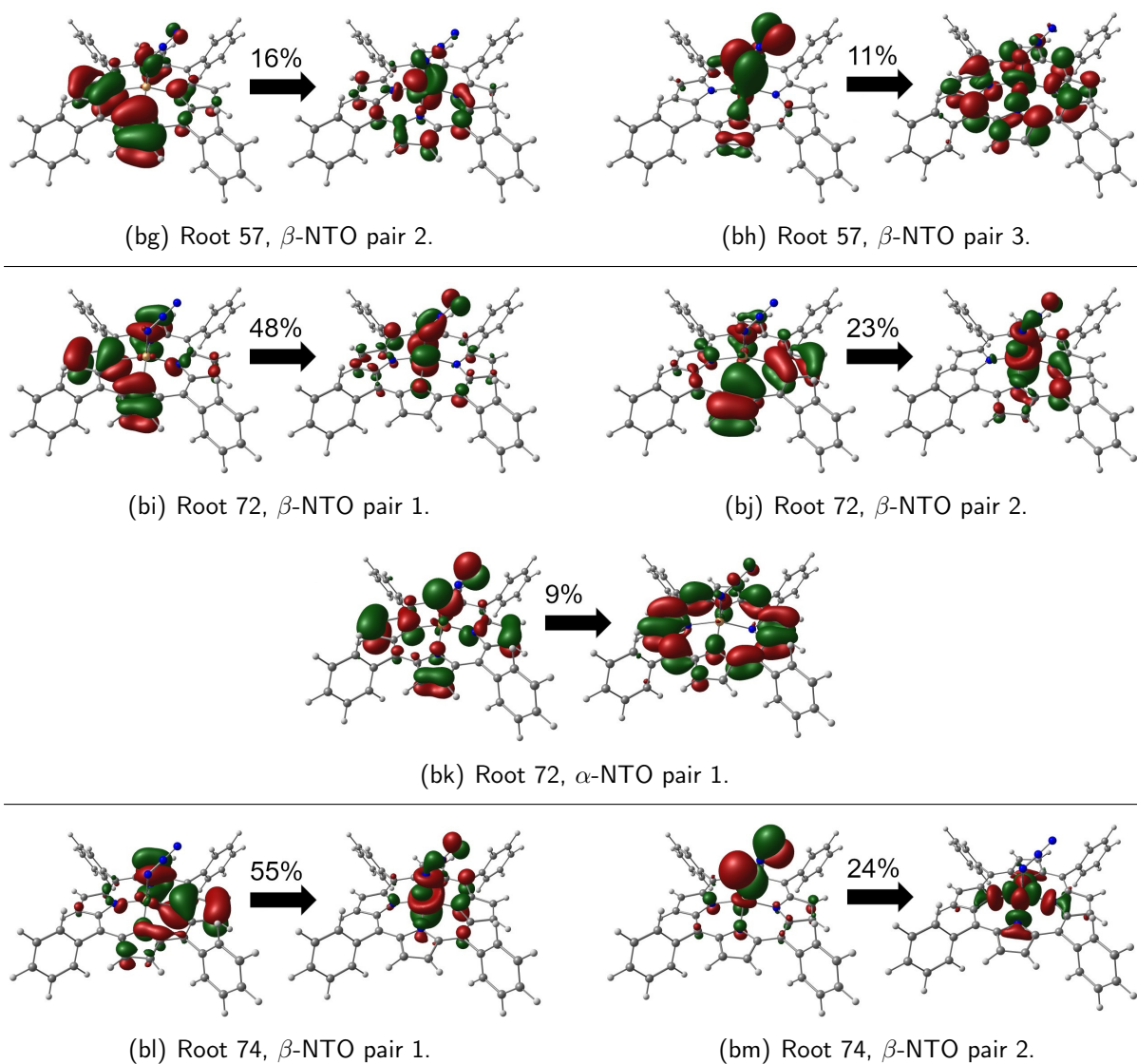


Figure A4: Ball-and-stick models of [1](5,0) and isosurface plots of the natural transition orbital pairs of highest eigenvalues of selected roots, calculated by TD-DFT. The subtitles indicate the corresponding root and the spin function of a NTO pair, while the numbers above the arrows specify their contribution to the excitation. Isovalues: ± 0.03 . Atomic color coding: H - white, C - gray, N - blue, Fe - brown.

8.3 Additional UV/Vis-Pump/mIR-Probe Data

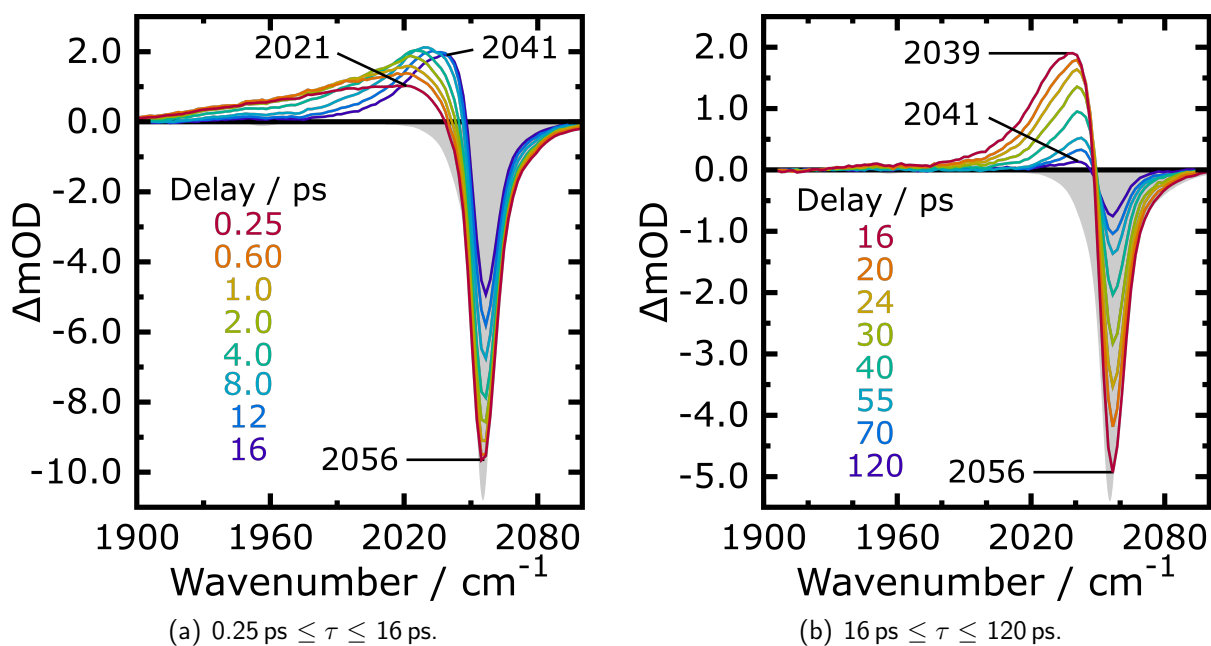


Figure A5: Transient $12 \mu\text{J}$, 400 nm -pump/ $1900\text{-}2100 \text{ cm}^{-1}$ -probe spectra of [1] in room-temperature DCM solution at various pump-probe delays, as specified in the legends. The gray areas represent the inverted, properly scaled, stationary FTIR spectrum of [1]. The black numbers indicate peak positions in cm^{-1} .

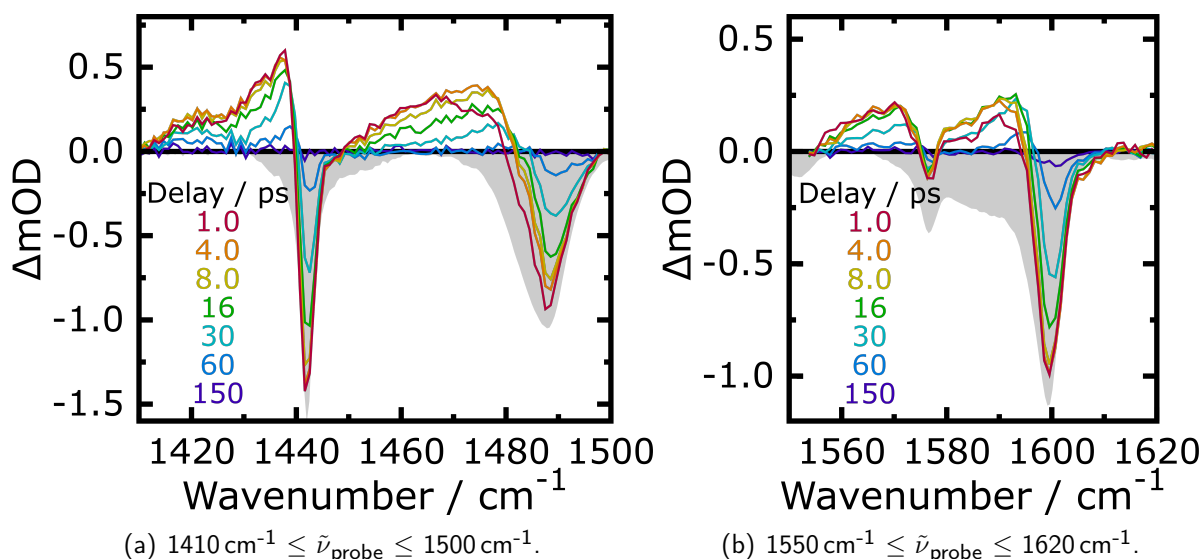


Figure A6: Transient $12 \mu\text{J}$, 400 nm -pump/mIR-probe spectra of [1] in room-temperature DCM solution, recorded in the probe regions (a) from 1410 cm^{-1} to 1500 cm^{-1} and (b) from 1550 cm^{-1} to 1620 cm^{-1} and at various pump-probe delays, as indicated by the legends. The gray areas represent the inverted, properly scaled, stationary FTIR spectrum of [1].

Table A3: (Multi)exponential fit parameters of the 16 μJ , 400 nm-pump/1300-1370 cm^{-1} -probe kinetic traces of [1] in room-temperature DCM solution.

$\tilde{\nu} / \text{cm}^{-1}$	$\Delta\text{mOD}(0)_1$	τ_1 / ps	$\Delta\text{mOD}(0)_2$	τ_2 / ps	$\Delta\text{mOD}(0)_3$	τ_3 / ps	$\Delta\text{mOD}(\infty)$
1306.3			0.41	10.1			-0.01
1306.9			0.41	8.9			0.01
1307.5			0.46	12.1			-0.02
1308.1			0.46	11.1			0.00
1308.7			0.48	11.6			0.01
1309.3			0.48	13.3			0.00
1309.9			0.50	11.5			-0.01
1310.5			0.52	12.5			-0.01
1311.1			0.53	12.6			0.00
1311.7			0.50	11.2			0.00
1312.3			0.53	12.4			-0.01
1312.9			0.51	11.3			0.01
1313.5			0.51	10.0			-0.02
1314.1			0.53	10.5			-0.02
1314.8			0.53	9.3			-0.01
1315.3			0.52	10.2			-0.04
1316.0			0.52	10.5			-0.02
1316.5			0.49	10.2			-0.01
1317.2			0.48	12.2			-0.03
1317.8			0.48	10.4			0.00
1318.4			0.48	11.8			-0.01
1319.0			0.51	11.9			-0.02
1319.6			0.50	11.2			0.00
1320.2			0.51	13.3			-0.05
1320.9			0.50	13.4			0.00
1321.4					0.52	14.9	-0.02
1322.1					0.56	17.5	-0.04
1322.7					0.57	17.1	0.01
1323.3					0.66	20.3	-0.05
1323.9					0.70	22.0	-0.03
1324.6					0.77	24.2	-0.01
1325.1			-2.24	12.8	3 ^[a]	15.8	-0.04
1325.8			-0.67	9.7	1.46	18.9	0.00
1326.4			-0.68	8.6	1.48	19.9	-0.02
1327.0			-2.18	12.6	3 ^[a]	17.5	-0.03
1327.6			-1.74	11.4	2.55	18.0	0.00
1328.3			-2.17	12.0	3 ^[a]	18.4	-0.05
1328.8			-2.22	12.5	3 ^[a]	19.1	-0.02
1329.5			-2.25	12.6	3 ^[a]	20.0	-0.04
1330.1	0.25	0.82	-1.08	7.6	1.61	24.3	-0.04
1330.8	0.24	0.79	-1.32	8.8	1.77	23.7	-0.03
1331.3	0.29	0.85	-1.16	7.9	1.48	26.6	-0.04
1332.0	0.36	0.70	-1.25	8.5	1.39	26.9	-0.03
1332.6	0.35	0.88	-1.23	8.4	1.24	28.5	-0.03
1333.2	0.40	0.81	-1.49	10.3	1.31	25.4	-0.04
1333.8	0.48	0.93	-1.22	9.0	0.86	29.8	-0.03
1334.5	0.49	0.93	-1.36	9.9	0.83	26.0	-0.03
1335.1	0.45	0.85	-3 ^[a]	13.7	2.40	18.7	-0.02

1335.8	0.49	0.75	-3 ^[a]	13.5	2.29	18.5	0.02
1336.3	0.45	0.93	-3 ^[a]	14.1	2.18	19.9	0.01
1337.0	0.49	0.91	-3 ^[a]	14.6	2.04	19.8	0.01
1337.6	0.39	0.80	-3 ^[a]	16.9	1.97	24.9	0.03
1338.3	0.38	1.14	-3 ^[a]	18.5	1.63	27.8	0.02
1338.9	0.45	1.02	-3 ^[a]	21.3	1.34	32.7	0.04
1339.5	0.47	1.41			-2.10	20.8	0.09
1340.1	0.54	1.27			-2.19	24.8	0.11
1340.8	0.53	1.38			-2.12	30.6	0.18
1341.4	0.46	3.13			-2.02	30.4	0.21
1342.1	0.35	1.63			-1.41	34.9	0.29
1342.6			0.30	5.2	-1.29	31.3	0.31
1343.3	0.22	3.59			-0.87	33.3	0.32
1343.9	0.25	3.06			-0.78	32.2	0.37
1344.6	0.12	3.38			-0.56	35.0	0.35
1345.2	0.17	1.17			-0.43	34.0	0.32
1345.9			0.12	5.2	-0.38	20.2	0.26
1346.5			0.48	8.6	-0.69	12.8	0.20
1347.1					-0.20	20.4	0.17
1347.7					-0.17	17.1	0.11
1348.4					-0.14	24.8	0.08
1349.1					-0.15	20.6	0.09
1349.7					-0.05	66.8	0.00
1350.3					-0.11	26.8	0.03

^[a] enforced boundary.

Table A4: (Multi)exponential fit parameters of the 16 μJ , 400 nm-pump/1300-1370 cm^{-1} -probe kinetic traces of **[1]** in room-temperature DCM-d₂ solution.

$\tilde{\nu} / \text{cm}^{-1}$	$\Delta\text{mOD}(0)_1$	τ_1 / ps	$\Delta\text{mOD}(0)_2$	τ_2 / ps	$\Delta\text{mOD}(0)_3$	τ_3 / ps	$\Delta\text{mOD}(\infty)$
1306.9			0.55	8.2			-0.01
1309.3			0.58	9.0			-0.01
1311.6			0.60	8.2			0.00
1313.9			0.51	9.1			-0.02
1316.3			0.44	15.0			-0.05
1318.7			0.42	13.2			-0.02
1321.0					0.45	17.6	-0.03
1323.4					0.61	29.9	-0.07
1325.8	-2.34	0.3	-0.82	6.0			1.41
1328.2	-3 ^[a]	0.2	-2.31	11.6			2.90
1330.6	-3 ^[a]	0.2	-2.55	11.4	3 ^[a]	20.0	-0.04
1333.0	-3 ^[a]	0.2	-3 ^[a]	12.6	2.94	20.7	-0.02
1335.5	-3 ^[a]	0.2	-3 ^[a]	13.9	2.28	21.4	0.03
1337.9	0.97	4.9	-3 ^[a]	11.2	1.10	26.6	0.06
1340.3					-2.05	23.5	3.00
1342.8	0.22	1.2			-3 ^[a]	22.6	1.49
1345.3	0.07	1.0			-2.64	27.2	1.93
1347.7	0.29	0.9			-3 ^[a]	23.8	2.72
1350.2					-0.16	48.3	0.13

^[a] enforced boundary.

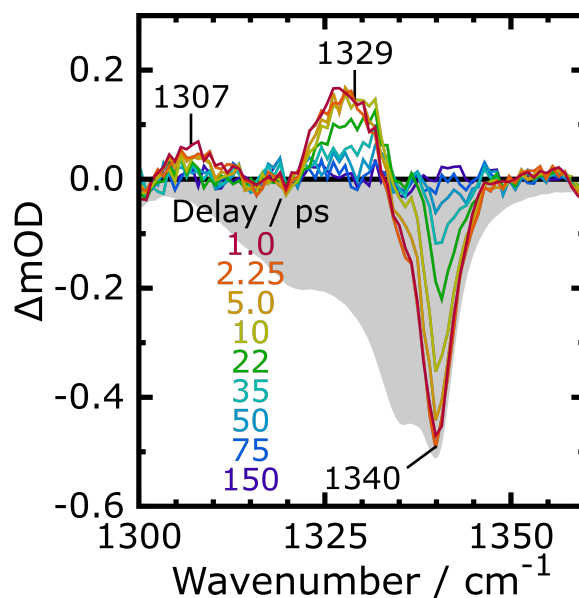


Figure A7: Transient $3 \mu\text{J}$, 400 nm -pump/ $1300\text{-}1370 \text{ cm}^{-1}$ -probe spectra of **[1]** in room-temperature DCM solution at various pump-probe delays, as specified in the legend. The gray area represents the inverted, properly scaled, stationary FTIR spectrum of **[1]**. The black number indicate peak positions in cm^{-1} .

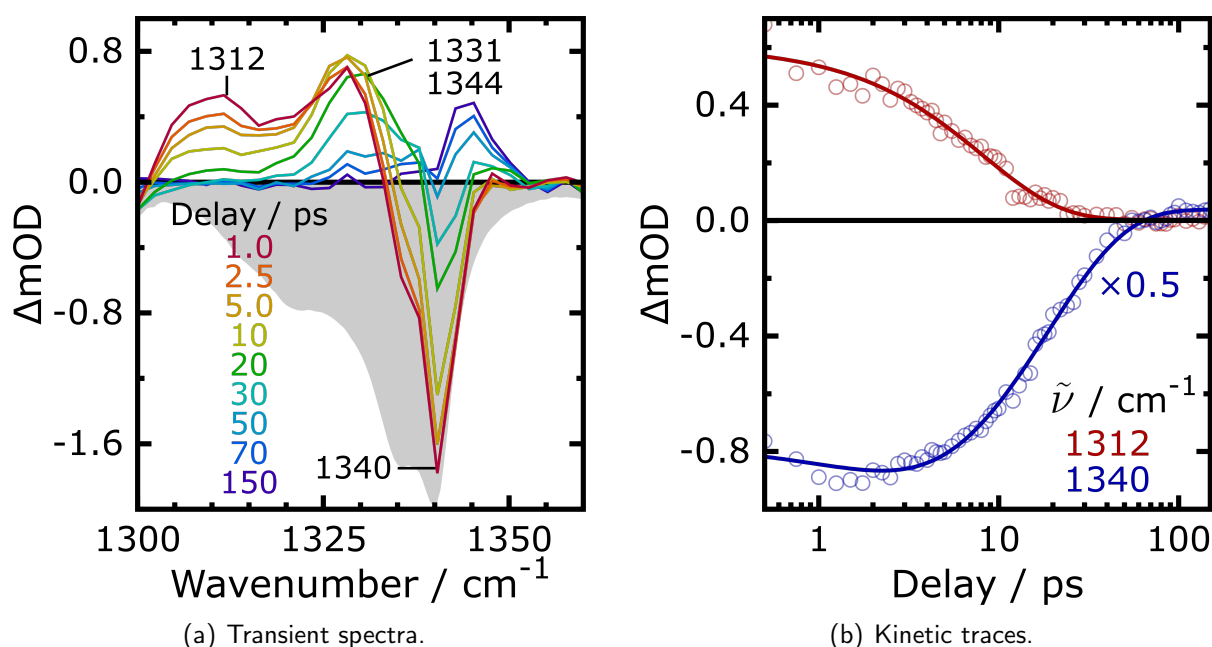


Figure A8: (a) Transient $16 \mu\text{J}$, 400 nm -pump/ $1300\text{-}1370 \text{ cm}^{-1}$ -probe spectra of **[1]** in room-temperature DCM- d_2 solution at various pump-probe delays, as specified in the legend. The gray area represents the inverted, properly scaled, stationary FTIR spectrum of **[1]**. The black numbers indicate peak positions in cm^{-1} . (b) Kinetic traces at the frequencies specified in the legend. Circles and solid lines represent experimental data and mono- or biexponential fit functions, respectively.

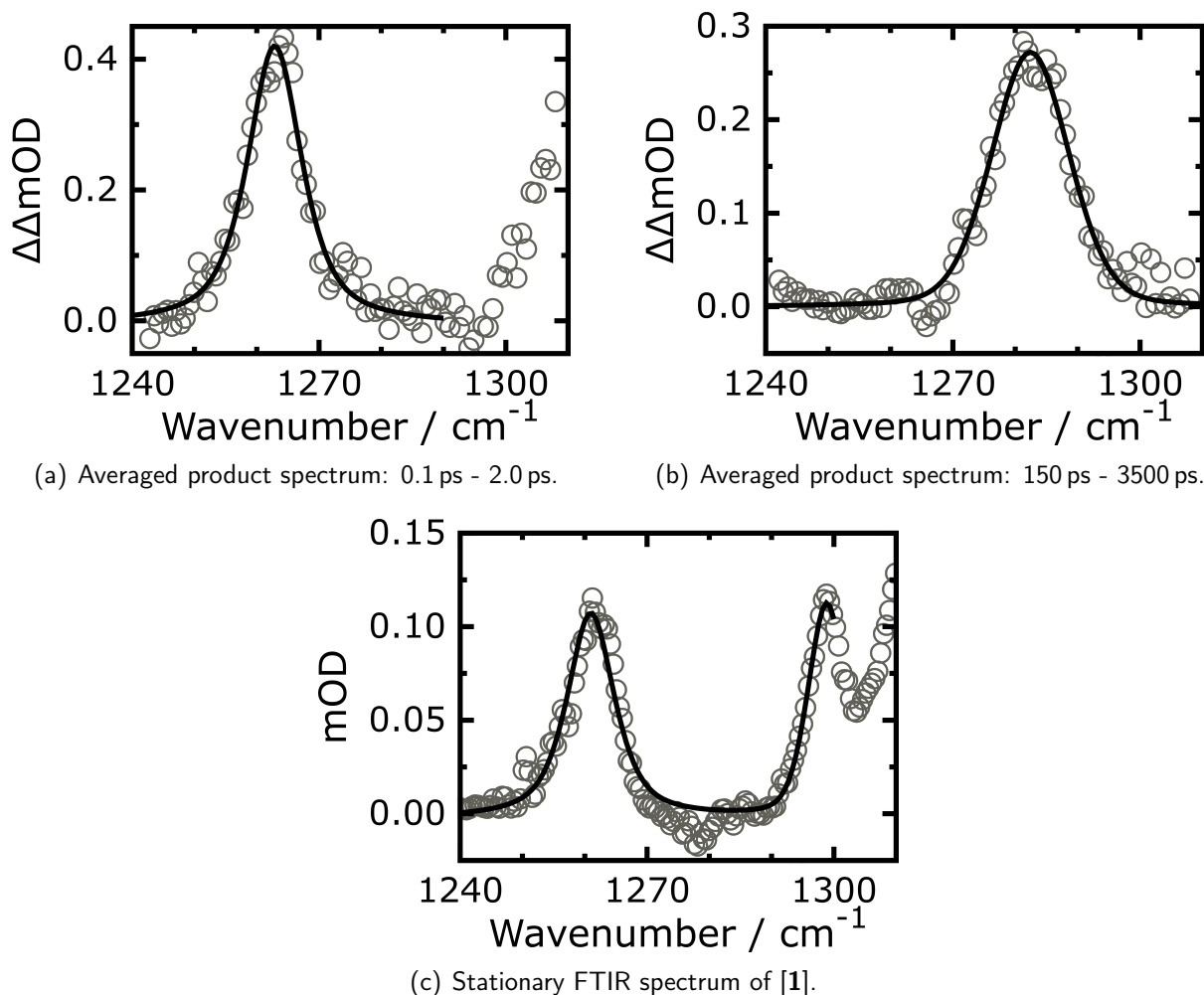


Figure A9: (a) & (b) Product spectra of the $16\ \mu\text{J}$, $400\ \text{nm}$ -pump/ 1240 - $1310\ \text{cm}^{-1}$ -probe experiment of [1], averaged over the delay ranges specified in the subtitles. (c) Stationary FTIR-spectrum of [1] in the same spectral region. The spectrum is normalized to the integral of the absorption band peaking at $1299\ \text{cm}^{-1}$. Gray circles represent the experimental data and black lines pseudo-Voigt regression functions (see also Table A5).

Table A5: Fit parameters of pseudo-Voigt functions describing the signals observed in the product spectra of the $16\ \mu\text{J}$, $400\ \text{nm}$ -pump/ 1240 - $1310\ \text{cm}^{-1}$ -probe experiment of [1] at early and late pump-probe delays, and the stationary FTIR spectrum of [1] in the same region. The product spectra were averaged within the delay ranges from $0.1\ \text{ps}$ to $2.0\ \text{ps}$ and from $150\ \text{ps}$ to $3500\ \text{ps}$, respectively. The parameter $(\Delta\Delta)\text{mOD}_{\text{off}}$ describes the offset of the pseudo-Voigt functions.

spectrum	A / cm^{-1}	$\tilde{\nu}_0 / \text{cm}^{-1}$	ω / cm^{-1}	η	$(\Delta\Delta)\text{mOD}_{\text{off}}$
product: 0.1-2.0 ps	6.29 ± 0.69	1262.9 ± 0.2	10.4 ± 0.5	0.77 ± 0.18	-0.0065 ± 0.0104
product: 150-3500 ps	4.63 ± 0.53	1282.4 ± 0.1	14.6 ± 0.4	0.25 ± 0.24	-0.0004 ± 0.0057
[1] (stat.) {	$1.00^{[a]} \pm 0.15$	1298.9 ± 0.7	7.1 ± 0.3	0.41 ± 0.22	$-0.0030^{[a]} \pm 0.0025$
	$1.40^{[a]} \pm 0.14$	1261.0 ± 0.2	9.1 ± 0.4	0.75 ± 0.17	

[a] normalized to integral of the band centered at $1298.9\ \text{cm}^{-1}$.

Table A6: Monoexponential fit parameters of the time-dependent integrals of the functions specified in Table A5.

$\tilde{\nu}_0 / \text{cm}^{-1}$	$A(\infty) / \text{cm}^{-1}$	A_1 / cm^{-1}	τ_1 / ps
1263	0.01 ± 0.04	6.12 ± 0.09	17.0 ± 0.7
1282	4.87 ± 0.04	-5.00 ± 0.05	27.3 ± 0.9
1299	-0.15 ± 0.02	-2.01 ± 0.03	20.6 ± 0.9

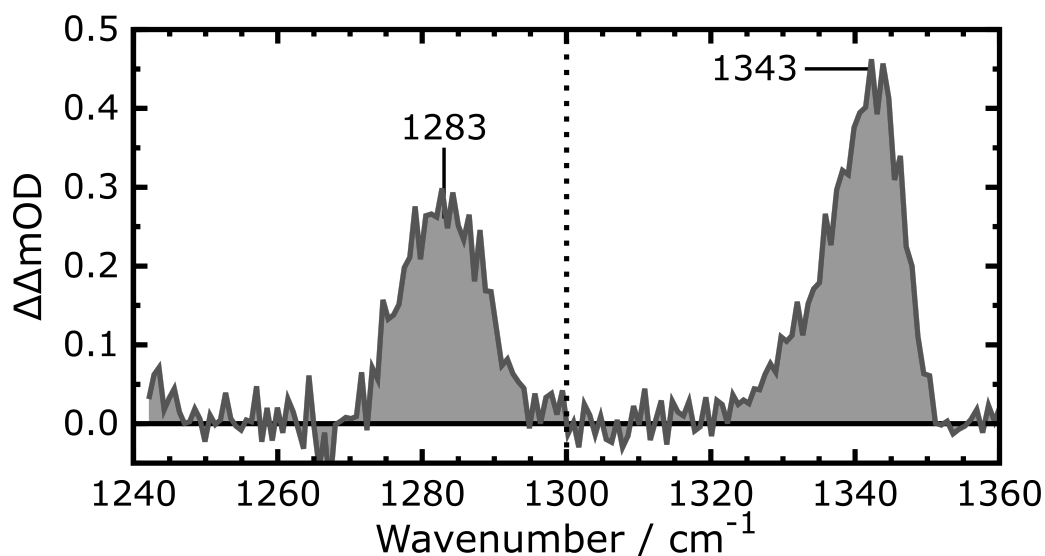


Figure A10: mlR product spectrum of the 16 μJ , 400 nm-photolysis of [6] in room-temperature DCM- d_2 (left panel) and DCM solution (right panel), averaged over pump-probe delays from 150 ps to 250 ps. The numbers indicate peak positions in cm^{-1} .

8.4 Additional UV/Vis-Pump/Vis-Probe Data

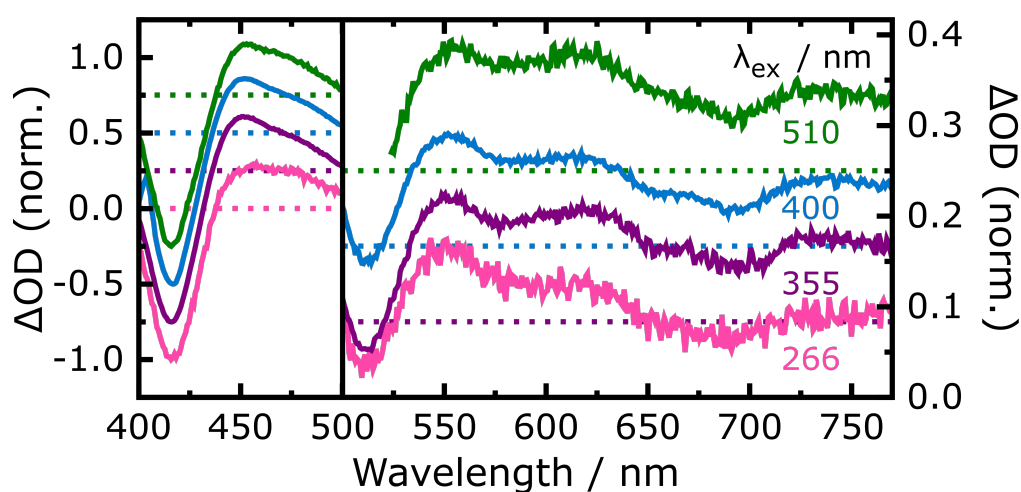
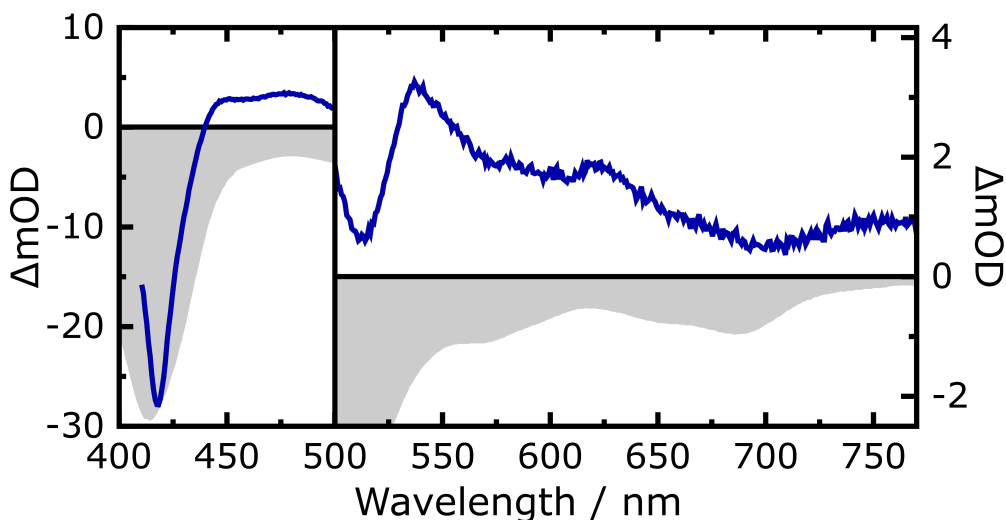
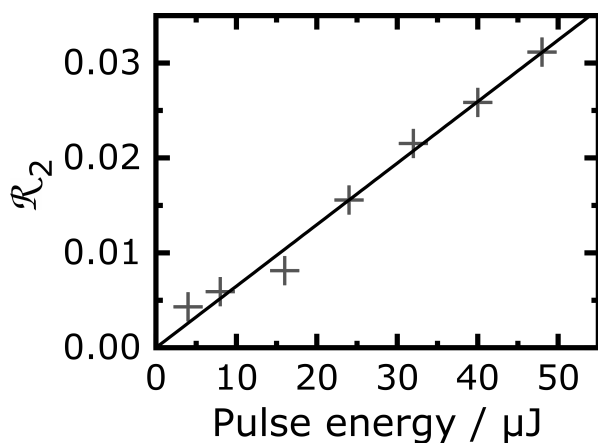


Figure A11: Normalized transient 35 μJ , UV/Vis-pump/Vis-probe spectra of [1] in room-temperature DCM solution, recorded at a pump-probe delay of 0.16 ps for different excitation wavelengths, as specified in the legend. Note that the scaling of the ordinate changes above a wavelength of 500 nm and that the spectra are vertically shifted. Dotted, colored lines represent the zero lines of the spectra.



(a) Transient Vis spectrum after 35 μJ , 400 nm excitation, averaged over delays from 150 ps to 1000 ps.



(b) Pulse energy dependent, relative signal strength.

$$\mathcal{R}_2 = -\frac{\Delta\text{OD}(535 \text{ nm}, 100\text{-}150 \text{ ps}, E_{\text{pump}})}{\Delta\text{OD}(415\text{-}420 \text{ nm}, 0.8\text{-}1.0 \text{ ps}, E_{\text{pump}})} \quad (42)$$

Figure A12: (a) Transient 35 μJ , 400 nm-pump/Vis-probe spectrum of [1] in room-temperature DCM solution, averaged over pump-probe delays from 150 ps to 1000 ps (blue line) and inverted, properly scaled, stationary UV-Vis spectrum of [1] (gray area). Note that the scaling of the ordinate changes above a wavelength of 500 nm. (b) Ratio of the signal strengths (gray crosses) of the residual transient absorption at 535 nm and the initial bleaching signal (415-420 nm) in dependence of the energy of the pump pulse. The black line represents a proportional regression function.

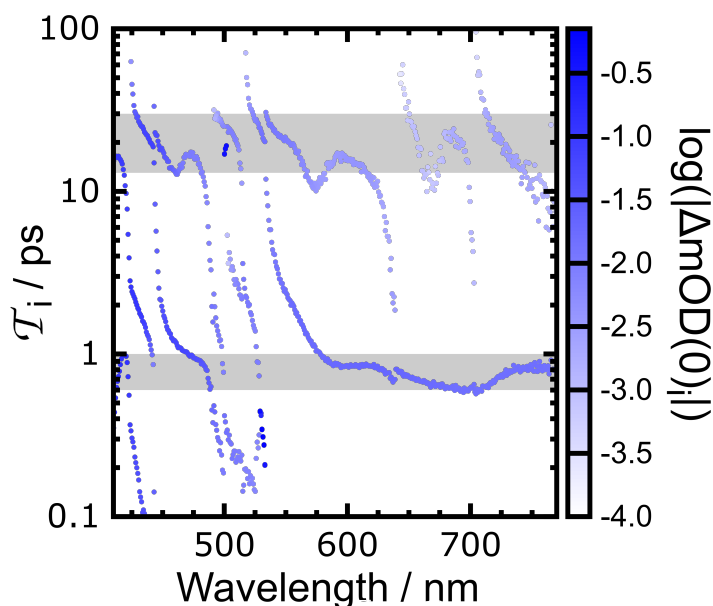


Figure A13: Time constants obtained from bi- or triexponential fits of the 8 μJ , 400 nm-pump/Vis-probe kinetic traces of [1] in room-temperature DCM solution. The saturation of a point indicates the absolute value of the amplitude corresponding to this time constant, as specified in the color map. Gray areas emphasize time frames with accumulations of individual time constants.

8.5 Detailed Computational Procedure and Results

Initially, the molecular orbitals and geometries of the relevant complexes were optimized in several feasible spin multiplicities without any restrictions. Table A7 list the electronic structures, in terms of the allocation of unpaired electrons, obtained this way.

Table A7: Simplified electron configurations of the DFT-optimized structures of the complexes relevant for this work for various feasible spin multiplicities.

complex	spin multiplicity	($S(\text{FeX}), S(\text{por})$)	complex	spin multiplicity	($S(\text{FeX}), S(\text{por})$)
[1]	doublet	(1,0)	[4]	doublet	(1,0)
	quartet	(3,0)		quartet	(3,0)
	sextet	(5,0) ^[a]		sextet	(5,0) ^[a]
	octet	(5,2)		[5]	doublet ^[b]
[2]	doublet	(1,0) ^[a]	[6]	sextet ^[b]	(5,0)
	quartet	(3,0)	[6 _{ox}]	singlet	(1,-1)
	sextet	(5,0)		triplet	(1,1)
[3]	doublet	(2,-1) ^[a]		quintet	(5,-1) ^[a]
	quartet	(3,0)	septet	(5,1)	
	sextet	(4,1)	[7]	doublet	(2,-1) ^[a]
[3 _{red}]	singlet	(2,-2)		quartet	(2,1)
	triplet	(2,0) ^[a]		sextet	(4,1)
	quintet	(4,0)	[1 _{ox}]	triplet	(3,-1)
	septet	(4,2)	quintet	(5,-1)	
			[Zn(p)]	singlet	(0,0) ^[c]

[a] electronic ground state according to these calculations. [c] calculated in closed-shell formalism.

[b] electronic ground state according to experimental findings.^[246,255]

These systems were utilized as starting points in the optimization of other electron configurations. Starting orbitals for new electron configurations were obtained by transferring a defined number of iron-centered d-orbitals with α -spin of the already converged structures to the β -orbital set. This procedure was realized by the built-in function 'flip' of the program package TURBOMOLE implemented in the setup program 'define'. This function performs a localization of the molecular orbitals and allows a transfer of occupied orbitals from the α - to the β -subset and vice versa. If the resulting configurations had more β - than α -electrons, contrary to the convention, the two orbital subsets were exchanged. In more detail, the starting orbitals of the individual electron configurations were set up as described in the following:

- ◆ Other triplet porphyrin states of [1]: [1](3,2), [1](1,2), [1](-1,2), [1](3,-2), and [1](5,-2) were generated by spin flip of one, two, three, four, and five $d(\alpha, \text{Fe})$ -orbitals of [1](5,2), respectively.
- ◆ π -radical porphyrin states of [1]: [1](4,-1) and [1](4,1) were generated by filling an additional electron into the lowest unoccupied $d(\beta, \text{Fe})$ -orbital of [1_{ox}](5,-1) and spin flip of four $d(\alpha, \text{Fe})$ -orbitals in the latter case. [1](2,-1), [1](0,-1), and [1](2,1) were

generated by filling an additional electron into the lowest unoccupied $d(\beta, \text{Fe})$ -orbital of $[\mathbf{1}_{\text{ox}}](3,-1)$ and spin flip of one and two $d(\alpha, \text{Fe})$ -orbitals in the latter two cases, respectively.

- ◆ Other triplet porphyrin states of $[\mathbf{2}]$ were generated analogously to those of $[\mathbf{1}]$ starting from $[\mathbf{2}](5,2)$.
- ◆ π -radical porphyrin states of $[\mathbf{2}]$: The optimized orbitals of $[\mathbf{7}](2,-1)$, $[\mathbf{7}](2,1)$, $[\mathbf{7}](4,-1)$, and $[\mathbf{7}](4,1)$ were directly used as starting orbitals for $[\mathbf{2}](2,-1)$, $[\mathbf{2}](2,1)$, $[\mathbf{2}](4,-1)$, and $[\mathbf{2}](4,1)$, respectively. A calculation of $[\mathbf{2}](0,1)$ was not attempted.
- ◆ Other triplet porphyrin states of $[\mathbf{3}_{\text{red}}]$: $[\mathbf{3}_{\text{red}}](2,2)$, $[\mathbf{3}_{\text{red}}](0,2)$, $[\mathbf{3}_{\text{red}}](2,-2)$, and $[\mathbf{3}_{\text{red}}](4,-2)$ were generated by spin flip of one, two, three, and four $d(\alpha, \text{Fe})$ -orbitals of $[\mathbf{3}_{\text{red}}](4,2)$, respectively.
- ◆ π -radical porphyrin states $[\mathbf{3}_{\text{red}}]$: $[\mathbf{3}_{\text{red}}](1,-1)$ and $[\mathbf{3}_{\text{red}}](1,1)$ were generated by filling an additional electron into the lowest unoccupied $d(\beta, \text{Fe})$ -orbital of $[\mathbf{3}](2,-1)$ and spin flip of one $d(\alpha, \text{Fe})$ -orbital in the latter case. $[\mathbf{3}_{\text{red}}](3,1)$ and $[\mathbf{3}_{\text{red}}](3,-1)$ were generated by filling an additional electron into the lowest unoccupied $d(\beta, \text{Fe})$ -orbital of $[\mathbf{3}](4,1)$ and spin flip of three $d(\alpha, \text{Fe})$ -orbitals in the latter case.
- ◆ $[\mathbf{3}_{\text{red}}](0,0)$ was calculated in the closed-shell formalism.
- ◆ $[\mathbf{6}_{\text{ox}}](3,-1)$ and $[\mathbf{6}_{\text{ox}}](3,1)$ were generated by spin flip of one $d(\alpha, \text{Fe})$ -orbital of $[\mathbf{6}_{\text{ox}}](5,-1)$ and $[\mathbf{6}_{\text{ox}}](5,1)$, respectively.
- ◆ $[\mathbf{7}](4,-1)$ was generated by spin flip of four $d(\alpha, \text{Fe})$ -orbitals of $[\mathbf{7}](4,1)$. A calculation of $[\mathbf{7}](0,1)$ was not attempted.

Subsequently, the molecular orbitals of all new electron configurations were optimized in self-consistent field (SCF) procedures within the geometry of the systems from which their respective starting orbitals were derived. In the calculations of the π -radical porphyrin states of $[\mathbf{2}]$, the geometry of the corresponding state of $[\mathbf{7}]$ was utilized after substitution of a nitrogen atom for the axial oxygen atom. Here, all π -radical configurations of $[\mathbf{1}]$, $[\mathbf{2}]$, and $[\mathbf{3}_{\text{red}}]$, except of $[\mathbf{2}](4,1)$, did not survive the SCF calculations, but converged to the respective configuration of the same spin multiplicity listed in Table A7 instead. Moreover, the SCF calculation of $[\mathbf{3}_{\text{red}}](0,2)$ failed to converge.

Next, the geometries of the remaining systems were optimized. In this step, the calculation of $[\mathbf{2}](4,1)$ lost its initial π -radical electron configuration and converged to $[\mathbf{2}](5,0)$ instead. Hence, the optimizations of all π -radical structures of $[\mathbf{1}]$, $[\mathbf{2}]$, and $[\mathbf{3}_{\text{red}}]$ as ground state configurations by DFT were unsuccessful. Similarly, the calculation of $[\mathbf{2}](5,-2)$ converged to the closed-shell porphyrin system $[\mathbf{2}](3,0)$. All other calculations, i.e. triplet porphyrin states of $[\mathbf{1}]$, $[\mathbf{2}]$, and $[\mathbf{3}_{\text{red}}]$ as well as $[\mathbf{6}_{\text{ox}}](3,1)$, $[\mathbf{6}_{\text{ox}}](3,-1)$, and $[\mathbf{7}](4,-1)$, retained the electron configuration provided by the starting orbitals during the geometry optimization. The optimized

structures were tested to be true, local minimum structures by stability analyses and frequency calculations. While the stability analysis was successful in all cases, the systems [1](1,2), [1](-1,2), [1](5,-2), [2](1,2), and [6_{ox}](3,-1) were found to be insufficiently converged after the frequency calculations. In contrast, the remaining systems represent metastable structures according to the theoretical method. Their relative energies and calculated distribution of unpaired electrons in terms of $S_c(\text{FeX})$ and $S_c(\text{por})$ are given in Table A8, and their optimized geometries are listed in section 8.9.

Table A8: Relative energies and calculated distribution of unpaired electrons of the complexes relevant for this work for different electron configuration.

complex	($s(\text{FeX})$, $s(\text{por})$)	($S_c(\text{FeX})$, $S_c(\text{por})$)	E_{rel} / cm^{-1} (E_{abs} / E_h)	
[1]	(1,0)	(1.07,-0.07)	3423	
	(3,0)	(2.94,0.05)	779	
	(5,0)	(4.49,0.50) ⁵	0 (-3339.798057)	
	(3,2)	(2.99,1.92)	12651	
	(5,2)	(4.56,2.32)	11444	
	(3,-2)	(2.82,-1.73)	10351	
[2]	(1,0)	(0.95,0.05)	0 (-3230.225223)	
	(3,0)	(2.94,0.06)	6631	
	(5,0)	(4.75,0.25)	11924	
	(3,2)	(2.72,2.18)	15964	
	(5,2)	(4.68,2.21)	22887	
	(-1,2)	(-0.93,1.83)	12412	
[3 _{red}]	(0,0)	(0.00,0.00)	11646	
	(2,0)	(1.98,0.02)	0 (-3175.591885)	
	(4,0)	(3.72,0.28)	1706	
	(2,2)	(2.01,1.88)	12560	
	(4,2)	(3.74,2.15)	12202	
	(2,-2)	(1.94,-1.85)	10418	
[4]	(1,0)	(1.06,-0.05)	3854	
	(3,0)	(2.93,0.06)	1179	
	(5,0)	(4.49,0.50) ⁵	0 (-3480.898520)	
	[6 _{ox}]	(1,1)	(1.15,0.87)	5602
		(3,1)	(3.00,0.97)	3376
		(5,1)	(4.52,1.44)	1227
(1,-1)		(0.98,-0.97)	6131	
(5,-1)		(4.47,-0.35)	0 (-3635.591784)	
[7]	(2,1)	(2.04,0.95)	1797	
	(4,1)	(3.92,1.11)	2848	
	(2,-1)	(1.98,-0.99)	0 (-3250.508384)	
	(4,-1)	(3.67,-0.68)	3404	

⁵ [1](5,0) and [4](5,0) were found to have a significant spin density localized at the porphyrin ligand (about 0.5 electrons). However, this is not indicative of a π -radical configuration of these cases, because the unpaired electron responsible for this effect occupies the $\sigma^*_{x^2-y^2}$ -orbital.

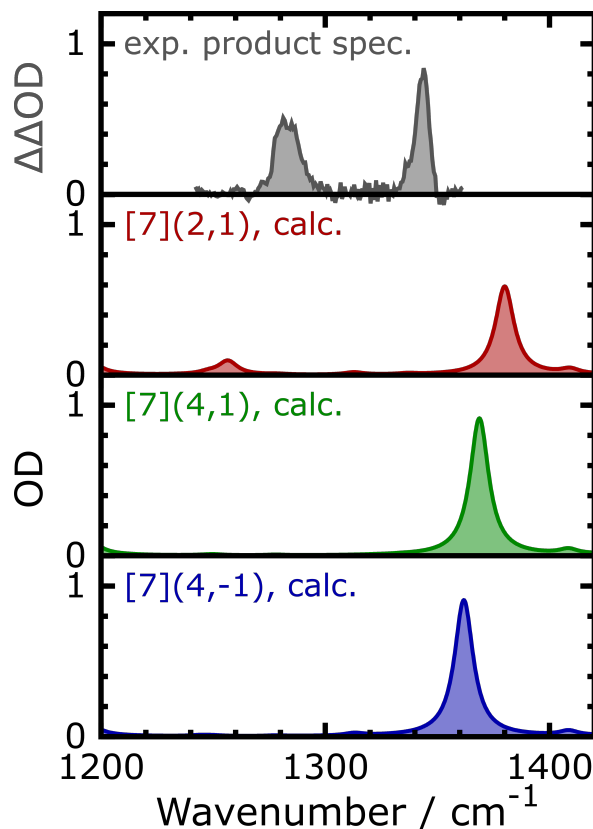


Figure A14: Upper panel: mIR product spectrum of the photolysis of [1] with 16 μJ , 400 nm-pump pulses in room-temperature DCM/DCM- d_2 solution, averaged over pump-probe delays from 150 ps to 3.5 ns. Other panels: DFT-predicted IR absorption spectra of [7](2,1) (red), [7](4,1) (green), and [7](4,-1) (blue), obtained by convolution of the stick spectra with a Lorentzian function ($\text{FWHM} = 10 \text{ cm}^{-1}$). In all panels, an optical density of one is equivalent to an extinction coefficient of ca. $3000 \text{ M}^{-1} \text{ cm}^{-1}$.

Table A9: Energetically lowest excitations of significant por \rightarrow Fe CT character of [1], [2], and [3_{red}] for three spin multiplicities, calculated by TD-DFT. Root numbers, assignments from NTO analyses, and excitation energies.

complex (<i>s</i> (FeX), <i>s</i> (por))	root	assignment	ΔE_{calc} / cm^{-1}
[1](1,0)	11	$a_{2u} \rightarrow d_{z^2}(\text{Fe}) (\alpha + \beta)$	16133
[1](3,0)	5	$a_{2u} + d_{z^2}(\text{Fe}) \rightarrow d_{x^2-y^2} (\beta)$	11757
[1](5,0)	3	$a_{2u} \rightarrow d_{xy/xz/yz}(\text{Fe})(\beta) + a_{1u} \rightarrow e_{g,y}(\alpha)$	14856
[2](1,0)	19	$a_{2u} \rightarrow d_{yz}(\text{Fe})(\alpha) + \pi_{xz}(\text{FeN}) \rightarrow d_{x^2-y^2}(\text{Fe})(\beta)$	26186
[2](3,0)	17	$a_{2u} \rightarrow \pi_{yz}(\text{FeN})(\beta) + a_{1u} \rightarrow e_{g,x}(\alpha)$	21476
[2](5,0)	9	$a_{2u} \rightarrow \pi_{yz}(\text{FeN})(\beta) + a_{1u} \rightarrow e_{g,x}(\alpha)$	13674
[3 _{red}](0,0)	4	$a_{2u} \rightarrow d_{z^2}(\text{Fe})$	20620
[3 _{red}](2,0)	>35	–	>33000
[3 _{red}](4,0)	11	$\pi(\text{por}) \rightarrow \sigma^*_{x^2-y^2} (\alpha)$	16244

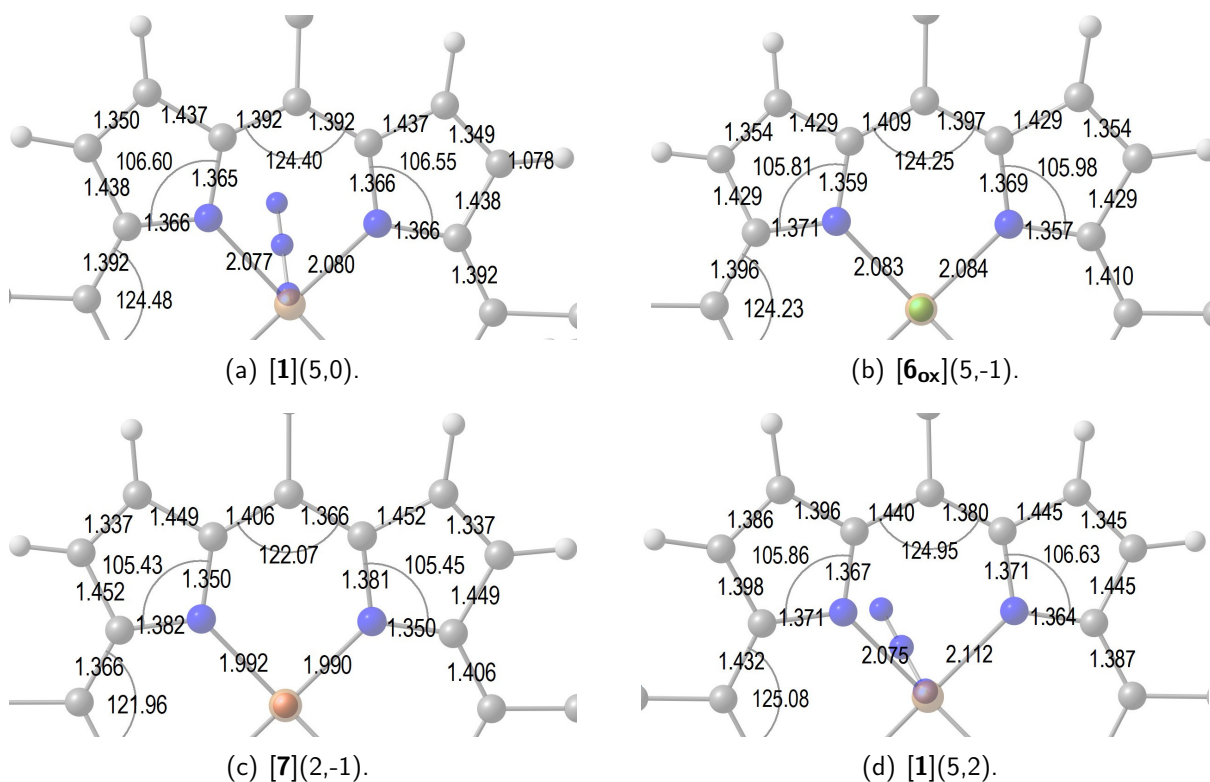


Figure A15: Selected bond lengths (in Å) and bond angles (in °) of the tpp²⁻-ligands of four complexes of distinct electronic structures, as specified in the subtitles. Atomic color coding: H - white, C - gray, N - blue, O - red, Cl - green, Fe - brown.

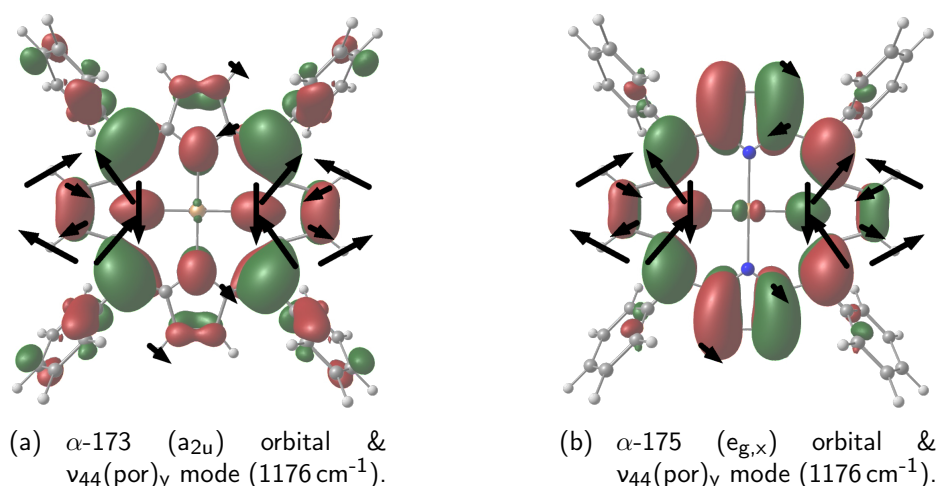


Figure A16: Ball-and-stick models of $[\mathbf{3}_{\text{red}}](2,2)$, isosurface plots of its porphyrin-centered SOMOs, and displacement vectors of the normal mode $\nu_{44}(\text{por})_y$ (black arrows), calculated via DFT. The subtitles specify the spin functions, the numbers of the orbitals (within a α -spin subset), and their assignments according to the Gouterman model as well as the computed resonance frequencies of the normal mode. Isovalues: ± 0.02 . Atomic color coding: H - white, C - gray, N - blue, Fe - brown.

8.6 List of Figures

1	Lewis formulae of Compound 1 and $[\text{Fe}(\text{tpp})(\text{N})]$ (2).	2
2	Illustrations of the working principle of time-resolved spectroscopy after UV/Vis-excitation. Schematic energy level diagrams and transient spectra.	11
3	Schematic visualization of a vibrational energy relaxation, including energy level diagrams and absorption spectra.	13
4	Stationary UV-Vis absorption spectrum of $[\text{Zn}(\text{p})]$ in room-temperature <i>n</i> -octane solution ^[226] and schematic energy level diagram of the frontier orbitals (Gouterman orbitals) of $[\text{Zn}(\text{p})]$, including ball-and-stick models of the complex and isosurface plots of the orbitals.	24
5	Schematic energy level diagram of the 3d-orbitals of the iron atoms in the complexes $[\mathbf{3}_{\text{red}}]$, 1 , and 2 .	26
6	Schematic energy level diagram of the frontier orbitals of 2 and 7 .	28
7	Ball-and-stick models of $[\text{Zn}(\text{p})]$, isosurface plots of its $3a_{2u}$ - and $1a_{1u}$ -orbital, and displacement vectors of the normal modes $\nu_{41}(\text{por})$ and $\nu_{37}(\text{por})$.	31
8	Schematic setup of the rapid-scan experiment.	36
9	Schematic setup of the UV/Vis-pump/mIR-probe experiment.	39
10	Schematic setup of the UV/Vis-pump/Vis-probe experiment.	40
11	Stationary FTIR absorption spectrum of 1 in room-temperature DCM (DCM- d_2) solution. (a) Experimental and DFT-predicted spectrum and assignment. (b) & (c) Expansions of the experimental spectrum in the spectral regions important in this work. (d), (e) & (f) Ball-and-stick models of 1 and calculated atomic displacement vectors of the normal modes corresponding to the absorption bands shown in (b) and (c).	44
12	Stationary UV-Vis absorption spectrum of 1 in room-temperature DCM solution. (a) Experimental and TD-DFT-predicted spectrum. (b) - (f): Ball-and-stick models of 1 and isosurface plots of natural transition orbitals of selected roots.	47
13	Dependence of the late 400 nm-pump/1900-2100 cm^{-1} -probe spectra of 1 in room-temperature DCM solution on the energy of the pump pulse at constant pulse diameter. (a) Transient spectra recorded 200 ps after photoexcitation, normalized to the initial bleaching signal. (b) Primary quantum yields determined for various pump pulse energies and proportional regression function. (c) Product spectrum after 12 μJ , 400 nm-excitation of 1 in the spectral region around the $\nu_{\text{as}}(\text{N}_3)$ resonance band, averaged over delays from 150 ps to 3.5 ns, and stationary FTIR spectrum of 1 .	54
14	Transient 3 μJ , 400 nm-pump/1900-2100 cm^{-1} -probe spectra of 1 in room-temperature DCM solution at various pump-probe delays and time dependence of fit parameters (band integrals, peak position and bandwidth).	56
15	Transient 8 μJ , 400 nm-pump/Vis-probe spectra of 1 in room-temperature DCM solution, at various pump-probe delays.	60

16	8 μJ , 400 nm-pump/Vis-probe kinetic traces of the [1] in room-temperature DCM solution at selected probe wavelengths and bi- or triexponential fit functions.	61
17	Product spectra obtained from the 8 μJ , 400 nm-pump/Vis-probe spectra of [1] in room-temperature DCM solution and TD-DFT-predicted spectra of the lowest sextet, quartet, and doublet state of [1].	63
18	De-excitation scheme of [1] following SPA and proposed schemes of [6] from references [369] and [377].	65
19	Transient 16 μJ , 400 nm-pump/1300-1370 cm^{-1} -probe spectra and kinetic traces of [1] in room-temperature DCM solution and ratio of the amplitudes of the residual transient absorption band and the initial bleaching signal in dependence on the energy of the pump pulse.	68
20	Transient 16 μJ , 400 nm-pump/1240-1310 cm^{-1} -probe spectra and kinetic trace of [1] in room-temperature DCM-d ₂ solution.	70
21	mIR product spectrum of the photolysis of [1] with 16 μJ , 400 nm-pump pulses in room-temperature DCM/DCM-d ₂ solution, averaged over pump-probe delays from 150 ps to 3500 ps.	71
22	Schematic energy level diagrams of the frontier orbitals of [1]. The individual panels show different electron configurations of an overall quartet multiplicity.	72
23	mIR product spectrum of the photolysis of [1] with 16 μJ , 400 nm-pump pulses in room-temperature DCM/DCM-d ₂ solution, averaged over delays from 150 ps to 3.5 ns, and DFT-predicted IR absorption spectra of [1](<i>n</i> ,0) (<i>n</i> = 1, 3, 5).	74
24	mIR product spectrum of the photolysis of [1] with 16 μJ , 400 nm-pump pulses in room-temperature DCM/DCM-d ₂ solution, averaged over delays from 150 ps to 3.5 ns, and DFT-predicted IR absorption spectra of [2](<i>n</i> ,0) (<i>n</i> = 1, 3, 5).	74
25	mIR product spectrum of the photolysis of [1] with 16 μJ , 400 nm-pump pulses in room-temperature DCM/DCM-d ₂ solution, averaged over delays from 150 ps to 3.5 ns, and DFT-predicted IR absorption spectra of [3 _{red}](<i>n</i> ,0) (<i>n</i> = 0, 2, 4).	75
26	mIR product spectrum of the photolysis of [1] with 16 μJ , 400 nm-pump pulses in room-temperature DCM/DCM-d ₂ solution, averaged over delays from 150 ps to 3.5 ns, and DFT-predicted IR absorption spectra of [6 _{ox}](5,-1) and [7](2,-1).	75
27	Ball-and-stick models of (a) [6 _{ox}](5,-1) and (b) [7](2,-1), isosurface plots of their lowest unoccupied and three highest occupied molecular spin orbitals, and displacement vectors of the normal mode having an unusually high absorption strength, calculated via DFT.	77
28	mIR product spectrum of the photolysis of [1] with 16 μJ , 400 nm-pump pulses in room-temperature DCM/DCM-d ₂ solution, averaged over delays from 150 ps to 3.5 ns, and DFT-predicted IR absorption spectra of [1](3,2), [1](3,-2), and [1](5,2).	80
29	mIR product spectrum of the photolysis of [1] with 16 μJ , 400 nm-pump pulses in room-temperature DCM/DCM-d ₂ solution, averaged over delays from 150 ps to 3.5 ns, and DFT-predicted IR absorption spectra of [2](-1,2), [2](3,2), [2](3,-2), and [2](5,2).	80
30	mIR product spectrum of the photolysis of [1] with 16 μJ , 400 nm-pump pulses in room-temperature DCM/DCM-d ₂ solution, averaged over delays from 150 ps to 3.5 ns, and DFT-predicted IR absorption spectra of [3 _{red}](<i>n</i> ,±2) (<i>n</i> = 2, 4).	81
31	Ball-and-stick models of [3 _{red}](2,2), isosurface plots of its porphyrin-centered SOMOs, and displacement vectors of the normal modes having unusually high absorption strengths, calculated via DFT.	83
A1	(a) & (b) Expansions of the stationary FTIR absorption spectrum of [1] in room-temperature DCM (DCM-d ₂) solution. (c) - (j) Ball-and-stick models of [1] and calculated atomic displacement vectors of the normal modes corresponding to the absorption bands shown in (a) and (b).	95
A2	Stationary FTIR absorption spectra of [1] and N ₃ ⁻ in the region of the antisymmetric N ₃ -stretching vibration band and tBuNC in the region of the C≡N-stretching vibration band. All spectra were recorded in room-temperature DCM solution.	95
A3	Experimental, stationary FTIR absorption spectra of [1] and [6] in room-temperature DCM solution in the region of the ν_{41} vibration band of the porphyrindiido ligand and inverted, DFT-calculated IR spectra.	95
A4	Ball-and-stick models of [1](5,0) and isosurface plots of the natural transition orbital pairs of highest eigenvalues of selected roots, calculated by TD-DFT.	103
A5	Transient 12 μJ , 400 nm-pump/1900-2100 cm^{-1} -probe spectra of [1] in room-temperature DCM solution at various pump-probe delays.	104
A6	Transient 12 μJ , 400 nm-pump/mIR-probe spectra of [1] in room-temperature DCM solution, recorded in the probe regions from 1410 cm^{-1} to 1500 cm^{-1} and from 1550 cm^{-1} to 1620 cm^{-1} and at various pump-probe delays.	104
A7	Transient 3 μJ , 400 nm-pump/1300-1370 cm^{-1} -probe spectra of [1] in room-temperature DCM solution at various pump-probe delays.	107
A8	Transient 16 μJ , 400 nm-pump/1300-1370 cm^{-1} -probe spectra and kinetic trace of [1] in room-temperature DCM-d ₂ solution.	107
A9	Product spectra of the 16 μJ , 400 nm-pump/1240-1310 cm^{-1} -probe experiment of [1], stationary FTIR spectrum of [1] in the same region, and pseudo-Voigt regression functions.	108
A10	mIR product spectrum of the 16 μJ , 400 nm-photolysis of [6] in room-temperature DCM/DCM-d ₂ solution, averaged over pump-probe delays from 150 ps to 250 ps.	109

A11	Normalized transient 35 μJ , UV/Vis-pump/Vis-probe spectra of [1] in room-temperature DCM solution, recorded at a pump-probe delay of 0.16 ps for different excitation wavelengths.	109
A12	Transient 35 μJ , 400 nm-pump/Vis-probe spectrum of [1] in room-temperature DCM solution, averaged over pump-probe delays from 150 ps to 1000 ps, and ratio of the signal strengths of the residual transient absorption at 535 nm and the initial bleaching signal (415-420 nm) in dependence of the energy of the pump pulse.	110
A13	Time constants obtained from bi- or triexponential fits of the 400 nm-pump/Vis-probe kinetic traces of [1] in room-temperature DCM solution.	110
A14	mIR product spectrum of the photolysis of [1] with 16 μJ , 400 nm-pump pulses in room-temperature DCM/DCM-d ₂ solution, averaged over pump-probe delays from 150 ps to 3.5 ns, and DFT-predicted IR absorption spectra of [7](2,1), [7](4,1), and [7](4,-1).	113
A15	Selected bond lengths and bond angles of the tpp ²⁻ -ligands of four complexes of distinct electronic structures.	114
A16	Ball-and-stick models of [3 _{red}](2,2), isosurface plots of its porphyrin-centered SOMOs, and displacement vectors of the normal mode $\nu_{44}(\text{por})_y$, calculated via DFT.	115

8.7 List of Tables

1	Bi- or triexponential fit parameters of selected 8 μJ , 400 nm-pump/Vis-probe kinetic traces of the [1] in room-temperature DCM solution.	61
A1	Excitation energies, (dipole-length) oscillator strengths, assignment to experimentally observed absorption bands, and characterization of selected electronic transitions of [1](5,0), calculated by TD-DFT.	96
A2	Excitation energies and (dipole-length) oscillator strengths of the electronic transitions of [1](5,0) not mentioned in Table A1, calculated by TD-DFT.	97
A3	(Multi)exponential fit parameters of the 16 μJ , 400 nm-pump/1300-1370 cm^{-1} -probe kinetic traces of [1] in room-temperature DCM solution.	105
A4	(Multi)exponential fit parameters of the 16 μJ , 400 nm-pump/1300-1370 cm^{-1} -probe kinetic traces of [1] in room-temperature DCM-d ₂ solution.	106
A5	Fit parameters of pseudo-Voigt functions describing the signals observed in the product spectra of the 16 μJ , 400 nm-pump/1240-1310 cm^{-1} -probe experiment of [1] at early and late pump-probe delays, and the stationary FTIR spectrum of [1] in the same region.	108
A6	Monoexponential fit parameters of the time-dependent integrals of the functions specified in Table A5.	109
A7	Simplified electron configurations of the DFT-optimized structures of the complexes relevant for this work for various feasible spin multiplicities.	111
A8	Relative energies and calculated distribution of unpaired electrons of the complexes relevant for this work for different electron configuration.	113
A9	Energetically lowest excitations of significant por \rightarrow Fe CT character of [1], [2], and [3 _{red}] for three spin multiplicities, calculated by TD-DFT. Root numbers, assignments from NTO analyses, and excitation energies.	114

8.8 List of Acronyms and Formula Symbols

\square	vacancy
[1]	azido(5,10,15,20-tetraphenylporphyrin-21,23-diido)iron(+III), [Fe ^{+III} (tpp)(N ₃)]
[1]*	azido(5,10,15,20-tetraphenylporphyrin-21,23-diido)iron(+III) in an excited state, [Fe ^{+III} (tpp)(N ₃)]*
<u>1</u>	lower quantum state
[1 _{ox}]	azido(5,10,15,20-tetraphenylporphirindyl)iron(+III), [Fe ^{+III} (tpp)(N ₃)] ⁺
[2]	nitrido(5,10,15,20-tetraphenylporphyrin-21,23-diido)iron(+V), [Fe ^{+V} (tpp)(N)]
<u>2</u>	upper quantum state
[3]	(5,10,15,20-tetraphenylporphyrin-21,23-diido)iron(+III), [Fe ^{+III} (tpp)(\square)] ⁺
[3 _{red}]	(5,10,15,20-tetraphenylporphyrin-21,23-diido)iron(+II), [Fe ^{+II} (tpp)(\square)]
[4]	<i>tert</i> -butylcarbodiimido(5,10,15,20-tetraphenylporphyrin-21,23-diido)iron(+III), [Fe ^{+III} (tpp)(NCN <i>t</i> Bu)]
[5]	bis(<i>tert</i> -butylisonitrilo)(5,10,15,20-tetraphenylporphyrin-21,23-diido)iron(+III), [Fe ^{+III} (tpp)(CN <i>t</i> Bu) ₂] ⁺
[5 _{red}]	bis(<i>tert</i> -butylisonitrilo)(5,10,15,20-tetraphenylporphyrin-21,23-diido)iron(+II), [Fe ^{+II} (tpp)(CN <i>t</i> Bu) ₂]
[6]	chlorido(5,10,15,20-tetraphenylporphyrin-21,23-diido)iron(+III), [Fe ^{+III} (tpp)(Cl)]
[6 _{ox}]	chlorido(5,10,15,20-tetraphenylporphirindyl)iron(+III), [Fe ^{+III} (tpp)(Cl)] ⁺
[7]	oxido(5,10,15,20-tetraphenylporphirindyl)iron(+IV), [Fe ^{+IV} (tpp)(O)] ⁺

[8]	μ -nitrido-bis((5,10,15,20-tetraphenylporphyrin-21,23-diido)iron(+III,+IV)), [Fe ^{+III,+IV} (tpp)] ₂ N
<i>A</i>	integral
<i>a</i>	high-frequency vibrational mode
<i>a</i> _{1u}	1a _{1u} orbital of metalloporphyrins (assuming D _{4h} symmetry)
<i>a</i> _{2u}	3a _{2u} orbital of metalloporphyrins (assuming D _{4h} symmetry)
α & β	spin functions
<i>A</i> _{2,1}	Einstein coefficient of spontaneous emission
α_a	frequency-integrated extinction coefficient / absorption strength
<i>b</i>	low-frequency vibrational mode
B97	Becke's GGA functional
BBO	β -barium borate
<i>B</i> _{1,2}	Einstein coefficient of absorption
<i>B</i> _{2,1}	Einstein coefficient of stimulated emission
bs	beam splitter
<i>c</i>	concentration
<i>c</i> ₀	speed of light
χ	anharmonicity constant
cor	corrole (with arbitrary substituents)
cor ³⁻	corrole-20,21,22-triido (with arbitrary substituents)
COSMO	conductor-like screening model
CT	charge transfer
cyclam	1,4,8,11-tetraazacyclotetradecane
cyclam-ac	1,4,8,11-tetraazacyclotetradecane-1-acetate
Cys	cysteine
<i>d</i>	optical path length
D4	Grimme's empirical dispersion correction, version 4
DCM	dichloromethane
DCM-d ₂	deuterated dichloromethane
def2-SVP	Ahlrichs' split-valence basis set
def2-TZVP	Ahlrichs' triple- ζ basis set
DFG	difference frequency generation
DFT	density functional theory
Δ OD	differential optical density
<i>E</i>	energy
ϵ	(molar, decadic) extinction coefficient
<i>e</i> _g	4 <i>e</i> _g orbitals of metalloporphyrins (assuming D _{4h} symmetry)
<i>e</i> _{g,x}	4 <i>e</i> _{g,x} orbital of metalloporphyrins (assuming D _{4h} symmetry)
<i>e</i> _{g,y}	4 <i>e</i> _{g,y} orbital of metalloporphyrins (assuming D _{4h} symmetry)
ENDOR	electron nuclear double resonance
EPR	electron paramagnetic resonance
ES	excited state
ESA	excited state absorption
<i>f</i>	filter
<i>f</i>	focal length
FHG	forth-harmonic generation
FHGS	forth-harmonic generation signal
fIR	far-infrared
foc	fiber optical cable
<i>f</i> _{osc}	oscillator strength
<i>f</i> _{red}	fractional yield of photoreduction
<i>f</i> _{ox}	fractional yield of photooxidation
FTIR	Fourier-transform infrared
FWHM	full width at half maximum
<i>G</i>	Gaussian function
Γ	irreducible representation
GGA	generalized gradient approximation
GS	ground state
GSR	ground state recovery
η	weighting factor of <i>V</i> _{<i>p</i>}
<i>h</i>	Planck constant
HOMO	highest occupied molecular orbital

hwp	half-wave plate
I	intensity
IC	internal conversion
i & j	integer indices
IR	infrared
ISC	intersystem crossing
J, \mathcal{K} & \mathcal{L}	parameters of O
κ	force constant
k_B	Boltzmann constant
k_u	first order rate constant
k_v	second order rate constant
l	convex lens
L	Lorentzian function
Λ	integrated second-order rate law
L	ligand
λ	wavelength
LMCT	ligand-to-metal charge transfer
LUMO	lowest unoccupied molecular orbital
M	metal atom
m	mirror
$\vec{\mu}$	electric dipole operator
\bar{m}	reduced mass
μ	transition dipole moment
m	mass
MCT; mct	mercury cadmium telluride (detector)
mIR	mid-infrared
MLCT	metal-to-ligand charge transfer
$\mathcal{M}_4(a_1), \mathcal{M}_5(a_1),$ $\mathcal{M}_6(a_1), \mathcal{M}_{23}(b_2)$ & $\mathcal{M}_{24}(b_2)$	phenyl-centered normal modes
nb	non-bonding
Nd:YAG	neodymium-doped yttrium aluminum garnet
$\tilde{\nu}$	wavenumber
nIR	near-infrared
NMR	nuclear magnetic resonance
n, N	integer number
ν	frequency
NTO	natural transition orbital
$\tilde{\nu}_0$	frequency of maximal absorbance
$\nu_{37}(\text{por})$	E_u -symmetric combination of the antisymmetric C_α - C_m stretching mode
$\nu_4(\text{por})$	A_{1g} -symmetric combination of the symmetric pyrrole half-ring stretching modes
$\nu_{40}(\text{por})$	E_u -symmetric combination of the pyrrole quarter-ring stretching and C-H rocking modes
$\nu_{41}(\text{por})$	E_u -symmetric combination of the symmetric pyrrole half-ring stretching modes
$\nu_{44}(\text{por})$	E_u -symmetric combination of the antisymmetric pyrrole half-ring stretching modes
$\nu_{51}(\text{por})$	E_u -symmetric combination of the pyrrole C-H rocking modes
$\nu_{52}(\text{por})$	E_u -symmetric combination of the pyrrole C-H scissoring modes
$\nu_{as}(N_3)$	antisymmetric azide stretching vibration
$\nu_s(N_3)$	symmetric azide stretching vibration
O	log-normal distribution
OAP; oap	90° off-axis parabolic mirror
OD	optical density (absorbance, extinction)
oep ²⁻	2,3,7,8,12,13,17,18-octaethylporphyrin-21,23-diido
oep ^{•-}	2,3,7,8,12,13,17,18-octaethylporphyrinidyl
ω	bandwidth
Ω	degeneracy
OPA	optical parametric amplifier
OPO	optical parametric oscillator
ωB97X	Chai's and Head-Gordon's range-separated hybrid functional
p ²⁻	porphin-21,23-diido
Ph	phenyl
Φ	primary quantum yield
pol	polarizer

por ^{••}	porphiridyl (with arbitrary substituents)
por ²⁻	porphyrin-21,23-diido (with arbitrary substituents)
ph	photon
Ψ	wavefunction
PTFE	polytetrafluoroethylene
P	product molecule
q	charge
Q	quencher
R	reactant molecule
\vec{r}	spatial coordinates
ρ	skewness
rms	root mean square
R'	organic substituent
rr	retroreflector
RR	resonance Raman
\mathcal{R}_1	ratio of signal strengths: $\Delta OD(1344 \text{ cm}^{-1}, 200 \text{ ps}, E_{\text{pump}}) / \Delta OD(1340 \text{ cm}^{-1}, 1.0 \text{ ps}, E_{\text{pump}})$
\mathcal{R}_2	ratio of signal strengths: $\Delta OD(535 \text{ nm}, 100\text{-}150 \text{ ps}, E_{\text{pump}}) / \Delta OD(415 \text{ nm}\text{-}420 \text{ nm}, 0.8\text{-}1.0 \text{ ps}, E_{\text{pump}})$
ρ_l	spectral radiation density
SCF	self-consistent field
$s_c(\text{FeX})$	sum of the (Löwdin) spin populations of an iron atom and all atoms of the axial ligand
s_c	(Löwdin) spin population of an atom
$s_c(\text{por})$	sum of the (Löwdin) spin populations of all C and N atoms of a porphyrin ligand
$S(\text{FeX})$	idealized number of unpaired electrons of an iron atom and axial ligand
SFGS	sum frequency generation signal
SHE	standard hydrogen electrode
SHG	second-harmonic generation
SI	supporting information
SOMO	singly occupied molecular orbital
SPA	single-photon absorption
$S(\text{por})$	idealized number of unpaired electrons of a porphyrin ligand
T	time constant / lifetime
t	time
T	temperature
$t_{1/2}$	half-life period
TAS	transient absorption spectrometer
τ	pump-probe delay
TD-DFT	time-dependent density functional theory
THG	third-harmonic generation
Ti:Sa	titanium-doped sapphire
TPA	two-photon absorption
tpp ²⁻	5,10,15,20-tetraphenylporphyrin-21,23-diido
tpp ^{••}	5,10,15,20-tetraphenylporphiridyl
UV	ultraviolet
UV-Vis	ultraviolet-to-visible
v	vibrational quantum number
V	Voigt function
V_p	pseudo-Voigt function
VER	vibrational energy relaxation
Vis	visible
wop	without pump pulse
wp	with pump pulse
X	axial ligand
Ξ	(multi)exponential function
X	oxidation state
XUV	extreme ultraviolet
$x, y \text{ \& } z$	Cartesian coordinates

8.9 DFT-Optimized Molecular Geometries

[1](1,0) $E = -3339.782462711 E_h$			[1](3,0) $E = -3339.7945309890 E_h$			[1](5,0) $E = -3339.798057079 E_h$						
80	Fe	-0.0622021	0.0100912	-0.0085319	Fe	-0.0296989	0.0232949	-0.1424284	Fe	-0.0530383	0.0098970	-0.2734684
	N	-1.0911451	-1.5930302	0.2523637	N	-0.2254187	-1.9424763	0.1634286	N	0.8554873	-1.7807064	0.2689536
	N	-1.6860917	-1.1417628	0.1648525	N	-1.9990020	0.2217332	0.1468976	N	-1.8686169	-0.9134424	0.1217133
	N	-1.2316119	1.6148014	0.1770614	N	0.1634267	1.9932335	0.1398694	N	-1.0001672	1.8063237	0.1629859
	N	1.5396504	1.1634802	0.2624510	N	1.9380218	-0.1709474	0.1533188	N	1.7239598	0.9386628	0.2669226
	C	2.4592290	-1.6326621	0.2833534	C	0.7711703	-2.8727615	0.0273269	C	2.2031465	-2.0054040	0.2601636
	C	0.6918905	-2.9016996	0.1787422	C	-1.3880047	-2.6587860	0.2465960	C	0.2563909	-3.0083068	0.2742869
	C	-1.7135011	-2.5082698	0.1581258	C	-2.9252985	-0.7750933	0.2964594	C	-2.0905983	-2.2574196	0.2166525
	C	-2.9907884	-0.7470721	0.1952573	C	-2.7135388	1.3860111	0.0950191	C	-3.0947527	-0.3142000	0.1153589
	C	-2.5997411	1.6549329	0.1448368	C	-0.8323229	2.9238347	0.0189899	C	-2.3451171	2.0323010	0.0908135
	C	-0.8291651	2.9206556	0.1146917	C	1.3302568	2.7068070	0.2019138	C	-0.4006413	3.0327981	0.2099037
	C	1.5738094	2.5320928	0.2407741	C	2.8685244	0.8247105	0.2770446	C	1.9433775	2.2842594	0.3442343
	C	2.8472094	0.7690355	0.3415206	C	2.6523030	-1.3355409	0.0783607	C	2.9500894	0.3403457	0.3125878
	C	2.9255799	-2.9882079	0.2342567	C	0.2197502	-4.1946026	0.0140343	C	2.4600416	-3.4192728	0.2523348
	C	1.8333044	-3.7728049	0.1669715	C	-1.1131826	-0.0635890	0.1677231	C	1.2606419	-4.0374618	0.2681056
	C	-3.0680877	-2.9790513	0.2147453	C	-4.2442338	-0.2183506	0.3710134	C	-3.5036903	-2.5105348	0.2848947
	C	-3.8584725	-1.8885589	0.2433459	C	-4.1143814	1.1161381	0.2315610	C	-4.1227562	-1.3129140	0.2184122
	C	-3.0608141	3.0099843	0.0558440	C	-0.2765647	4.2445109	-0.0173933	C	-2.5979011	3.4469909	0.0600359
	C	-1.9649119	3.7933232	0.0323763	C	1.0585407	4.1111553	0.1101836	C	-1.4000466	4.0634723	0.1375453
	C	2.9275162	3.0003497	0.3472250	C	4.1882287	0.2670644	0.3255758	C	3.3528729	2.5380331	0.4723966
	C	3.7148876	1.9098836	0.4081787	C	4.0553283	-1.0668026	0.1807697	C	3.9739425	1.3402268	0.4429544
	C	-0.6147059	-3.3539749	0.1342595	C	-2.6666132	-2.1347342	0.3430861	C	-1.1147267	-3.2506436	0.2635906
	C	-3.4469636	0.5600771	0.1719034	C	-2.1921094	2.6644595	-0.0197346	C	-3.3378914	1.0566097	0.0607515
	C	0.4804379	3.3747420	0.1452457	C	2.6089705	2.1850342	0.3009038	C	0.9676904	3.2762114	0.3014699
	C	3.3044564	-0.5375450	0.3318547	C	2.1276236	-2.6107333	-0.0451330	C	3.1950174	-1.0290145	0.2657971
	C	-0.8568748	-4.8263056	0.0752998	C	-3.8160153	-0.3787612	0.4669501	C	-1.5717226	-4.6718517	0.3038360
	C	-4.9201898	0.7999814	0.1574775	C	-3.1401960	3.8098110	-0.1473413	C	-4.7605191	1.5052929	-0.0075147
	C	0.7264122	4.8465604	0.0867534	C	3.7600297	3.1305962	0.3963216	C	1.4213392	4.6985769	0.3532254
	C	4.7784813	-0.7751807	0.3352193	C	3.0701890	-3.7468941	-0.2646490	C	4.6187984	-1.4765740	0.2100164
	C	-0.6864254	-5.6227667	1.2119337	C	-4.0556414	-3.7493905	1.6703426	C	-1.4345693	-5.4317016	1.4702064
	C	-1.2601870	-5.4264533	-1.1214092	C	-4.6668674	-3.3069106	-0.6194219	C	-2.1442052	-5.2626749	-0.8273401
	C	-5.6634559	0.5605888	-1.0025880	C	-3.8116564	4.0321584	1.3536293	C	-5.4996504	1.3205088	-1.1812963
	C	-5.5752023	1.2685643	1.3004220	C	-3.3731882	4.6712587	0.9295362	C	-5.3750697	2.1044125	1.0968318
	C	0.4892025	5.4518448	1.2070912	C	4.0182620	3.8151232	1.5878569	C	1.2397331	5.4620743	1.5106796
	C	1.1947578	5.4365049	-1.0911977	C	4.5941289	3.2450854	-0.7057421	C	2.0362685	5.2849277	-1.7576235
	C	5.4956244	-0.7092333	-0.8634483	C	5.3933344	-4.0015559	-1.5573509	C	5.3224708	-1.3905496	-0.9956810
	C	5.4539879	-1.0668388	1.5233077	C	3.4929646	-4.558972	0.7937545	C	5.2612618	1.9845208	1.3428250
	C	-0.9148923	-6.9964190	1.1530994	C	-5.1300637	-4.6295075	1.7875264	C	-1.8622022	-6.7571777	1.5049070
	C	-1.4872661	-6.8002570	-1.1812607	C	-5.7405264	-4.8776462	-0.5032421	C	-2.5705490	-6.5889678	-0.7937576
	C	-7.0385674	0.7861920	-1.0195000	C	-4.6974213	5.1005162	-1.4824675	C	-6.8283440	1.7411902	-1.2505683
	C	-6.9507467	1.4928478	1.2845563	C	-4.2596067	5.7389707	0.8015350	C	-6.7042177	2.5179676	1.0288200
	C	0.7378227	7.0238705	1.1512603	C	5.0942847	4.6965513	1.6778267	C	1.6658782	6.7882766	1.5571871
	C	1.4323991	6.8086779	-1.1479913	C	5.6695639	4.2267711	-0.6165205	C	2.4615058	6.6113083	-0.7112254
	C	6.8713294	-0.9324103	-0.8712582	C	4.4226525	-5.0554843	-1.7849081	C	6.6501438	-1.8084741	-1.0656688
	C	6.8303146	-1.2888415	1.5144746	C	4.3774828	-5.608591	0.5635220	C	6.5898203	-2.4007087	1.2721462
	C	-1.3153678	-7.5881395	-0.0440496	C	-5.9750767	-4.8500367	0.7009913	C	-2.4308966	-7.3394766	0.3728053
	C	-7.6852628	1.2524915	0.1242893	C	-4.9227890	5.9564645	-0.4054643	C	-7.4336423	2.3380201	-0.1456445
	C	1.2050532	7.6051866	-0.0266667	C	5.9224591	4.9037786	0.5758590	C	2.2776231	7.3658424	0.4455684
	C	7.5411479	-1.2221014	0.3170860	C	4.8434875	-5.9597812	-0.7263472	C	7.2864050	-2.3137308	0.0675418
	H	3.9631977	-3.2815870	0.2421152	H	0.7972676	-5.0986422	-0.0960611	H	3.4402461	-3.8687815	0.2335951
	H	1.7855669	-4.8482876	0.1061456	H	-1.8616695	-4.8389092	-0.2480400	H	1.0603417	-5.0971053	0.2625051
	H	-3.3586661	-4.0170972	0.2433406	H	-5.1462235	-0.7912443	0.5149077	H	-3.9530682	-3.4853704	0.3884430
	H	-4.9343209	-1.8431748	0.2995097	H	-4.8869597	1.8684879	0.2401134	H	-5.1812031	-1.1092117	0.2564785
	H	-4.0962174	3.3067568	0.0064599	H	-0.8503572	5.1507964	-0.1263112	H	-3.5735624	3.9001217	-0.0152707
	H	-1.9124235	4.8679583	-0.0389510	H	1.8098218	4.8844576	0.1248640	H	-1.1973538	5.1227032	0.1388772
	H	3.2185262	4.8383015	0.3748226	H	5.0935852	0.8398718	0.4469914	H	3.7978672	3.5148393	0.5764981
	H	4.7888160	1.6030920	0.4931233	H	4.8268508	-1.8200344	0.1588497	H	5.0303527	1.1353218	0.5172096
	H	-0.3734249	-5.1557138	2.1501984	H	-3.3919137	-3.7336559	2.5217575	H	-0.9907862	-4.9725371	2.3580332
	H	-0.7808997	-7.6081073	2.0495044	H	-5.3093799	-5.1442714	2.7353942	H	-1.7523893	-7.3394183	2.4242371
	H	-1.4938280	-8.6658644	-0.0907590	H	-6.8180021	-5.5403806	0.7925103	H	-2.7658479	-8.3799335	0.3997568
	H	-1.7985506	-7.2581449	-2.1241266	H	-6.3964457	-4.3595622	-1.3609737	H	-3.0120148	-7.0395186	-1.6868717
	H	-1.3927103	-4.8055052	-2.0119351	H	-4.4780202	-2.7886550	-1.5639031	H	-2.2498620	-4.6726961	-1.7422299
	H	-5.1519714	0.1974951	-1.8986005	H	-3.6296919	3.3600660	-2.1970965	H	-5.0212960	0.8605788	-2.0475324
	H	-7.6078402	0.5987053	-1.9340255	H	-5.2125422	5.2666385	-2.4325040	H	-7.3934764	1.5987845	-2.1757200
	H	-8.7641475	1.4294728	0.1112334	H	-5.6171869	6.7949544	-0.5066482	H	-8.4760262	2.6635761	-0.1999037
	H	-7.4519946	1.8560938	2.1859170	H	-4.4349543	6.0389116	1.6516717	H	-7.1737430	2.9811413	1.9009623
	H	-4.9965320	1.4557964	2.2094920	H	-2.8539308	4.4968115	1.8763311	H	-4.8018216	2.2417396	2.0182030
	H	0.1346814	5.1929560	2.1306597	H	3.3680081	3.6494322	2.4515925	H	0.7619092	5.0058715	2.3824400
	H	0.5601715	7.6422988	2.0353602	H	5.2881896	5.226099	2.6165886	H	1.5212150	7.3733174	2.4695724
	H	1.3927651	8.6314584	-0.0706187	H	6.7669246	5.5947317	0.6492004	H	2.6119580	8.4062310	0.4817723
	H	1.7967220	7.2581254	-2.0757926	H	6.3127934	4.3871917	-1.4860129	H	2.9377004	7.0584667	-1.5890974
	H	1.3722155	4.8087462	-1.9690780	H	4.3915861	2.8147392	1.6406777	H	2.1778787	4.6912737	-1.6653298
	H	4.9613337	-0.4847538	-1.7917165	H	3.1980691	-3.3666050	-2.3813483	H	4.8151346	-0.9981109	-1.8826458
	H	7.4232687	-0.8813371	-1.8137138	H							

C	2.0743086	-2.6648146	-0.1301807	C	2.1267821	-2.6731415	0.0347424	C	2.0819525	-2.6390916	-0.1444339
C	-3.8121429	-3.0771960	0.6705401	C	-3.8323236	-3.1248389	0.2898565	C	-3.8052464	-3.0739378	0.6277709
C	-3.1085543	3.7999299	-0.3356741	C	-3.1613222	3.8295225	0.0528999	C	-3.1123217	3.8003681	-0.3011523
C	3.7529210	3.1057800	0.5630586	C	3.7681675	3.1516223	0.1688558	C	3.7510396	3.1107661	0.5469712
C	3.0331548	-3.7509637	-0.4640067	C	3.0920412	-3.7995576	-0.0651865	C	3.0348839	-3.7423697	-0.4367930
C	-3.9227523	-3.8436962	1.8356747	C	-3.9978617	-3.9874483	1.3787602	C	-3.8901356	-3.8742936	1.7714390
C	-4.7909573	-3.2045227	-0.3215065	C	-4.7740593	-3.1478455	-0.7456114	C	-4.8016863	-3.1722944	-0.3495455
C	-3.8784051	3.8271034	-1.5043045	C	-4.0363073	3.9590576	-1.0322549	C	-3.8993468	3.8160651	-1.4583160
C	-3.2708027	4.8161830	0.6112286	C	-3.2150596	4.7707315	1.0862608	C	-3.2546736	4.8286750	0.6357871
C	3.8273178	3.9553884	1.6722195	C	3.9661597	4.0180904	1.2491883	C	3.8739017	3.9178640	1.6821745
C	4.7660286	3.1598791	-0.4012556	C	4.6787713	3.1698655	-0.8942416	C	4.7135501	3.2037340	-0.4644315
C	3.6596831	-3.7432757	-1.7162838	C	3.9099762	-3.9176136	-1.1953579	C	3.6844074	-3.7741894	-1.6758328
C	3.3323703	-5.7649561	0.4501649	C	3.2016338	-4.7460940	0.9585654	C	3.3070143	-4.7330293	0.5108747
C	-4.9947168	-4.7174235	2.0087914	C	-5.0836920	-4.8595743	1.4310317	C	-4.9557151	-4.7572587	1.9372103
C	-5.8581598	-4.0835897	-0.1516186	C	-5.8537543	-4.0259389	-0.6970589	C	-5.8628855	-4.0594420	-0.8628025
C	-4.7811098	4.8630057	-1.7286417	C	-4.9354324	5.0204643	-1.0897226	C	-4.8003870	4.8537617	-1.6815863
C	-4.1799736	5.8498662	0.3890339	C	-4.1220967	5.8278213	1.0324430	C	-4.1631804	5.8629108	0.4147990
C	4.8963332	4.8369501	1.8192281	C	5.0531447	4.8901845	1.2657998	C	4.9460006	4.7998825	1.8072939
C	5.8341636	4.0427140	-0.2556516	C	5.7594312	4.0480782	-0.8810911	C	5.7807950	4.0903728	-0.3416928
C	4.5637873	-4.7488022	-2.0488267	C	4.8094839	-4.9747527	-1.3044137	C	4.5904510	-4.7927281	-1.9611137
C	4.2459512	-5.7647768	0.1163140	C	4.1098355	-5.7982670	0.8523158	C	4.2187261	-5.7480907	0.2324621
C	-5.9637626	-4.8410952	1.0143636	C	-6.0122857	-4.8825961	0.3920997	C	-5.9428376	-4.8527023	0.9579994
C	-4.9331775	5.8775040	-0.7828834	C	-4.9814479	5.9568618	-0.0569020	C	-4.9351793	5.8788615	-0.7451495
C	5.9035484	4.8818393	0.8560796	C	5.9502099	4.9091160	0.1994204	C	5.9005351	4.8883090	0.9554442
C	4.8614942	-5.7588472	-1.1334658	C	4.9126409	-5.9165794	-0.2805605	C	4.8613690	-5.7796071	-1.0129030
H	0.7048737	-5.1405363	-0.3491770	H	0.7823212	-5.1933481	-0.1815111	H	0.7131418	-5.1036752	-0.4241871
H	-1.9160450	-4.8575015	0.1312559	H	-1.8705697	-4.9284608	-0.0384427	H	-1.9149291	-4.8332768	0.0243800
H	-5.1011307	-0.7367606	0.8718889	H	-5.1360077	-0.8268959	0.7082835	H	-5.0996636	-0.7395749	0.8734003
H	-4.8190919	1.9262104	0.4672366	H	-4.8751923	1.8584172	0.6194841	H	-4.8311083	1.9209944	0.4804097
H	0.7707883	5.1473624	-0.4462840	H	-0.8584656	5.2196894	-0.1643236	H	-0.7781600	5.1459203	-0.4115126
H	1.8567887	4.8644020	-0.0369116	H	1.7972150	4.9544494	-0.1110809	H	1.8549770	4.8659370	-0.0183057
H	5.0414451	0.7551573	0.8170625	H	5.0829265	0.8542070	0.5537483	H	5.0532143	0.7554290	0.7562662
H	4.7520945	-1.9043486	0.4072478	H	4.8199512	-1.8322068	0.4697358	H	4.7709214	-1.8826954	0.3448343
H	-3.1599746	-3.7466966	2.6136091	H	-3.2699456	-3.9652695	2.1946729	H	-3.1132757	-3.7982478	2.5372711
H	-5.0742630	-5.3046978	2.9277158	H	-5.2050533	-5.5237785	2.2910145	H	-5.0155785	-5.3741449	2.8379989
H	-6.8030644	-5.5294577	1.1481323	H	-6.8627538	-5.5685629	0.4313665	H	-6.7768980	-5.5476183	1.0862752
H	-6.6127717	-4.1778123	-0.9371699	H	-6.5772583	-4.0410696	-1.5166544	H	-6.6321863	-4.1320242	-0.9595244
H	-4.7048409	-2.6104706	-1.2353871	H	-4.6491189	-2.4732320	-1.5969069	H	-4.7352371	-2.5500846	-1.2462286
H	-3.7583573	3.0294244	-2.2425155	H	-4.0009986	3.2209279	-1.8381492	H	-3.7931123	3.0081925	-2.1877367
H	-5.3703062	4.8784098	-2.6497498	H	-5.6057687	5.1170313	-1.9480537	H	-5.4022576	4.8622662	-2.5942561
H	-5.6426578	6.6909914	-0.9579057	H	-5.6909172	6.7875985	-0.1008341	H	-5.6455642	6.6912485	-0.9199251
H	-4.3006874	6.6378413	1.1375746	H	-4.1577891	6.5338980	1.8491380	H	-4.2694696	6.6596302	1.1562697
H	-2.6838094	4.7868203	1.5335560	H	-2.5435798	4.6647659	1.9429471	H	-2.6527914	4.8108411	1.5488298
H	3.0392171	3.9175351	2.4296269	H	3.2629697	3.9989860	2.0865981	H	3.1218258	3.8477489	2.4734100
H	4.9409981	5.4909051	2.6939532	H	5.2002517	5.5573988	2.1194221	H	5.0357991	5.4223169	2.7017298
H	6.7435626	5.5732886	0.9690574	H	6.8013157	5.5953466	0.2104274	H	6.7405986	5.5811118	0.8907727
H	6.6149562	4.0762115	-1.0202140	H	6.4582634	4.0596883	-1.7218611	H	6.5236834	4.1587699	-1.1409018
H	4.7066309	2.505713	-1.2750718	H	4.5293508	2.4914486	-1.7387027	H	4.6153914	2.5772573	-1.3554870
H	3.4185101	-2.9473448	-2.4279390	H	3.8288538	-3.1753781	-1.9947351	H	3.4573537	-2.9998369	-2.4146209
H	5.0409172	-4.7477009	-3.0324361	H	5.4350910	-5.0635719	-2.1966432	H	5.0878192	-4.8166036	-2.9346255
H	5.5754685	-6.5431723	-1.3988271	H	5.6222468	-6.7440080	-0.3659645	H	5.5754293	-6.5763446	-1.2394233
H	4.4757535	-6.5517545	0.8397727	H	4.1911688	-6.5284837	1.6620327	H	4.4283564	-6.5172572	0.9719782
H	2.8483824	-4.7651659	1.4310329	H	2.5735208	-4.6484911	1.8485523	H	2.8040227	-4.7025997	1.4815826
N	-0.0069804	-0.0625069	-2.0804230	N	-0.0045811	-0.0215334	-2.2450659	N	0.0222047	0.0191225	-2.0702945
N	0.8867844	-0.5630457	-2.7011832	N	0.8790017	-0.3834237	-2.9776284	N	0.8306758	-0.6620104	-2.6332583
N	1.7238028	-1.0364212	-3.3070911	N	1.6863169	-0.7166594	-3.6948286	N	1.5942844	-1.2980744	-3.1863577

$$E = -3230.225223285 E_h$$

$$E = -3230.195009259 E_h$$

$$E = -3230.170894933 E_h$$

78	Fe	0.0372307	0.0233909	-0.1819311	78	Fe	-0.0209164	0.0250056	-0.0326506	78	Fe	-0.0371176	0.0240861	-0.1946387
	N	-0.2198201	-1.9329243	0.1422665		N	-0.2268813	-1.9447469	0.1108871		N	-0.2260874	-1.9871848	-0.1580377
	N	-0.0232026	0.2159432	0.0856491		N	-2.0067376	0.2262615	0.2246684		N	-2.0692609	0.2200778	0.1574348
	N	-2.1574564	1.9766507	0.1530421		N	-0.1756325	1.9914182	0.1345600		N	0.1631920	2.0332181	0.1264919
	N	1.9574344	-0.1713378	0.0137940		N	1.9463403	-0.1774104	0.0845360		N	2.0064939	-0.1741817	0.0810731
	C	0.7828267	-2.8657235	0.0737594		C	0.7652744	-2.8767949	-0.0117968		C	0.7873846	-2.9032616	0.0306308
	C	-1.3860273	-2.6529881	0.1692815		C	-1.3993796	-2.6568882	0.1400142		C	-1.3987171	-2.6919654	0.1025314
	C	-2.9470340	-0.7842879	0.1643036		C	-2.9334338	-0.7701264	0.3232192		C	-2.9775610	-0.7906258	0.2295768
	C	-2.7380830	1.3767605	0.1124350		C	-2.7158533	1.3895437	0.2159762		C	-2.7675427	1.3867468	0.2089905
	C	-0.8468550	2.9098361	0.1286776		C	-0.8277092	2.9240027	0.0527225		C	-0.8524814	2.9496654	0.0886847
	C	1.3240377	2.6966842	0.1448956		C	1.3418228	2.7044324	0.1257818		C	1.3344278	2.7381317	0.0740123
	C	2.8835867	0.8233361	0.0673784		C	2.8806734	0.8188865	0.1731080		C	2.9168668	0.8361873	0.1292029
	C	2.6727038	-1.3322795	0.0066332		C	2.6579068	-1.3464250	0.0547074		C	2.7058620	-1.3411142	0.0984840
	C	0.2329775	-4.1898040	0.0691023		C	0.2064629	-4.1947153	0.0439369		C	0.2322589	-4.2251750	-0.0464166
	C	-1.1057444	-0.4585066	0.1330151		C	-1.1310421	-0.4590307	0.0188228		C	-1.1124652	-0.4953218	-0.0033107
	C	-4.2748819	-0.2386233	0.2505295		C	-4.2542431	-0.2055769	0.4393969		C	-4.3045179	-0.2395894	0.3667280
	C	-4.1457581	1.1003143	0.2132811		C	-4.1202080	1.1223555	0.3645367		C	-4.1753355	1.1021913	0.3515313
	C	-0.2974113	4.2340831	0.1178831		C	-0.2721141	4.2432656	-0.0269696		C	-0.3006532	4.2719865	-0.0069536
	C	1.0426822	4.1024905	0.1326092		C	1.0679795	4.1084817	0.0260046		C	1.0447832	4.1420232	-0.0136100
	C	4.2135889	0.2822923	0.1030058		C	4.2042136	0.2587049	0.2383501		C	4.2478949	0.2840277	0.2142231
	C	4.0830603	-1.0563718	0.0608962		C	4.0672756	-1.0764023	0.1557633		C	4.1180087	-1.0575366	0.1926966
	C	-2.6730189	-2.1410630	0.1916134		C	-2.6733062	-2.1311896	0.2712540		C	-2.6841205	-2.1526292	0.1811573
	C	-2.2083698	2.6559881	0.1041553		C	-2.1863180	2.6664510	0.0916665		C	-2.2183925	2.6666609	0.1462795
	C	2.6109121	2.1848796	0.1151859		C	2.6247925	2.1776576	0.1792752		C	2.6219695	2.1983193	0.1022179
	C	2.1428462	-2.6114868	0.0053913		C	2.1301179	-2.6206207	-0.0334132		C	2.1546282	-	

H	-6.8267783	-5.5688833	0.4018472	H	-6.8373762	-5.5440367	0.5093496	H	-6.8266148	-5.6007105	0.2938263
H	-6.3241170	-4.3388942	-1.7064151	H	-6.3964597	-4.2516322	-1.5751528	H	-6.4150431	-4.2044358	-1.7287167
H	-4.4038160	-2.7594561	-1.7979243	H	-4.4733226	-2.6759101	-1.6791642	H	-4.5031714	-2.6135803	-1.7747321
H	-3.7109675	3.5153099	-1.9727225	H	-3.7121994	3.3917966	-2.0168518	H	-3.8765171	3.4237383	-1.8538844
H	-5.2891661	5.4384828	-2.0182505	H	-5.2941413	5.3097806	-2.1651968	H	-5.4631474	5.3395576	-1.8741016
H	-5.6247630	6.8236687	0.0259650	H	-5.6110165	6.8164455	-0.2073718	H	-5.6508075	6.8235247	0.1129522
H	-4.3735288	6.2744586	2.1097204	H	-4.3381595	6.3985069	1.8937298	H	-4.2429719	6.3797148	0.1266882
H	-2.7961264	4.3513564	2.1436282	H	-2.7563483	4.4836278	2.0300664	H	-2.6567866	4.4639400	2.1354233
H	3.4963404	3.6529439	2.2097489	H	3.4245591	3.7068222	2.2687532	H	3.4120903	3.8377016	2.1127169
H	5.4134600	5.2475990	2.2476898	H	5.3508301	5.2785217	2.3529178	H	5.3240778	5.4282930	2.1145470
H	6.7617917	5.6220680	0.1857919	H	6.7970476	5.5858216	0.3471352	H	6.7656467	5.6466924	0.0935821
H	6.1824055	4.4014282	-1.9080309	H	6.3043563	4.3135405	-1.7381404	H	6.2842630	4.2638483	-1.9226641
H	4.2646714	2.8164700	-1.9343501	H	4.3767417	2.7423444	-1.8111040	H	4.3715617	2.6731498	-1.9131233
H	3.5836822	-3.4492891	-2.1244644	H	3.6039879	-3.3580565	-2.1786487	H	3.7402016	-3.3686013	-2.0165574
H	5.1580703	-5.3727226	-2.2364888	H	5.1690169	-5.2839105	-2.3615098	H	5.3180060	-5.2897413	-2.1051135
H	5.5515197	-6.7802767	-0.2181388	H	5.5211086	-6.7930638	-0.4103326	H	5.5721675	-6.7861070	-0.1286607
H	4.3627576	-6.2052877	1.9073810	H	4.3025155	-6.3028809	1.7203996	H	4.2400733	-6.3487901	1.9314447
H	2.7889017	-4.3287176	2.0078583	H	2.7379275	-4.4369745	1.8917604	H	2.6621432	-4.4279525	2.0084156
N	-0.0650443	0.0305395	-1.7731870	N	-0.3369647	0.1294853	-1.7945054	N	-0.0705035	0.0372633	-2.0127699

$$E = -3230.152485173 E_h$$

$$E = -3230.120942978 E_h$$

$$E = -3230.168671478 E_h$$

78	Fe	-0.0436804	0.0263084	-0.3598148	78	Fe	-0.0329870	0.0266430	0.1475538	78	Fe	-0.0052265	0.0008051	-0.2587715
	N	-0.2278110	-1.9817490	0.0757104		N	-0.2253499	-1.9818181	-0.0910605		N	0.2993641	-1.9457550	0.0535246
	N	-2.1025120	0.2512773	0.1033586		N	-2.1115297	0.2293014	0.1491203		N	-1.9988209	-0.2937684	-0.0238614
	N	0.1581070	2.0301241	0.0935695		N	0.1658388	2.0316547	0.1057186		N	-0.3087793	1.9461742	0.0627998
	N	2.0339296	-0.1749702	0.0092169		N	2.0539307	-0.1802202	0.0834202		N	1.9872344	0.2945411	-0.0216949
	C	0.7798781	-2.9077959	-0.0024947		C	0.7834239	-2.9087445	-0.0050694		C	1.4848632	-2.6150276	-0.1734735
	C	-1.3954852	-2.6972961	0.0642794		C	-1.3983780	-2.6943453	0.0569975		C	-0.6402240	-2.9224021	0.1886427
	C	-3.0136448	-0.7880587	0.1825557		C	-3.0213738	-0.7829948	0.2256015		C	-2.6535651	-1.4906715	0.2218683
	C	-2.8048954	1.3917715	0.1670349		C	-2.8089476	1.3974203	0.1993146		C	-2.9656167	0.6392489	-0.1217331
	C	-0.8515400	2.9568523	0.0616672		C	-0.8455006	2.9594900	0.0508212		C	-1.4948138	2.6140488	-0.1660733
	C	1.3252140	2.7459018	0.0454621		C	1.3377290	2.7442538	0.0476495		C	0.6316799	2.9238185	0.1880435
	C	2.9479190	0.8359966	0.0713148		C	2.9664150	0.8308217	0.1369671		C	2.6424467	1.4892706	0.2329022
	C	2.7357518	-1.3433682	0.0406275		C	2.7518059	-1.3497391	0.1025141		C	2.9531272	-0.6389104	-0.1276179
	C	0.2503450	-4.1986356	-0.0747985		C	0.2498318	-4.1917640	-0.1217400		C	1.2669748	-4.0011366	-0.1921119
	C	1.1281350	-0.4065363	-0.0315305		C	-1.1333784	-0.4059388	-0.0818550		C	-0.0770912	-4.1926598	0.0057182
	C	-4.3436107	-0.2345438	0.3319717		C	-4.3526458	-0.2261932	0.3738811		C	-0.4079901	-1.2581398	0.3004422
	C	-4.2161491	1.1030109	0.3209123		C	-4.2233707	1.1107460	0.3547725		C	-4.2751142	0.0466478	0.0649901
	C	-0.3240251	4.2484386	-0.0174212		C	-0.3153819	4.2441068	-0.0618942		C	-1.2760392	3.9995628	-0.1948536
	C	1.0547390	4.1146226	-0.0262926		C	1.0679990	4.1076765	-0.0621230		C	0.0685594	4.1937949	0.0471294
	C	4.2816055	0.7836882	0.1707584		C	4.3024427	0.2717460	0.2343950		C	4.0672589	1.2522130	0.3191688
	C	4.1510002	-1.0588034	0.1493849		C	4.1708437	-1.0649267	0.2108172		C	4.2631748	-0.0487242	0.0657389
	C	-2.7166368	-2.1367334	0.1454894		C	-2.7202001	-2.1310201	0.1666228		C	-2.0591017	-2.7033221	0.3525212
	C	-2.2560667	2.6604807	0.1190139		C	-2.2531422	2.6630059	0.1242947		C	-2.7605743	2.0089546	-0.2797523
	C	2.6495120	2.1859092	0.0683000		C	2.6627036	2.1795919	0.1031711		C	2.0505059	2.7050264	0.3555718
	C	2.1849199	-2.1008046	0.0050283		C	2.1924687	-2.6137080	0.0338167		C	2.7496198	-2.0089558	-0.2909386
	C	-3.8496474	-3.1009429	0.2021085		C	-3.8502958	-3.0992499	0.2174585		C	-2.8928107	-3.9067943	0.6134861
	C	-3.1897764	3.8196214	0.1380344		C	-3.1843762	3.8237421	0.1243779		C	-3.9519851	2.8721482	-0.4963424
	C	3.7855812	3.1466903	0.0967173		C	3.7935526	3.1473045	0.1171577		C	2.8891512	3.9060397	0.9107959
	C	3.1188074	-3.7704734	-0.0128457		C	3.1182603	-3.7789130	-0.0066168		C	3.9429031	-2.8703990	-1.5080060
	C	-4.0530392	-3.8884723	1.3407412		C	-4.0370093	-3.9102072	1.3424172		C	-2.7970854	-4.5720436	-0.8408360
	C	-4.7246118	-2.3309423	-0.8807771		C	-4.7366398	-3.2122498	-0.8580880		C	-3.7576542	-4.4033032	-0.3662920
	C	-4.0383157	4.0619692	-0.9471568		C	-4.0416025	4.0432756	-0.9588425		C	-4.6718749	2.7817109	-1.6930696
	C	-3.2364982	4.6784748	1.2418447		C	-3.2236260	4.7035409	1.2118336		C	-4.3827442	3.7691478	0.4883265
	C	4.0107440	3.9477128	1.2222383		C	4.0115233	3.9706563	1.2275491		C	2.7604512	4.6096216	1.8139082
	C	4.6479177	3.2560113	-0.9929252		C	4.6504029	3.2484445	-0.9832048		C	3.8004513	4.3597448	-0.3481609
	C	3.8936537	-4.0355876	-1.1464379		C	3.9008023	-4.0150859	-1.1415772		C	4.6679822	-2.7721155	-1.7003669
	C	3.2394411	-6.4040121	1.1047470		C	3.2170905	-6.4502415	1.0839772		C	4.3741995	-3.7692793	0.4759236
	C	-5.1188594	-4.7826523	1.3988748		C	-5.0987386	-4.8097195	1.3947383		C	-3.5622891	-5.7087865	2.0860448
	C	-5.7862953	-4.1326142	-0.8258163		C	-5.7939014	-4.1199931	-0.8095466		C	-5.4182629	-5.5461646	-0.1223343
	C	-4.9180206	5.1425805	-0.9298347		C	-4.9246610	5.1218845	-0.9538083		C	-5.7962030	3.5764935	-1.9054993
	C	-4.1216884	5.736853	1.2622861		C	-4.1126023	5.7753426	1.2207628		C	-5.5125751	4.5572241	0.2791878
	C	5.0867515	4.8315328	1.2547880		C	5.0718079	4.8735926	1.2381812		C	3.5494701	5.7293677	2.0636581
	C	5.7196982	4.1466499	-0.9685942		C	5.7081013	4.1650169	-0.9744702		C	4.5801569	5.4893398	-0.1042726
	C	4.7734796	-5.1165173	-1.1632992		C	4.7709560	-5.1031724	-1.1858968		C	5.8002026	-3.5579598	-1.9064712
	C	4.1247410	-5.6786958	1.0900867		C	4.0934255	-5.7322164	1.0418414		C	5.5100309	-4.5488918	-0.2718107
	C	-5.9868348	-4.9082329	0.3142741		C	-5.9792704	-4.9175317	0.3183222		C	-4.4230222	-6.2001887	1.1043914
	C	-4.9633444	5.9901303	0.1754510		C	-4.9640419	5.9883114	0.1369248		C	-6.2192644	4.4663758	-0.9196130
	C	5.9445760	4.9335682	0.1594318		C	5.9212490	4.9704812	0.1362232		C	4.4611115	6.1722299	1.1048084
	C	4.8936162	-5.9383713	-0.0441965		C	4.8706061	-5.9623349	-0.0931548		C	6.2251601	-4.4475200	-0.9211794
	H	0.8200670	-5.1104804	-0.1499547		H	0.8152359	-5.1040740	-0.2233878		H	2.0201970	-4.7531165	-0.3611485
	H	-1.8642769	-4.8517370	-0.0669345		H	-1.8695281	-4.8408433	-0.1457077		H	-0.6125763	-5.1259491	0.1192342
	H	-5.2452352	-0.8153384	0.4477143		H	-5.2562371	-0.8044908	0.4871231		H	-4.8140208	-2.0172362	0.5184207
	H	-4.9920397	1.8444755	0.4276871		H	-4.9989888	1.8541044	0.4494919		H	-5.2035767	0.5952095	0.0496700
	H	-0.8926954	5.1629748	-0.0649816		H	-0.8815448	5.1584445	-0.1360868		H	-2.0282048	4.7513094	-0.3685147
	H	1.7888180	4.9015674	-0.0845742		H	1.8018429	4.8936836	-0.1362678		H	6.0021163	5.1287029	0.9648885
	H	5.1871368	0.8561333	0.2654389		H	5.2099989	0.8483439	0.3214403		H	4.8037339	2.0036404	0.5533852
	H	4.9264855	-1.8046943	0.2206966		H	4.9485009	-1.8098460	0.2742133		H	5.1926922	-0.5950259	0.0489977
	H	-3.3681176	-3.7925976	2.1874361		H	-3.3423866	-3.8280360	2.1830433		H	-2.1121358	-4.1927037	2.6046617
	H	-5.2723338	-5.3871278	2.2969546		H	-5.2394806	-5.4322724	2.2824715		H	-3.4825304	-6.2178395	3.0503556

C	2.9449268	0.8337801	0.0788652	C	2.8776195	0.8398148	0.1222821	C	2.9089552	0.8160924	0.0036984
C	2.7311595	-1.3452913	0.0456100	C	2.6690179	-1.3298453	0.0822419	C	2.7003976	-1.3532575	-0.0381051
C	0.2471672	-4.2024633	-0.0866768	C	0.2321308	-4.2134102	-0.0402998	C	0.2674262	-4.2323309	-0.1493361
C	-1.1308992	-4.0677826	-0.0433090	C	-1.1075147	-4.0853048	0.0102387	C	-1.0734566	-4.1041147	-0.0972001
C	-4.3373567	-0.2346892	0.3413782	C	-4.2689208	-0.2444264	0.3250494	C	-4.2299329	-0.2692905	0.0249719
C	-4.2102005	1.1032752	0.3285155	C	-4.1411246	1.0959887	0.3015736	C	-4.1020241	1.0723524	0.1801642
C	-0.3219122	4.2496488	-0.0251152	C	-0.3040538	4.2635136	-0.0006998	C	-0.2708529	4.2347135	-0.1109274
C	1.0561295	4.1138674	-0.0308420	C	1.0365102	4.1351978	0.0002730	C	1.0708747	4.1063078	-0.1087976
C	4.2765993	0.2754673	0.1892108	C	4.2068161	0.2923551	0.1749441	C	4.2358904	0.2695637	0.0565405
C	4.1450220	-1.0623663	0.1654499	C	4.0780212	-1.0478846	0.1469094	C	4.1070029	-1.0718531	0.0270126
C	-2.7152650	-2.1366961	0.1426842	C	-2.6707238	-2.1522187	0.1865708	C	-2.6370397	-2.1764357	0.0740232
C	-2.2540407	2.6612915	0.1127228	C	-2.2101649	2.6626463	0.1313956	C	-2.1763697	2.6393233	0.0149908
C	2.6483188	2.1846299	0.0715230	C	2.6048570	2.2010137	0.1064479	C	2.6394788	2.1776189	-0.0064692
C	2.1819672	-2.6146698	0.0034865	C	2.1420308	-2.6133992	0.0345307	C	2.1766362	-2.6376843	-0.0812880
C	-3.8505423	-3.0977240	0.2060544	C	-3.8210817	-3.1035552	0.2302173	C	-3.7872000	-3.1273911	0.1184879
C	-3.1896709	3.8184863	0.1300576	C	-3.1619648	3.8134228	0.1265409	C	-3.1278352	3.7899086	0.0091372
C	3.7854627	3.1439661	0.1029048	C	3.7562592	3.1520318	0.1152048	C	3.7906704	3.1283028	0.0037877
C	3.1189780	-3.7722798	-0.0183303	C	3.0919841	-3.7647140	-0.0139511	C	3.1262292	-3.7887580	-0.1311124
C	-4.0507936	-3.8833745	1.3466436	C	-4.0730730	-3.8596486	1.3796054	C	-4.0412474	-3.8796549	1.2699858
C	-4.7309124	-3.2269147	-0.8722368	C	-4.6639857	-3.2538247	-0.8757988	C	-4.6280414	-3.2806410	-0.9887498
C	-4.0407242	4.0563938	-0.9542535	C	-3.9346688	4.0896545	-1.0060868	C	-3.8964122	4.0684698	-1.1257892
C	-3.2357789	4.6801769	1.2318947	C	-3.2968281	4.6318769	1.2527263	C	-3.2660818	4.6060122	1.1366751
C	4.0068330	3.9484530	1.2266919	C	4.0491029	3.9005599	1.2598355	C	4.0842106	3.8737754	1.1503122
C	4.6523489	3.2499735	-0.9894373	C	4.5598716	3.3089644	-1.0188000	C	4.5934216	3.2877839	-1.1305327
C	3.8973911	-4.0285547	-1.1517878	C	3.8216896	-4.0338293	-1.1764292	C	3.8530868	-4.0583941	-1.2953238
C	3.2401479	-4.6117071	1.0945399	C	3.2655968	-4.5927848	1.0998376	C	3.3021726	-4.6160648	0.9829422
C	-5.1185581	-4.7749736	1.4110597	C	-5.1463550	-4.7476096	1.4233193	C	-5.1151947	-4.7667720	1.3146016
C	-5.7059124	-4.1247497	-0.8105742	C	-5.7372027	-4.1471990	-0.8340441	C	-5.7018390	-4.1680403	-0.9458717
C	-4.9233430	5.1350635	1.9372493	C	-4.8241123	5.1625612	-1.0135593	C	-4.7851785	5.1419377	-1.1341554
C	4.1240734	5.7527875	1.2519314	C	4.1863330	5.7048207	1.2471495	C	4.1550905	5.6793543	1.1300397
C	5.0831468	4.8318426	1.2603989	C	5.1242067	4.7873138	1.2716438	C	5.1596335	4.7601205	1.1636100
C	5.2553800	4.1387514	-0.9573213	C	5.6349199	4.1958656	-1.0089174	C	5.6687019	4.1743763	-1.1189580
C	4.7820023	-5.1047114	-1.1727273	C	4.7057860	-5.1100661	-1.2257218	C	4.7369351	-5.1347736	-1.3450496
C	4.1315652	-5.6818848	1.0765271	C	4.1500425	-5.6688304	1.0525474	C	4.1863426	-5.6225272	0.9340528
C	-5.9931150	-4.8984453	0.3314244	C	-5.9812401	-4.8910290	0.3161477	C	-5.9482429	-4.9131325	0.2064066
C	-4.9683543	5.9851147	0.1663233	C	-4.9522831	5.9288116	0.1135632	C	-4.9168162	5.9500197	-0.0057933
C	5.9440442	4.9317344	0.1675468	C	5.9199263	4.9372154	0.1368325	C	5.9546421	4.9125807	0.0286163
C	4.9037921	-5.9317679	-0.0575647	C	4.8720973	-5.9304745	-0.1109640	C	4.9055660	-5.9545927	-0.2310858
H	0.8171228	-5.1142325	-0.1637116	H	0.8125938	-5.1180482	-0.1270843	H	0.8475707	-5.1369595	-0.2381750
H	-1.8692219	-4.8517842	-0.0821271	H	-1.8536273	-4.8630412	-0.0267058	H	-1.8195381	-4.8818597	-0.1345540
H	-5.2381699	-0.8152559	0.4633416	H	-5.1723890	-0.8266468	0.4122741	H	-5.1333750	-0.8512858	0.2938754
H	-4.9852629	1.8446126	0.4402105	H	-4.9810792	1.8410792	0.3656651	H	-4.8789777	1.8174294	0.2443706
H	-0.8891641	5.1646527	-0.0780403	H	-0.8870804	5.1687327	-0.0599976	H	-0.8537700	5.1398697	-0.1721571
H	1.7913778	4.9000989	-0.0881493	H	1.7808125	4.9133548	-0.0580481	H	1.8151352	4.8844528	-0.1677898
H	5.1818742	0.8531553	0.2912097	H	5.1132029	0.8739014	0.2336677	H	5.1420496	0.8509129	0.1176600
H	4.9192148	-1.8089504	0.2449671	H	4.8565806	-1.7934068	0.1781098	H	4.8855718	-1.8173330	0.0589885
H	-3.3592646	-3.7885221	2.1882583	H	-3.4181180	-3.7442411	2.2479222	H	-3.3879191	-3.7613275	2.1391408
H	-5.2680964	-5.3777578	2.3108498	H	-5.3330408	-5.3293173	2.3302489	H	-5.3039533	-5.3452945	2.2231233
H	-6.8293740	-5.6101982	0.3791673	H	-6.8233712	-5.5876352	0.3497111	H	-6.7908818	-5.6090813	0.2407836
H	-6.4758808	-4.2190977	-1.6617355	H	-6.3856146	-4.2513455	-1.7077346	H	-6.3487877	-4.2759002	-1.8203170
H	-4.5734828	-2.6203301	-1.7685225	H	-4.4699846	-2.6666484	-1.7779646	H	-4.4316055	-2.6968716	-1.8926055
H	-4.0028159	3.3886538	-1.8195576	H	-3.8312988	3.4537430	-1.8899360	H	-3.7897317	3.4345007	-2.0166479
H	-5.5719155	5.3124758	-1.7939187	H	-5.4191312	5.3681864	-1.9076635	H	-5.3767236	5.3498875	-2.0300119
H	-5.6624569	6.8298969	0.1822766	H	-5.6501295	6.8146400	0.1085449	H	-5.6142528	6.7921110	-0.0115630
H	-4.1591620	6.4111879	2.1243473	H	-4.2834971	6.3341120	2.1361327	H	-4.2552320	6.3068133	2.0199761
H	-2.5730952	4.4960125	2.0815563	H	-2.6968699	4.4185665	2.1420463	H	-2.6695126	4.3903179	2.0277001
H	3.3304943	3.8723937	2.0828175	H	3.4248365	3.7799735	2.1497855	H	3.4606627	3.7506315	2.0404256
H	5.2510298	5.4485447	2.1476089	H	5.3432824	5.3628179	2.1752757	H	5.3795753	5.3331326	2.0680010
H	6.7875426	5.6280285	0.1930171	H	6.7634470	5.6328986	0.1453109	H	6.7985169	5.6078142	0.0384076
H	6.3925137	4.2160352	-1.8201846	H	6.2526713	4.3101704	-1.9039401	H	6.2857802	4.2910122	-2.0141326
H	4.4797844	2.6301187	-1.8731092	H	4.3335944	2.7279635	-1.9174413	H	4.3658927	2.7095583	-2.0306569
H	3.8043361	-3.3747964	-2.0240569	H	3.6882583	-3.3903126	-2.0506974	H	3.7170737	-3.4156546	-2.1897737
H	5.3813463	-5.2974888	-2.0670314	H	5.2660695	-5.3107404	-2.1430915	H	5.2950866	-5.3360335	-2.2644759
H	5.6045801	-6.7706576	-0.0724034	H	5.5655234	-6.7750380	-0.1490084	H	5.5985704	-6.7994423	-0.2703669
H	-4.2245411	-6.3229955	1.9576707	H	4.2774674	-6.3058074	1.9321844	H	4.3158382	-6.3287086	1.8137551
H	2.6360861	-4.4128617	1.9840413	H	2.6992803	-4.3852164	2.0122575	H	2.7384608	-4.4073736	1.8967256
N	-0.0753035	0.0388346	-1.9833829								

$$E = -3175.584113407 E_h$$

$$E = -3175.534656153 E_h$$

$$E = -3175.536289239 E_h$$

77

Fe	-0.0338885	0.0248455	0.1147987
N	-0.2297591	-2.0177102	0.1382135
N	-2.0765451	0.2211127	0.1272316
N	0.1629463	2.0673350	0.1455379
N	2.0077429	-0.1712971	0.0486699
C	0.7855434	-2.9237566	0.0656972
C	-1.4011835	-2.7135421	0.1235611
C	-2.9818111	-0.7954990	0.1901506
C	-2.7716855	1.3919401	0.1776923
C	-0.8542349	2.9737637	0.1174229
C	1.3330777	2.7633538	0.0924144
C	2.9148998	0.8449930	0.0856261
C	2.7040906	-1.3423455	0.0652235
C	0.3026554	-4.2514890	-0.0092216
C	-1.1137573	-4.1223501	0.0281649
C	-4.3080733	-0.2424491	0.2965865
C	-4.1790298	1.1025094	0.2871349
C	-0.3023189	4.3020213	0.0316607
C	1.0425926	4.1272348	0.0181569
C	4.2441448	0.2911806	0.1390220
C	4.1145606	-1.0536559	0.1245943
C	-2.6863884	-2.1628381	0.1707359
C	-2.2211944	2.6778668	0.1504572
C	-2.6191171	2.1231119	0.0877210
C	2.1528324	-2.6281241	0.0498556
C	-3.8376542	-3.1146177	0.2011364
C	-3.7129287	3.8295176	0.1573746
C	3.3712066	3.1635310	0.0846876
C	3.1032840	-3.7803560	0.0151766
C	-4.0809850	-3.8990414	1.3336970
C	-4.6889781	-3.2392116	-0.9020074
C	-3.9716949	4.0967172	-0.9596759
C	-3.2827291	4.6576254	1.2795730
C	4.0563899	3.9366481	1.2152551
C	4.5829767	3.2970732	-1.0468525
C	3.8603582	-4.0424493	-1.1317201
C	3.2515848	-4.6157543	1.1275231
C	-5.1522732	-4.7898624	1.3631312
C	-5.7600722	-4.1304523	-0.8744711
C	-4.8619780	5.1688255	-0.9554005
C	-4.1734970	5.7294887	1.2857756
C	5.1307241	4.8242704	1.2153929
C	5.6570053	4.1851896	-1.0486352
C	4.7463426	-5.1175890	-1.1667550
C	4.1381007	-5.6905795	1.0944128
C	-5.9944		

C	4.8875990	-5.9445059	-0.0533214	C	4.8970366	-5.9383595	-0.0403053	C	4.8998696	-5.9405013	-0.0399267
H	0.8039435	-5.1611737	-0.0947957	H	0.8094213	-5.1376256	-0.1419103	H	0.8062925	-5.1464272	-0.1393588
H	-1.8533956	-4.9060049	-0.0201119	H	-1.8699840	-4.8762751	-0.0638517	H	-1.8701112	-4.8847897	-0.0612325
H	-5.2165910	-0.8175441	0.3825335	H	-5.2485137	-0.8096441	0.3857253	H	-5.2591821	-0.8067106	0.3884694
H	-4.9617202	1.8408652	0.3630220	H	-4.9919934	1.8454739	0.3623382	H	-5.0026347	1.8457945	0.3644829
H	-0.8781356	5.2123281	-0.0257991	H	-0.8935625	5.1824381	-0.1114018	H	-0.8913748	5.1913703	-0.1124007
H	1.7800144	4.9568624	-0.0517276	H	1.7906757	4.9243369	-0.1395141	H	1.7905584	4.9336663	-0.1409060
H	5.1554370	0.8655264	0.1954915	H	5.1829957	0.8560842	0.2016336	H	5.1924273	0.8533898	0.2001751
H	4.8992467	-1.7926106	0.1662812	H	4.9238459	-1.8001596	0.1640010	H	4.9330509	-1.8005811	0.1628056
H	-3.4215014	-3.8025721	2.2008951	H	-3.3920034	-3.8121480	2.1963141	H	-3.3991490	-3.8147491	2.1982642
H	-5.3316049	-5.3936161	2.2570583	H	-5.2918327	-5.4126950	2.2724768	H	-5.2963070	-5.4185168	2.2699323
H	-6.8345536	-5.6077264	0.2805599	H	-6.8227766	-5.6264674	0.3166247	H	-6.8233508	-5.6337665	0.3109399
H	-6.4139098	-4.2202069	-1.7463602	H	-6.4435972	-4.2231690	-1.7078424	H	-6.4415110	-4.2297213	-1.7125124
H	-4.5014702	-2.6316103	-1.7919468	H	-4.5532329	-2.6084876	-1.7656338	H	-4.5540684	-2.6118573	-1.7655209
H	-3.8867564	3.4553199	-1.8415234	H	-3.9513654	3.4403161	-1.8220178	H	-3.9522802	3.4454583	-1.8224525
H	-5.4768666	5.3671209	-1.8376556	H	-5.5223121	5.3673489	-1.7934549	H	-5.5222845	5.3733079	-1.7941283
H	-5.6644894	6.8286584	0.1723989	H	-5.6524699	6.8401653	0.2145854	H	-5.6534364	6.8452795	0.2147948
H	-4.2516671	6.3650960	2.1721428	H	-4.1912069	6.3820382	2.1786423	H	-4.1933353	6.3859157	2.1790255
H	-2.6636543	4.4514806	2.1574033	H	-2.6058087	4.4666921	2.1318270	H	-2.6085395	4.4703618	2.1324213
H	3.4277252	3.8332657	2.1042731	H	3.3693427	3.8580077	2.0845826	H	3.3740095	3.8576487	2.0850210
H	5.3435352	5.4185829	2.1083023	H	5.2796923	5.4467363	2.1209030	H	5.2839753	5.4460177	2.1211492
H	6.7766880	5.6474925	0.8222770	H	6.7622869	5.6645815	0.1319337	H	6.7643805	5.6681177	0.1317222
H	6.2799406	4.2817701	-1.9421553	H	6.3392530	4.2599980	-1.8837164	H	6.3410280	4.2645995	-1.8849714
H	4.3625819	2.6982100	-1.9352006	H	4.4415052	2.6524323	-1.9033265	H	4.4438124	2.6563581	-1.9050010
H	3.7457456	-3.951054	-2.0058311	H	3.8097481	-3.3680642	-1.9957531	H	3.8088577	-3.3731045	-1.9975168
H	5.3277988	-5.3123583	-0.0721590	H	5.3853147	-5.2894819	-0.0439727	H	5.3852753	-5.2939358	-0.0465997
H	5.5827273	-6.7880801	-0.0801250	H	5.5917357	-6.7828942	-0.0565214	H	5.5950887	-6.7848279	-0.0556111
H	4.2460686	-6.3322463	1.9732511	H	4.1981254	-6.3492660	1.9638685	H	4.2028268	-6.3491987	1.9656707
H	2.6657171	-4.4132381	2.0286734	H	2.6079319	-4.4407199	1.9931911	H	2.6119195	-4.4419915	1.9941604

$$E = -3175.544418228 E_h$$

$$E = -3175.541269517 E_h$$

$$E = -3635.566258601 E_h$$

77

Fe	-0.0306645	0.0252669	0.1195656
N	-0.2232365	-1.9695908	0.1126266
N	-2.0268470	0.2177832	0.1423673
N	0.1605826	2.0205004	0.1255062
N	1.9646985	-0.1671300	0.0884289
N	0.7834183	-2.9043669	0.0309598
C	-1.3860902	-2.6932482	0.1204797
C	-2.9587981	-0.7834218	0.2221371
C	-2.7525622	1.3743952	0.1793147
C	-0.8476897	2.9560145	0.0840652
C	1.3233257	2.7435551	0.1039064
C	2.8992944	0.8327370	0.1566209
C	2.6897411	-1.3245051	0.0989366
C	0.2290144	-4.2344278	-0.0466446
C	-1.1053005	-4.1050181	0.0164497
C	-4.2528653	-0.2613246	0.3288750
C	-4.1218331	1.1125431	0.2993158
C	-0.2950811	4.2867714	0.0032224
C	1.0403056	4.1566395	0.0205491
C	4.1948799	0.3078852	0.2341034
C	4.0611910	-1.0655037	0.1942906
C	-2.6622890	-2.1737346	0.1934884
C	-2.1949875	2.6890497	0.1136260
C	2.6016278	2.2252588	0.1364699
C	2.3190804	-2.6373932	0.0303779
C	-3.8113292	-3.1178965	0.2428676
C	-3.1502246	3.8205337	0.1017068
C	3.7530133	3.1664909	0.1396800
C	3.0837020	-3.7789596	-0.0325295
C	-4.0581175	-3.8719907	1.3940419
C	-4.6628272	-3.2542931	-0.8582234
C	-3.9403160	4.0732357	-1.0266276
C	-3.2792053	4.6623159	1.2173195
C	4.0484207	3.9220718	1.2783479
C	4.5566042	3.3027750	-0.9973107
C	3.8098735	-4.0280009	-1.2012739
C	3.2655577	-4.6135594	1.0743110
C	-5.1938989	-4.7491258	1.4439441
C	-5.7366891	-4.1402130	-0.8122826
C	-4.8351819	5.1404769	-1.0422719
C	-4.1830270	5.7234018	1.2051932
C	5.1259385	4.8057732	1.2792272
C	5.6293614	4.1913807	-0.9981269
C	4.6896611	-5.1059865	-1.2674847
C	4.1500357	-5.8886380	1.0096891
C	-5.9787691	-4.8884953	0.3393827
C	-4.9611338	5.9662862	0.0748931
C	5.9160585	4.9448959	0.1397870
C	4.8607857	-5.9390126	-0.1625441
H	0.8081590	-5.1387273	-0.1448207
H	-1.8543144	-4.7995311	-0.0180073
H	-5.1593807	-0.8375393	0.3244885
H	-4.9036504	1.8519419	0.3640071
H	-0.8749747	5.1933170	-0.0650460
H	1.7871633	4.9326797	-0.0306732
H	5.1043043	0.8813191	0.3145474
H	4.8421576	-1.8077293	0.2340711
H	-3.3980337	-3.7590472	2.2588619
H	-5.3296137	-5.3255748	2.3534037
H	-6.8252136	-5.7953888	1.7568899
H	-6.3908592	-4.2454276	-1.6821561
H	-4.7413389	-2.6591339	-1.7560520
H	3.8453757	3.4191661	-1.8977536
H	-5.4416053	5.3252160	-1.9332397
H	-5.6677695	6.8007543	0.0650724
H	-4.2809652	6.3620869	2.0871612
H	-2.6663846	4.4693268	2.1025442
H	3.4257314	3.8091534	2.1701112
H	5.3487513	5.3868348	2.1781480
H	6.7565550	5.6433915	0.1381438
H	6.2461145	4.2966353	-1.8947562
H	4.3303017	2.7093372	-1.8875005
H	3.6750103	-3.3718867	-2.0656846
H	5.2448385	-5.2984061	-2.1899236
H	5.5513169	-6.7843993	-0.2181731
H	4.2826661	-6.3340923	1.8822309
H	2.7059706	-4.4145412	1.9927571

$$E = -3635.576402394 E_h$$

77

Fe	-0.0424114	0.0199440	0.0547082
N	-0.2357953	-2.0287927	0.1334429
N	-2.1004918	0.2194741	0.0157425
N	0.1553376	2.0678109	0.1498881
N	2.0126493	-0.1772021	-0.0643849
N	0.7709210	-2.9345522	-0.0512689
C	-1.4031907	-2.7249696	0.0008077
C	-3.0049755	-0.7990484	0.1676801
C	-2.7956551	1.3902144	0.1660249
C	-0.8568389	2.9753554	0.0117277
C	1.3173322	2.7649051	-0.0202681
C	2.9231497	0.8389908	0.0637017
C	2.7127504	-1.3492836	0.0438549
C	0.2393653	-4.2073717	-0.3036773
C	-1.1362749	-4.0748241	-0.2712199
C	-4.3162844	-0.2439685	0.4251605
C	-4.1885803	1.0943925	0.4231279
C	-0.3338086	4.2501132	-0.2511568
C	1.0418282	4.1168338	-0.2704647
C	4.2433491	0.2812284	0.2622991
C	4.1149104	-1.0567341	0.2491572
C	-2.7167590	-2.1535745	0.1178197
C	-2.2553972	2.6658039	0.1168797
C	2.6337774	2.1932659	0.0404330
C	2.1715544	-2.6244490	0.0017042
C	-3.8510955	-3.1119654	0.1891703
C	-3.1874978	3.8228209	0.1716982
C	3.7716078	3.1495944	0.0782845
C	3.1129079	-3.7757299	0.0149022
C	-3.9408207	-4.0219213	1.2496928
C	-4.8402155	-3.1250045	-0.8004690
C	-4.1445549	4.0149282	-0.8308929
C	-3.1107030	4.7469640	1.2211927
C	3.9138727	4.0356396	1.1529857
C	4.7127626	3.1811944	-0.9563529
C	4.0237603	-3.9645759	-1.0305075
C	3.1062698	-4.6828857	1.0814236
C	-5.0073761	-4.9132569	1.3275917
C	-5.9017768	-4.0254127	-0.7284570
C	-5.0081684	5.1081376	-0.7859845
C	-3.9804557	5.8328830	1.2718128
C	4.9864667	4.9220706	1.1999833
C	5.7804547	0.4760519	-0.9143247
C	4.9174158	-5.0339975	-1.0061594
C	4.0081074	-5.7433291	1.1119927
C	-5.9900463	-4.9185367	0.3376732
C	-4.9297865	6.0180467	0.2666021
C	5.9225292	4.9448567	0.1658732
C	4.9160133	-5.9218526	0.0681667
H	0.8088751	-5.1020714	-0.4997305
H	-1.8739051	-4.8438052	-0.4371501
H	-5.2070604	-0.8222748	0.6128289
H	-4.9540553	1.8313580	0.6081137
H	-0.9084830	5.1467305	-0.4200110
H	1.7740577	4.8863341	-0.4566725
H	5.1413709	0.8567520	0.4207377
H	4.8863707	-1.7958978	0.3949905
H	-3.1659051	-4.0205513	2.0207964
H	-5.0713964	-5.6102157	2.1675099
H	-6.8243038	-5.6227329	0.3968156
H	-6.6635421	-4.0297951	-1.5128309
H	-4.7667590	-2.4267879	-1.6389250
H	-4.1990313	3.3033463	-1.6593500
H	-5.7454334	5.2498302	-1.5810303
H	-5.6082665	6.8746597	0.3037157
H	-3.9157424	6.5412075	2.1023306
H	-2.3609011	4.6045100	2.0039331
H	3.1761173	4.0184049	1.9596849
H	5.0923084	5.6009390	2.0506867
H	6.7623457	5.6438926	0.2006925
H	6.5048715	4.0944643	-1.7329704

N	-0.0548804	-2.0084798	0.1691131	N	-0.0574390	-2.0079525	0.1215468	N	0.0237275	-1.9617999	0.2025262
N	-1.9905698	0.0757401	0.1787063	N	-2.0098323	0.0765237	0.1274836	N	-1.9589904	-0.0193669	0.2411243
N	0.0802846	2.0293275	0.1876263	N	0.0756318	2.0302641	0.1381121	N	-0.0083359	1.9644629	0.2057255
N	1.9874390	-0.0506711	0.1403087	N	2.0242462	-0.0518553	0.1267933	N	1.9597470	0.0227971	0.2238043
C	0.9724530	-2.8540707	0.1318425	C	0.9799186	-2.8536925	0.1223237	C	1.1037279	-2.7695522	-0.0849353
C	-1.1965463	-2.7868884	0.0593927	C	-1.2006614	-2.7935720	0.0466302	C	-1.0337438	-2.7964873	0.3172870
C	-2.8399030	-0.9648642	0.2268391	C	-2.8525661	-0.9653925	0.1951282	C	-2.7727222	-1.1079843	0.5201288
C	-2.7756479	1.2125582	0.2925426	C	-2.7866119	1.2139473	0.2612211	C	-2.7847479	1.0273041	0.1252312
C	-0.9660153	2.8739202	0.1640444	C	-0.9703257	2.8804600	0.1495579	C	-1.1063300	2.7774097	-0.0838540
C	1.2046938	2.8128293	0.0866898	C	1.2111084	2.8132216	0.0735050	C	1.0341206	2.7942565	0.3235477
C	2.8424098	0.9916202	0.2067919	C	2.8679652	0.9907557	0.1908354	C	2.7739290	1.1113234	0.4979134
C	2.7760017	-1.1922530	0.2579133	C	2.8016671	-1.1919012	0.2446700	C	2.7910640	-1.0318696	0.0942576
C	0.5285946	-4.2170605	-0.0193444	C	0.5318878	-4.2204854	0.0171925	C	0.6719551	-4.1432399	-0.1900253
C	-0.8157251	-4.1753343	-0.0766625	C	-0.8113559	-4.1830371	-0.0415413	C	-0.6433981	-4.1609704	0.0903747
C	-4.1891369	-0.5202606	0.4420758	C	-4.2026366	-0.5203764	0.4100881	C	-4.1429711	-0.6645569	0.6507505
C	-4.1506691	0.8243098	0.4838069	C	-4.1633388	0.8261952	0.4484384	C	-4.1533291	0.6504044	0.3784842
C	-0.5241034	4.2369925	0.0328821	C	-0.5184369	4.2433393	0.0628562	C	-0.6658825	4.1549697	-0.1911984
C	0.8223915	0.4993417	-0.0244401	C	0.8270510	0.4202917	0.0052156	C	0.6410591	4.1704711	0.0979067
C	4.1948219	0.5371779	0.4152850	C	4.2250385	0.5388751	0.3855759	C	4.1493650	0.6706931	0.6103313
C	4.1545629	-0.8020870	0.4476892	C	4.1846372	-0.8042253	0.4203623	C	4.1626724	-0.6400694	0.3308328
C	-2.4845947	-2.3452108	0.1058961	C	-2.4902927	-2.3461413	0.0884311	C	-2.3731542	-2.4119815	0.5657021
C	-2.3352288	2.5102542	0.2493996	C	-2.3414618	2.5120194	0.2336357	C	-2.3976153	2.3746753	-0.1511527
C	2.4988120	2.3686300	0.1161378	C	2.5094835	2.3642385	0.1048869	C	2.3786716	2.4136884	0.5649408
C	2.3481486	-2.4904409	0.2165768	C	2.3598631	-2.4858662	0.2097553	C	2.4112908	-2.3620877	-0.1624934
C	-3.5962298	-3.3355304	0.0626880	C	-3.6012028	-3.3376577	0.0547435	C	-3.3732938	-3.4879016	0.8091168
C	-3.3419838	3.6072445	0.2943249	C	-3.3473427	3.6082745	0.2958877	C	-3.4797597	3.3531983	-0.4491010
C	3.6101892	3.3604313	0.0866635	C	3.6166089	3.3609858	0.0821789	C	3.3765248	3.4913906	0.8128301
C	3.3548529	-3.5877463	0.2580829	C	3.3611553	-3.5767495	0.2628314	C	3.4844697	-3.3534993	-0.4550442
C	-3.8014931	-4.2176934	1.1285266	C	-3.8063918	-4.2089806	1.1294532	C	-3.3156920	-4.2376820	1.9889017
C	-4.4500197	-3.3811933	-0.0451962	C	-4.4545501	-3.3954086	-0.0529108	C	-4.3608979	-3.7708986	-0.1400334
C	-4.2141481	3.7992194	-0.7822515	C	-4.2224168	3.8158932	-0.7755347	C	-4.1772315	3.2592873	-1.6584048
C	-3.4241534	4.4514256	1.4074216	C	-3.4258538	4.4382818	1.4203438	C	-3.8211995	4.3510181	0.4692483
C	3.8289550	4.2127841	1.1740095	C	3.8289780	4.2098447	1.1734920	C	3.3339326	4.2183577	2.0074969
C	4.4484709	3.4403409	-1.0309424	C	4.4573708	3.4491207	-1.0329281	C	4.3459297	3.8012240	-0.1467152
C	4.2168711	-3.7878529	-0.8250411	C	4.2265156	-3.7996619	-0.8153136	C	4.1838464	-3.2800621	-1.6592967
C	3.4446946	-4.4269622	1.3745021	C	3.4423954	-4.4194436	1.3854266	C	3.8136344	-4.3475776	0.4768941
C	-4.8473812	-5.1380033	1.0851074	C	-4.8517528	-5.1302753	1.0950761	C	-4.2427232	-5.2504038	2.2212227
C	-5.4888541	-4.3078201	-1.0892621	C	-5.4928517	-4.3228147	-1.0879041	C	-5.2832762	-4.7896801	0.0920774
C	-5.1574755	4.8244735	-0.7456276	C	-5.1649646	4.8411458	-0.7225880	C	-5.1958273	4.1633467	-1.9489519
C	-4.3737635	5.4695363	1.4448067	C	-4.3746882	5.4563890	1.4740144	C	-4.8449627	5.2508334	0.1769404
C	4.8722185	5.1363673	1.1423561	C	4.8683072	5.1380506	1.1482242	C	4.2569292	5.2344428	2.2437769
C	5.4858258	4.3693053	-1.0628008	C	5.4907698	4.3826759	-1.0584406	C	5.2661299	4.8209865	0.0902414
C	5.1585914	-4.8149300	-0.7912313	C	5.1630137	-4.8311328	-0.7704834	C	5.1932904	-4.1978571	-1.9416997
C	4.3916629	-5.4475451	1.4087045	C	4.3841214	-5.4444272	1.4306703	C	4.8276186	-5.2610110	0.1946268
C	-5.6899130	-5.1856594	-0.0239655	C	-5.6938459	-5.1897889	-0.0137514	C	-5.2269325	-5.5280722	1.2729441
C	-5.2399520	5.6584787	0.3678526	C	-5.2437869	5.6602492	0.4021570	C	-5.5312222	5.1592412	-1.0327420
C	5.6996446	5.2173384	0.0236796	C	5.6981862	5.2271910	0.0319888	C	5.2237691	5.5370609	1.1853682
C	5.2482309	-5.6439603	0.3252587	C	5.2440503	-5.6527258	0.3521440	C	5.5166207	-5.1885017	-1.0515434
H	1.1746825	-5.0769487	-0.0885716	H	1.1773014	-5.0826373	-0.0231732	H	1.3149349	-4.9719764	-0.4395070
H	-1.5048367	-4.9956559	-0.1996921	H	-1.4970535	-5.0298334	-0.1367578	H	-1.3121100	-5.0058830	0.1185994
H	-5.0433284	-1.1669916	0.5590959	H	-5.0570590	-1.1665102	0.5289336	H	-4.9721688	-1.3032320	0.9097437
H	-4.9660011	1.5096290	0.6519801	H	-4.9791987	1.5121656	0.6114404	H	-4.9908966	1.3289493	0.3651255
H	-1.1706166	5.0973454	-0.0244043	H	-1.1600736	5.1087364	0.0326978	H	-1.3080592	4.9842183	-0.4416488
H	1.5092164	5.0235739	-0.1326979	H	1.5146979	5.0294994	-0.0773811	H	1.3132328	5.0125129	0.1328914
H	5.0496442	1.1821629	0.5381552	H	5.0807676	1.1846050	0.4979423	H	4.9776241	1.3120245	0.8653037
H	4.9698334	-1.4898637	0.6060370	H	5.0007855	-1.4927066	0.5710527	H	5.0042443	-1.3136538	0.3059958
H	-3.1436904	-4.1742611	2.0014127	H	-3.1489295	-4.1562608	2.0020748	H	-2.5433330	-4.0195907	2.7327368
H	-5.0051322	-5.8200199	1.9244956	H	-5.0094396	-5.8037287	1.9413601	H	-4.1969623	-5.8259671	3.1492335
H	-6.5079091	-5.9097081	-0.0589276	H	-6.5114364	-5.9146042	-0.0415932	H	-5.9520421	-6.3253919	1.4547719
H	-6.1445759	-4.3461658	-1.9628110	H	-6.1482210	-4.3704672	-1.9612609	H	-6.0480932	-5.0097794	-0.65970135
H	-4.2906598	-2.6950952	-1.8821397	H	-4.2953184	-2.7176049	-1.8967616	H	-4.3975216	-3.1979727	-1.0711903
H	-4.1440879	3.1467787	-1.6573383	H	-4.1553274	3.1751117	-1.6594168	H	-3.9106628	2.4798814	-2.3784416
H	-5.8306124	4.9724381	-1.5938729	H	-5.8403694	5.0008549	-1.5669925	H	-5.7295048	4.0911712	-2.9009414
H	-5.9822215	6.4601917	0.3972096	H	-5.9854596	6.4619429	0.4443271	H	-6.3324000	5.8664651	-1.2619847
H	-4.4397829	6.1181812	2.3202442	H	-4.4377823	6.0933059	2.3599954	H	-5.1090639	6.0261664	-0.9606171
H	-2.7477587	4.3013131	2.2540956	H	-2.7471514	4.2764855	2.2629979	H	-3.2883371	4.4162553	1.4224878
H	3.1825165	4.1441886	2.0538172	H	3.1806817	4.1348860	2.0513700	H	3.1979577	2.7605042	1.6224850
H	5.0398342	5.7951777	1.9982271	H	5.0309181	5.7940715	2.0071953	H	4.2224033	5.7918696	3.1833137
H	6.5155182	5.9441679	-0.0019469	H	6.5109590	5.9576532	0.0113738	H	5.9462677	6.3359794	1.4705710
H	6.1295993	4.4334211	-1.9437140	H	6.1364809	4.4531321	-1.9374522	H	6.0183028	5.0593444	-0.6660650
H	4.2780633	2.7783685	-1.8851607	H	4.2920567	2.7898531	-1.8902249	H	4.3713928	3.2459695	-1.0889469
H	4.1460181	-3.1398291	-1.7029265	H	4.1571282	-3.1574273	-1.6979991	H	3.9256491	-2.5050251	-2.3875679
H	5.8244662	-4.9683015	-1.6442493	H	5.8315374	-4.9938085	-1.6196991	H	5.7289894	-4.1401542	-2.8926577
H	5.9888760	-6.4472535	0.3523612	H	5.9805884	-6.4594491	0.3879113	H	6.3102396	-5.9066697	-1.2365440
H	4.4635985	-6.0921127	2.2884683	H	4.4492981	-6.0831088	2.1532414	H	5.0825061	-6.0321344	0.9260805
H	2.7758524	-4.2715440	2.2263188	H	2.7708971	-4.2547563	2.2339588	H	3.2785889	-4.3985270	1.4297826
Cl	0.0719313	0.0151425	-2.4361838	Cl	0.0068533	0.0172285	-2.5498229	Cl	-0.0203218	0.0065577	-2.1878753

$$E = -3635.591784088 E_h$$

$$E = -3250.515701702 E_h$$

$$E = -3250.510917474 E_h$$

78	Fe	-0.0002818	-0.0000164	-0.3549726	78	Fe	0.0014795	-0.0034945	-0.2039895	78	Fe	-0.0393546	0.0247155	-0.3181692
N	0.0563071	-2.0195736	0.1524882	N	-0.3300977	-1.9509656	0.0482964	N	-0.2288222	-1.9825397	0.1514445			
N	-2.0221514	-0.0558009	0.1487056	N	-1.9308383	0.3330720	0.1199140	N	-2.0354028	0.2225895	0.1932326			
N	-0.0564137	2.0192737	0.1536334	N	0.3351437	1.9421425	0.0605201	N	0.1671918	2.0282777	0.1597484			
N	0.0220303	0.0555112	0.1469414	N	1.9363229	-0.3423261	0.1015702	N	1.9738419	-0.1769980	0.1189815			
N	1.1732535	-2.8069141	0.0376872	C	0.6060891	-2.9473355	-0.1837684	C	0.784					

C	-5.3080963	-4.6534342	-0.7421437	C	-6.0647616	-3.7185446	-0.3384627	C	-5.7017316	-4.1592993	-0.8814727
C	-5.5623431	4.2977545	-0.8992230	C	-4.4765905	5.1613976	-1.6602580	C	-4.7790000	5.1663084	-1.0737208
C	-4.6811153	5.2815135	1.1225990	C	-3.7600805	6.0542790	0.4648434	C	-4.2392262	5.6928733	1.2193121
C	4.3225741	5.5375308	1.2757929	C	5.2192125	4.4499324	1.7781837	C	5.1746359	4.7610302	1.2567246
C	5.3076072	4.6532092	-0.7440355	C	6.0686525	3.7099097	-0.3565895	C	5.5947223	4.2175037	-1.0573397
C	5.5625285	-4.2966782	-0.9042484	C	4.4649189	-5.1539395	-1.7446860	C	4.6699869	-5.1145410	-1.2740226
C	4.6823950	-5.2812729	1.1176440	C	3.7706979	-0.6655817	0.3798624	C	4.2006703	-5.6609525	-1.0298219
C	-5.2938280	-5.6027457	0.2787858	C	-6.1902042	-4.5075074	0.8035622	C	-5.9834026	-4.8885335	0.2727277
C	-5.6336538	5.2631713	0.1045937	C	-4.5392570	6.1575343	-0.6861646	C	-4.9571908	5.9645058	0.0555897
C	5.2944261	5.6018125	0.2775662	C	6.2006452	4.4937723	0.7881959	C	5.9212848	4.9355660	0.0920277
C	5.6349251	-5.2619303	0.0996485	C	4.5380163	-6.1584595	-0.7799681	C	4.8805058	-5.9241417	-0.1584874
H	1.4776649	-4.9904192	-0.3152652	H	0.4283591	-5.1559561	-0.5444269	H	0.8011111	-5.1516498	-0.0695678
H	-1.1992827	-5.0646770	-0.2679511	H	-2.1858042	-4.7041793	-0.1467475	H	-1.8625057	-4.8836342	0.0352115
H	-4.9589335	-1.4762316	0.7806148	H	-5.1234980	-0.4343096	0.7575925	H	-5.1982984	-0.8145334	0.4475000
H	-5.0353093	1.2024971	0.7371416	H	-4.6774868	2.1872319	0.3953188	H	-4.9323811	1.8523334	0.4009505
H	-1.4771695	4.9903396	-0.3114477	H	-0.4280365	5.1513455	-0.5023048	H	-0.8695039	5.1991020	0.0029702
H	1.1987936	5.0645956	-0.2664136	H	2.1893897	4.6966074	-0.1303893	H	1.7960284	4.9306722	0.0115428
H	4.9593571	1.4755973	0.7770996	H	5.1338144	0.4196530	0.7212380	H	5.1439545	0.8588759	0.2683544
H	5.0356839	-1.2031102	0.7321427	H	4.6849003	-2.1986462	0.3403863	H	4.8762830	-1.8076455	0.2133381
H	-2.5984817	-4.4808839	2.0341557	H	-3.3199846	-3.6102401	2.4051276	H	-3.4981806	-3.7073430	2.2827900
H	-4.3119623	-6.2774304	2.0818185	H	-5.2999619	-5.0827776	2.6866367	H	-5.4112895	-5.2930618	2.3167998
H	-6.0442301	-6.3971454	0.2971665	H	-7.0603109	-5.1573208	0.9270251	H	-6.8241575	-5.5867760	0.2873993
H	-6.0642259	-4.7048662	-1.5295249	H	-6.8330643	-3.7506419	-1.1151661	H	-6.3183446	-4.88362108	-1.7749726
H	-4.3644495	-2.8935394	-1.5656664	H	-4.8527401	-2.2747987	-1.3955097	H	-4.4052671	-2.6989019	-1.8079717
H	-4.4874227	2.5910633	-1.6710166	H	-3.5856207	3.2840188	-2.2501758	H	-3.7415048	-3.4739012	-1.9274699
H	-6.3041185	4.2844567	-1.7016988	H	-5.0836008	5.2408127	-2.5656958	H	-5.3367728	5.3785973	-1.9894148
H	-6.4368331	6.0048645	0.0936628	H	-5.1993629	7.0175615	-0.8246861	H	-5.6586861	6.8022412	0.0283561
H	-4.7390151	6.0315496	1.9153756	H	-3.8103227	6.8298531	1.2534487	H	-4.3784355	6.3144117	2.1075645
H	-2.9079233	4.3534544	1.9340106	H	-2.3108409	4.8732992	1.5481692	H	-2.7824393	4.4097157	2.1688105
H	2.5981771	4.4798311	2.0339895	H	3.3394647	3.5896729	2.4019782	H	3.5181977	3.7318489	2.1869202
H	4.3138325	6.2758677	2.0815280	H	5.3210560	5.0680001	2.6787844	H	5.4302711	5.3191475	2.1610715
H	6.0452727	6.3957886	0.2960848	H	7.0714662	5.1430164	0.9095854	H	6.7614224	5.6346107	0.0803125
H	6.0630887	4.7050080	-1.5320149	H	6.8325484	3.7453966	-1.1374829	H	6.1756183	4.3537637	-1.9713309
H	4.3627703	2.8941926	-1.5680628	H	4.8503871	2.2712588	-1.4133498	H	4.2634347	2.7650799	-1.9463339
H	4.4859788	-2.5909543	-1.6759123	H	3.5671822	-3.2718871	-2.3089397	H	3.6124839	-3.4107099	-2.0789881
H	6.3039566	-4.2826333	-1.7070380	H	5.0624553	-5.2252131	-2.6570785	H	5.1976799	-5.3202711	-2.2088363
H	6.4385685	-6.0025813	0.0889048	H	5.1969773	-0.7169558	-0.9327246	H	5.5774136	-6.7641801	-0.2157940
H	4.7407923	-6.0315535	1.9101527	H	3.8291992	-6.8477907	-1.1410229	H	4.3653126	-6.2913205	1.9074378
H	2.9084675	-4.3548117	1.9292723	H	2.3321480	-4.8948370	1.4883048	H	2.7791660	-4.3819741	2.0365557
Cl	-0.0012981	0.0006348	-2.5205278	O	-0.0048503	0.0042301	-1.7871324	O	-0.0686779	0.0308889	-1.9208953

$$E = -3250.523894400 E_h$$

$$E = -3250.508384459 E_h$$

78

Fe	-0.0364858	0.0234236	-0.1537344
N	-0.2386879	-1.9397451	0.1154528
N	-1.9875763	0.2337702	0.1765335
N	0.1754414	1.9848820	0.1208746
N	1.9252294	-0.1887179	0.1049439
C	0.7625967	-2.8800500	-0.0321892
C	-1.3887335	-2.6450718	0.1695406
C	-2.9243955	-0.7726649	0.3097867
C	-2.6952713	1.3833459	0.1561191
C	-0.8304655	2.9259468	0.0154683
C	1.3267328	2.6900550	0.1381968
C	2.8663537	0.8169025	0.2120744
C	2.6314590	-1.3381883	0.0529641
C	0.1856371	-4.2113188	-0.0918757
C	-1.1362040	-4.0669524	0.0484012
C	-4.2526739	-0.1974925	0.4277623
C	-4.1119762	1.1278173	0.3211020
C	-0.2560592	4.2576188	-0.0562760
C	1.0699819	4.1126368	0.0353119
C	4.1976664	0.2407952	0.2812972
C	4.0530050	-1.0838463	0.1712554
C	-2.6852020	-2.1178503	0.3039583
C	-2.1745085	2.6828951	0.0225522
C	2.6272606	2.1621430	0.2228659
C	2.1060318	-2.6368756	-0.0712908
C	-3.8314143	-3.0676958	0.4123131
C	-3.1313800	3.8242326	-0.0707586
C	3.7763040	3.1117626	0.2965159
C	3.0583814	-3.7777061	-0.2073290
C	-4.0665757	-3.7531814	1.6083460
C	-4.6753120	-3.2818167	-0.6817887
C	-3.8287828	4.0563946	-1.2603818
C	-3.3431420	4.6638398	1.0272581
C	4.0455156	3.7993721	1.4841720
C	4.5885379	3.3243497	-0.8216342
C	3.7104080	-4.0025604	-1.4237853
C	3.3098841	-4.6249926	0.8763028
C	-5.1383426	-4.6379550	1.7100859
C	-5.7455025	-4.1690146	-0.5785822
C	-4.7232473	5.1211109	-1.3514666
C	-4.2399343	5.7268604	0.9345989
C	5.1193044	4.6847250	1.5536921
C	5.6608823	4.2121235	-0.7506130
C	4.5987883	-5.0681238	-1.5556931
C	4.2005962	-5.6887889	0.7427688
C	-5.9787045	-4.8467075	0.6170624
C	-4.9298401	5.9570301	-0.2547025
C	5.9278302	4.8920778	0.4366371
C	4.8446750	-5.9120406	-0.4732592
H	0.7561694	-5.1171074	-0.2213673
H	-1.9013455	-4.8262841	0.0574802
H	-5.1532750	-0.7717971	0.5753069
H	-4.8700840	1.8932898	0.3601098
H	-0.8308587	5.1640762	-0.1595014
H	1.8348270	4.8721591	0.0216579
H	5.1029336	0.8139812	0.4021435
H	4.8117380	-1.8496527	0.1801535
H	-3.4093399	-3.5870056	2.4670942
H	-5.3201390	-5.1649011	2.6502836
H	-6.8191044	-5.5408575	0.6978550
H	-6.3997780	-4.3323634	-1.4387615
H	-4.4886669	-2.7522496	-1.6206911
H	-3.6632515	3.4026637	-2.1218395
H	-5.2594088	5.3008739	-2.2868051
H	-5.6315912	6.7918308	-0.3274436
H	-4.4012993	6.3778212	1.7976862
H	-2.8041797	4.4800874	1.9614686
H	3.4131950	3.6344000	2.3616610
H	5.3277644	5.2131939	2.4874690
H	6.7696995	5.5869335	0.4920661
H	6.2901293	4.3743439	-1.6294827
H	4.3751619	2.7935311	-1.7541153
H	3.5137488	-3.3426242	-2.2738975
H	5.0991897	-5.2423409	-2.5116689
H	5.5412730	-6.7477438	-0.5781300

78

Fe	-0.0360045	0.0245426	-0.3232475
N	-0.2290850	-1.9843908	0.1253784
N	-2.0320342	0.2223571	0.1640533
N	0.1707163	2.0277366	0.1405032
N	1.9740786	-0.1777438	0.0940936
C	0.7880093	-2.9060176	0.0515080
C	-1.3850799	-2.6864985	0.1285927
C	-2.9520884	-0.7966096	0.2338136
C	-2.7330434	1.3769925	0.2009387
C	-0.8485966	2.9507634	0.1081574
C	1.3253533	2.7297897	0.1106339
C	2.8952821	0.8410392	0.1397332
C	2.6758696	-1.3332558	0.0946337
C	0.2212300	-4.2479448	-0.0042537
C	-1.1093618	-4.1124656	0.0459449
C	-4.2892698	-0.2318509	0.3570037
C	-4.1546953	1.0997184	0.3340273
C	-0.2835942	4.2920644	0.0425914
C	1.0476849	4.1564838	0.0484748
C	4.2364360	0.2752702	0.2076359
C	4.1017719	-1.0558796	0.1779278
C	-2.6851507	-2.1484220	0.1970778
C	-2.1988760	2.6800047	0.1389142
C	2.6271235	2.1924642	0.1301901
C	2.1393242	-2.6346614	0.0385218
C	-3.8334829	-3.1024035	0.2333600
C	-3.1595820	3.8230120	0.1150417
C	3.7743204	3.1487207	0.1288699
C	3.0964927	-3.7794923	-0.0249227
C	-4.1065499	-3.8331896	1.3940639
C	-4.6440490	-3.2728057	-0.8931027
C	-3.8900419	4.0980882	-1.0449871
C	-3.3379428	4.6241555	1.2466279
C	4.0959565	3.8689236	1.2842248
C	4.5316321	3.3353249	-1.0319491
C	3.7886769	-4.0519544	-1.2090481
C	3.3055393	-4.5892302	1.0955836
C	-5.1818058	-4.7186142	1.4290485
C	-5.7188949	-4.1597676	-0.8562126
C	-4.7874114	5.1638526	-1.0726156
C	-4.2347144	5.6907230	1.2166786
C	5.1628766	4.7648816	1.2773102
C	5.5989357	4.2325429	-1.0359924
C	4.6748507	-5.1259621	-1.2724934
C	4.1948968	-5.66	

H	4.3930699	-6.3460221	1.5946568	H	4.3539894	-6.2862718	1.9122404
H	2.8065299	-4.4468503	1.8312287	H	2.7695224	-4.3764468	2.0254065
O	-0.0652427	0.0286211	-1.7370195	O	-0.0608517	0.0353064	-1.9141093

8.10 Research Article: Photolysis of an Archetypal Model Complex. Photooxidation Versus Photoreduction of Azido(porphinato)iron(III)

S. Fleisch, P. Vöhringer, *Chem. Eur. J.* **2023**, *29*, e202301207.

DOI: <https://doi.org/10.1002/chem.202301207>

No changes were made. Available under license: CC BY-NC-ND 4.0

<https://creativecommons.org/licenses/by-nc-nd/4.0/>

Photolysis of an Archetypal Model Complex. Photooxidation Versus Photoreduction of Azido(porphinato)iron(III)

Stefan Flesch^{*[a]} and Peter Vöhringer^[a]

Azidoporphinatoiron(III) ([1]) is an archetypal model complex for the photochemical generation of nitridoiron(V) complexes via cleavage of dinitrogen. So far, this process has only been studied with continuous irradiation in thin films under cryogenic conditions or in frozen solutions. In addition, the photooxidation from iron(III) to iron(V) competes with photoreduction to iron(II) via cleavage of an azidyl radical. The quantum yields of both pathways remained hitherto undisclosed. Here, we investigated the photolysis of this model complex in room temperature liquid solution using stationary

and time-resolved infrared spectroscopy. The two reaction pathways are unambiguously identified in quenching studies and their quantum yields are accurately determined. Nitridoporphinatoiron(V) ([2]) exhibits N-atom-2-electron-transfer reactivity toward *tert*-butyl isonitrile and forms a carbodiimido species. In the presence of *tert*-butyl isonitrile, the two products of the photoreduction pathway react to cationic diisonitriloporphinatoiron(III) and azide anions, which in turn combine to reform [1] and the quencher.

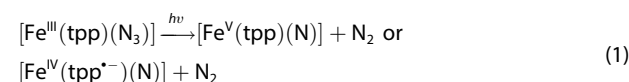
Introduction

Enzymes containing the heme moiety catalyze a vast variety of metabolic conversions.^[1] For example, the cytochrome P450 superfamily of enzymes catalyze hydroxylation reactions by inserting oxygen into aliphatic C–H bonds.^[2] Today, it is widely accepted that the reactive intermediate in the catalytic cycle of these enzymes adopts a so-called “ π -cation radical” state – a somewhat misleading term meant to represent a cationic complex of iron(IV) exhibiting an axial oxido ligand and an equatorial porphirindyl radical anion ligand, i.e. $[(\text{por}^{\bullet-})\text{Fe}^{\text{IV}}=\text{O}^{2-}]^+$. This notation should be given preference over representations like $(\text{por}^{\bullet+})\text{Fe}^{\text{IV}}=\text{O}$, which are frequently used in the literature^[1,3] although violating the conservation of charge. Related compounds carrying the nitridoiron motif, $\text{Fe}\equiv\text{N}$, are at the core of significant research efforts due to their implication in corresponding nitrogenation reactions.^[4] For example, nitrido(porphinato)chromium and manganese complexes were observed to undergo reversible and irreversible complete nitride exchange reactions.^[5]

Trigonal symmetrical metal nitrides are typically stable isolable species and their reactions with phosphines,^[6] carbon

monoxide,^[7] and isonitriles^[8] producing phosphoraniminato, isocyanato, and carbodiimido products, respectively, have been studied in great detail. In tetragonal symmetry, nitrido complexes of late transition metals are non-isolable and elucidating their reactivity requires complex time-resolved spectroscopies.^[9] Despite these promising applications, the properties of high-valent nitridoiron complexes are not yet fully understood. Specifically for neutral porphyrin-containing iron nitrides, $[(\text{por})\text{Fe}\equiv\text{N}]^0$, their reactivity in liquid solution under ambient conditions has not yet been addressed at all.

Here, we examine the photochemistry of the complex, azido(5,10,15,20-tetraphenylporphyrin-21,23-diido)iron(III), aka azidoporphinatoiron(III) (in short, $[\text{Fe}(\text{tpp})(\text{N}_3)]$ or [1]), in liquid solution at room temperature. Compound [1] is a paradigmatic compound, which was utilized in seminal work in the late 1980's by Wagner and Nakamoto^[10] to generate, for the first time, a complex of a late transition metal that featured a terminal nitrido ligand, specifically the species, $[\text{Fe}(\text{tpp})(\text{N})]$ ([2]), via Reaction (1).



Since this product is inherently unstable, a thin film of the precursor was deposited and subsequently irradiated under cryogenic conditions, thereby, trapping the nitride and enabling its detection by resonance Raman spectroscopy.

In liquid solution, an investigation of the photochemistry is challenging because of the inherent instability of [2], which can only be overcome in experiments that provide a sufficient time-resolution. In addition, the photochemistry of transition metal azides is more complex because apart from the photooxidation (1), the photoreduction according to Reaction (2)

[a] S. Flesch, Prof. Dr. P. Vöhringer
 Clausius-Institut für Physikalische und Theoretische Chemie
 Rheinische Friedrich-Wilhelms-Universität
 Wegelerstraße 12, 53115 Bonn (Germany)
 E-mail: flesch@pc.uni-bonn.de

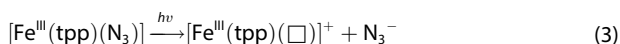
Supporting information for this article is available on the WWW under <https://doi.org/10.1002/chem.202301207>

© 2023 The Authors. Chemistry – A European Journal published by Wiley-VCH GmbH. This is an open access article under the terms of the Creative Commons Attribution Non-Commercial NoDerivs License, which permits use and distribution in any medium, provided the original work is properly cited, the use is non-commercial and no modifications or adaptations are made.



must also be taken into account.^[9a,11] The release of the azidyl radical generates a ferrous product ($[\mathbf{3}_{\text{red}}]$) with an axial vacancy, \square . A cryomatrix, which greatly reduces the molecular mobilities, suppresses photoreduction by promoting the prompt geminate recombination.^[11a,b,d] In contrast, liquid solutions facilitate the cage escape and shift the product recombination partially also into the bulk phase where it occurs as a diffusion-driven bimolecular process on microsecond time scales and longer.^[9a,11d,12] Cage escape typically results in the coordination of a molecule from the immediate solvent shell of $[\mathbf{1}]$.

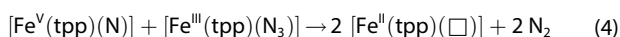
Finally, a redox-neutral release of an azide anion according to Reaction (3)



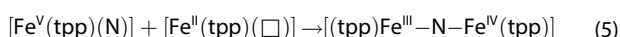
can also occur, which conserves the oxidation state of the metal. Reaction (3) will be preferred in highly polar media due to the additional solvent stabilization of its charged products. Just like before, filling of the axial vacancy by the solvent as well as geminate and non-geminate bulk recombination of the azide anion with the under-coordinated ferric product, $[\mathbf{3}]$, has to be considered.^[9b,13]

The relative quantum yields of Reactions (1)–(3) depend not only on the environment but also on the wavelength of the excitation light. For octahedral non-heme azidoiron(III) bearing an ancillary tetradentate secondary amine ligand, it was found that the reductive and the redox-neutral Fe– N_α bond cleavage prevail in the visible-to-near ultraviolet region whereas the oxidative N_α – N_β dissociation emerges in substantial yields only for shorter wavelengths in the ultraviolet region.^[9b,13a] This is a direct consequence of a prompt internal conversion following the initial optical excitation and the wavelength-dependent excess vibrational energy with which the parent complex is dressed following its radiation-less return to the ground-state. All three processes then occur as quasi-thermal unimolecular reactions from the “hot” ground-state in a competitive fashion.^[14]

The thermal instability of high-valent nitridoiron complexes with fourfold symmetry reveals itself even in the absence of reagents through the formation of dinuclear, μ -N bridged complexes as final products.^[11a,15] According to Ref. [15b], a reaction of the nitride with the parent via Reaction (4)



can produce two molecules of $[\mathbf{3}_{\text{red}}]$ upon dinitrogen release. Continuous irradiation results in a gradual consumption of $[\mathbf{1}]$ and progressively accumulates $[\mathbf{3}_{\text{red}}]$. Therefore, the formation of the diiron mixed-valence product according to Reaction (5)



becomes more likely over time.

In this work, we wish to clarify the relative importance of the three competing decay paths for $[\text{Fe}(\text{tpp})(\text{N}_3)]$ in liquid dichloromethane (DCM) solution at room temperature as a function of the excitation wavelength. To this end, solutions of $[\mathbf{1}]$ were photolyzed in the absence and in the presence of suitable quenching reagents and the obtained products were identified by stationary and time-resolved infrared spectroscopy. Such studies are urgently needed for elucidating the molecular-level mechanisms responsible for high-valent iron formation as well as for understanding the chemical reactivity patterns of the captivating terminal nitridometal ($\text{M}\equiv\text{N}$) and oxidometal ($\text{M}=\text{O}$) cores that are frequently encountered in nature and technology.

Experimental Section

Complex $[\mathbf{1}]$ was prepared according to the procedure described by Adams et al.^[16] The electronic absorption spectra in the ultraviolet-to-visible (UV-Vis) region were measured with a UV-160 spectrophotometer (Shimadzu) and stationary and rapid-scan Fourier-transform infrared (FTIR) spectra were recorded with a Vertex 70 spectrometer (Bruker). Excitation pulses with a duration of 5 ns and a center wavelength of 355 nm were obtained by frequency tripling the fundamental output of a Q-switched Nd:YAG laser (Continuum Surelite II-10). In addition, the 355 nm pulses were employed to drive a tunable optical parametric oscillator (OPO, Continuum Surelite) to generate excitation pulses centered at 412 and 510 nm. Femtosecond pump-probe data were recorded with a laser system described elsewhere.^[17]

Computational

Quantum chemical calculations within the framework of density functional theory (DFT) were performed using the TURBOMOLE program package (version 7.5).^[18] Specifically, Head-Gordon's range separated hybrid-functional $\omega\text{B97X}^{[19]}$ was used together with Grimme's D4-dispersion correction.^[20] For all atoms of porphyrin, azide and isonitrile moieties, and the central iron atom, Ahlrichs' triple- ζ basis set, def2-TZVP,^[21] was used whereas for all atoms of the peripheral phenyl and *tert*-butyl groups, the smaller double- ζ basis set, def2-SVP,^[21b,22] was applied. Molecular geometries were optimized using the program's default convergence criteria. The converged structures were confirmed to be true minima on the potential energy surface by performing harmonic frequency calculations and verifying that all eigenvalues of the hessian matrix were positive. Energies and unrelaxed difference densities of electronic transitions were computed by time-dependent density functional theory (TD-DFT).

Results and Discussion

Stationary spectroscopy

The UV-Vis spectrum of $[\mathbf{1}]$ in room temperature DCM solution is reproduced in Figure 1(a). At first glance, it displays all the features that are prototypical for the electronic spectra of metalloporphyrins.^[23] In the near-UV region, it consists of two very strong bands peaking at 414 nm and 361 nm with extinction coefficients of $1.25 \times 10^5 \text{ M}^{-1} \text{ cm}^{-1}$ and

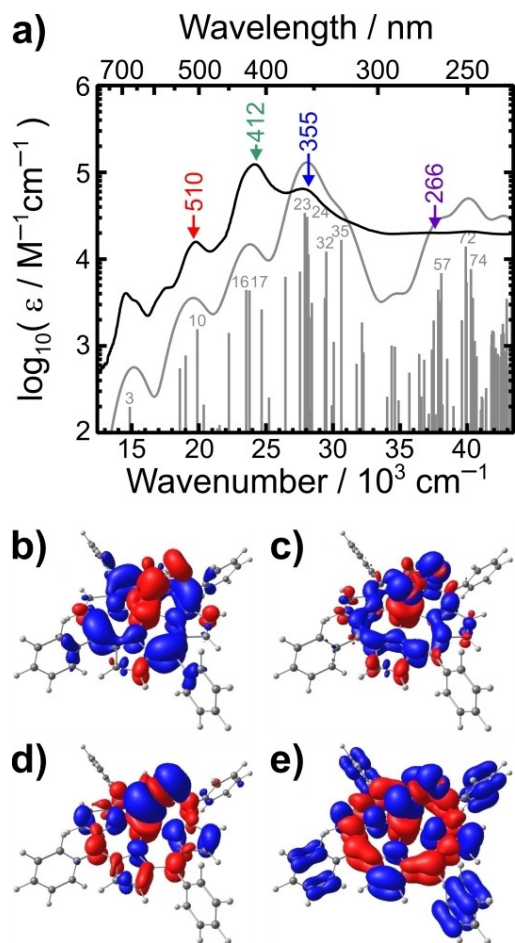


Figure 1. a) Stationary UV-Vis spectrum of [1] in DCM solution (black line) and theoretically calculated electronic excitation spectrum (gray sticks). The numbers indicate the root of some selected excitations. The stick spectrum was convoluted by a Gaussian function with a full width at half maximum of 2000 cm^{-1} (gray line). Labeled arrows indicate the excitation wavelengths (in nm) used in the photolysis experiments. b–e) Isosurfaces of the unrelaxed difference density of root 16, 23, 35 and 72, respectively (isovalues: red: $+0.0003$, blue: -0.0003).

$6.45 \times 10^4\text{ M}^{-1}\text{ cm}^{-1}$, respectively. In the visible region, four resonances can be distinguished; namely, two bands centered at 506 nm and 687 nm with extinction coefficients of $1.58 \times 10^4\text{ M}^{-1}\text{ cm}^{-1}$ and $4.1 \times 10^3\text{ M}^{-1}\text{ cm}^{-1}$, respectively, and two pronounced shoulders around 568 nm and 655 nm. According to Gouterman's four-orbital model^[24] and more recent considerations based on TD-DFT^[25] one would assign the 414 nm-resonance to the B-band (or Soret band) and the resonances in the visible to the Q-bands. However, in the presence of metal centers with an open d-shell such as iron(III), the spectra and the electronically excited states must be understood in terms of configuration interaction between the porphyrin singlet and triplet $\pi\pi^*$ states with the tpp-to-Fe charge-transfer excited states. In addition, there will be heavy mixing with N_3 -to-Fe charge-transfer excitations as well. A very careful analysis has been conducted by Kobayashi et al.^[26] for a series of different complexes of the type $[\text{Fe}^{\text{III}}(\text{tpp})\text{X}]$ with $\text{X}=\text{Cl}, \text{Br}, \text{I}, \text{SCN}$, and

CH_3CO_2 , all of which occupy a d^6 -high-spin ($S=5/2$) ground-state. Not surprisingly, the spectrum shown in Figure 1(a) closely resembles that reported for $\text{X}=\text{SCN}$.

As shown in Figure 1(a), the TD-DFT-calculation is able to reproduce the spectrum reasonably well except for the typical overall blue-shift (here, ca. 4000 cm^{-1}). An analysis based on natural transition orbitals demonstrates that the majority of transitions cannot be assigned in a simple fashion to electronic promotions between only one or two pairs of orbitals around the HOMO-LUMO gap. The nature of the transitions can however be interpreted qualitatively with unrelaxed electron difference densities as follows. Transitions in the visible region of the spectrum shift electronic density mostly from the porphyrinato moiety to the metal center and the azido ligand, i.e., $\text{tpp} \rightarrow \text{Fe}/\text{tpp} \rightarrow \text{N}_3$ charge-transfer (see Figure 1b). The strongest 414 nm-band is best described as a mixed ligand-to-metal charge transfer (LMCT) of the type $\text{tpp} \rightarrow \text{Fe}/\text{N}_3 \rightarrow \text{Fe}$ (cf. Figure 1c). Farther in the UV near 360 nm, the optical transition also carries $\text{N}_3 \rightarrow \text{Fe}$ CT-character, which is now mixed with $\text{tpp} \rightarrow \pi\pi^*$ (cf. Figure 1d). Finally, deep in the UV, electronic transitions begin to involve charge shifts from the peripheral phenyl rings to the porphyrindiide core (cf. Figure 1e).

The stationary FTIR spectrum of [1] in DCM solution is depicted in Figure 2, which emphasizes the antisymmetric stretching region of the azido ligand only. The N_3 -stretching mode absorbs at 2056 cm^{-1} with a molar decadic peak extinction coefficient of $2150\text{ M}^{-1}\text{ cm}^{-1}$, i.e., similar to other transition metal azides.^[27] The N_3 -resonance of [1] is frequency-upshifted by 50 cm^{-1} relative to the corresponding resonance of the free azide anion in the same solvent. It is worth stressing that the absorption strength of the antisymmetric stretching mode of the azide barely changes upon ligation to the iron(III) center. As we have shown in a series of publications,^[9a,11c,13,28] this property can be exploited in photolysis experiments to quantify accurately the fraction of photoexcited parent complexes that release an N_3^- anion. Also shown in Figure 2 is the absorption spectrum of *tert*-butyl isonitrile in the same spectral

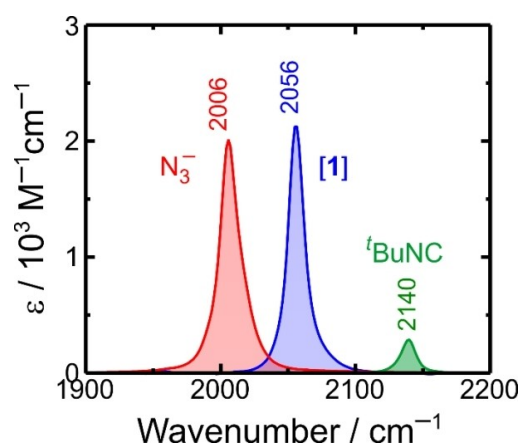


Figure 2. Stationary FTIR-spectra in the region of the antisymmetric N_3^- -stretching vibration of [1] (blue) and tetrabutylammonium azide (red), and of the $-\text{N}=\text{C}$ stretching region of *tert*-butyl isonitrile (green), each measured in DCM solution. The numbers indicate peak positions in cm^{-1} .

region. Following previous work^[8] we will use this molecule as a quenching reagent to test for the presence of a metal nitride. Its FTIR-spectrum exhibits a highly characteristic $\text{N}\equiv\text{C}$ stretching absorption that peaks in DCM solution at 2140 cm^{-1} and although this band is significantly weaker than that of the azide stretching mode, it can nonetheless serve as sensitive vibrational probe of the reactivity of the $\text{Fe}\equiv\text{N}$ core.

Stationary photolysis difference spectroscopy

In a first experiment, solutions of [1] in DCM were exposed to a single 412 nm laser pulse and a total of 400 rapid-scan FTIR-spectra were recorded in the time window ranging from 70 ms to 0.5 min. Since no temporal evolution was observed during this time period, all spectra were averaged to improve the signal-to-noise ratio and the result is reproduced in Figure 3(a) by the blue curve. Given the temporal invariance of the data, this spectrum corresponds to a stationary difference spectrum,

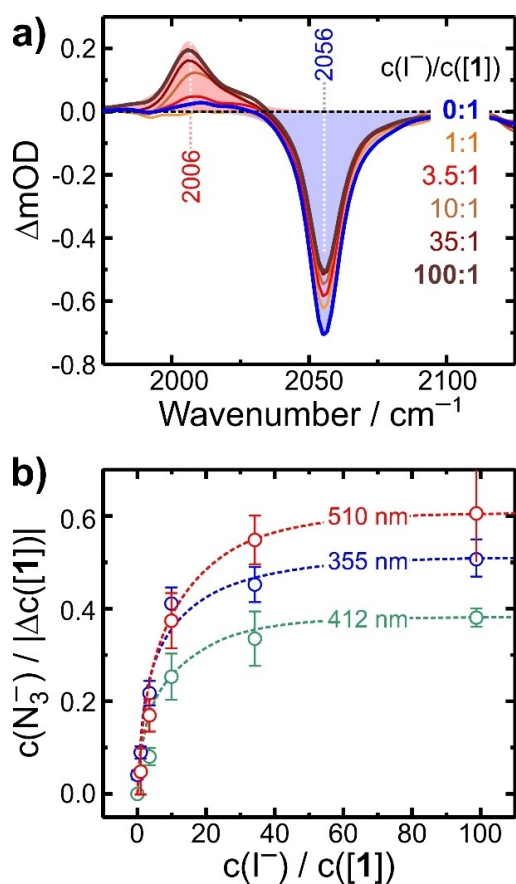


Figure 3. a) 412 nm-photolysis difference spectra of a pure solution of [1] in DCM (blue) and solutions containing tetrabutylammonium iodide with various concentrations relative to the parent. The blue and red areas represent the (inverted) properly scaled stationary FTIR spectrum of [1] and N_3^- , respectively. Numbers indicate peak positions in cm^{-1} . b) Concentration of generated azide anions relative to that of photolyzed [1] as a function of the iodide quencher concentration for the three excitation wavelengths, 355 nm (blue circles), 412 nm (green), and 510 nm (red). The dashed curves are intended for guiding the eye.

which is equal to the difference between the sample's absorbance with and without the photolysis pulse. As such, the negative signal that peaks at 2056 cm^{-1} with an amplitude of -0.7 mOD indicates a steady-state bleaching of the azide antisymmetric stretching band of [1] and, hence, a permanent photoconversion of the sample (see the blue-shaded area in Figure 3a for the inverted and scaled stationary FTIR-spectra of the solution). The net transformation of the sample does not appear to generate stable products that absorb in the azide stretching region unless their IR-absorption band is accidentally identical to that of [1]. Similarly, the generation of free azide anions can also be ruled out since the spectrum lacks a positive flash-induced positive band at the characteristic position of 2006 cm^{-1} . Preliminary UV-pump/IR-probe experiments on time scales ranging between 500 fs all the way up to 3.5 ns did not reveal any spectroscopic signature of free N_3^- either.^[29] Therefore, we can dismiss the redox-neutral pathway (3) in the 412 nm-photolysis of [1] in liquid DCM entirely.

This leaves the photooxidation (1) and the photoreduction (2) as the only two reaction pathways; however, neither of them generates products that exhibit a characteristic and sufficiently strong IR-absorption. Instead, the primary photoproducts must be converted by suitable quenching reagents to secondary products that are amenable to an IR-detection. Ideally, the quencher should react quantitatively and selectively with either one of the two primary fragments. For pathway (2), the azidyl radical can be quenched with iodide anions in the one-electron transfer reaction (6)^[11d,30]



This process has been reported^[12b] to occur with a bimolecular rate constant of $4.5 \times 10^8\text{ M}^{-1}\text{ s}^{-1}$, which is sufficiently high to suppress the self-quenching Reaction (7).



Therefore, stationary 412 nm-photolysis difference spectra were recorded again but now in the presence of tetrabutylammonium iodide at various concentrations. The results of this quenching study are also displayed in Figure 3(a).

It can clearly be seen that the characteristic azide absorption at 2006 cm^{-1} grows in as the I^- -concentration is gradually increased. This finding demonstrates undeniably that azidyl radicals are formed via the photoreduction pathway, $[1] \rightarrow [3_{\text{red}}] + \text{N}_3^*$. In addition, it can also be noticed that the negative permanent bleaching band markedly decreases as the concentration of the quencher is raised. This is a quite surprising observation, which actually contradicts the initial expectations: Since the quencher effectively removes the azidyl radicals, its geminate recombination, $[3_{\text{red}}] + \text{N}_3^* \rightarrow [1]$, back to the parent should be suppressed and consequently, the permanent bleach should increase with increasing quencher concentration and not decrease as observed in Figure 3a. Thus, this unexpected observation gives evidence for a bimolecular reaction that consumes the parent, [1], but that is inhibited upon addition of the quencher.

Finally, the absorption-to-bleach ratio in Figure 3(a) never reaches a value of one even for the highest quencher concentrations, at which all azidyl radicals are quantitatively converted to azide anions. However, the equally intense stationary FTIR-spectra of [1] and N_3^- (cf. Figure 2) requests the positive azide absorption to be almost exactly as strong as the parent bleach. Therefore, the data in Figure 3(a) clearly reveal that photoreduction cannot be the only pathway in the 412 nm-photolysis of [1]. Since the involvement of the redox-neutral pathway was already dismissed above, we must conclude here that the remaining consumption of [1] follows the photooxidation pathway.

If indeed photooxidation and photoreduction occur simultaneously, we must take into account a reaction of the high-valent Fe(V)-product with the iodide quencher. Such a reaction would in fact suppress the bimolecular process (4), which reads in short $[1] + [2] \rightarrow 2[3_{\text{red}}] + 2N_2$. Thus, an iodide-induced quenching of [2] represents a bimolecular reaction that suppresses the consumption of the parent and is therefore indeed able to rationalize the decreasing permanent bleach with increasing iodide concentration as observed above in Figure 3(a).

To be more quantitative, Figure 3(b) plots the flash-induced azide concentration, $c(N_3^-)$, normalized to the flash-induced parent consumption, $-\Delta c([1])$, as a function of the iodide quencher concentration, $c(I^-)$. In the limit, $c(I^-) \rightarrow \infty$, the quantity, $c(N_3^-)/|\Delta c([1])|$, is equal to the fractional yield of Reaction (2), f_{red} . This is because all azidyl radicals formed therein are quantitatively converted to azide anions and all bimolecular reactions affecting the total conversion yield of [1] after the initial photodissociation (i.e., through the bulk recombination of N_3^* and $[3_{\text{red}}]$ and Reaction (4)) are fully suppressed. From Figure 3(b), we infer a photoreduction fraction of roundabout 40% for the 412 nm photolysis. The photoreduction fraction, does not seem to follow a systematic trend as it is found to be about 50% for the shortest wavelength (355 nm) and 60% for the longest wavelength (510 nm).

In addition, we emphasize that the complement, i.e., 60% at 412 nm, 50% at 355 nm, and 40% at 510 nm, is equal to the fraction of photooxidation, f_{ox} , according to Reaction (1).

Note that the fractions, f_{red} and f_{ox} , need to be interpreted under the restraint that they pertain only to the portion of complexes, [1], that has been successfully photoconverted. Thus, they differ from the primary photoreduction and photooxidation yields, Φ_{red} and Φ_{ox} . The latter are limited by the primary quantum yield for photodecomposition, $\Phi_{\text{prim}} = \Phi_{\text{red}} + \Phi_{\text{ox}}$, which has to compete with the non-reactive recovery of the ground state (e.g., through geminate recombination and/or non-reactive internal conversion). The primary quantum yield of these non-reactive channels is actually much closer to unity, i.e., $(1 - \Phi_{\text{prim}}) \rightarrow 1$, as will be demonstrated below.

Time-resolved FTIR-spectroscopy

Having obtained indirect evidence for the photooxidation pathway, we are now confronted with the task of quenching the nitrido-complex, [2]. To this end, we conducted photolysis experiments in the presence of 1 equivalent of *tert*-butyl isonitrile (${}^t\text{BuNC}$), the results of which are depicted in Figure 4. The reaction with isonitriles has been carried out previously only with air-stable, isolable transition metal nitrides such as nitridoferryl species with threefold-symmetry^[7] or distorted octahedral complexes with 4f and 5f-metals.^[8a,31] The quenching reaction when transferred to [2] becomes a N-atom-two-electron transfer reaction, which generates (*tert*-butylcarbodiimido)(5,10,15,20-tetraphenylporphyrin-21,23-diido)iron(III) ([4]) according to Reaction (8).



The asymmetric stretching vibration of the heterocumulene moiety is known to be a very strong IR-absorber in the region between 2100 cm^{-1} and 2200 cm^{-1} .^[7,8,17,32]

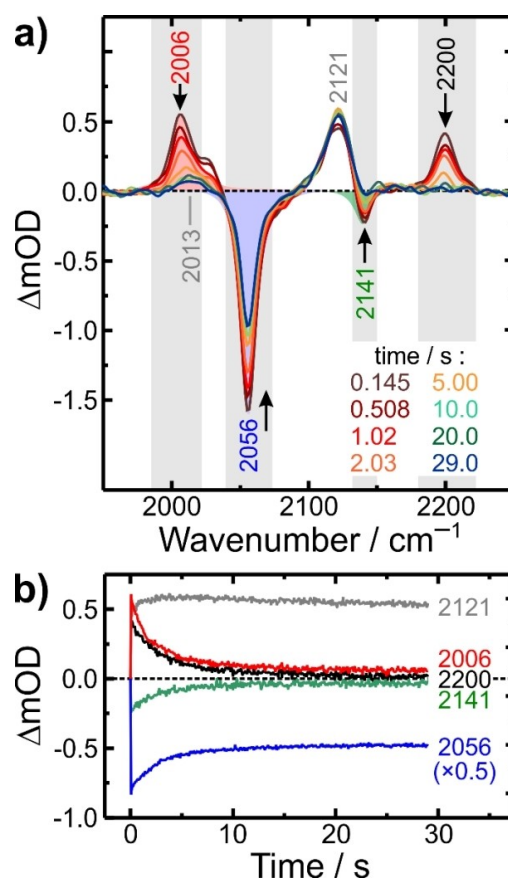


Figure 4. a) Rapid-scan-FTIR spectra following 412 nm-photolysis of [1] in DCM at room temperature and in the presence of 1 equiv. of ${}^t\text{BuNC}$ for selected time delays as specified in the legend. Numbers indicate peak positions in cm^{-1} . b) Kinetic traces at selected spectral positions as indicated by the numbers.

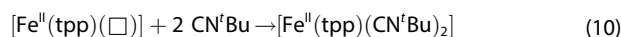
In Figure 4(a), such a band is indeed observed at a peak wavenumber of 2121 cm^{-1} and its intensity remains constant for tens of seconds indicating that the ferric carbodiimide, [4], is a stable species. In addition, the consumption of the quencher is indicated by the negative bleaching signal at 2141 cm^{-1} thereby further corroborating that Reaction (8) takes indeed place.

Yet, two additional positive bands are also noticed in Figure 4(a); namely, at 2006 cm^{-1} and 2200 cm^{-1} , the first of which clearly originates again from free azide anions. Both of these bands decay fully to zero on a time scale of several seconds and, as evidenced by the kinetic traces (cf. red and black curves in Figure 4b), their decays are highly correlated. Interestingly, on exactly the same time scale, the bleaching bands of [1] at 2056 cm^{-1} and ${}^t\text{BuNC}$ at 2141 cm^{-1} partially recover. The kinetic match of the four bands implies that [1] and the quencher are reformed at the expense of N_3^- and a species that absorbs at 2200 cm^{-1} . Moreover, from the amplitude changes, $\Delta\text{mOD}(t=0) - \Delta\text{mOD}(t=30\text{ s})$, at 2006 cm^{-1} , 2056 cm^{-1} , and 2141 cm^{-1} together with the independently determined extinction coefficients of N_3^- , [1], and ${}^t\text{BuNC}$ (cf. Figure 2), it can be concluded that with each consumed azide ion, one parent complex is regenerated and simultaneously two isonitriles are released. In turn, this stoichiometry then suggests that the 2200 cm^{-1} -band arises from a diisonitrilo complex, [5], and that the kinetic traces in Figure 4(b) track Reaction (9).

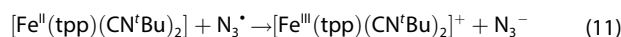


Previous studies of the binding of alkyl isonitriles to both, ferrous and ferric forms of cytochrome P450 showed that the ligation to Fe(II) results in a downshift and the ligation to Fe(III) in an upshift of the $-\text{N}\equiv\text{C}$ stretching mode relative to the free isonitrile.^[33] Therefore, the frequency-upshift observed in Figure 4(a) (from 2141 cm^{-1} in free ${}^t\text{BuNC}$ to 2200 cm^{-1} in species, [5]) is consistent with the two isonitriles being bound to a ferric center in a monocationic complex as expressed in Reaction (9) and not to a ferrous center of a neutral species, [5_{red}], with the same stoichiometry. More convincingly, ferric diisonitrile, [5], has been prepared previously,^[34] crystallographically characterized, and the IR-absorption of its nitrile stretching vibration in a KBr pellet reported at 2200 cm^{-1} , in quantitative agreement with our assignment.

The occurrence of the six-coordinate species, [5], is rather puzzling and its formation mechanism must be addressed. Interestingly, the $\text{N}_3^-/[1]$ absorption-to-bleach ratio in the isonitrile quenching experiment is maximal at $t=0$ when the Reaction (9) has barely set in. From Figure 4(a), we determine a value of 0.4, which is identical to the photoreduction yield deduced from the iodide quenching data shown in Figure 3(a) (brown spectrum). This agreement can be rationalized if the N_3^- -formation is intimately connected with the photoreduction pathway producing azidyl radicals and [3_{red}] as primary products. The latter is an under-coordinated species that is in principle able to bind up to two isonitrile molecules according to Reaction (10).



In short, Reaction (10) reads $[3_{\text{red}}] + 2\text{CN}^t\text{Bu} \rightarrow [5_{\text{red}}]$, which competes with the non-geminate (bulk) recombination with azidyl, i.e., with $[3_{\text{red}}] + \text{N}_3^{\bullet} \rightarrow [1]$. The simple ligation process (10) is likely to prevail because in our experiments, $c({}^t\text{BuNC}) \gg c(\text{N}_3^{\bullet})$, and a subsequent bimolecular electron transfer (11) can then be held responsible for the appearance of [5] and azide anions.



The kinetic traces from Figure 4(b) can be analyzed as follows. Since the IR-bands of the two reactants ($R=[5]$, N_3^-) decay synchronously and nearly completely within a few tens of seconds, we assume that the condition, $c([5]) \approx c(\text{N}_3^-) = c_R$, holds at each instant in time, t . Thus, the integrated rate law for either one of the reactants of (9) reads as in the following Equation (12):

$$\frac{1}{c_R(t)} - \frac{1}{c_R(0)} = kt \quad (12)$$

where $c_R(0)$ is the reactant concentration at $t=0$ (taking the limited time-resolution into account), and k is the bimolecular rate constant describing the kinetics of (9). The integrated rate law can also be written in terms of the product (P) concentrations. One equivalent of R is converted into κ_P equivalents of P ($\kappa_P=1$ for $P=[1]$ or $\kappa_P=2$ for $P={}^t\text{BuNC}$), which dictates that $c_P(t) - c_P(0) = \kappa_P[c_R(0) - c_R(t)]$ for all times. Moreover, since the IR-bands of [5] and N_3^- decay almost completely to zero, both reactants are quantitatively consumed and thus, $c_P(\infty) - c_P(0) = \kappa_P c_R(0)$. Solving for $c_R(t)$ and $c_R(0)$ and inserting into (12) yields Equation (13).

$$\frac{1}{c_P(\infty) - c_P(t)} - \frac{1}{c_P(\infty) - c_P(0)} = kt \quad (13)$$

The experimental observable is the photolysis-induced optical density, $\Delta\text{OD}(t)$, as a function of time. This quantity is connected to the reactant concentrations via Lambert-Beer's law, $\varepsilon_R(\tilde{\nu}_R) c_R(t) d = \Delta\text{OD}(\tilde{\nu}_R, t) - \Delta\text{OD}(\tilde{\nu}_R, \infty)$, where $\varepsilon_R(\tilde{\nu}_R)$ is the extinction coefficient at the peak wavenumber, $\tilde{\nu}_R$, of the IR-band associated with reactant, R, and d is the optical path length. The signal must be corrected for a small asymptotic signal offset, $\Delta\text{OD}(\tilde{\nu}_R, \infty)$, that may arise from a minor photochemical side product (see Figure 4a, residual absorption band peaking at 2013 cm^{-1}). We then find from (12) the relation (14)

$$\delta_R^{-1} = k'_R t = \frac{1}{\Delta\text{OD}(\tilde{\nu}_R, t) - \Delta\text{OD}(\tilde{\nu}_R, \infty)} - \frac{1}{\Delta\text{OD}(\tilde{\nu}_R, 0) - \Delta\text{OD}(\tilde{\nu}_R, \infty)} \quad (14)$$

with the effective rate constant, $k'_R = k/[\varepsilon_R(\tilde{\nu}_R) d]$. Likewise, for the products, Lambert-Beer's law must be written as $\varepsilon_P(\tilde{\nu}_P) c_P(t) d = \Delta\text{OD}(\tilde{\nu}_P, t) - \Delta\text{OD}(\tilde{\nu}_P, 0)$, where $\varepsilon_P(\tilde{\nu}_P)$ is the extinction coefficient at the peak wavenumber, $\tilde{\nu}_P$, of the IR-

band associated with product, P. Note here that both product absorptions are measured against an initial flash-induced bleach, denoted as $\Delta OD(\tilde{\nu}_p, 0)$. Inserting into (13) yields Equation (15)

$$\delta_p^{-1} = -k'_p t$$

$$= \frac{1}{\Delta OD(\tilde{\nu}_p, t) - \Delta OD(\tilde{\nu}_p, \infty)} - \frac{1}{\Delta OD(\tilde{\nu}_p, 0) - \Delta OD(\tilde{\nu}_p, \infty)} \quad (15)$$

with the effective rate constant, $k'_p = k/[\kappa_p \epsilon_p(\tilde{\nu}_p) d]$. According to (14) and (15) the inverse of the properly referenced flash-induced optical densities should correlate linearly with time with the slope being proportional to the bimolecular rate constant of Reaction (9). Such an analysis is carried out in Figure 5, in which the time-dependent optical densities were averaged over a certain wavenumber window (cf. gray-shaded areas in Figure 4a) to improve the signal-to-noise ratio. It can be seen that all IR-bands associated with the reactants and products, respectively, nicely obey the bimolecular kinetics as was initially presumed for Reaction (9). Linear regressions over the time range from 0 s to 11 s yield slopes, $k'_{R/Pr}$ listed in

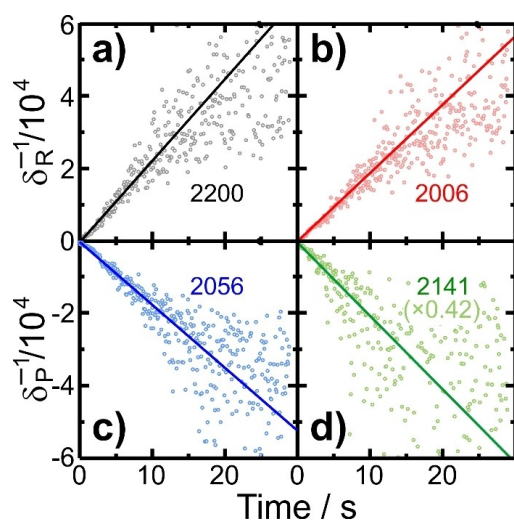


Figure 5. Analysis of the time-dependent traces displayed in Figure 4(b) according to bimolecular kinetics [cf. Equations (14) and (15)] for a) N_3^- , b) N_3^- , c) [1], and d) $^t\text{BuNC}$. The symbols are the experimental data and the straight lines are linear least squares fits. The numbers indicate the spectral position of the band maxima in cm^{-1} .

Table 1, and a bimolecular rate constant k of $(2.03 \pm 0.35) \times 10^4 \text{ M}^{-1} \text{ s}^{-1}$.

UV-pump/IR-probe spectroscopy

We finally need to determine the primary quantum yield for photooxidation and photoreduction. The relative weights of photoreduction and photooxidation, f_{red} and f_{ox} , can be inferred directly from the data displayed in Figure 3(b) in their asymptotic limit, $c(I^-)/c([1]) \rightarrow \infty$. However, to derive the combined quantum yield of these reactive processes, i.e., $\Phi_{\text{red}} + \Phi_{\text{ox}}$, knowledge of the primary yield of all non-reactive processes like internal conversion and geminate recombination is needed. This information must be extracted from kinetic measurements that are sensitive to the population in the electronic ground-state of [1] and that have a sufficient time-resolution to monitor these non-reactive dynamics.

To this end, we have chosen to conduct femtosecond UV-pump/IR-probe experiments with excitation wavelengths equivalent to those utilized in Figure 3(b). The probe pulses were tuned to the azide's antisymmetric stretching region and consequently, such experiments report on the depletion of the parent's ground-state as a result of the initial optical excitation and the ensuing dynamics of ground-state population recovery. These ground-state bleaching traces are depicted in Figure 6.

The data have been normalized to the initial bleach at the earliest delays and, hence, their magnitude is equal to the time-dependent fraction of initially excited molecules that have been able to avoid the return to the electronic ground-state of [1]. This fraction is then identical to the primary quantum yield of photoconversion, Φ_{prim} . It can be seen that the bleaching traces recover on a time scale of several tens of picoseconds and approach an offset signal that remains for delays in excess of 1 ns. Note that the combined primary photoconversion yield, $\Phi_{\text{prim}} = \Phi_{\text{red}} + \Phi_{\text{ox}}$, determined here differs from the total yield of photoconversion, which in turn is given by $\Phi_{\text{conv}} = \Phi_{\text{red}} + 2\Phi_{\text{ox}}$. The latter takes into account the additional consumption of [1] caused by the bimolecular Reaction (4) with the photooxidation product [2], amounting to another Φ_{ox} . This process, however, takes place on time scales longer than those captured in Figure 6. In fact, additional 400 nm-pump/IR-probe experiments for delays of the order of microseconds unveiled a

Table 1. Kinetic analysis of the time-dependent IR-traces probing the species involved in Reaction (9). The quantities, $\tilde{\nu}_{\text{low}}$ and $\tilde{\nu}_{\text{high}}$, are upper and lower limits of the spectral windows in which the extinction coefficient and the slopes were averaged. The mean values, $\langle \epsilon \rangle$, together with slopes, $k'_{R/Pr}$, were then used to determine the rate constant, k .

Species	$\tilde{\nu}_{\text{low}}$ [cm^{-1}]	$\tilde{\nu}_{\text{high}}$ [cm^{-1}]	$\langle \epsilon \rangle$ [$\text{M}^{-1} \text{cm}^{-1}$]	$k'_{R/Pr}$ [10^4 s^{-1}]	k [$10^4 \text{ M}^{-1} \text{ s}^{-1}$]
N_3^-	1990	2021	1154	1.97 ± 0.30	2.27 ± 0.35
[1]	2041	2075	1004	1.88 ± 0.30	1.88 ± 0.30
$^t\text{BuNC}$	2134	2149	195	4.98 ± 1.00	1.94 ± 0.39
[5]	2183	2222	832 ^[a]	2.44 ± 0.30	2.03 ± 0.35 ^[b]

[a] corresponds to the value that is consistent with a rate of $2.03 \times 10^4 \text{ M}^{-1} \text{ s}^{-1}$. [b] corresponds to the average of the entries for the other three species.

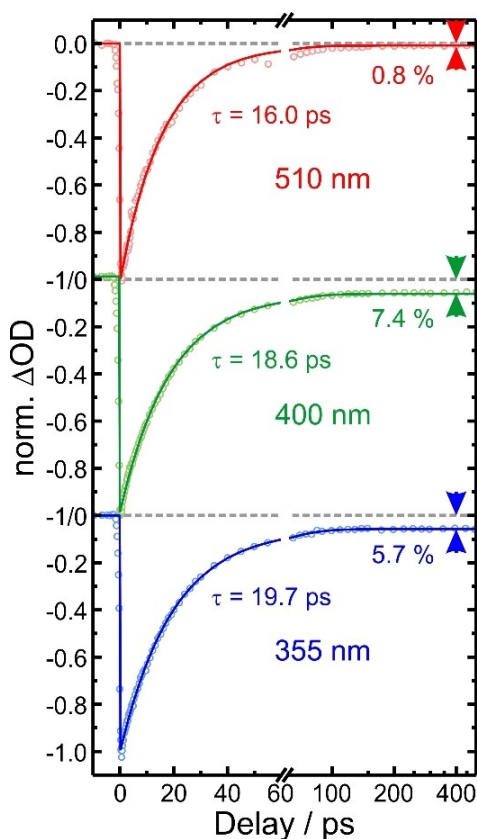


Figure 6. Femtosecond UV-pump/IR-probe kinetic traces for various excitation wavelengths. All three traces are normalized to their respective maximal bleach around a delay of zero. The data were recorded at a probe wavenumber of 2056 cm^{-1} corresponding to the peak of the N_3^- antisymmetric stretching vibration of [1]. Note that the abscissa switches from linear to logarithmic scaling at a delay of 60 ps.

retarded increase of the bleaching signal by a factor of ca. 1.6 as expected according to Reaction (4).^[29]

Together with the data from Figure 3(b), we finally find quantum yields of photooxidation, $\Phi_{\text{ox}} = f_{\text{ox}} \Phi_{\text{prim}}$ (photoreduction, $\Phi_{\text{red}} = f_{\text{red}} \Phi_{\text{prim}}$) of 0.3% (0.5%) for irradiation with 510 nm light, 4.4% (3.0%) for excitation around 400 nm and 2.9% (2.9%) for the photolysis at 355 nm.

At this stage, we particularly emphasize the paltry quantum yield for the nitridoiron(V) formation of 0.3% when the precursor is excited at 510 nm, i.e., at almost exactly the same wavelength that was used by Wagner and Nakamoto in their original work.^[10] In addition, thin film samples at cryogenic temperatures were used in Ref. [10] to perform the photoconversion. The highly restricted molecular mobilities in such samples strongly favor the geminate recombination of the primary products and should lower the photooxidation quantum yield even more. It is therefore only fair to wonder, how such an experiment can actually be conducted successfully.

In Ref. [10], a continuous-wave argon ion laser emitting at 514 nm was used for excitation with optical powers as high as 70 mW. In addition, the excitation light was even focused onto

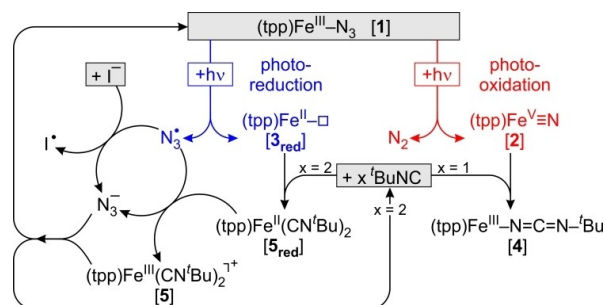


Figure 7. Summary of the photochemical processes revealed in this study. Optical excitation results in two pathways, photoreduction (blue) and photooxidation (red). The appearance of the photoproducts was exposed in quenching experiments using iodide anion and *tert*-butyl isocyanide as reagents.

the sample with a cylindrical lens of unspecified focal length. Notice that nearly all parent complexes return to their electronic ground-state non-radiatively, either by internal conversion or geminate recombination. In other words, the photon energy is quantitatively converted into kinetic energy of the nuclei and eventually dissipated as heat within the excitation focal volume. It is therefore quite likely that the sample was locally heated to above the melting point. In addition, the porphyrin ancillary ligand is exceptionally photo-stable and pathways other than photooxidation and photoreduction have been observed neither in Ref. [10] nor by us. As a result, the complexes can be optically cycled many times without being irreversibly bleached. Thus, a continuous and sufficiently intense irradiation over extended periods may eventually result in an appreciable accumulation of the desired nitridoiron(V) product.

Conclusions

In summary, we have explored the photolysis of Nakamoto's paradigmatic complex, azidoporphinatoiron(III), in liquid solution at room temperature using stationary and time-resolved infrared spectroscopy. Surprisingly, the complex is photochemically remarkably robust, with total conversion yields of just a few percent for excitation in the visible-to-near-UV spectral region. The photoconversion splits roughly evenly between photooxidation and photoreduction as summarized in Figure 7. The former process generates nitridoporphinatoiron(V) by $\text{N}_\alpha\text{-N}_\beta$ bond breakage with loss of N_2 . The appearance of the high-valent product was verified by its quenching reaction with an isocyanide, which yields a ferric carbodiimido species that could be detected by its highly characteristic $\text{N}=\text{C}=\text{N}$ -stretching vibration. The latter process generates porphinatoiron(II) by Fe-N_α bond breakage with loss of N_3^* . The appearance of the azidyl radicals was verified by their quenching with iodide ions, which yields azide anions that could be detected by their unmistakable antisymmetric stretching band. The appearance of the lower-valent product was also verified indirectly in the isocyanide

quenching study, in which it gave rise to a ferric diisonitrilo species that was observed through its characteristic nitrile stretching mode. This unexpected reactivity requires the initial ligation of the quencher and a subsequent Fe(II)-to-azidyl electron transfer. The ferric diisonitrilo is unstable under the quenching conditions and combines with N_3^- to release the quencher and reform the parent. Further experiments are currently underway in our laboratories to explore in greater detail the primary processes using femtosecond UV-pump/IR-probe experiments with detection of vibrational bands of the porphyrinato ligand that are specifically sensitive to the electronic structure of the intriguing high-valent species, $(tpp)Fe^V=N$.

Supporting Information

The authors have provided a Supporting Information including: synthesis of [1], detailed experimental and computational methods, detailed computational results, difference spectra and transient spectra after 355 nm and 510 nm excitation, kinetic trace after 266 nm excitation, details regarding the regressions of the kinetic traces shown in Figure 5. The authors have cited references within the Supporting Information.^[16–22,29]

Acknowledgements

Financial support by the German Research Foundation, grant no. 404522842 (VO 593/8-1) and 397162618 (VO 593/7-2), is gratefully acknowledged. SF thanks the Chemical Industry Foundation (Fonds der chemischen Industrie) for a dissertation stipend. Open Access funding enabled and organized by Projekt DEAL.

Conflict of Interests

The authors declare no conflict of interest.

Data Availability Statement

The data that support the findings of this study are available from the corresponding author upon reasonable request.

Keywords: flash-photolysis · high-valent iron · time-resolved infrared spectroscopy · photochemistry · transition metal nitrides

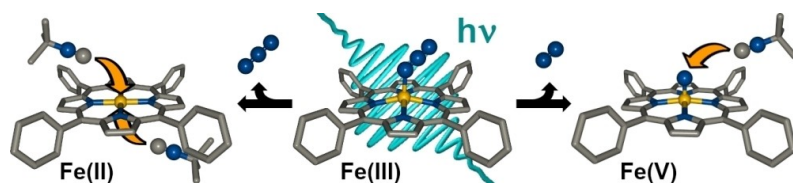
- [1] *Metal-Oxo and Metal-Peroxo Species in Catalytic Oxidations*, (Ed.: B. Meunier), Springer, Berlin, Heidelberg, 2000.
- [2] a) M. Sono, M. P. Roach, E. D. Coulter, J. H. Dawson, *Chem. Rev.* **1996**, *96*, 2841–2887; b) *Cytochrome P-450: Structure, Mechanism, and Biochemistry*, (Ed.: P. R. Ortiz de Montellano), Kluwer Academic/Plenum Publishers, New York, 2005.
- [3] a) I. G. Denisov, T. M. Makris, S. G. Sligar, I. Schlichting, *Chem. Rev.* **2005**, *105*, 2253–2277; b) D. Dolphin, R. H. Felton, *Acc. Chem. Res.* **1974**, *7*, 26–32; c) E. G. Hrycay, S. M. Bandiera, *Arch. Biochem. Biophys.* **2012**, *522*, 71–89.
- [4] J. Hohenberger, K. Ray, K. Meyer, *Nat. Commun.* **2012**, *3*, 720.
- [5] a) L. K. Woo, J. G. Goll, *J. Am. Chem. Soc.* **1989**, *111*, 3755–3757; b) L. K. Woo, J. G. Goll, D. J. Czaplá, J. A. Hays, *J. Am. Chem. Soc.* **1991**, *113*, 8478–8484; c) L. A. Bottomley, F. L. Neely, *J. Am. Chem. Soc.* **1989**, *111*, 5955–5957; d) L. A. Bottomley, F. L. Neely, *Inorg. Chem.* **1997**, *36*, 5435–5439; e) F. L. Neely, L. A. Bottomley, *Inorg. Chem.* **1997**, *36*, 5432–5434.
- [6] a) X. Y. Yi, Y. Liang, C. Li, *RSC Adv.* **2013**, *3*, 3477–3486; b) J. J. Scepianiak, M. D. Fulton, R. P. Bontchev, E. N. Duesler, M. L. Kirk, J. M. Smith, *J. Am. Chem. Soc.* **2008**, *130*, 10515–10517.
- [7] a) B. L. Tran, M. Pink, X. F. Gao, H. Park, D. J. Mindiola, *J. Am. Chem. Soc.* **2010**, *132*, 1458–1459; b) J. J. Scepianiak, R. P. Bontchev, D. L. Johnson, J. M. Smith, *Angew. Chem. Int. Ed.* **2011**, *50*, 6630–6633.
- [8] a) H. K. Kwong, W. L. Man, J. Xiang, W. T. Wong, T. C. Lau, *Inorg. Chem.* **2009**, *48*, 3080–3086; b) J. M. Smith, D. Subedi, *Dalton Trans.* **2012**, *41*, 1423–1429.
- [9] a) J. Torres-Alacan, O. Krahe, A. C. Filippou, F. Neese, D. Schwarzer, P. Vöhringer, *Chem. Eur. J.* **2012**, *18*, 3043–3055; b) H. Vennekate, D. Schwarzer, J. Torres-Alacan, P. Vöhringer, *J. Am. Chem. Soc.* **2014**, *136*, 10095–10103.
- [10] W. D. Wagner, K. Nakamoto, *J. Am. Chem. Soc.* **1988**, *110*, 4044–4045.
- [11] a) C. A. Grapperhaus, B. Mienert, E. Bill, T. Weyhermüller, K. Wieghardt, *Inorg. Chem.* **2000**, *39*, 5306–5317; b) H. Vennekate, D. Schwarzer, J. Torres-Alacan, O. Krahe, A. C. Filippou, F. Neese, P. Vöhringer, *Phys. Chem. Chem. Phys.* **2012**, *14*, 6165–6172; c) J. Torres-Alacan, P. Vöhringer, *Int. Rev. Phys. Chem.* **2014**, *33*, 521–553; d) J. Torres-Alacan, P. Vöhringer, *Chem. Eur. J.* **2017**, *23*, 6746–6751; e) D. Rehorek, T. Berthold, H. Hennig, T. J. Kemp, *Z. Chem.* **1988**, *28*, 72–73.
- [12] a) V. Balzani, L. Moggi, F. Scandola, V. Carassiti, *Inorg. Chim. Acta Rev.* **1967**, *1*, 7–34; b) Z. B. Alfassi, A. Harriman, R. E. Huie, S. Mosseri, P. Neta, *J. Phys. Chem.* **1987**, *91*, 2120–2122.
- [13] a) J. Torres-Alacan, U. Das, A. C. Filippou, P. Vöhringer, *Angew. Chem. Int. Ed.* **2013**, *52*, 12833–12837; b) S. Flesch, L. I. Domenianni, P. Vöhringer, *Phys. Chem. Chem. Phys.* **2020**, *22*, 25618–25630.
- [14] J. Torres-Alacan, J. Lindner, P. Vöhringer, *ChemPhysChem* **2015**, *16*, 2289–2293.
- [15] a) D. A. Summerville, I. A. Cohen, *J. Am. Chem. Soc.* **1976**, *98*, 1747–1752; b) J. W. Buchler, C. Dreher, *Z. Naturforsch. B* **1984**, *39*, 222–230; c) K. Meyer, E. Bill, B. Mienert, T. Weyhermüller, K. Wieghardt, *J. Am. Chem. Soc.* **1999**, *121*, 4859–4876; d) A. Niemann, U. Bossek, G. Haselhorst, K. Wieghardt, B. Nuber, *Inorg. Chem.* **1996**, *35*, 906–915.
- [16] K. M. Adams, P. G. Rasmussen, W. R. Scheidt, K. Hatano, *Inorg. Chem.* **1979**, *18*, 1892–1899.
- [17] S. Flesch, P. Vöhringer, *Angew. Chem. Int. Ed.* **2022**, *61*, e202205803.
- [18] a) TURBOMOLE V7.5 2020, a development of Karlsruhe and Forschungszentrum Karlsruhe GmbH, 1989–2007, TURBOMOLE GmbH, since 2007; available from <http://www.turbomole.com>; b) R. Ahlrichs, M. Bär, M. Häser, H. Horn, C. Kölmel, *Chem. Phys. Lett.* **1989**, *162*, 165–169; c) O. Treutler, R. Ahlrichs, *J. Chem. Phys.* **1995**, *102*, 346–354; d) M. Von Arnim, R. Ahlrichs, *J. Comput. Chem.* **1998**, *19*, 1746–1757.
- [19] J. D. Chai, M. Head-Gordon, *J. Chem. Phys.* **2008**, *128*, 084106.
- [20] a) E. Caldeweyher, C. Bannwarth, S. Grimme, *J. Chem. Phys.* **2017**, *147*; b) E. Caldeweyher, S. Ehlert, A. Hansen, H. Neugebauer, S. Spicher, C. Bannwarth, S. Grimme, *J. Chem. Phys.* **2019**, *150*, 154122.
- [21] a) A. Schäfer, C. Huber, R. Ahlrichs, *J. Chem. Phys.* **1994**, *100*, 5829–5835; b) F. Weigend, R. Ahlrichs, *Phys. Chem. Chem. Phys.* **2005**, *7*, 3297–3305.
- [22] A. Schäfer, H. Horn, R. Ahlrichs, *J. Chem. Phys.* **1992**, *97*, 2571–2577.
- [23] a) R. Giovannetti, in *Macro to Nano Spectroscopy* (Ed.: J. Uddin), InTech, Rijeka, 2012, pp. 87–108; b) W. S. Caughey, R. M. Deal, C. Weiss, M. Gouterman, *J. Mol. Spectrosc.* **1965**, *16*, 451–463.
- [24] a) M. Gouterman, *J. Mol. Spectrosc.* **1961**, *6*, 138–163; b) M. Gouterman, in *The Porphyrins, Vol. III* (Ed.: D. Dolphin), Academic Press, New York, **1978**, pp. 1–165.
- [25] J. Mack, J. Stone, T. Nyokong, *J. Porphyrins Phthalocyanines* **2014**, *18*, 630–641.
- [26] H. Kobayashi, Y. Yanagawa, H. Osada, S. Minami, M. Shimizu, *Bull. Chem. Soc. Jpn.* **1973**, *46*, 1471–1479.
- [27] K. Nakamoto, *Infrared and Raman spectra of inorganic and coordination compounds, 5th ed.*, Wiley & Sons Inc., New York, **1997**.
- [28] S. Straub, L. I. Domenianni, J. Lindner, P. Vöhringer, *J. Phys. Chem. B* **2019**, *123*, 7893–7904.
- [29] to be published

- [30] a) G. Ferraudi, J. F. Endicott, *Inorg. Chem.* **1973**, *12*, 2389–2396; b) J. F. Endicott, M. Z. Hoffman, L. S. Beres, *J. Phys. Chem.* **1970**, *74*, 1021–1029.
- [31] M. H. V. Huynh, P. S. White, C. A. Carter, T. J. Meyer, *Angew. Chem. Int. Ed.* **2001**, *40*, 3037–3039.
- [32] a) Y. J. Kim, Y. S. Kwak, Y. S. Joo, S. W. Lee, *J. Chem. Soc. Dalton Trans.* **2002**, 144–151; b) G. Veneziani, S. Shimada, M. Tanaka, *Organometallics* **1998**, *17*, 2926–2929.
- [33] D. S. Lee, S. Y. Park, K. Yamane, E. Obayashi, H. Hori, Y. Shiro, *Biochemistry* **2001**, *40*, 2669–2677.
- [34] F. A. Walker, H. Nasri, I. Turowska-Tyrk, K. Mohanrao, C. T. Watson, N. V. Shokhirev, P. G. Debrunner, W. R. Scheidt, *J. Am. Chem. Soc.* **1996**, *118*, 12109–12118.

Manuscript received: April 17, 2023

Accepted manuscript online: July 12, 2023

Version of record online: ■■, ■■



Photolysis: The yield and product distribution of the photolysis of the archetypal azidoporphinatoiron(III) complex are examined by stationary and transient IR spectroscopy in conjunction with chemical quenching reactions with iodide and an isonitrile.

The complex decomposes almost equally to the Fe(II) and the nitrido-Fe(V) product, with small absolute yields. Moreover, subsequent bimolecular reactions of the products are considered.

S. Flesch, Prof. Dr. P. Vöhringer*

1 – 11

Photolysis of an Archetypal Model Complex. Photooxidation Versus Photoreduction of Azido(porphinato)iron(III)



Chemistry–A European Journal

Supporting Information

Photolysis of an Archetypal Model Complex. Photooxidation Versus Photoreduction of Azido(porphinato)iron(III)

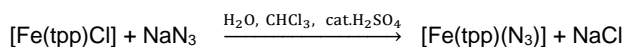
Stefan Flesch* and Peter Vöhringer

Contents

1 Experimental Details	2
1.1 Synthesis	2
1.2 Experimental Methods	2
1.3 Computational Methods	3
2 Computational Results	3
2.1 XYZ Coordinates	3
2.2 Vibrational Frequencies	7
2.3 Calculated Spectra	14
2.4 TDDFT Excitation Energies	15
2.5 TDDFT Unrelaxed Difference Densities	17
3 Transient Absorption Spectra	20
3.1 510 nm Excitation	20
3.2 355 nm Excitation	21
4 Kinetic Trace after 266 nm Excitation	22
5 UV-Vis Absorption Spectrum of Tetrabutylammonium Iodide	22
6 Parameters of Linear Regressions	23
7 References	24

1 Experimental Details

1.1 Synthesis



The synthesis of Azido(5,10,15,20-tetraphenylporphyrin-21,23-diido)iron(III) [Fe(tpp)(N₃), [1)] was performed as described by Adams *et al.* in the literature.^[1] 501 mg (0.71 mmol, 1.0 equiv.) [Fe(tpp)(Cl)] (Thermo Fisher) were treated with 250 ml of Chloroform (Thermo Fisher, 99%, stab. with 0.8-1% ethanol), a solution of 3.52 g (54 mmol, 76 equiv.) of sodium azide (Sigma Aldrich, purum p.a., ≥99.0% (T)) in 75 ml of water and 8 drops of concentrated sulfuric acid (Merck, 95-97%). After stirring the mixture at ambient temperature for 30 hours, the organic phase was separated from the aqueous one, filtered and dried by addition of 370 mg of anhydrous sodium sulfate, stirring for 3 hours and filtered again. Afterwards, the solvent was removed under reduced pressure and the purple product was dried for 20 hours under vacuum at 70 °C. Yield: 412mg (82 %).

IR: (CH₂Cl₂, 295 K): $\tilde{\nu} / \text{cm}^{-1}$ ($\epsilon / \text{L mol}^{-1} \text{cm}^{-1}$) = 1074 (330), 1179 (110), 1202 (220), 1340 (430), 1442 (380), 1488 (250), 1599 (180), 2056 (2150).

UV-Vis: (CH₂Cl₂, 295 K): λ / nm ($\log_{10}(\epsilon / \text{L mol}^{-1} \text{cm}^{-1})$) = 250 (4.32), 270 (4.30), 362 (4.81), 414 (5.09), 506 (4.20), 567 (3.67), 656 (3.52), 687 (3.61).

Elemental analysis: (mass fraction / %)

Experimentally found: C - 72.78, H - 4.198, N - 13.25.

Anal. calc. for C₄₄H₂₈FeN₇: C - 74.37, H - 3.972, N - 13.80.

1.2 Experimental Methods

The stationary UV-Vis spectrum was recorded on an UV-160 spectrophotometer (Shimadzu) with a spectral resolution of 3 nm. To this end, 3.3 mmolL⁻¹ and 0.33 mmolL⁻¹ solutions of [1] in dichloromethane (>=99.8, analytical reagent grade, stabilized with amylene) were filled into 1 mm quartz cuvettes (Hellma Analysitcs). Stationary and Rapid-Scan FTIR spectra were measured on a Vertex 70 spectrometer (Bruker) with a resolution of 5 cm⁻¹. All stationary spectra were referenced against the pure solvent CH₂Cl₂ measured under identical conditions. Unless stated otherwise, difference spectra were recorded immediately after the excitation pulse and averaged over 30 s. Rapid-scan and steady-state difference measurements were carried out with a temporal resolution of 72.5 ms. Excitation pulses were generated by a Q-switched Nd:YAG laser (Continuum Surelite II-10). In more detail, 355 nm pulses are produced by third harmonic generation of the fundamental frequency. 412 nm and 510 nm pulses were obtained by application of an optical parametric oscillator (OPO, Continuum Surelite) driven by third harmonic of the laser output. Excitation pulses were set to an energy of ca. 18 mJ. Photolyzed solution of [1] in CH₂Cl₂ had a concentration of 3 mmolL⁻¹. Tetra-*n*-butylammonium iodide (Alfa Aesar, 98%) was added in amounts equal to concentrations of 3, 10.5, 30, 105 and 300 mmolL⁻¹. The concentrations of *tert*-butyl isonitrile (Alfa Aesar, 98%) was adjusted to 3 mmolL⁻¹ when required. For all FTIR measurements, solutions were filled into home-built stainless steel cell equipped with two CaF₂ windows (4 mm, Korth Kristalle GmbH) and PTFE spacers providing an optical path length of 0.1 mm. The experimental setup employed in the femtosecond pump-probe measurements is described in detail in Ref. [2].

1.3 Computational Methods

Quantum chemical calculations were carried out using the program package TURBOMOLE 7.5.^[3] All calculations employed the range-separated hybrid density functional ω B97X,^[4] dispersion correction D4^[5] and the basis sets def2-TZVP^[6] (for all atoms of the porphyrin, azide and isonitrile moieties and the central iron atom) and def2-SVP^[6b, 7] (for all atoms of the phenyl and *tert*-butyl groups). Geometry optimizations were converged with the following thresholds (in atomic units): energy change < 1e-6, rms displacement < 5e-4, max. displacement < 1e-3, rms gradient < 5e-4, max gradient < 1e-3. Analytical frequency analyses of the converged structures within the harmonic approximation yielded exclusively positive eigenvalues of the hessian matrix and, thus, verifies them to be true minima on the potential energy surface. The electronic excitation spectrum of [1] was calculated by time-dependent density functional theory (TD-DFT). The calculation was considered as converged at an Euclidian norm of the residual vector of less than 1e-7 au.

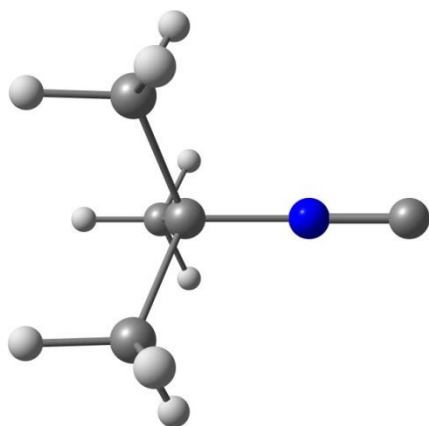
2 Computational Results

2.1 XYZ coordinates

¹BuNC, S = 0
E = -250.5256084295 au

15

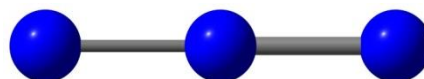
C	-0.0002521	-0.0000251	2.3148353
N	-0.0000369	0.0000022	1.1520102
C	0.0000323	0.0000033	-0.2922364
C	1.4556797	0.0000017	-0.7643627
H	1.9842844	0.8922773	-0.3981878
H	1.9842860	-0.8922675	-0.3981746
H	1.4899852	-0.0000066	-1.8643946
C	-0.7277989	1.2606406	-0.7643069
C	-0.7277990	-1.2606364	-0.7643017
H	-1.7648066	1.2723028	-0.3980491
H	-0.2193720	-2.1645400	-0.3980594
H	-1.7648063	-1.2722971	-0.3980425
H	-0.2193724	2.1645463	-0.3980694
H	-0.7450113	1.2904256	-1.8643329
H	-0.7450123	-1.2904271	-1.8643275



N₃, S = 0
E = -164.2451801355 au

3

N	0.0166730	0.0000005	0.1666668
N	1.1797271	-0.1293123	0.1973535
N	-1.1464001	0.1293117	0.1359797



[Fe(tp)(N₃)], [1], S = 5/2
E = -3339.798057079 au

80

Fe	-0.0530383	0.0098970	-0.2734684
N	0.8554873	-1.7807064	0.2689536
N	-1.8686169	-0.9134424	0.1217133
N	-1.0001672	1.8063237	0.1692859
N	1.7239598	0.9386628	0.2669226
C	2.2031465	-2.0054040	0.2601636
C	0.2563909	-3.0083068	0.2742869
C	-2.0905983	-2.2574196	0.2166525
C	-3.0947527	-0.3142000	0.1153589
C	-2.3451171	2.0323010	0.0908135
C	-0.4006413	3.0327981	0.2099037
C	1.9433775	2.2842594	0.3442343
C	2.9500894	0.3403457	0.3125878
C	2.4600416	-3.4192728	0.2523348
C	1.2606419	-4.0374618	0.2681056
C	-3.5036903	-2.5105348	0.2848947
C	-4.1227562	-1.3129140	0.2184122
C	-2.5979011	3.4469909	0.0600359
C	-1.4000466	4.0634723	0.1375453
C	3.3528729	2.5380331	0.4723966
C	3.9739425	1.3402268	0.4429544
C	-1.1147267	-3.2506436	0.2635906
C	-3.3378914	1.0566097	0.0607515
C	0.9676904	3.2762114	0.3014699
C	3.1950174	-1.0290145	0.2657971
C	-1.5717226	-4.6718517	0.3038360
C	-4.7605193	1.5052929	-0.0075147
C	1.4213392	4.6985769	0.3532254
C	4.6187984	-1.4765740	0.2100164
C	-1.4345693	-5.4317016	1.4700264
C	-2.1442052	-5.2626749	-0.8273401
C	-5.4996504	1.3265088	-1.1812963
C	-5.3750697	2.1044125	1.0968318
C	1.2397331	5.4620743	1.5106796
C	2.0362685	5.2849277	-0.7576225
C	5.3224708	-1.3905496	-0.9956810
C	5.2612613	-1.9845208	1.3428250
C	-1.8622022	-6.7577177	1.5049070
C	-2.5705490	-6.5889678	-0.7937576
C	-6.8283440	1.7411902	-1.2505683
C	-6.7042177	2.5179676	1.0288200
C	1.6658782	6.7882766	1.5571871
C	2.4615058	6.6113083	-0.7122514
C	6.6501438	-1.8084741	-1.0656688
C	6.5898203	-2.4007087	1.2721462
C	-2.4308966	-7.3394766	0.3728053
C	-7.4336423	2.3380201	-0.1456445
C	2.2776231	7.3658424	0.4455684
C	7.2864050	-2.3137308	0.0675418
H	3.4402461	-3.8687815	0.2335951
H	1.0603417	-5.0971053	0.2625051
H	-3.9530682	-3.4853704	0.3884340
H	-5.1812031	-1.1092117	0.2564785
H	-3.5735624	3.9001217	-0.0152707
H	-1.1973538	5.1227032	0.1388772
H	3.7978672	3.5148393	0.5764981
H	5.0303527	1.1353218	0.5172096
H	-0.9907862	-4.9725371	2.3580332
H	-1.7523893	-7.3394183	2.4242371
H	-2.7658479	-8.3799335	0.3997568
H	-3.0120148	-7.0395186	-1.6868717
H	-2.2498620	-4.6726961	-1.7422299
H	-5.0212960	0.8605788	-2.0475324
H	-7.3934764	1.5987845	-2.1757200
H	-8.4760262	2.6635761	-0.1999037
H	-7.1737430	2.9811413	1.9009623

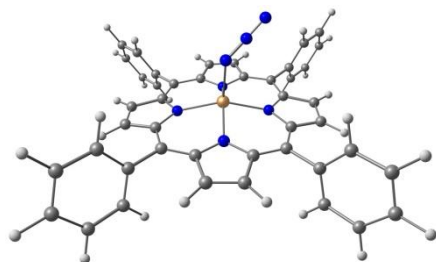
4

[Fe(tp)(NCN'Bu)], [4], S = 5/2
E = -3480.898519609 au

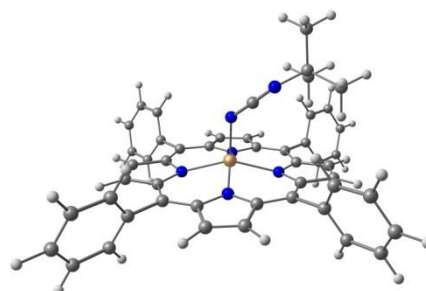
93

Fe	-0.0063336	0.4984072	-0.6026221
N	-0.2222551	-1.5723389	-0.4286674
N	-2.0224799	0.6255863	-0.0994059
N	0.1992390	2.3876215	0.2516720
N	1.9980708	0.2031824	-0.1345201
C	0.7797662	-2.4770242	-0.6333600
C	-1.3960041	-2.2638275	-0.5241936
C	-2.9463663	-0.3750836	-0.2033950
C	-2.7171622	1.7753024	0.1296968
C	-0.8031038	3.3053500	0.3860721
C	1.3728468	3.0657989	0.4131472
C	2.9212011	1.1733330	0.1179376
C	2.6939790	-0.9532853	-0.3433786
C	0.2194113	-3.7789714	-0.8651401
C	-1.1230667	-3.6488342	-0.7901090
C	-4.2667406	0.1638336	-0.0216656
C	-4.1255107	1.4903423	0.1831319
C	-0.2394156	4.6088153	0.6211824
C	1.1004625	4.4604749	0.6423557
C	4.2424647	0.6048425	0.0962037
C	4.1027111	-0.7045684	-0.1975167
C	-2.6757430	-1.7216994	-0.4242739
C	-2.1677978	3.0426110	0.3249605
C	2.6510242	2.5188850	0.3600285
C	2.1459675	-2.2006466	-0.6210187
C	-3.8374779	-2.6472798	-0.5785006
C	-3.1114812	4.1863561	0.5037201
C	3.8124367	3.4347729	0.5698512
C	3.0894606	-3.3146600	-0.9339384
C	-4.1796738	-3.5443657	0.4379761
C	-4.5991749	-2.6266132	-1.7513642
C	-3.8374199	4.6768460	-0.5865228
C	-3.2873300	4.7801299	1.7578452
C	4.1193443	3.9161589	1.8464604
C	4.6087652	3.8239924	-0.5120431
C	3.7276204	-3.3471791	-2.1783389
C	3.3506268	-4.3275904	-0.0064827
C	-5.2654263	-4.4049678	0.2851393
C	-5.6841439	-3.4875449	-1.9053169
C	-4.7210728	5.7425699	-0.4265229
C	-4.1712742	5.8456205	1.9188631
C	5.2029715	4.7715774	2.0384487
C	5.6917612	4.6800928	-0.3210148
C	4.6122481	-4.3778366	-2.4900776
C	4.2370961	-5.3573352	-0.3179955
C	-6.0199715	-4.3784816	-0.8869027
C	-4.8897887	6.3297397	0.8266201
C	5.9915173	5.1556007	0.9548266
C	4.8692518	-5.3846668	-1.5604044
H	0.7901736	-4.6732810	-1.0600669
H	-1.8719213	-4.4149093	-0.9154060
H	-5.1774813	-0.4139817	-0.0325686
H	-4.8970960	2.2192919	0.3743658
H	-0.8090668	5.5155222	0.7493399
H	1.8508300	5.2206933	0.7916975
H	5.1529841	1.1491367	0.2911728
H	4.8750824	-1.4517663	-0.2905063
H	-3.5880009	-3.5612077	1.3577347
H	-5.5251750	-5.0990829	1.0890898
H	-6.8717633	-5.0534530	-1.0067374
H	-6.2694423	-3.4628518	-2.8285330
H	-4.3310846	-1.9273835	-2.5490273
H	-3.7002609	4.2163362	-1.5690904
H	-5.2792308	6.1185984	-1.2883201
H	-5.5826052	7.1662446	0.9523731
H	-4.3016435	6.2983885	2.9056233

H	-4.8018216	2.2417396	2.0182030
H	0.7619092	5.0058715	2.3824400
H	1.5212150	7.3733174	2.4695724
H	2.6119580	8.4062310	0.4817723
H	2.9377004	7.0584467	-1.5890974
H	2.1778787	4.6912737	-1.6653298
H	4.8151346	-0.9981109	-1.8826458
H	7.1896831	-1.7413177	-2.0142334
H	8.3281075	-2.6414753	0.0116277
H	7.0840627	-2.7941554	2.1647212
H	4.7117779	-2.0508840	2.2863700
N	0.1530499	-0.0185684	-2.1761057
N	1.1927099	-0.1764775	-2.7602214
N	2.1562543	-0.3225719	-3.3353128



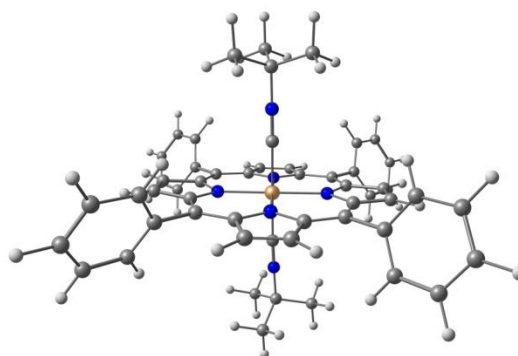
H	-2.7252988	4.3966659	2.6142895
H	3.5003828	3.6118873	2.6954197
H	5.4339740	5.1383739	3.0423586
H	6.8414944	5.8268736	1.1047839
H	6.3035956	4.9800983	-1.1761512
H	4.3694978	3.4514528	-1.5122403
H	3.5177017	-2.5557523	-2.9045477
H	5.1030945	-4.3938538	-3.4669800
H	5.5644522	-6.1926291	-1.8043232
H	4.4378284	-6.1419347	0.4167310
H	2.8556748	-4.3021277	0.9686434
N	0.0456608	0.7424479	-2.4866764
C	0.3882966	-0.0145815	-3.3637593
N	0.8080066	-0.7338004	-4.2585278
C	0.0663486	-1.8047033	-4.9380389
C	-0.0116107	-1.4412673	-6.4223396
C	-1.3393015	-1.9630469	-4.3540006
C	0.8634210	-3.0977990	-4.7535380
H	-0.5774523	-0.5075328	-6.5624908
H	-0.5091666	-2.2406097	-6.9946095
H	0.9986768	-1.2921320	-6.8316802
H	1.8830675	-2.9779367	-5.1506592
H	0.9399350	-3.3546906	-3.6849090
H	0.3789336	-3.9361582	-5.2792055
H	-1.9159251	-1.0303574	-4.4613532
H	-1.8868054	-2.7677798	-4.8686289
H	-1.2924205	-2.2160541	-3.2823946



[Fe(tpb)(CN^tBu)₂]⁺, [5], S = 1/2
E = -3676.492306638 au

107

Fe	0.0059070	-0.0118762	-0.0306716
N	0.0204897	2.0086034	0.1097847
N	-0.0144859	0.1304736	-2.0507036
N	0.0039078	-2.0308624	-0.1724732
N	0.0118458	-0.1531237	1.9886188
C	0.1023533	2.7449374	1.2479587
C	0.0700642	2.8974084	-0.9152175
C	-0.0633188	1.2705532	-2.7881692
C	-0.0978278	-0.8927964	-2.9382800
C	-0.0215352	-2.7697403	-1.3117349
C	0.0212973	-2.9221627	0.8519707
C	-0.0104646	-1.2916218	2.7275097
C	0.0341179	0.8719530	2.8798064
C	0.2341667	4.1413897	0.9336904
C	0.2145547	4.2361389	-0.4123253
C	-0.2094092	0.9585823	-4.1843326
C	-0.2304921	-0.3870632	-4.2777046
C	0.0031969	-4.1736575	-0.9996544
C	0.0176587	-4.2686543	0.3455898
C	-0.0105952	-0.9791381	4.1310722
C	0.0060022	0.3665609	4.2256786
C	0.0040128	2.5727740	-2.2775164
C	-0.0811179	-2.2562516	-2.6132507
C	0.0026956	-2.5957115	2.2139120



C	0.0865410	2.2326071	2.5522283
C	0.0070199	3.6961151	-3.2543935
C	1.0874243	3.8702875	-4.1257078
C	1.0929005	4.9243072	-5.0364854
C	0.0138691	5.8052720	-5.0930476
C	-1.0681972	5.6335223	-4.2308445
C	-1.0697434	4.5873859	-3.3109468
C	-0.1406895	-3.2305468	-3.7384337
C	0.9408560	-3.3600274	-4.6156251
C	0.8885757	-4.2748472	-5.6650035
C	-0.2486556	-5.0588922	-5.8534184
C	-1.3325133	-4.9288437	-4.9862928
C	-1.2777646	-4.0219908	-3.9301241
C	-0.0068686	-3.7198920	3.1918549
C	1.1282982	-4.5185370	3.3620004
C	1.1184429	-5.5664904	4.2801276
C	-0.0275125	-5.8297325	5.0290887
C	-1.1633406	-5.0392577	4.8600866
C	-1.1524749	-3.9857275	3.9485447
C	0.1334347	3.2128035	3.6726836
C	1.2634366	3.3008997	4.4921267
C	1.3065127	4.2273991	5.5317241
C	0.2174652	5.0651934	5.7677661
C	-0.9136342	4.9777462	4.9575336
C	-0.9540027	4.0594938	3.9107195
H	0.3430115	4.9359632	1.6538297
H	0.3046883	5.1239038	-1.0168692
H	-0.2993732	1.6808533	-4.9793070
H	-0.3404511	-0.9900351	-5.1643809
H	0.0069349	-4.9733871	-1.7222204
H	0.0211327	-5.1622343	0.9483356
H	-0.0171563	-1.7011491	4.9312992
H	-0.0002929	0.9694233	5.1191383
H	1.9320513	3.1769198	-4.0821033
H	1.9458068	5.0579956	-5.7068948
H	0.0161917	6.6287530	-5.8117907
H	-1.9180234	6.3196170	-4.2741288
H	-1.9174605	4.4526134	-2.6331991
H	1.8310887	-2.7419919	-4.4685791
H	1.7422885	-4.3757116	-6.3401136
H	-0.2906551	-5.7736093	-6.6793127
H	-2.2280090	-5.5383314	-5.1325719
H	-2.1273832	-3.9198202	-3.2489593
H	2.0265837	-4.3119611	2.7732150
H	2.0124614	-6.1815920	4.4112236
H	-0.0354468	-6.6537933	5.7470844
H	-2.0655099	-5.2438433	5.4423810
H	-2.0423941	-3.3635957	3.8167594
H	2.1168662	2.6421169	4.3075434
H	2.1971693	4.2953818	6.1616950
H	0.2505046	5.7891122	6.5860226
H	-1.7713524	5.6301140	5.1407080
H	-1.8393437	3.9916662	3.2722516
C	1.9425836	0.0103434	-0.0078863
N	3.0952783	0.0510045	0.0416921
C	-1.9300539	-0.0334862	-0.0356381
N	-3.0837423	-0.0720981	-0.0528892
C	4.5386272	0.1305660	0.1335913
C	4.9863108	1.3354821	-0.6953833
C	4.8939071	0.3089447	1.6108414
C	5.1111148	-1.1735207	-0.4234059
H	4.6966151	1.2145706	-1.7495748
H	6.0807774	1.4318035	-0.6447315
H	4.5368521	2.2633393	-0.3118781
H	4.4497964	1.2326422	2.0105900
H	5.9862547	0.3719384	1.7225652
H	4.5313996	-0.5414203	2.2068722
H	4.8195000	-1.3121454	-1.4747555
H	4.7541106	-2.0375573	0.1559908
H	6.2092295	-1.1473960	-0.3680846
C	-4.5301088	-0.1383921	-0.0872335
C	-5.0541192	1.2891334	-0.2505477

C	-4.9210131	-1.0149491	-1.2784148
C	-4.9938362	-0.7544460	1.2337690
H	-4.6865101	1.7361576	-1.1858736
H	-4.7352325	1.9219013	0.5906164
H	-6.1534995	1.2774215	-0.2796598
H	-4.5469902	-0.5862496	-2.2198704
H	-6.0168576	-1.0870469	-1.3396018
H	-4.5116767	-2.0299672	-1.1670459
H	-6.0917945	-0.8184570	1.2456986
H	-4.6716035	-0.1397104	2.0870446
H	-4.5852988	-1.7682988	1.3572136

2.2 Vibrational Frequencies

Table S1. Calculated vibrational frequencies and IR intensities of ^tBuNC, S = 0.

mode	Wavenumber / cm ⁻¹	IR intensity / km mol ⁻¹
1	0	0
2	0	0
3	0	0
4	0	0
5	0	0
6	0	0
7	173.69	2.59829
8	173.92	2.59952
9	214.14	0.00128
10	276.19	0.07558
11	279.57	0.07138
12	360.32	0.01496
13	360.47	0.01577
14	396.73	0.69660
15	520.11	3.34694
16	520.35	3.34942
17	722.74	4.87607
18	899.65	3.08549
19	948.49	1.18525
20	948.95	1.17721
21	965.68	0.00163
22	1053.29	0.32768
23	1053.63	0.31902
24	1256.26	55.19963
25	1277.37	9.93553
26	1277.77	10.02681
27	1397.65	18.69248
28	1398.62	18.5512
29	1420.00	6.76627
30	1447.30	0.00020
31	1459.60	0.21241
32	1460.68	0.25474
33	1476.09	5.29001
34	1476.43	5.19179
35	1494.14	8.72208
36	2266.68	170.56966
37	3071.20	11.43217
38	3071.28	11.46690
39	3075.73	8.10897
40	3176.24	1.26920
41	3176.33	1.40490
42	3181.44	27.88811
43	3181.86	0.00884
44	3184.49	15.38467
45	3184.60	15.5958

Table S2. Calculated vibrational frequencies and IR intensities of N₃⁻, S = 0.

mode	Wavenumber / cm ⁻¹	IR intensity / km mol ⁻¹
1	0	0
2	0	0
3	0	0
4	0	0
5	0	0
6	706.86	13.05365
7	707.24	13.05232
8	1423.22	0.00000
9	2170.45	1233.72982

Table S3. Calculated vibrational frequencies and IR intensities of [Fe(tp)(N₃)], [1], S = 5/2.

mode	Wavenumber / cm ⁻¹	IR intensity / km mol ⁻¹
1	0	0
2	0	0
3	0	0
4	0	0
5	0	0
6	0	0
7	9.09	0.00088
8	18.15	0.18379
9	25.35	0.55606
10	26.61	0.36002
11	30.10	0.36681
12	33.27	0.10285
13	37.18	0.29298
14	38.53	0.36210
15	44.90	0.05885
16	46.94	0.05359
17	49.26	0.25218
18	50.95	0.16593
19	58.91	0.24077
20	64.84	0.01110
21	80.10	0.00220
22	95.23	0.60296
23	101.01	0.04923
24	117.36	0.02741
25	122.68	0.14093
26	127.32	0.32193
27	145.98	0.03767
28	147.16	0.19317
29	196.56	0.65387
30	199.96	0.70421
31	205.99	1.30788
32	222.54	0.59279
33	223.63	0.79745
34	226.06	1.20545
35	233.31	1.48045
36	235.74	0.49921
37	238.47	0.64721
38	246.53	0.51167
39	257.81	0.58409
40	270.05	4.99112
41	291.60	0.14197
42	292.93	0.42681
43	297.87	0.42684
44	299.29	0.11110
45	331.92	0.01190
46	332.39	0.00940
47	348.07	0.04541
48	401.92	7.30299
49	412.59	9.29365
50	414.58	7.07618
51	417.48	0.01204
52	421.68	0.17468
53	422.03	0.03897
54	422.67	0.02055
55	423.23	0.05064
56	449.27	9.93433
57	449.50	11.96226
58	462.18	1.21332
59	465.73	70.05778
60	469.72	0.03672
61	523.52	0.82374
62	528.17	2.02347
63	533.34	1.65304
64	568.52	0.01394
65	582.35	0.15873

Table S4. Calculated vibrational frequencies and IR intensities of [Fe(tp)(NCN'Bu)], [4], S = 5/2.

mode	Wavenumber / cm ⁻¹	IR intensity / km mol ⁻¹
1	0	0
2	0	0
3	0	0
4	0	0
5	0	0
6	0	0
7	3.26	0.0345
8	10.41	0.0538
9	19.13	0.4916
10	20.24	0.1098
11	25.73	0.6636
12	27.75	0.2026
13	30.15	0.2535
14	32.55	0.1072
15	34.71	0.0237
16	44.64	0.0591
17	46.20	0.0875
18	49.67	0.2824
19	50.10	0.3989
20	52.45	0.2132
21	57.12	0.1062
22	65.92	0.2651
23	71.72	0.4171
24	80.14	0.0042
25	94.32	1.7423
26	101.71	0.0190
27	113.05	0.5479
28	123.92	0.0108
29	140.96	0.3886
30	145.25	0.0916
31	173.22	4.2350
32	196.15	0.6352
33	199.39	0.7105
34	206.23	1.1351
35	222.73	0.4583
36	223.23	0.8864
37	229.41	0.8647
38	230.66	1.2983
39	231.84	0.0272
40	236.36	0.1897
41	245.77	1.0870
42	246.95	2.4813
43	257.79	0.4287
44	269.02	4.7326
45	289.85	0.4029
46	292.25	0.0122
47	292.67	0.6647
48	294.48	0.0682
49	296.09	0.5740
50	299.17	0.0441
51	324.49	1.8849
52	332.33	0.0140
53	332.67	0.0115
54	346.20	1.6781
55	348.61	0.0030
56	389.63	14.4535
57	399.48	11.4368
58	412.53	10.1125
59	413.89	6.8662
60	417.14	0.0058
61	421.79	0.1744
62	422.25	0.0121
63	422.94	0.2629
64	423.62	0.1133
65	448.79	12.5311

66	584.18	0.61784	66	449.81	8.7333
67	586.18	1.93975	67	452.25	1.2867
68	597.50	1.75774	68	462.17	0.5595
69	636.98	0.11882	69	463.24	17.2511
70	637.46	0.86506	70	468.97	0.0279
71	637.95	0.56073	71	485.82	59.4549
72	639.82	0.16708	72	524.39	0.7247
73	642.10	3.11425	73	536.29	2.6102
74	657.85	2.28353	74	539.34	3.3398
75	673.51	31.61117	75	569.18	0.0234
76	675.75	48.27808	76	581.43	0.0750
77	681.26	37.16198	77	584.91	0.8792
78	684.24	2.18736	78	585.62	2.0703
79	688.79	0.52127	79	597.47	2.4110
80	691.77	10.54594	80	632.60	22.4493
81	701.38	0.18150	81	636.73	0.3911
82	702.04	6.83280	82	637.33	0.7068
83	702.43	4.51681	83	638.48	0.3749
84	709.92	0.59358	84	640.06	0.4177
85	733.55	14.85622	85	657.30	14.1106
86	733.76	1.52057	86	666.99	73.8869
87	734.63	63.00526	87	682.15	27.0285
88	735.24	68.17774	88	682.88	19.2997
89	759.71	46.79803	89	687.41	0.5850
90	779.10	0.04744	90	698.88	3.8568
91	784.45	0.33697	91	700.02	0.3117
92	786.00	0.60789	92	701.55	0.2649
93	790.43	0.05975	93	704.01	16.0550
94	814.64	4.83086	94	712.06	9.4525
95	815.40	11.48410	95	728.46	0.9576
96	818.25	4.43187	96	732.75	12.6084
97	834.43	0.09409	97	733.52	9.1487
98	849.39	0.49036	98	735.09	77.1918
99	850.62	1.20708	99	737.79	106.3007
100	854.35	0.19706	100	758.53	47.0124
101	857.10	67.02644	101	769.90	6.5203
102	882.89	0.56111	102	778.68	0.2827
103	887.80	0.06219	103	783.80	1.0394
104	888.18	0.20559	104	784.92	2.3851
105	888.47	0.31424	105	790.05	0.0858
106	888.86	0.12756	106	813.84	1.1285
107	900.59	0.02741	107	819.67	5.0588
108	902.29	0.93900	108	827.98	1.1276
109	902.84	1.17416	109	832.70	0.0388
110	917.17	0.42212	110	847.58	2.2799
111	919.84	0.13208	111	849.13	0.4507
112	922.49	0.98063	112	854.27	0.1191
113	962.88	0.08635	113	855.79	68.4659
114	966.16	0.32939	114	882.11	0.3404
115	968.31	0.33580	115	884.01	0.0014
116	969.89	0.46101	116	886.23	0.1708
117	971.12	0.01645	117	886.88	0.1873
118	973.58	0.72170	118	888.96	0.0369
119	974.04	0.58590	119	899.89	0.0707
120	974.29	0.46034	120	904.48	1.5735
121	1022.97	29.51030	121	905.32	1.2689
122	1023.38	39.84779	122	906.38	11.4747
123	1023.73	5.91795	123	917.03	0.7668
124	1024.68	2.29860	124	924.65	1.7796
125	1027.85	0.13935	125	936.64	7.7110
126	1028.00	0.15701	126	939.44	0.7824
127	1028.27	0.14898	127	942.81	0.8838
128	1028.45	0.02623	128	956.88	0.1537
129	1044.76	3.25483	129	961.52	0.1060
130	1046.78	0.30902	130	964.26	0.3764
131	1047.74	1.80149	131	966.31	0.3473
132	1048.39	0.50014	132	967.66	0.3175
133	1048.45	0.23777	133	969.96	0.2148
134	1049.20	67.02724	134	972.46	0.6872
135	1050.53	2.52106	135	973.47	1.1324
136	1050.70	64.89722	136	973.92	1.1351
137	1055.31	2.77130	137	1022.74	32.8021

138	1061.92	0.03892	138	1023.31	6.5441
139	1069.91	0.37696	139	1023.49	30.4579
140	1072.02	0.01217	140	1024.49	1.3590
141	1072.25	0.05821	141	1024.57	0.2339
142	1088.50	0.04321	142	1026.46	0.1649
143	1091.07	1.23980	143	1026.58	0.1628
144	1091.40	1.45831	144	1028.39	0.0555
145	1109.07	12.32669	145	1043.30	4.4076
146	1109.15	5.39953	146	1045.60	0.4658
147	1109.70	4.91485	147	1045.83	0.0075
148	1109.96	5.41071	148	1046.70	0.2623
149	1114.95	0.39222	149	1047.59	0.1528
150	1121.99	1.67845	150	1047.85	0.0828
151	1148.60	40.73733	151	1048.40	3.7542
152	1152.35	37.88625	152	1049.42	6.9004
153	1168.21	0.14212	153	1050.09	57.4065
154	1168.35	0.18742	154	1051.20	57.1129
155	1168.48	0.28885	155	1053.94	1.9711
156	1168.67	0.20076	156	1061.95	0.1634
157	1193.82	4.21077	157	1070.37	0.4990
158	1194.36	4.67866	158	1072.80	0.0041
159	1195.25	3.85877	159	1073.25	0.0158
160	1195.91	3.93713	160	1088.81	0.0378
161	1225.73	0.07838	161	1090.76	0.9193
162	1266.56	8.27499	162	1092.83	0.4650
163	1266.81	7.65085	163	1109.32	11.2879
164	1290.20	3.80079	164	1109.45	5.9377
165	1309.08	0.03064	165	1109.91	3.8574
166	1321.84	3.58091	166	1110.59	4.7988
167	1322.30	3.73396	167	1113.53	0.6255
168	1323.32	1.50503	168	1121.06	1.5608
169	1325.97	0.05954	169	1152.09	36.1250
170	1331.59	7.58330	170	1163.93	36.1978
171	1332.57	25.50030	171	1168.81	0.1720
172	1333.86	31.98284	172	1168.94	0.9718
173	1353.96	1.51948	173	1169.34	0.4784
174	1354.13	0.08493	174	1169.72	1.1507
175	1354.59	0.37203	175	1194.63	4.0288
176	1355.35	1.61739	176	1195.11	6.3278
177	1357.28	0.23391	177	1195.34	1.7961
178	1388.91	18.00433	178	1197.07	2.4622
179	1389.56	17.91376	179	1223.63	0.4411
180	1390.47	0.06523	180	1228.35	130.3967
181	1410.07	149.05148	181	1266.42	8.4519
182	1424.08	12.33929	182	1267.31	8.6443
183	1439.38	0.12209	183	1270.17	7.9983
184	1489.18	11.52100	184	1275.55	18.6026
185	1489.73	13.26622	185	1290.83	2.9424
186	1493.49	3.72680	186	1309.67	0.8295
187	1493.76	20.39466	187	1322.12	3.1508
188	1494.47	1.04167	188	1322.81	2.4894
189	1494.71	0.82858	189	1323.60	1.8200
190	1532.87	2.75124	190	1326.23	0.5458
191	1540.04	5.38366	191	1332.38	2.8063
192	1540.48	59.81585	192	1333.65	26.6393
193	1541.05	59.33785	193	1334.04	33.4912
194	1561.69	1.29342	194	1354.36	1.1884
195	1569.74	0.05664	195	1354.46	0.2120
196	1571.90	5.84160	196	1355.12	0.3443
197	1572.36	7.56729	197	1356.22	0.6549
198	1583.17	0.20933	198	1358.03	0.6178
199	1585.59	0.00283	199	1389.20	5.3877
200	1618.11	6.40630	200	1389.56	22.1342
201	1618.95	7.60512	201	1390.80	14.3053
202	1645.29	2.92948	202	1392.06	17.2157
203	1645.77	1.23765	203	1394.38	25.6208
204	1686.11	0.44554	204	1412.67	7.0666
205	1686.32	0.56064	205	1418.70	9.3027
206	1686.41	0.22877	206	1437.95	0.2097
207	1686.67	5.67612	207	1446.90	0.0645
208	1714.33	7.85233	208	1453.33	3.8704
209	1714.50	15.58180	209	1456.17	12.2663

210	1714.85	22.04570	210	1457.81	2.9423
211	1715.20	1.82699	211	1474.27	1.5112
212	2241.92	764.88106	212	1477.51	3.5150
213	3204.48	1.46199	213	1488.92	10.2069
214	3207.18	3.34709	214	1489.40	7.7083
215	3207.34	3.30097	215	1491.91	6.6307
216	3207.45	3.16587	216	1493.86	0.5246
217	3208.48	0.92203	217	1494.09	20.7139
218	3211.96	0.19984	218	1494.97	1.3440
219	3212.28	0.23782	219	1495.09	1.3133
220	3212.35	0.26486	220	1533.12	9.9673
221	3217.10	3.96588	221	1539.36	4.2440
222	3219.69	7.09529	222	1541.50	58.0234
223	3219.95	7.06528	223	1541.88	58.4540
224	3220.06	6.69190	224	1561.72	3.2574
225	3225.70	9.48230	225	1568.53	0.1931
226	3226.76	9.56438	226	1572.20	7.0322
227	3227.01	2.71278	227	1572.80	6.8236
228	3227.03	18.58111	228	1580.99	1.8646
229	3234.69	20.57573	229	1586.48	0.2669
230	3235.53	19.04751	230	1617.87	8.5641
231	3235.62	16.97057	231	1619.42	7.7915
232	3235.74	13.18884	232	1644.23	11.5923
233	3274.00	0.50789	233	1645.30	1.9220
234	3274.55	0.56772	234	1685.94	0.4540
235	3274.09	0.39319	235	1686.23	1.2464
236	3275.34	0.40477	236	1686.40	1.9074
237	3292.34	1.90552	237	1686.94	3.1677
238	3292.79	2.20423	238	1714.44	10.2001
239	3293.16	2.10622	239	1714.79	20.1576
240	3293.56	1.85987	240	1715.08	15.7267
			241	1715.47	3.3040
			242	2186.15	1914.0918
			243	3055.99	13.9101
			244	3058.44	11.5476
			245	3064.05	27.1199
			246	3157.33	3.4636
			247	3157.66	3.0987
			248	3161.16	9.2858
			249	3164.53	39.1991
			250	3166.18	20.2296
			251	3173.59	14.4162
			252	3204.92	2.2060
			253	3206.21	3.5072
			254	3206.95	2.8454
			255	3207.07	3.0936
			256	3209.12	0.4592
			257	3210.69	0.0704
			258	3212.13	0.2388
			259	3212.19	0.3282
			260	3217.24	4.6288
			261	3218.77	6.5312
			262	3219.48	7.6179
			263	3219.78	7.8128
			264	3225.48	9.6200
			265	3226.58	10.1161
			266	3226.80	9.3191
			267	3226.94	12.2853
			268	3234.55	19.5665
			269	3235.22	21.7059
			270	3235.30	17.5294
			271	3235.35	11.2067
			272	3272.86	0.2855
			273	3273.01	0.8237
			274	3273.17	0.4736
			275	3274.32	0.4171
			276	3291.12	1.3527
			277	3291.36	2.9979
			278	3291.51	2.0108
			279	3292.71	2.2755

Table S5. Calculated vibrational frequencies and IR intensities of $[\text{Fe}(\text{tp})\text{(CN}^t\text{Bu)}_2]^+$, [5], $S = 1/2$.

mode	Wavenumber / cm^{-1}	IR intensity / km mol^{-1}	mode	Wavenumber / cm^{-1}	IR intensity / km mol^{-1}
1	0	0	162	1027.98	1.60676
2	0	0	163	1028.44	1.58085
3	0	0	164	1029.27	1.35090
4	0	0	165	1043.95	0.01142
5	0	0	166	1050.22	0.33533
6	0	0	167	1052.76	0.08240
7	5.87	0.00016	168	1053.21	0.20603
8	7.94	0.10445	169	1053.81	0.23034
9	10.84	0.21322	170	1054.65	0.14290
10	11.18	0.13755	171	1054.86	0.34419
11	15.54	0.22179	172	1054.93	0.27548
12	17.48	0.03430	173	1055.05	0.24409
13	17.78	0.04202	174	1055.29	0.18941
14	23.39	0.05533	175	1056.71	0.32011
15	25.87	0.09980	176	1056.97	0.75238
16	35.56	0.00470	177	1057.14	0.49381
17	37.65	0.06311	178	1062.41	0.01057
18	45.61	0.19762	179	1070.33	0.09563
19	47.74	0.02169	180	1074.60	15.91387
20	50.87	0.02340	181	1074.70	15.81916
21	51.05	0.04060	182	1088.60	1.27561
22	52.73	0.15705	183	1090.27	62.98865
23	53.75	0.61271	184	1090.60	64.17938
24	71.72	0.37338	185	1111.72	4.81715
25	81.62	0.01175	186	1112.23	5.39374
26	84.86	0.19238	187	1113.04	8.81383
27	92.69	0.05684	188	1113.24	0.72955
28	93.28	0.02152	189	1113.40	1.95916
29	99.38	0.00599	190	1121.66	1.90971
30	101.58	0.04424	191	1138.52	92.10850
31	102.26	0.09169	192	1138.60	92.76450
32	124.38	0.00010	193	1171.81	0.33326
33	145.92	0.13919	194	1172.82	0.08635
34	146.15	0.07717	195	1172.91	0.60557
35	159.14	0.00101	196	1173.55	0.30541
36	187.08	8.86001	197	1196.05	2.91589
37	201.89	0.01129	198	1196.96	3.62069
38	218.53	0.00335	199	1197.26	2.83926
39	221.05	0.00714	200	1197.92	2.54951
40	222.44	2.07242	201	1221.99	0.03268
41	223.96	1.78157	202	1244.02	194.50376
42	228.44	1.28798	203	1246.18	0.14533
43	230.30	0.12328	204	1265.11	5.53015
44	232.30	3.58741	205	1265.23	5.51247
45	243.17	0.61986	206	1279.35	4.77911
46	244.97	1.33918	207	1279.75	5.14784
47	245.48	1.17685	208	1280.08	5.29897
48	254.67	0.91885	209	1280.27	6.18218
49	278.39	0.00554	210	1292.36	0.12114
50	281.09	0.00129	211	1320.93	0.33488
51	281.62	0.00241	212	1323.92	20.64158
52	282.06	0.00440	213	1324.13	30.45882
53	287.53	0.07320	214	1325.27	10.75412
54	298.39	0.23095	215	1331.27	137.65324
55	298.77	0.16259	216	1331.39	156.41265
56	301.86	5.28667	217	1332.56	15.56551
57	302.18	4.83140	218	1352.78	0.07505
58	319.24	1.96273	219	1355.41	0.59943
59	319.71	0.05188	220	1356.04	0.88964
60	331.71	0.33081	221	1356.77	1.40883
61	345.04	0.01326	222	1356.90	0.10063
62	345.20	0.02348	223	1397.62	18.48391
63	352.27	1.70040	224	1397.69	20.50931
64	354.88	0.15548	225	1399.29	1.97250
65	355.52	0.59359	226	1401.12	15.16072
66	387.88	0.20928	227	1401.45	13.78329
67	400.24	39.99463	228	1401.64	18.44721

68	401.01	41.37446	229	1401.73	17.13630
69	410.23	0.10185	230	1422.32	0.12513
70	410.67	1.20830	231	1423.35	11.24038
71	417.38	0.05956	232	1423.70	7.75915
72	418.98	0.02386	233	1430.27	0.11453
73	419.28	0.02672	234	1448.49	0.00413
74	420.05	0.00464	235	1448.58	0.00439
75	420.42	0.02562	236	1459.41	0.37924
76	436.98	14.52067	237	1460.03	0.17911
77	439.01	0.18250	238	1460.19	0.36096
78	452.43	5.16661	239	1460.51	0.28934
79	452.59	5.48885	240	1475.27	12.10983
80	459.45	0.03309	241	1475.41	12.72087
81	464.51	0.17528	242	1477.49	2.52696
82	482.92	29.07134	243	1477.50	10.61695
83	483.05	30.02521	244	1477.58	7.26207
84	518.64	89.03753	245	1477.68	7.67375
85	520.59	153.28376	246	1483.76	2.41043
86	521.36	86.81014	247	1493.73	6.20212
87	523.56	6.18151	248	1494.37	8.41770
88	539.16	0.64471	249	1494.58	11.05499
89	539.51	0.43169	250	1494.89	30.02982
90	567.36	1.66194	251	1495.01	6.63137
91	567.64	1.75421	252	1500.12	4.51928
92	585.78	0.08336	253	1504.90	0.12003
93	602.36	2.19443	254	1523.80	0.00155
94	602.48	0.22851	255	1540.69	12.53738
95	616.97	1.29326	256	1540.85	12.60789
96	623.07	0.02990	257	1553.74	0.14119
97	635.91	11.15908	258	1557.17	0.02233
98	636.75	20.55848	259	1564.61	0.54757
99	639.55	1.90540	260	1564.68	0.51192
100	648.94	24.06882	261	1569.88	0.22083
101	656.76	0.03585	262	1596.04	8.84242
102	677.90	463.31178	263	1596.09	8.87735
103	678.21	449.13810	264	1617.96	0.15006
104	694.93	50.15586	265	1625.75	0.31895
105	699.60	508.86881	266	1685.04	0.79159
106	699.79	401.79346	267	1685.45	1.19496
107	701.98	100.05042	268	1685.61	3.17368
108	710.11	102.42348	269	1686.10	1.32054
109	710.90	112.11112	270	1711.99	0.13579
110	711.67	108.00880	271	1712.49	0.00505
111	732.49	2.41069	272	1712.97	0.20117
112	733.14	22.64330	273	1713.13	0.49362
113	736.53	325.90927	274	2317.67	982.91954
114	736.96	2.97350	275	2337.05	0.09262
115	737.69	299.36345	276	3072.97	6.08420
116	745.19	0.00835	277	3073.10	6.51989
117	767.85	62.19509	278	3073.72	6.69515
118	774.65	32.29199	279	3073.82	6.64778
119	785.54	51.63036	280	3077.46	3.74953
120	789.10	10.51210	281	3077.59	2.89610
121	805.44	26.43230	282	3180.47	0.44285
122	813.84	107.80135	283	3180.53	0.71451
123	818.99	142.37989	284	3182.05	1.92937
124	825.77	37.54177	285	3182.20	0.07953
125	832.77	1.41523	286	3182.62	0.19744
126	851.09	0.61291	287	3182.62	0.29330
127	851.37	1.03049	288	3183.25	9.47799
128	861.97	40.77220	289	3183.59	7.29083
129	884.18	0.26569	290	3184.49	8.67746
130	885.78	0.41636	291	3184.68	9.34850
131	886.21	0.42049	292	3187.36	24.71868
132	887.17	0.69454	293	3187.61	17.32465
133	888.21	0.33360	294	3210.89	4.67666
134	896.34	0.72584	295	3211.05	5.05302
135	898.26	98.47386	296	3211.27	3.86011
136	898.37	97.59079	297	3211.86	4.38502
137	900.49	0.00690	298	3213.27	0.58079
138	901.68	0.38103	299	3213.59	0.56911
139	918.74	0.23159	300	3214.07	0.64512

140	927.43	264.33831	301	3214.35	0.35053
141	927.69	275.65452	302	3223.58	1.66159
142	928.64	7.99880	303	3223.68	1.77209
143	950.60	1.54183	304	3223.88	1.61567
144	950.89	1.72621	305	3223.94	1.81974
145	951.19	1.62811	306	3231.50	4.95610
146	951.47	1.75578	307	3231.55	5.36343
147	970.14	0.09412	308	3231.88	2.48556
148	971.40	0.04817	309	3231.90	8.21370
149	971.46	0.27009	310	3240.86	8.10756
150	972.01	3.91272	311	3240.92	8.10042
151	972.25	0.10412	312	3240.95	6.12677
152	972.33	0.28499	313	3241.04	5.64014
153	972.95	6.18711	314	3282.20	0.00249
154	973.76	3.55919	315	3282.50	0.00242
155	974.47	11.84668	316	3282.79	0.00654
156	975.33	9.34200	317	3282.93	0.00133
157	1022.89	1.99878	318	3299.81	0.13982
158	1022.98	15.83532	319	3300.06	0.18542
159	1023.26	14.72997	320	3300.36	0.19978
160	1024.13	0.42281	321	3300.49	0.08179
161	1027.39	1.68958			

2.3 Calculated IR Spectra

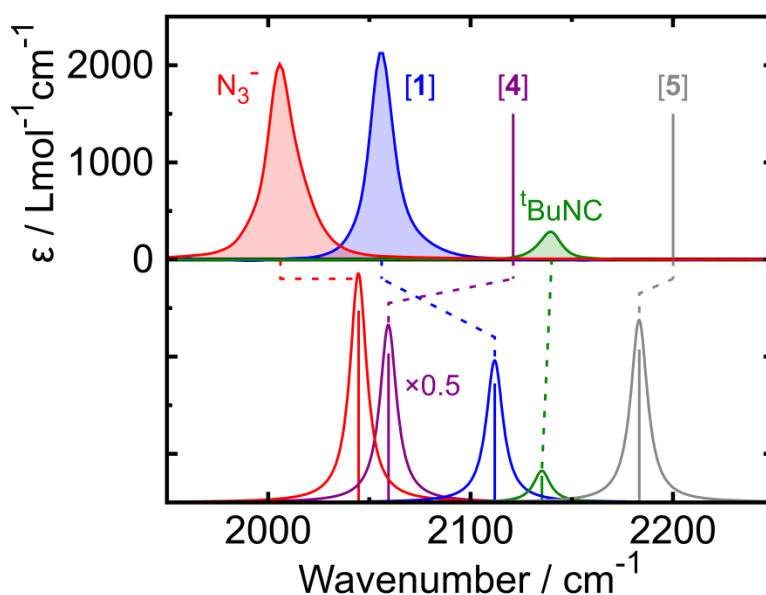


Figure S1. Upper panel: Stationary FTIR-spectra in the region of the antisymmetric N_3^- -stretching vibration of [1] (blue) and tetrabutylammonium azide (red), and of the $-\text{N}\equiv\text{C}$ stretching region of *tert*-butyl isonitrile (green), each measured in CH_2Cl_2 solution, and positions of the absorption bands of [4] (violet) and [5] (gray) observed after photolysis of a solution of [1] and $^t\text{BuNC}$ marked by vertical lines. Lower panel: Calculated stick spectra of the same species, corrected by an empirical scaling factor of 0.942 for all frequencies. Dashed lines emphasize the assignment to the experimentally observed signals. Spectra (solid lines) are obtained by convolution of the stick spectra with a Lorentzian function with a FWHM of 10 cm^{-1} .

A comparison of the theoretically calculated spectra of the species relevant for this work in the spectral range from 2000 cm^{-1} to 2200 cm^{-1} is displayed in Figure S1. The accuracy of the computed resonance frequencies differs significantly between the various molecules. While the spectral position of the absorption band of $^t\text{BuNC}$ is reproduced well, the signals of both azide species, N_3^- and [1], are predicted distinctly too high. At the same time, the signals of [4] and [5] are predicted to appear at lower frequencies than experimentally observed. This mismatch can be rationalized by the typical overestimation of vibrational frequencies by hybrid-DFT methods as used in this work. Although this error can

often be corrected by application of a global scaling factor for all computed frequencies, this factor depends not only on the chosen density functional but also on the investigated substances. Thus, the optimal scaling factor has to be determined for each class of compounds individually. Since the vibrations giving rise to the signals illustrated in Figure S1 originate from normal modes centered at different functional groups, the DFT results in conjunction with the application of a *global* scaling factor (here 0.942) cannot provide an accurate description of all absorption spectra at the same time.

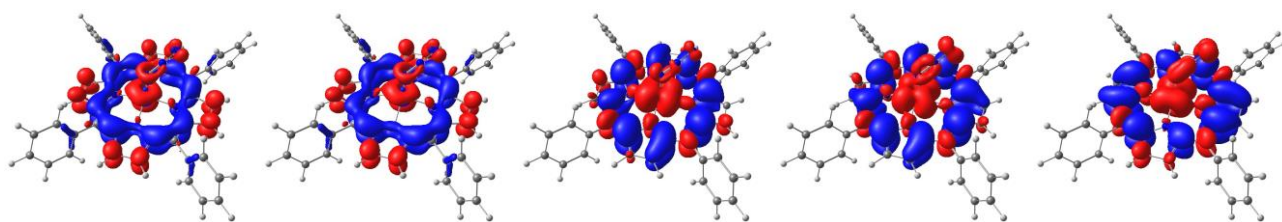
2.4 TDDFT Excitation Energies

Table S6. Excitation energies and corresponding oscillator strengths of [1] calculated by TD-DFT.

root	energy / cm ⁻¹	fosc(vel.)	fosc(len.)
1	3279.106	0.00000675	0.00000463
2	3736.492	0.00000410	0.00000390
3	14856.067	0.00330735	0.00300889
4	15226.338	0.00175550	0.00164812
5	15518.051	0.00180123	0.00167908
6	16254.651	0.00016081	0.00015919
7	16495.253	0.00044390	0.00042780
8	18588.582	0.00921960	0.00868976
9	19020.818	0.01296091	0.01242581
10	19890.305	0.02600042	0.02590952
11	20367.034	0.00351932	0.00311714
12	21383.211	0.00187396	0.00188070
13	21551.417	0.00205101	0.00180091
14	22238.240	0.02356117	0.02528765
15	23067.442	0.00084348	0.00083471
16	23534.222	0.07376582	0.07340224
17	23776.822	0.07255805	0.07111802
18	24683.763	0.04388121	0.04407340
19	25234.169	0.00424625	0.00292392
20	25539.214	0.00123388	0.00099836
21	26455.031	0.10455529	0.11116384
22	27538.998	0.12002834	0.11962127
23	27897.530	0.56877042	0.56352751
24	28074.580	0.51375980	0.51422949
25	28162.727	0.19037863	0.19041899
26	28176.249	0.00873548	0.00872473
27	28224.639	0.03585863	0.03594091
28	28278.155	0.00301177	0.00301415
29	28427.356	0.05231845	0.05245025
30	29147.883	0.00014373	0.00013947
31	29394.299	0.05940159	0.05902615
32	29494.297	0.20356896	0.20426323
33	29912.607	0.00346068	0.00337858
34	30055.704	0.01861683	0.01886927
35	30621.868	0.27759740	0.28395945
36	31759.853	0.01038753	0.01127982
37	32158.027	0.03104222	0.03145321
38	32262.427	0.01408766	0.01449099
39	32922.796	0.00040201	0.00041102
40	34037.766	0.00433837	0.00410870
41	34369.541	0.01688601	0.01635975
42	34610.894	0.01638607	0.01602781
43	34884.112	0.00393111	0.00377342
44	35193.943	0.00051744	0.00049208
45	35684.751	0.00820403	0.00830765
46	36060.992	0.00043838	0.00051694
47	36136.068	0.00012977	0.00009967
48	36424.501	0.01349927	0.01380733

49	36587.691	0.00435754	0.00456684
50	36796.109	0.01156139	0.01175710
51	37135.082	0.00276142	0.00287593
52	37365.042	0.01511935	0.01612827
53	37503.428	0.03277418	0.03335636
54	37633.251	0.00272328	0.00275328
55	37840.285	0.07423480	0.07477187
56	37910.374	0.05479063	0.05536594
57	38068.247	0.11518193	0.11619441
58	38154.452	0.00352702	0.00353659
59	38504.646	0.01187002	0.01205195
60	38717.085	0.00170709	0.00179415
61	38751.695	0.00132012	0.00134854
62	38823.512	0.00168018	0.00175144
63	38854.409	0.00071679	0.00073055
64	38888.585	0.00011116	0.00012313
65	38895.178	0.00013921	0.00013964
66	38937.997	0.00012251	0.00013533
67	38974.993	0.00337641	0.00365287
68	39031.290	0.00022032	0.00022752
69	39437.209	0.00002121	0.00002319
70	39494.417	0.00187309	0.00193812
71	39603.089	0.03299820	0.03403842
72	39890.592	0.23287127	0.24102249
73	39949.490	0.09052038	0.09330138
74	40274.554	0.12800885	0.13263517
75	40417.895	0.05957535	0.06231870
76	40563.826	0.01902724	0.01965041
77	40697.680	0.01266537	0.01321826
78	41022.437	0.00306545	0.00305071
79	41092.765	0.00435976	0.00456698
80	41130.333	0.00404712	0.00400757
81	41361.834	0.00110912	0.00108314
82	41390.573	0.00425168	0.00430445
83	41408.310	0.00544221	0.00547780
84	41507.212	0.00104824	0.00106240
85	41599.145	0.00064202	0.00070289
86	41793.636	0.01686752	0.01775056
87	41827.171	0.02272045	0.02507625
88	41877.449	0.02508596	0.02863995
89	41963.889	0.02433831	0.02750789
90	42033.405	0.00028610	0.00040850
91	42124.034	0.01582654	0.01648903
92	42238.330	0.00625757	0.00653449
93	42285.859	0.01345925	0.01381483
94	42486.177	0.01248689	0.01210012
95	42557.088	0.02270729	0.02310605
96	42654.408	0.03001083	0.03151807
97	42713.653	0.02340934	0.02419405
98	42760.743	0.01436454	0.01392217
99	42939.451	0.05832480	0.05749169
100	43032.948	0.00979780	0.00946361
101	43229.562	0.01487788	0.01472741
102	43304.270	0.08277158	0.08110216
103	43518.604	0.04470560	0.04601485
104	43604.551	0.00578822	0.00597321
105	43674.825	0.01069804	0.01045384

2.5 TDDFT Unrelaxed Difference Densities



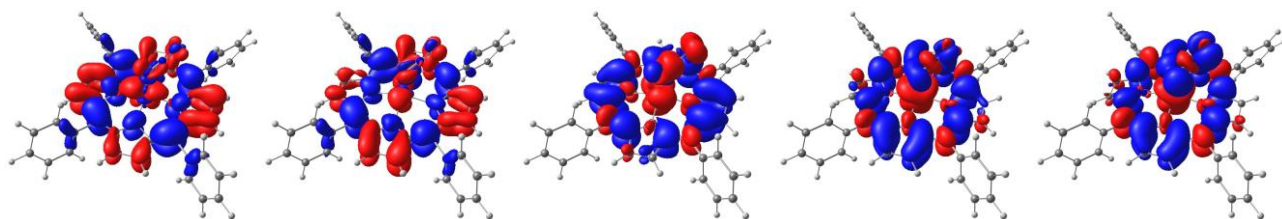
a) root 1

b) root 2

c) root 3

d) root 4

e) root 5



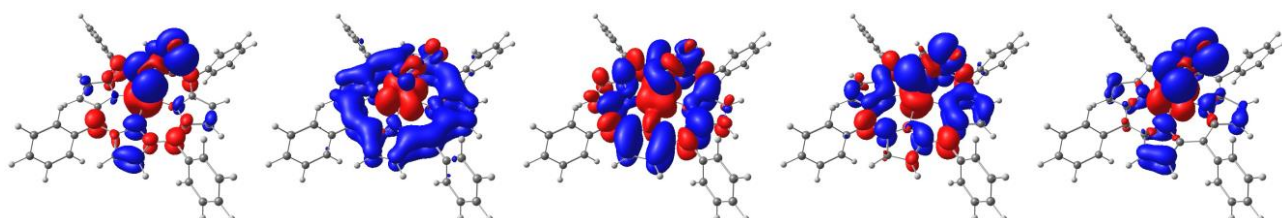
f) root 6

g) root 7

h) root 8

i) root 9

j) root 10



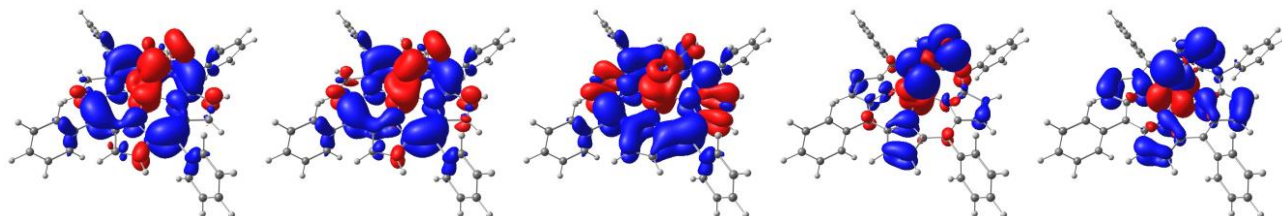
k) root 11

l) root 12

m) root 13

n) root 14

o) root 15



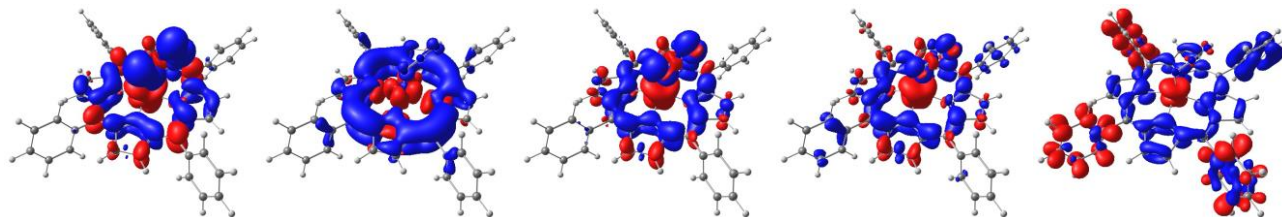
p) root 16

q) root 17

r) root 18

s) root 19

t) root 20



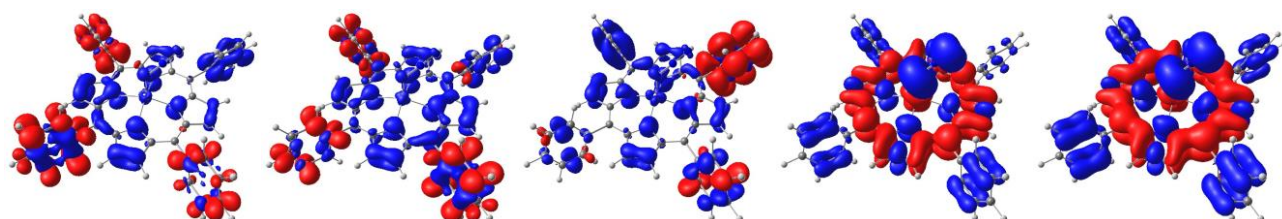
u) root 21

v) root 22

w) root 23

x) root 24

y) root 25



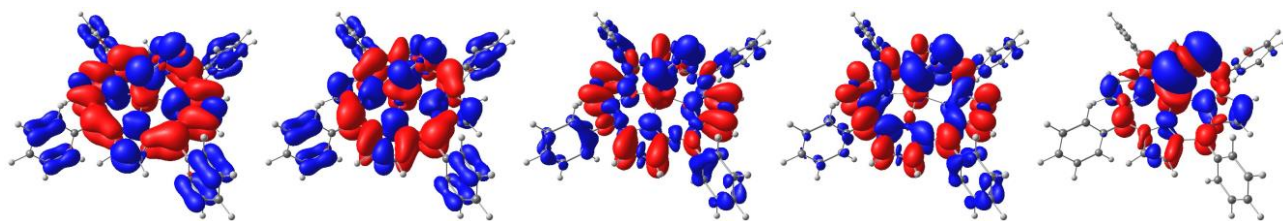
z) root 26

aa) root 27

ab) root 28

ac) root 29

ad) root 30



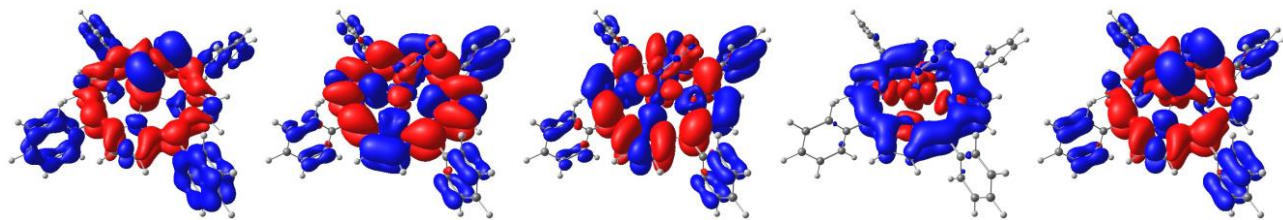
ae) root 31

af) root 32

ag) root 33

ah) root 34

ai) root 35



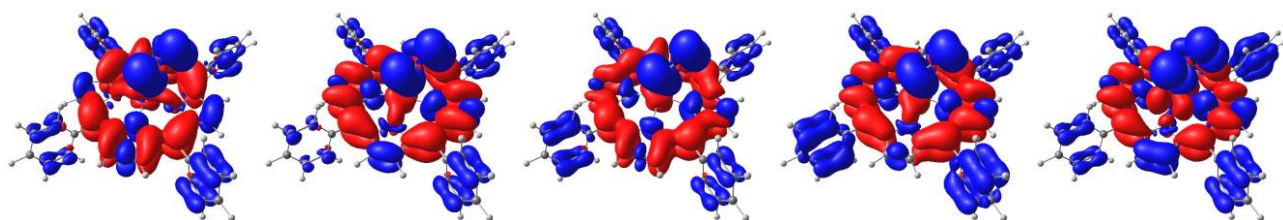
aj) root 36

ak) root 37

al) root 38

am) root 39

an) root 40



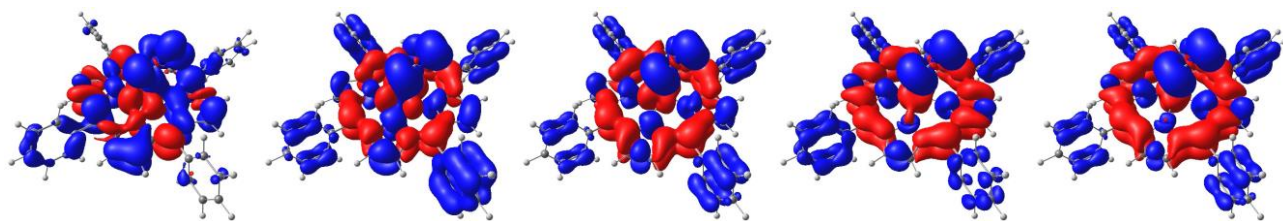
ao) root 41

ap) root 42

aq) root 43

ar) root 44

as) root 45



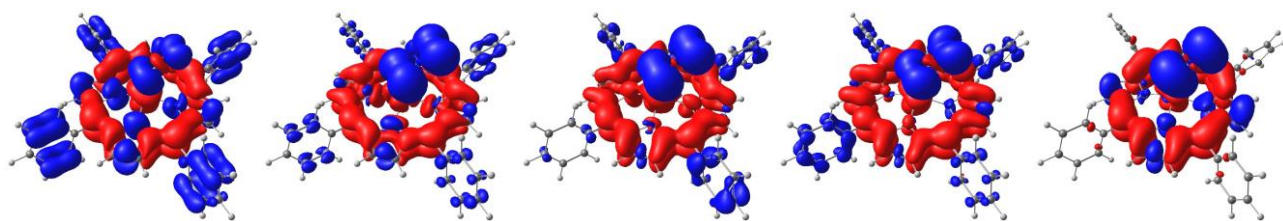
at) root 46

au) root 47

av) root 48

aw) root 49

ax) root 50



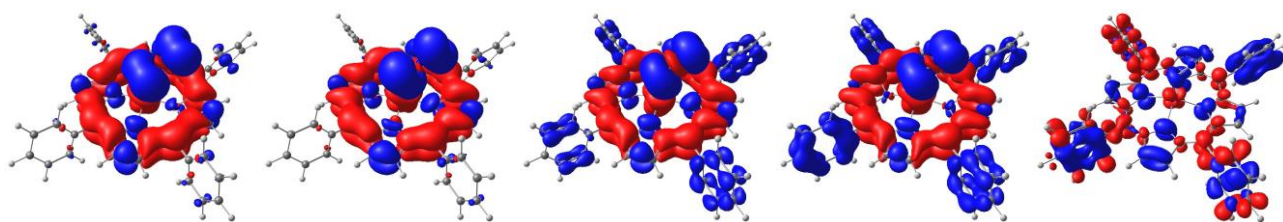
ay) root 51

az) root 52

ba) root 53

bb) root 54

bc) root 55



bd) root 56

be) root 57

bf) root 58

bg) root 59

bh) root 60

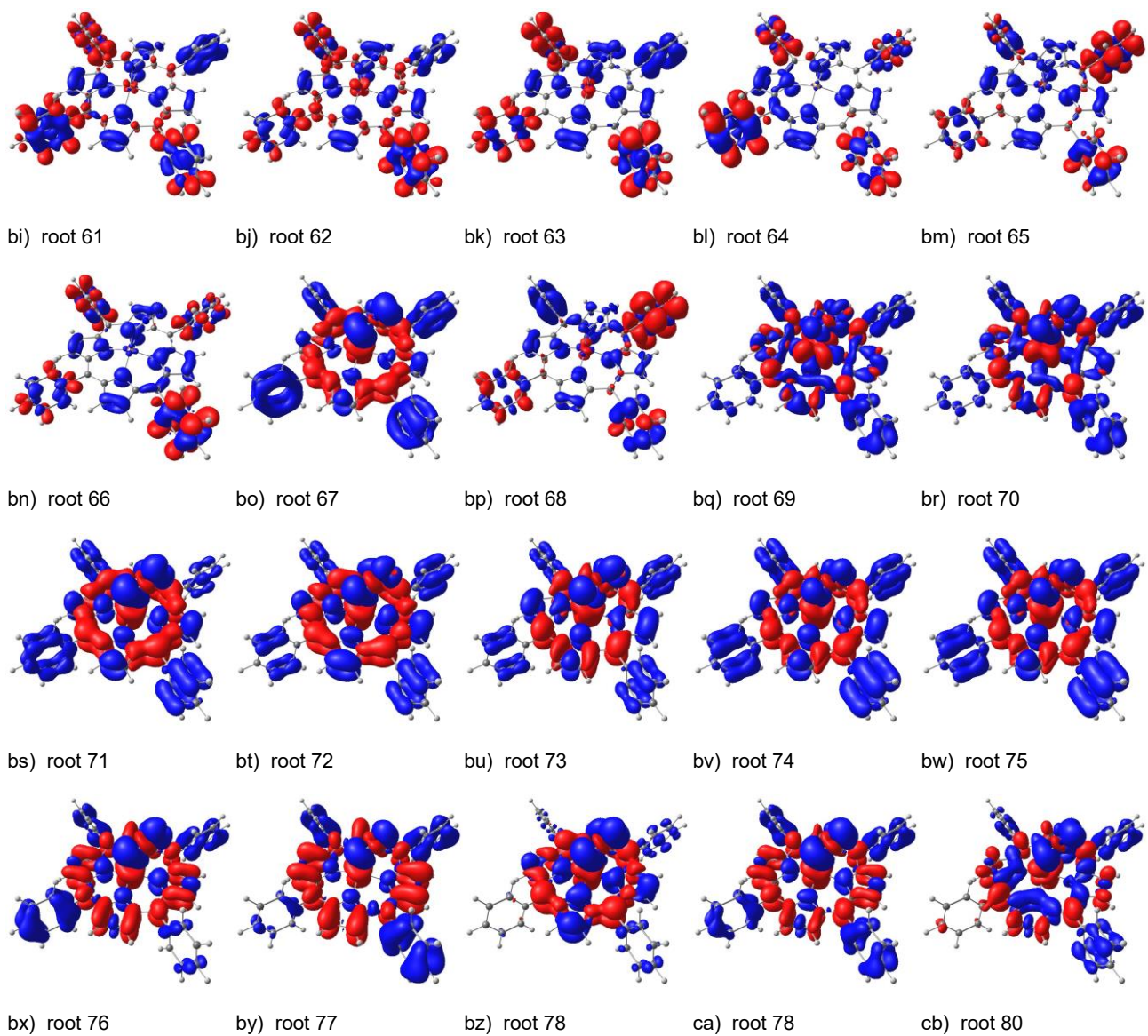


Figure S2. TD-DFT calculated unrelaxed transition densities of [1], isovalues: red: +0.0003, blue -0.0003.

3 Transient Absorption Spectra

3.1 510 nm Excitation

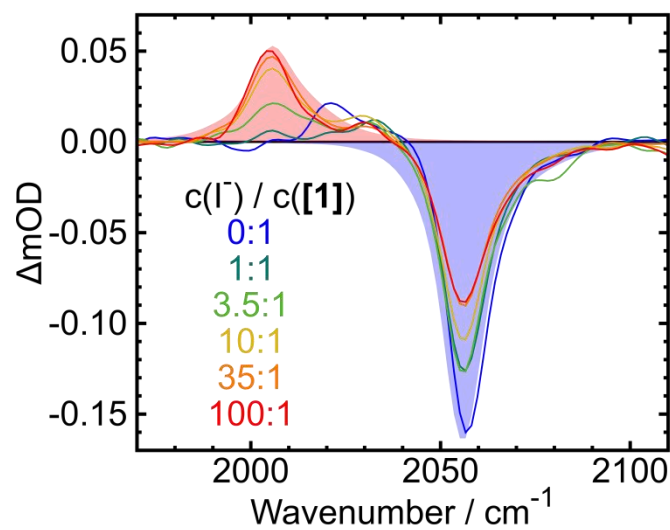


Figure S3. Difference spectra of solutions of [1] and $^{13}\text{Bu}_4\text{NI}$ after 510 nm excitation for various concentration ratios of the two reactants, as indicated by the legend. The blue and red areas represent the (inverted,) properly scaled, stationary FTIR spectrum of [1] and N_3^- , respectively.

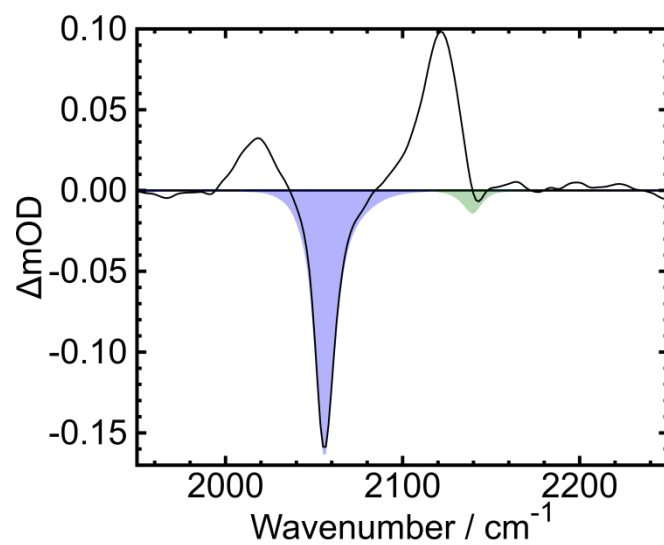


Figure S4. Difference spectrum of a solution of [1] and $^{13}\text{BuNC}$ of equal concentrations recorded 10-40 seconds after 510 nm excitation. The blue and green areas represent the inverted, properly scaled, stationary FTIR spectrum of [1] and $^{13}\text{BuNC}$, respectively.

3.2 355 nm Excitation

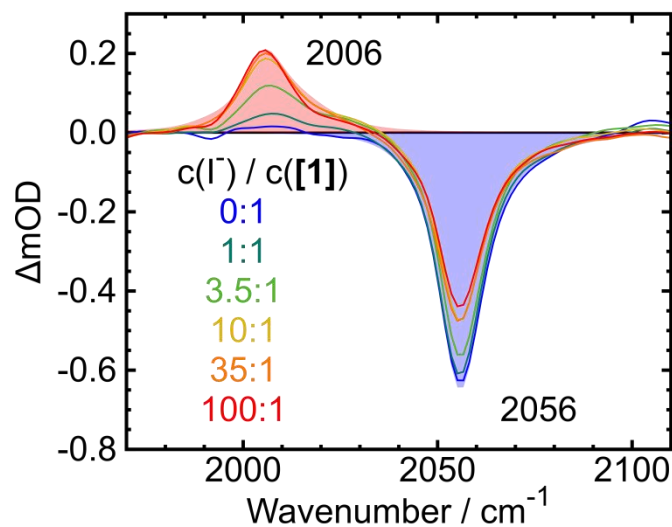


Figure S5. Difference spectra of solutions of [1] and ⁹Bu₄NI after 355 nm excitation for various concentration ratios of the two reactants, as indicated by the legend. The blue and red areas represent the (inverted,) properly scaled stationary FTIR spectrum of [1] and N₃⁻, respectively.

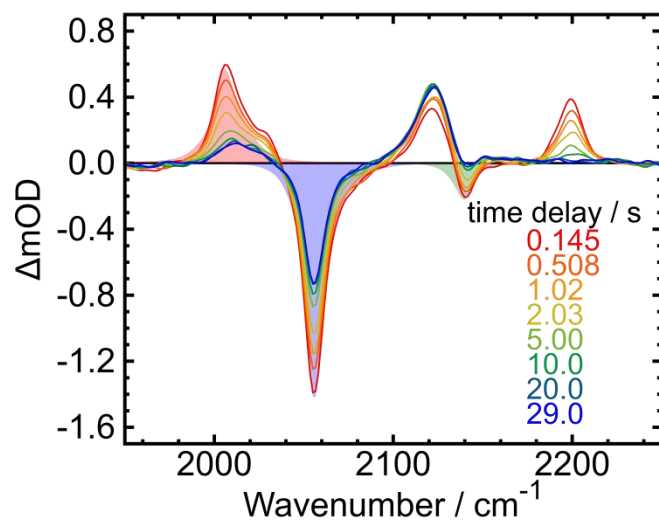


Figure S6. Transient Rapid-Scan spectra of a solution of [1] and ⁴BuNC of equal concentrations recorded at various time delays after 355 nm excitation, as indicated by the legend. The blue, red and green areas represent the (inverted,) properly scaled stationary FTIR spectrum of [1], N₃⁻ and ⁴BuNC, respectively.

4 Kinetic Trace after 266 nm Excitation

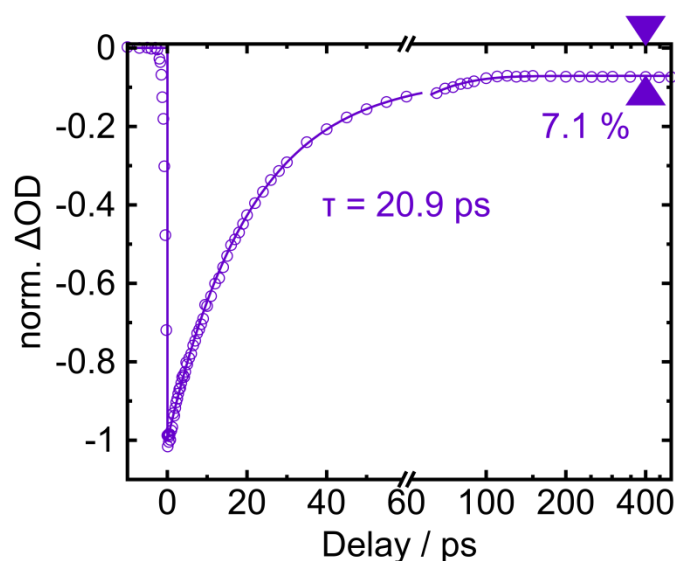


Figure S7. Femtosecond 266 nm-pump/IR-probe kinetic trace of a solution [1] in CH_2Cl_2 normalized to the maximal bleach around a delay of zero. The data were recorded at a probe wavenumber of 2056 cm^{-1} corresponding to the peak of the N_3^- antisymmetric stretching vibration of [1]. Note that the abscissa switches from linear to logarithmic scaling at a delay of 60 ps.

The femtosecond 266 nm-pump/ 2056 cm^{-1} -probe kinetic trace [1] in CH_2Cl_2 solution displayed in Figure S7 allows quantification of the combined primary photoconversion yield Φ_{prim} at this excitation wavelength: $\Phi_{\text{prim}} = 7.1\%$. The determination of the fractional yields of photoreduction and photooxidation as conducted for the excitation wavelengths 355 nm, 400 nm and 510 nm is not feasible for 266 nm photolysis since the utilized quencher, tetrabutylammonium iodide, exhibits an absorption ($\epsilon = 1.0 \cdot 10^3\text{ L mol}^{-1}\text{ cm}^{-1}$) at this wavelength (cf. Figure S8). However, the fractional yield of the redox-neutral N_3^- cleavage is zero, as the characteristic absorption band of the azide anion is absent in the corresponding transient spectra.^[8]

5 UV-Vis Absorption Spectrum of Tetrabutylammonium Iodide

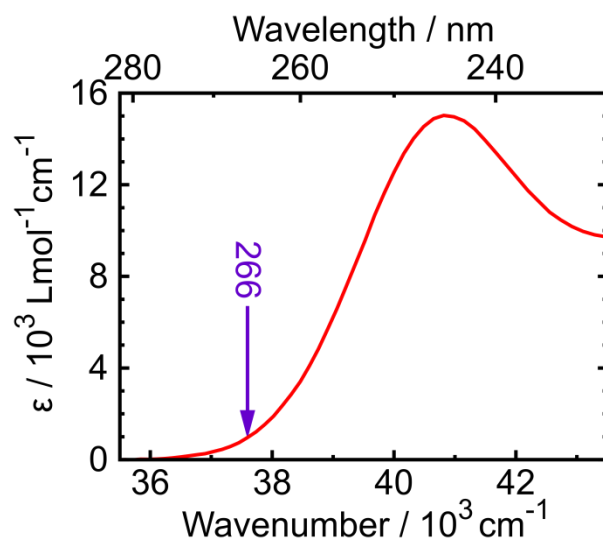


Figure S8. Stationary UV-Vis absorption spectrum of tetrabutylammonium iodide, $(\text{tBu}_4\text{N})\text{I}$, in CH_2Cl_2 . The labeled, violet arrow points towards a wavelength of 266 nm, one of the excitation wavelengths used in the photolysis experiments.

6 Parameters of Linear Regressions

Linear regression to determine the bimolecular rate constant k of the reaction, $[5] + \text{N}_3^- \longrightarrow [1] + 2 \text{ }^t\text{Bu-NC}$, were obtained by solving the rate equation of second order for $c([5]) = c(\text{N}_3^-)$ and reformulation in terms of the differential optical density ΔOD as shown in equation (1) for reactants and equation (2) for products.

$$\delta_R^{-1} = k'_R t = \frac{1}{\Delta\text{OD}(\tilde{\nu}_R, t) - \Delta\text{OD}(\tilde{\nu}_R, \infty)} - \frac{1}{\Delta\text{OD}(\tilde{\nu}_R, 0) - \Delta\text{OD}(\tilde{\nu}_R, \infty)} \quad (1)$$

$$\delta_P^{-1} = -k'_P t = \frac{1}{\Delta\text{OD}(\tilde{\nu}_P, t) - \Delta\text{OD}(\tilde{\nu}_P, \infty)} - \frac{1}{\Delta\text{OD}(\tilde{\nu}_P, 0) - \Delta\text{OD}(\tilde{\nu}_P, \infty)} \quad (2)$$

Here, $\Delta\text{OD}(\tilde{\nu}_{R/P}, 0)$ and $\Delta\text{OD}(\tilde{\nu}_{R/P}, \infty)$ are the initial ($t = 0$ s) and asymptotic values of ΔOD , respectively, and $k'_{R/P}$ the effective rate constants. In order to improve the signal-to-noise ratio, the median of ΔOD within a spectral range defined by the boundaries $\tilde{\nu}_{low}$ and $\tilde{\nu}_{high}$ was determined for each signal and time. In addition, the averaged extinction coefficient $\langle \varepsilon_{R/P} \rangle$ within the same range was calculated from the stationary absorption spectra, if available. The parameters $\Delta\text{OD}(\tilde{\nu}_{R/P}, 0)$ and $\Delta\text{OD}(\tilde{\nu}_{R/P}, \infty)$ were adjusted manually. $k'_{R/P}$ were obtained by least square fits of the linearized kinetic traces in the temporal window from 0 s to 11 s and converted to k by equation (3). All parameters are listed in Table S7.

$$k'_{R/P} = k / [\varepsilon_{R/P}(\tilde{\nu}_{R/P}) d] \quad (3)$$

Table S7. Lower and upper frequency boundaries, $\tilde{\nu}_{low}$ and $\tilde{\nu}_{high}$, chosen for the evaluation of the time dependence of the signals observed in the photolysis of a solution of [1] and $^t\text{BuNC}$; averaged extinction coefficients, $\langle \varepsilon_{R/P} \rangle$, initial and asymptotic differential optical densities, $\Delta\text{OD}(\tilde{\nu}_{R/P}, 0)$ and $\Delta\text{OD}(\tilde{\nu}_{R/P}, \infty)$, determined within these boundaries; bimolecular rate constants, k , and effective rate constants, $k'_{R/P}$, calculated by linear regressions using equations (1)-(3). Reduced χ^2 , R^2 and correlation coefficients, $\rho_{exp,fit}$, of the regressions.

	N_3^-	[1]	$^t\text{BuNC}$	[5]
$\tilde{\nu}_{low} / \text{cm}^{-1}$	1990	2041	2134	2183
$\tilde{\nu}_{high} / \text{cm}^{-1}$	2021	2075	2149	2222
$\langle \varepsilon_{R/P} \rangle / \text{M}^{-1}\text{cm}^{-1}$	1154	1004	195	832 ^[a]
$\Delta\text{OD}(\tilde{\nu}_{R/P}, 0) \cdot 10^5$	3.57	-7.39	-1.59	2.00
$\Delta\text{OD}(\tilde{\nu}_{R/P}, \infty) \cdot 10^5$	0.21	-4.09	0.36	-0.06
$k'_{R/P} / 10^3 \text{ s}^{-1}$	1.97 ± 0.30	1.88 ± 0.30	4.98 ± 1.00	2.44 ± 0.30
$k / 10^4 \text{ M}^{-1} \text{ s}^{-1}$	2.27 ± 0.35	1.88 ± 0.30	1.94 ± 0.39	2.03 ± 0.35 ^[b]
χ^2_{red}	4.388	3.551	151.7	7.843
R^2	0.8989	0.9088	0.6077	0.8837
$\rho_{exp,fit}$	0.9594	0.9537	0.7813	0.9405

[a] corresponds to the value that is consistent with a rate of $2.03 \cdot 10^4 \text{ M}^{-1} \text{ s}^{-1}$.

[b] corresponds to the average of the entries for the other three species.

7 References

- [1] K. M. Adams, P. G. Rasmussen, W. R. Scheidt, K. Hatano, *Inorg. Chem.*, **1979**, *18*, 1892- 1899.
- [2] S. Flesch, P. Vöhringer, *Angew. Chem. Int. Ed.* **2022**, *61*.
- [3] a) TURBOMOLE V7.5 2020, a development of University of Karlsruhe and Forschungszentrum Karlsruhe GmbH, 1989-2007, TURBOMOLE GmbH, since 2007; available from <http://www.turbomole.com>. b) R. Ahlrichs, M. Bär, M. Häser, H. Horn, C. Kölmel, *Chem. Phys. Lett.* **1989**, *162*, 165-169. c) O. Treutler, R. Ahlrichs, *J. Chem. Phys.* **1995**, *102*, 346-354. d) M. Von Arnim, R. Ahlrichs, *J. Comput. Chem.* **1998**, *19*, 1746-1757.
- [4] J.-D. Chai, M. Head-Gordon, *J. Chem. Phys.* **2008**, *128*, 084106.
- [5] a) E. Caldeweyher, C. Bannwarth, S. Grimme, *J. Chem. Phys.* **2017**, *147*, 034112. b) E. Caldeweyher, S. Ehlert, A. Hansen, H. Neugebauer, S. Spicher, C. Bannwarth, S. Grimme, *J. Chem. Phys.* **2019**, *150*, 154122.
- [6] a) A. Schäfer, C. Huber, R. Ahlrichs, *J. Chem. Phys.* **1994**, *100*, 5829-5835. b) F. Weigend, R. Ahlrichs, *Phys. Chem. Chem. Phys.* **2005**, *7*, 3297-3305.
- [7] A. Schäfer, H. Horn, R. Ahlrichs, *J. Chem. Phys.* **1992**, *97*, 2571-2577.
- [8] to be published